Fault-Tolerant Integrated Modular Motor Drive for Applications with Demanding Reliability Requirements

by

James A. Swanke III

A dissertation submitted in partial fulfillment

of the requirements for the degree of

Doctor of Philosophy

(Electrical Engineering)

at the

UNIVERSITY OF WISCONSIN - MADISON

2023

Date of final oral examination: 01/20/2023

The dissertation is approved by the following members of the Final Oral Committee:

Thomas Jahns, Professor Emeritus, Electrical and Computer Engineering

Bulent Sarlioglu, Professor, Electrical and Computer Engineering

Daniel Ludois, Associate Professor, Electrical and Computer Engineering

Gregory Nellis, Professor, Mechanical Engineering

Thomas Tallerico, Aerospace Research Engineer, NASA Glenn Research Center

Abstract

Permanent magnet synchronous machines (PMSMs) are commonly used in transportation vehicle applications due to their high efficiency and low mass features. Additional performance benefits including enhanced fault tolerance can be achieved by integrating the associated drive power electronics into the machine housing to form an integrated motor drive (IMD). The PMSM IMD is a promising candidate for emerging electric aircraft propulsion applications that have much more demanding reliability requirements compared to typical automotive and industrial applications.

The incorporation of fault-tolerant (FT) features into the IMD design provides a path for significantly improving the overall drive system reliability. One of the more promising techniques for enhancing a motor drive's fault tolerance is to divide it into multiple modular three-phase channels, enabling continued operation after one or more faults. Maintaining electrical and electromagnetic isolation between the three-phase channels is critical in modular motor drives to avoid fault propagation.

Combining this modularity with the basic IMD concept results in an integrated modular motor drive (IMMD) that is the focus of this PhD research program. Specific IMMD research topics addressed during this program include machine power density, module isolation, performance, reliability, and tradeoffs between these features. Lessons from the tradeoff study are initially applied to a modular propulsor machine used in a six-passenger quadrotor aircraft. A promising IMMD configuration with appealing electromagnetic and thermal isolation characteristics has been proposed and evaluated consisting of a 24-slot, 28-pole PMSM with double-layer (DL) concentrated windings arranged into a four-module IMMD configuration. To enhance the

electromagnetic isolation, open cavities have been introduced into the stator yoke, and the stator tooth tip shapes have been manipulated to minimize electromagnetic interactions between adjacent phase modules while minimizing the negative impact on the machine's mass and volume. In addition, direct cooling inside the stator slots and careful design of the electrical/thermal insulation system provides the desired thermal isolation between machine phases. A thorough evaluation of this modular machine topology confirmed that it ranks high in providing promising levels of module isolation and fault tolerance with only a modest negative impact on power density.

Reliability analysis has been carried out for the target four-module IMMD configuration using Markov chain and state-space analysis tools. This analysis addresses the major components in the drive system's machine and electronics, including their associated stresses during healthy and faulted operation. Specific faults that are being studied include stator winding turn-to-turn faults which can be particularly dangerous for PMSMs. The importance of frequent repairs and the critical role of the single-point failure rate in determining the complete IMMD's failure rate are highlighted. These stresses are evaluated using a combination of closed-form analysis and finite element analysis (FEA) tools. Finally, the analysis is generalized to also consider the impact of the IMMD's module count and the number of faulted modules on the motor drive's reliability metrics in order to evaluate and enhance the IMMD's potential for meeting the highly demanding reliability requirements of motor drives developed for aircraft propulsion applications. The tool is further generalized, and figures of merit are established to compare FT topologies on the basis of their improved reliability potential measured against their offsetting penalties (mass, etc.).

The developed isolation concepts have been subsequently refined and simplified during the design and fabrication of a two-module low-power PMSM with fractional slot concentrated windings (FSCW). The demonstrator machine's parameters and performance characteristics were

first validated experimentally under healthy operating conditions, followed by a series of tests that applied a variety of module fault conditions which encompassed both open-circuit and short-circuit fault conditions, including challenging turn-to-turn winding faults. The results of these tests confirmed both the effectiveness of the electromagnetic and thermal isolation features that were incorporated into the design, as well as the ability of the healthy module to continue delivering its pre-fault rated torque following the fault. These positive test results have strengthened confidence in the value and importance of modularity in future fault tolerant motor drives that are critical to the success of demanding drive applications including electrically-propelled aircraft.

Acknowledgements

There are countless people to acknowledge and thank for their support and guidance throughout the duration of this thesis, and for their impact on my graduate school experience here at the University of Wisconsin (UW) and within the Wisconsin Electric Machines and Power Electronics Consortium (WEMPEC). I will do my best to acknowledge their impact here.

First and foremost, I want to thank my advisor Professor Thomas M. Jahns for his incredible guidance, advice, and support throughout this PhD program. I owe so much of my personal and technical growth to him through the many opportunities he gave to me—learning from him on these projects has been second-to-none. Further, his work-ethic, energy, and conduct as a researcher is an inspiration as I move into the next phase of my career.

I also want to thank Professor Bulent Sarlioglu for being my co-advisor and for his impact on my PhD experience including his participation in my PhD oral exam committee. I have always valued his advice and experience surrounding electrical machines and their application to aerospace applications. Similarly, thank you to the other oral exam committee members including Professor Dan Ludois, Professor Greg Nellis, and NASA Glenn research engineer Tom Tallerico. I appreciate the time you invested in this work, and for your valuable feedback and comments.

I want to thank NASA and the Ohio State University (OSU) for funding this research through the NASA ULI research program. Special thanks to NASA's Linda Taylor, Tim Kranz, and others who supported this work and provided regular technical feedback related to this work. Thanks to Arnold Magnetics Technology Center engineers Dave Farnia, Ryan Halverson, and Frank Roach for allowing me to participate in the 1MW and 200kW rated machine builds for the ULI research program.

I want to thank the WEMPEC professors, staff, and students for their support and guidance throughout my PhD experience. Special thanks to Kyle Hanson and Pia Strampp for their sage guidance and advice related to the lab work completed for this thesis. Additionally, thanks to Kathy Young for her administrative support. I will always appreciate her lending me my own conference room key to help me manage my gruesome meeting schedule. Last, thanks to current and former students Wenda Feng, Ken Chen, Xiaoyuan Zhang, Justin Paddock, Sangwhee Lee, Dr. Hao Zeng, Dr. Renato Torres, Dr. Pablo Castro Palavicino, Dr. Dheeraj Bobba, and Dr. Jayer Fernandez for your colleagueship and friendship.

Special thanks to Dr. Hao Zeng and Xiaoyuan Zhang who played a crucial role in the completion of this thesis. Dr. Zeng applied his electrical machine controls and power electronics expertise to the experiments presented in this thesis. Xiaoyuan was instrumental to the fabrication and assembly of the presented fault-tolerant demonstrator machine, keeping the build going while I was away from campus participating in remote machine testing.

Finally, thanks to my parents Jim and Barbara Swanke, my siblings Katie Lutes, Maria Johnson, and John Swanke, and my partner Sarah Miller for their endless love and support. This thesis is dedicated to them.

Table of Contents

Contents

List of Figures

List of Tables

Nomenclature

Acronym	Description
CL	Closed Loop
CSI	Current Source Inverter
CTE	Coefficients of Thermal Expansion
DL	Double Layer
EM	Electromagnetic
FEA	Finite Element Analysis
FoM	Figure of Merit
FSCW	Fractional Slot Concentrated Winding
FT	Fault Tolerance
FTA	Fault Tree Analysis
IM	Induction Machines
IMD	Integrated Motor Drive
IMMD	Integrated Modular Motor Drive
IPM	Interior Permanent Magnet
LIIR	Leakage Inductance Isolation Ratio
MIR	Module Isolation Ratio
MIIR	Mutual Inductance Isolation Ratio
MLIR	Mutual Leakage Inductance Ratio
MMD	Modular Motor Drives
MMF	Magnetomotive Force
MTTF	Mean Time to Failure
NASA	National Aeronautics and Space Administration
PCB	Printed Circuit Board
PE	Power Electronics
PM	Permanent Magnet
PMSM	Permanent Magnet Synchronous Machine
PoF	Physics of Failure
OC	Open Circuit
OL	Open Loop
RVLT	Revolutionary Vertical Lift Technology
SC	Short Circuit
SL	Single Layer
SP	Single Point
SPM	Surface Permanent Magnet
SPP	Slot Per Pole Per Phase
SR	Switched Reluctance
SynRM	Synchronous Reluctance Machine
UAM	Urban Air Mobility
ULI	University Led Initiative
VSI	Voltage Source Inverter
VTOL	Vertical Takeoff and Landing
WBG	Wide Bandgap Devices
WFSM	Wound Field Synchronous Machine
λ	Failure rate [1/hours]
μ	Repair Rate [1/hours]

Chapter 1

Introduction

1.1. Background and Motivations

High system reliability is a primary concern in safety-critical applications. This crucial importance of reliability is exemplified by emerging electrically-propelled aircraft where failures of one or more propulsor machines or drives could lead to a catastrophic loss of the aircraft. Compared to terrestrial applications, a major improvement in motor drive reliability is necessary to ensure safe operation of these new vehicles while simultaneously achieving both low mass and high-performance characteristics. Fault-tolerant integrated motor drives can be introduced to improve machine drive reliability, but this change is often accompanied by negative impacts on drive cost, performance, and mass. This section discusses the background and motivation that underlies this research program which directly addresses these tradeoffs.

1.1.1. Emergence of electrically propelled passenger aircraft

A steady progression towards increased aircraft electrification has been under way since the early 1990s when the More-Electric Aircraft (MEA) initiative was launched by the US Air Force to investigate the replacement of traditional hydraulic and pneumatic systems with electrical machines and drives (e.g., pumps, starter/alternators, etc.) [1]–[3]. In the 2000s, this electrification trend has gradually shifted to electrifying the main aircraft propulsion powertrain by replacing the traditional gas-turbines, opening the door to innovative aircraft power systems and vehicle designs. Studies by NASA and the US National Academy of Engineers (NAE) during this time confirmed that an electric propulsion approach held promise as a means to reduce aircraft emissions, fuel-burn, and noise [4]–[6]. Since then, numerous conceptual single-aisle aircraft concepts have been

developed [4], [6]–[10], and several smaller aircraft (1 to 10 passenger) have demonstrated electrified flight architectures [6], [9]–[11].

Transportation congestion and projected population growth in large metropolitan areas have also motivated the development of Vertical Takeoff and Landing (VTOL) Urban Air Mobility (UAM) vehicles as an alternative to larger single-aisle commercial aircraft with conventional winged designs. These aircraft vary drastically in appearance compared to a traditional passenger aircraft with several concept vehicles shown in [12], [13]. This space is highly active in the 2020s with well-established aerospace companies including Boeing and Airbus, as well as a myriad of startups including Joby, Lilium, and many others introducing innovative UAM aircraft designs [6], [9], [14], [15].

This emerging application of electric machines and drives has demanding performance requirements not previously experienced in cost-sensitive industrial and automotive applications. For larger single-aisle aircraft, this requires megawatt-class electrical machine drives with total power densities (motor plus drive) exceeding 12 kW/kg which is a massive increase in power density compared to existing terrestrial machine drives in the range of 1 to 3 kW/kg [5], [6], [16].

This pursuit of megawatt-scale power-dense machines has been thoroughly pursued in recent years with several examples discussed in the literature and industry [5], [17]–[23]. Many of these machines use expensive high-performance materials including cobalt-iron laminations, rare-earth magnets, and litz wire; aggressive direct cooling of the stator windings is often necessary. Often these machines are permanent magnet synchronous machines (PMSM) designed with fractional-slot concentrated winding (FSCW) stators due to their appealing power density characteristics [17], [22], although other topologies including cryogenically-cooled wound-field synchronous machine (WFSMs) are also being aggressively developed [20]. Further system power density benefits can

be realized by adopting an integrated motor drive (IMD) configuration that combines the machine, power electronics, and shared cooling systems into one housing, while also dramatically shortening the machine cables connecting the machine and drive [24].

In addition to power density and performance, these aircraft propulsor systems also need to achieve ultra-high reliability to avoid catastrophic hard-landing scenarios. In general, commercial aircraft are designed to achieve 10^{-9} catastrophic failures per hour for the complete aircraft, which is extremely demanding compared to other terrestrial transportation vehicles [25]. As a rule of thumb, this aircraft-level failure rate requirement is typically interpreted to require failure rates of the aircraft propulsion equipment to be a least an additional order of magnitude lower, corresponding to 10^{-10} failures per hour or less [26]. The use of Distributed Electric Propulsion (DEP) can be introduced to achieve machine drive redundancy along plus additional associated aerodynamic performance benefits [9]. However, there are likely to be many cases where DEP is not practical from a mission standpoint or inadequate by itself to achieve the necessary reliability levels. For instance, a UAM VTOL aircraft reliability study has been performed on NASA concept vehicles in [26] that identifies electrical machines and drives as being limiting reliability components for the electric VTOL because their lowest known failure rates are on the order of 10^{-6} failures per hour, which is 3 orders of magnitude higher than the 10^{-9} target.

1.1.2. Permanent Magnet Synchronous Machine Fault Tolerance Benefits and Challenges

The incorporation of fault-tolerant (FT) features into electric machines and drives provides a highly promising path to improve aircraft reliability without the need for propulsor redundancy or DEP. First, it is necessary to clarify the relationship between system reliability, component

reliability, and machine-drive fault-tolerance. In the context of this thesis, the system reliability refers to aircraft and the component reliability refers to the propulsor machine-drive as illustrated in Fig. 1.1-1. For a safety-critical application like aviation the system reliability is paramount and is the reliability metric of interest. The introduction of fault-tolerance into the propulsor motor-drive allows for possible component level failure (i.e., poor component reliability) without directly affecting the system reliability. In other words, FT decouples system reliability from component reliability.

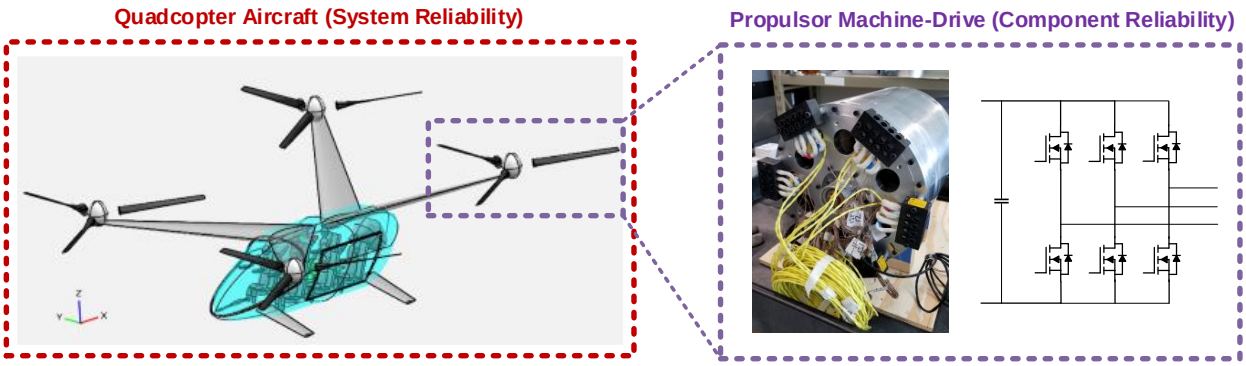

Figure 1.1-1 Quadcopter aircraft system and component reliability differentiation (image modified from [27])

The incorporation of FT features in aircraft motor-drives allow full or partial operation of a propulsor after one or multiple failures in the power electronics drive or electrical machine. However, the use of power-dense PMSM topologies pose unique challenges to FT systems due to the constant rotor magnetic field produced by the rotor magnets that cannot be turned off in the event of a failure.

The study of fault-tolerant machines and drives has been a topic of research for many decades. Desirable FT PMSM machine drive features are enumerated in [28], including: (1) electric

(galvanic) isolation of modular drives; (2) electromagnetic isolation of modular windings; (3) inherent short-circuit current limiting; (4) physical module separation; (5) thermal module isolation; and (6) higher phase number. One approach to implementing these features adopts multi-phase machines with single-layer (SL) concentrated windings, with each phase excited by its own full-bridge inverter [28] as shown in the example machine in Fig. 1.1-2. A major challenge with this design approach is to achieve high modular isolation while minimizing any negative impact on power density.

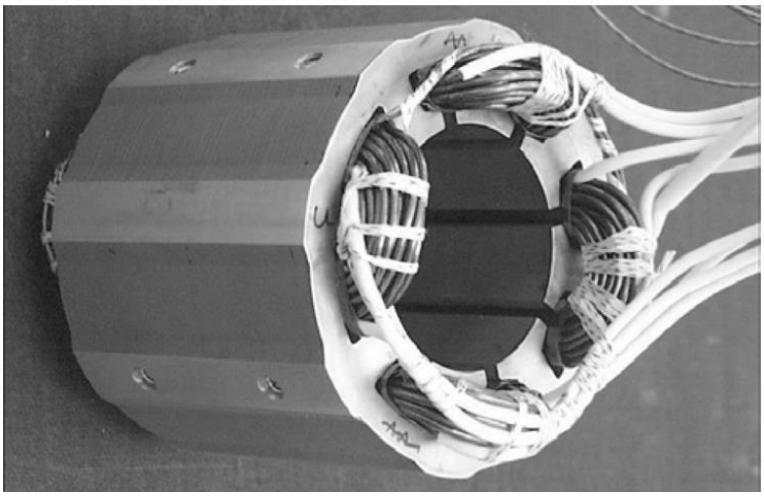

Figure 1.1-2 Example FT stator utilizing SL windings and four-phases [29]**.**

A modified approach to applying these FT design principles is to break the machine stator into multiple three-phase winding groups instead of individual phases, with each winding group excited by its own dedicated 3-phase inverter. Modular isolation can be achieved by using a SL winding, as demonstrated in a 4-module 24s/28p FT machine (Slot/phase/pole = SPP = 2/7) [30]. However, the use of SL windings penalizes the machine efficiency and power density because of bulky end-turns that contribute to higher loss and mass compared to a double-layer (DL) winding alternative.

A 4-module DL winding is used in an aerospace alternator in [31]. Spacer teeth are inserted between the stator modules to improve their electromagnetic isolation. Similar to SL winding isolation, this approach suffers a serious mass and performance penalty compared to standard DL windings.

Looking beyond machine drive modularization, FT features can be directly applied to the drive itself following similar FT principles related to isolation and redundancy. Significant effort has been applied to traditional two-level voltage-source inverters (VSI). A thoroughly-studied approach introduces redundant phase legs allowing for drive reconfiguration after loss of a drive switch [32]–[36]. Alternatively, an open winding (i.e., both sides of each phase winding brought out of the machine with external terminals) can be used with two VSIs making it possible to achieve a higher level of switch fault capability compared to a redundant-phase approach [33], [37]–[39]. Beyond two-level VSIs, alternative converter topologies such as the matrix converter or current-source inverter (CSI) have been considered for FT applications due to their elimination of dc link capacitors that typically have lifetimes that are shorter than those of many other power electronics components [40]–[42].

Conventional reliability estimation techniques such as Markov Chains can be used to evaluate the benefits of FT features in machine-drive systems. Markov chains have been used to develop comparisons of FT power electronics arrangements in [32] and FT machine drives in [43]. A three-module configuration was studied in [43], identifying modularity in combination with repairability as a promising path for significantly improving reliability. More recently the relationship between drive fault tolerance and quadcopter aircraft reliability is studied in [44]. However, these published reliability studies lack generality due to a dependence on underlying failure components, technical tradeoffs between different fault-tolerant approaches are not explored, or limited study scope.

1.2. Problem Statement and Research Objectives

Based on the background provided, the following problem statement and research objectives are defined for this research program:

1.2.1. Overall Research Program Overview

This research program is focused on investigating FT machine and drive configurations in the context of a quadrotor UAM VTOL vehicle. Traditional FT machine modular isolation approaches are evaluated for their isolation capability and performance impact. Subsequently, new alternative isolation approaches are proposed and evaluated that incorporate specialized stator magnetic, slot, and cooling designs. These concepts are applied to developing a FT machine drive design intended for a six-passenger quadrotor UAM vehicle. This design is used to evaluate the healthy and faulted stress of a motor drive system, and the results are fed into a reliability study using Markov chains to explore avenues for reaching ultra-low failures rates of 10^{-9} failures per hour or less required for future electrically-propelled aircraft. The reliability study is generalized to consider different levels of modularity and stresses in the system. Finally, experimental machines are developed and tested to illustrate the impact of high electromagnetic coupling between modules and techniques that effectively suppress it.

1.2.2. Problem Statement Summary

The reasons for pursuing investigations into power dense PMSM utilizing FT for improved reliability are summarized below:

1. Existing studies surrounding power-dense machines for aerospace applications are focused on the demanding challenges of high power density and efficiency, but they fail to strongly focus on reliability requirements and the resulting implications on fault tolerance. More

specifically, comparative evaluations of the reliability characteristics of established FT approaches for electrical machines and drives, and their impact on power density and performance are not thoroughly documented in the literature. Furthermore, Figures of Merit (FoM) metrics do not exist for comparing FT electrical machine drive configurations in a way that reflects inevitable tradeoffs between reliability and the resulting mass and performance of alternative fault-tolerant machine drive configurations.

2. Modular FT machine drives represent an attractive approach for significantly improving machine drive reliability in safety-critical applications. A major consideration for these types of machine drives is the ability of the machines to isolate modules electrically, electromagnetically, and thermally to avoid the propagation of faults between modules. Often these factors have led to the adoption of a SL FSCW stator winding, which has a negative impact on the machine's winding losses and power density. Alternative isolation techniques that do not require spacer teeth have not been investigated in the literature for fault-tolerant PMSMs.
3. Electrical machines and drives are identified as low reliability components in aerospace applications using existing technologies. Minimal quantitative and qualitative evaluations have appeared in the literature to address the potential reliability benefits associated with specific FT motor drive architectures. Often these FT reliability analyses are completed without consideration to the overall system reliability.

1.2.3. Research Objectives

The research objectives of this program are set to overcome the challenges described in the previous section. The specific objectives are summarized as follows:

1. *Evaluate conventional FT machine topologies that initially target a quadrotor aircraft application and then extended to other aircraft applications*

The design and analysis of candidate FT machine configurations for a six-passenger quadrotor aircraft is being evaluated considering multiple performance metrics including power density, efficiency, and torque ripple. In addition to modular machine designs, this comparative analysis will also consider the FT configuration that incorporates a redundant stator on the same shaft. An important part of this evaluation requires the development of sizing equations for high-level differentiation of machine winding types considering tradeoffs between power density and loss. In addition, figures of merit will be developed to enable quantitative comparisons of FT machines and drives for the quadrotor UAM aircraft application and then extended to other electrified aircraft propulsion applications.

2. *Investigate and evaluate alternative modular isolation approaches compared to traditional spacer teeth approaches.*

Alternative electromagnetic, thermal, and physical module isolation approaches are being investigated for FT machine drive applications using DL windings in addition to the SL windings that have been preferred by other researchers in this field to date. An alternative electromagnetic isolation approach is applied to a machine topology with a slot-per-phase-per-pole (SPP) value of 2/7 and compared with a baseline machine topology without this isolation that uses a SPP value of 1/2. Analytical models will be developed to assess the impact of electromagnetic coupling between modules and the potential negative impacts of this approach. Furthermore, this electromagnetic isolation study investigates alternative module arrangements and the corresponding isolation impact. Finally, thermal and physical module isolation approaches are evaluated considering aggressive cooling techniques that incorporate in-slot cooling features.

Specifically, a winding bobbin configuration that uses in-slot cooling channels is introduced and evaluated using lumped parameters thermal circuits and finite element analysis (FEA) tools. This cooling approach is further refined to consider simplified coolant path geometries which are demonstrated experimentally.

3. *Develop a candidate FT PMSM drive design that incorporates integrated power electronics that is sized to address quadrotor aircraft requirements.*

Next, a combination of these isolation approaches is applied to the design of a FT PMSM drive to meet the performance requirements for a six-passenger UAM VTOL quadrotor aircraft. The selected approach breaks the machine into four modules allowing for continued operation after two faulted modules. The machine is required to meet the demanding performance requirements for this application, including achieving a minimum active machine mass power density of 13.3 kW/kg. The developed machine utilizes promising alternative isolation approaches to meet these requirements. In addition, the power electronics for an integrated modular motor drive (IMMD) configuration is developed using modular 2-level voltage-source inverters. After the FT drive is developed, fault analysis of the machine drive will be carried out beginning with more benign faults such as symmetrical motor terminal three-phase faults, and then extended to consider more serious fault modes including stator winding turn-to-turn faults.

4. *Develop reliability tools and evaluate reliability benefits of modular machine-drives.*

The developed four-module FT PMSM machine for a quadrotor application will be investigated to achieve quantification of the reliability benefits provided by the FT motor drive configuration. The results of the integrated modular machine drive design developed during the preceding task will supply the required inputs for a reliability study using Markov chains as the primary reliability analysis tool. Failure rates will be determined from component data sheets as well as from the

literature and then adjusted to reflect the calculated stresses during healthy and faulted operation. The critical role of the single-point failure and repair rate in determining the IMMD failure rate will be highlighted. The impacts of multiple module failures and total elimination of single-point failures will also be examined.

1.3. Document Organization

This thesis is organized into nine chapters addressing the research objectives described in the preceding section. Chapter 1 of this document has discussed the motivations, challenges, and objectives associated with this research program.

Chapter 2 presents a thorough literature review of FT electrical machines and drives, faulted machine modeling considering fault response and post-fault operation, and existing reliability studies that address electrical machines and power electronics. In addition, a brief review of the current state of electric aircraft and high-performance machines is presented. Opportunities for research are identified and highlighted based on this state-of-the-art review.

Chapter 3 presents sizing equations and design methodology for developing power-dense permanent-magnet synchronous machines. This tool is useful for screening different slot-pole combinations, materials, and exploring the general machine design space before detailed Finite Element optimization. This sizing approach is then extended to the experimental testing of both a 200kW and 1MW power-dense machines. The concept of electromagnetic isolation in FT machines is demonstrated via open circuit and short circuit terminal faults on the 200kW machine.

Chapter 4 presents a tradeoff study of fault-tolerant IMD topologies for an electric VTOL UAM quadcopter aircraft application. Requirements for the electrical machine propulsors are presented and the sizing methodology of Chapter 3 is applied to candidate FSCW PM machines using surface

PM rotor designs and are optimized using 2D finite element analysis. Performance penalties of traditional FT machine approaches are highlighted. An alternative promising electromagnetic isolation approach is presented and evaluated which adopts a DL winding configuration and incorporates features that enhance the electromagnetic isolation.

Chapter 5 elaborates on the Chapter 4 enhanced electromagnetic isolation approach for FT motor drives tailored for the six-passenger quadcopter application. A detailed machine and integrated power electronics design process is followed considering electromagnetic, thermal, and structural aspects of the machine design. The machine tooth tips are optimized to boost slot leakage inductance in order to minimize the short-circuit fault current amplitudes. The developed machine is analyzed under both healthy and faulted conditions. This includes terminal-based faults including three-phase open- and short-circuit faults. Further analysis is also presented on more dangerous fault conditions including stator winding turn-to-turn faults.

Chapter 6 presents a reliability assessment of a fault-tolerant IMD for a six passenger quadrotor aircraft. First, a thorough introduction to Markov chains is presented and generic conclusions about FT motor drive systems are summarized. Markov chains are then applied to the four-module IMD, and the drive system's Mean Time to Failure (MTTF) metric is calculated. This analysis is expanded to consider the impact of drive system single-point failures, the number of modules, and the number of module failures on the FT motor drive system reliability. Additionally, a set of FT Figures of Merit (FoM) used for comparing different types of FT topologies. These FoMs consider the system reliability benefit (i.e., MTTF) against associated penalties (e.g, weight). A detailed discussion and derivation of analytical MTTF using continuous time Markov Chains is provided, which is essential to the calculation of these FT FoMs. Last, a procedure for using these FoMs is given.

Chapter 7 presents investigations into the scaling relationships of the developed isolation concepts. A 2MW version of the modular machine drive is developed using the Chapter 3 sizing methodology. Similarly, these isolation features are applied to a 7kW demonstrator which is scaled from the presented Chapter 5 design. A simplified version of the in-slot cooling concept is presented. General isolation-feature power scaling observations are made.

Chapter 8 presents the fabrication and testing of the 7kW machine described in Chapter 7. This machine is designed with two-modules and incorporates the proposed isolation features developed in this thesis. General machine performance is validated against the developed module. Further, the machine response to terminal and turn-to-turn faults is observed.

Chapter 9 provides a summary of the research accomplished including conclusions drawn from this research and the associated technical contributions. A detailed summary of the remaining work is presented discussing the four key research areas discussed above.

Chapter 2

State of the Art Review

A review of published literature is presented in this chapter addressing topics related to aircraft electrification and corresponding machine designs, machine failures and modeling, fault-tolerant motor and drive configurations, and reliability evaluation methodologies. This chapter concludes with a summary of the most compelling research opportunities for this PhD program that build on the substantial foundation of work that has completed and published to date in this field.

2.1. Advancements in Electrically Propelled Aircraft

Aircraft electrification has been a research topic for many decades, primarily focusing on the electrification of small aircraft systems. In more recent years this effort has expanded to include electrifying aircraft propulsion, i.e., using electric machines to drive thrust-generating fans. Key motivations for this effort include reduction of both the environmental impact of aircraft emissions and fuel-burn. Looking into the future, the adverse environmental effects of commercial aviation will be exacerbated by increasing worldwide demand for passenger air travel. A 2016 International Air Transport Association report forecasts worldwide demand to nearly double during the next 15 years, with 7.2 billion passengers projected to travel by air in the year 2035 [45]. Other potential benefits of electrical propulsion include reductions in noise, lower operating costs, and the realization of aircraft concepts not compatible with existing turbine technology.

A critical component of electrified aircraft is the propulsive electric machine. It must be designed for high power, low mass, high efficiency, and high reliability to meet the demanding metrics required for adoption in commercial aircraft [5], [6]. Unfortunately, the technology

required to make these specialized machines is immature and requires major advances in machine design, cooling, and materials. This subsection reviews the current state of electrified aircraft and highlights the unique aspects of this emerging application.

2.1.1. More-Electric Aircraft (MEA) Initiative

Although historical and modern aircraft propulsion has been dominated by combustion-based technologies, significant effort has been invested in replacing traditional aircraft mechanical, pneumatic, and hydraulic systems with lightweight electric motors and drives. Specifically, the Air Force launched the “More-Electric Aircraft” (MEA) initiative in the 1990s focused on these efforts [1]. Since then, MEA has become a common, general term for aircraft electrification. The ongoing MEA initiative is an excellent steppingstone towards electrically-propelled flight, providing valuable insight into the required electrical machine design specifications and limitations.

Examples of MEA applications and electric machine designs used in modern aircraft and research are surveyed in [1]–[3], [46]. These non-propulsive MEA machine-drive efforts include aircraft-flap actuation [47]–[51], landing gear actuation [51], [52], electric taxiing [53], [54], fuel pumps [29], on-board generation [31], [55], [56], and general aerospace applications [38], [40], [57], [58]. Greater discussions surrounding these electric machines and drives will be discussed in a later subsection.

2.1.2. Electric Propulsion Systems for Regional and Long-Range Civil Aircraft

In the 2000s NASA sought to stimulate academia and industry to work towards its goal of reducing commercial aircraft emissions, fuel-burn, and aircraft noise for new aircraft in service

between 2030-2035 (also referred to the "N+3" generation of aircraft) [4]. These goals are summarized in TABLE 2.1-1, with N referencing the generation of aircraft around 2010 and N+i referring to generations after.

TABLE 2.1-1 NASA N+3 SUBSONIC FIXED WING PROJECT METRICS (MODIFIED FROM [4])

Trade Space Metrics	N+1 (2015) Technology Benefits Relative to a Single Aisle Reference Configuration	N+2 (2020) Technology Benefits Relative to a Large Twin Aisle Reference Configuration	N+3 (2025) Technology Benefits Relative to Either a Single or Twin Aisle Reference
Noise	-32 dB	-42 dB	-71 dB
Landing/Takeoff NOx Emissions	-60%	-75%	Better than -75%
Performance Aircraft Fuel-Burn	-33%	-50%	Better than -70%

Many concept vehicles have been proposed to meet the TABLE 2.1-1 targets [59]. The use of electrically-driven fans for propulsion in combination with advanced aircraft structures have been shown to improve emissions and fuel-burn [4], [7], [8], [60], with two example vehicles shown in Fig. 2.1-1.

First, a Boeing-led team proposed the first concept as a variation of the Subsonic Ultra Green Aircraft Research (SUGAR) concept called the Sugar Volt (pictured in Fig. 2.1-1(a)). The concept uses a hybrid electric-gas turbine engine with battery assist during high load points including takeoff. Second, while the Boeing concept resembles a conventional aircraft, a NASA-led team proposed the hybrid wing body N3-X Turboelectric Distributed Propulsion concept (Fig. 2.1-1(b)), which has distributed superconducting electric machines driving fans located on the rear of the aircraft. These machines are powered by turbo-generators located on the aircraft wing tips.

(a) (b)

Figure 2.1-1 NASA N+3 Subsonic Fixed Wing Project aircraft concepts using electric machines: (a) Boeing SUGAR Volt; (b) NASA N3-X [59].

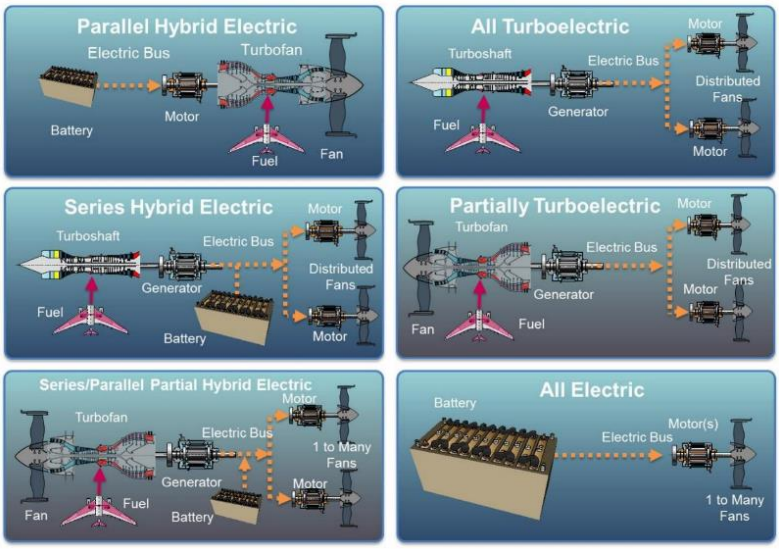

Figure 2.1-2 Possible aircraft drivetrain configurations for electrical propulsion [61].

Both the SUGAR Volt and N3-X use electric machines for propulsion, although their electric drivetrains are fundamentally different. Aircraft electrical powertrains can be classified in six groups, shown in Fig. 2.1-2, with subsets of hybrid, turboelectric, and all-electric propulsion [61]. The SUGAR Volt and N3-X aircraft fall into the Parallel Hybrid Electric and All Turboelectric categories, respectively.

As suggested by Fig. 2.1-1(b) and 2.1-2, distributed electric propulsion (DEP) is a promising approach to meet the aggressive goals set by NASA. While any aircraft with two or more propulsors could be considered distributed, some researchers consider distributed propulsion to be

an enabling technology to improve the efficiency, capability, and aerodynamic performance of the aircraft system [4], [9]. An explicit demonstration of DEP is the NASA X-57 aircraft concept shown in Fig. 2.1-3, with fourteen electrically-driven fans distributed along the wings of the aircraft [62]. This is also observed on the previously discussed NASA N3-X aircraft also uses a DEP with fifteen fans distributed along the tail of the aircraft [2]. Further, locating propulsors on the aircraft tail allows for boundary layer ingestion (BLI) benefits, where the tail thrusters ingest slow moving air located on the aircraft fuselage [4].

Figure 2.1-3 NASA's X-57 Maxwell flight demonstrator concept with distributed electrified propulsion [62].

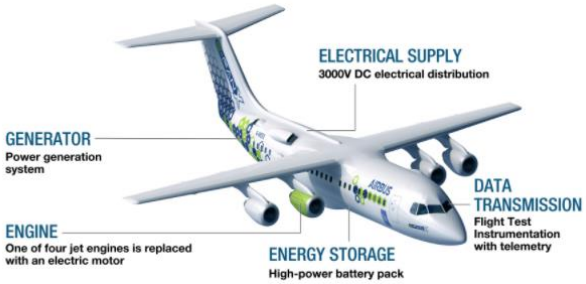

Figure 2.1-4 Airbus E-Fan X demonstrator aircraft with single 2MW electric propulsor [63].

In the commercial sector, it is worth briefly highlighting a couple of the numerous electrical propulsion efforts being carried out by industry. Airbus' E-Fan X project attempted to develop hybrid-electric aircraft demonstrator is shown in Fig. 2.1-4, which utilizes a single 2 MW rated propulsor to investigate challenges with electrified aircraft. More recently the E-Fan X effort has been in question [64], though Airbus is still involved in aircraft electrification efforts like EcoPulse [65], which uses DEP (seven propulsors total) on a small aircraft. Other smaller propulsion electrification efforts are being led by Magnix suppling electric machines and drives to startups like Eviation [6], [11], [66].

2.1.3. Electric Vertical Takeoff and Landing (VTOL) Urban Air Mobility (UAM) Vehicles

Electrical propulsion has also enabled the realization of new aircraft categories. Transportation congestion and projected population growth in large metropolitan areas have motivated the development of Vertical Takeoff and Landing (VTOL) Urban Air Mobility (UAM) vehicles [10], [12], [13]. Many of the previously mentioned benefits like DEP still apply, though unique differences exist considering the aircraft duty-cycle and relatively low-altitude operation. Concept vehicles developed by NASA are shown in Fig 2.1-5 which highlights the broad implementation scope of these vehicles. Like the preceding subsection, this type of aircraft is being actively pursued commercially with startups like Lilium pursuing a dual DEP concept with thirty-six electric machine propulsors [14], and Beta Technologies' Alia-250 with only five propulsors with built in propulsor redundancy [67].

Recently, NASA funded a Boeing led study [26] that investigated aircraft failure modes and reliability for conceptual vehicles such as those shown in Fig. 2.1-5. The Boeing study identifies propulsor motors and associated electronics as low-reliability components based on existing technologies that have a negative impact on the overall reliability and feasibility of the UAM aircraft. A follow up study by the same authors in [68] expands on their previous work to better detail subsystems, aircraft architectures, and pathways for improving aircraft reliability (including considering electrical machine redundancy).

This section highlights the recent activity in electrified aerospace propulsion, and the vast potential implementations of these aircraft. To meet the demanding needs of this application, a new generation of power dense electrical machines and drives must be developed.

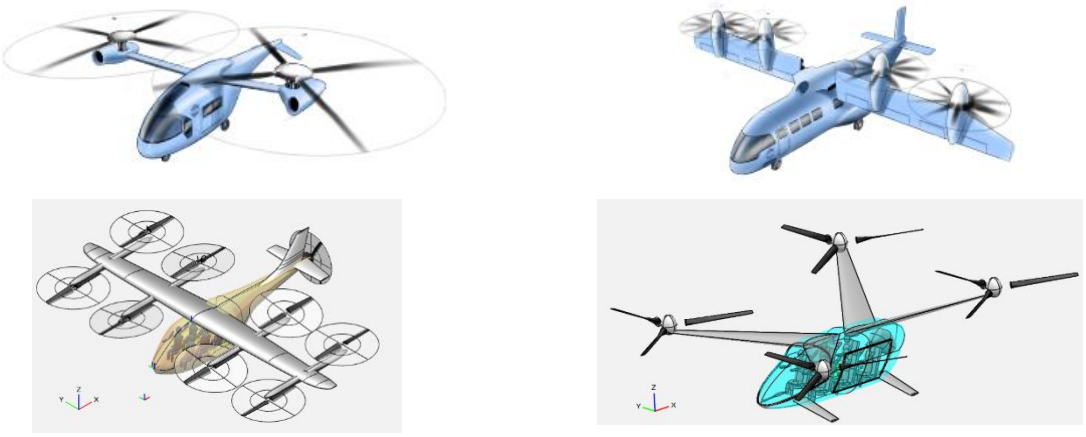

Figure 2.1-5 NASA concept vehicles for UAM VTOL applications (image credit: top [12] and bottom [13] rows).

2.2. Review of Aerospace Electrical Machines and Drives

The requirements for aerospace electric machines are very demanding and [69] defines important design factors for these machines: (1) electromagnetic mass; (2) power density; (3) efficiency; (4) control complexity and features; (5) complexity of design and fabrication; (6) reliability and fault tolerance; and (7) thermal robustness. Further challenges exist for the insulation material and voltage level selection due to increased partial discharge at high operating altitudes [70], and compatibility with the propulsor-fan for aerospace propulsion applications [71]. This section reviews notable electrical machines from the literature and industry for aerospace applications.

2.2.1. Megawatt-Scale Propulsion Electrical Machines and Drives

Power-dense megawatt-scale propulsion machines are critical to realize the large commercial electrified aircraft concepts shown in Fig. 2.1-1. Megawatt-scale electric machines are required for larger aircraft and need to achieve total power density greater than 12 kW/kg, which is a jump

from the state-of-the-art machines used in aircraft today [5], [16]. High-power-density machines are being aggressively pursued in academia and industry with some prominent examples listed here.

First, researchers at the University of Illinois at Urbana-Champaign developed a high-speed 1 MW surface permanent magnet (SPM) synchronous machine (shown in Fig. 2.2-1(a)) with a target power density equal to 14 kW/kg [17]. The machine rotor features an outer-rotor and Halbach magnet array used to minimize the rotor back iron thickness. The stator uses a toothless winding to reduce stator core mass and transposed litz wire to minimize high-frequency skin and proximity effects. The design presented in [17] assumes air cooling for both the stator and rotor, taking advantage of the ambient air flowing through the aircraft nacelle. Greater details on the final machine construction and features can be found in [72]. Testing of the 1MW machine were completed in April of 2021, achieving power densities and efficiencies in excess of 15 kW/kg and 96%, respectively [73].

Related University of Illinois designs are generated in [74] using the same stator and rotor configuration with alternative cooling schemes. Further power density benefits can be realized with liquid cooling at the cost of a more complex cooling system. The design concept was again revisited for the tail-cone thruster in the STARC-ABL electric aircraft concept [18]. The design process and analysis of a 2.6 MW 3,000 rev/min direct drive machine are presented with expected 11 kW/kg power density and 98% efficiency.

Next, Ohio State University researchers are developing a 2.7 MW induction machine (IM) with power density goals over 13 kW/kg and 96% efficiency [19]. This machine is targeted for integration with a turbofan in a parallel hybrid concept. Unfortunately, at the time of this writing very little has been published about the exact performance and construction of the machine.

Third, the High Efficiency Megawatt Motor (HEMM) concept is another example of a NASA-led project investigating high power density machines. A machine active material cross-section is provided in Fig. 2.2-1(b). The HEMM concept aims to develop a 9-phase 1.4 MW wound field synchronous machine (WFSM) with anticipated 17.2 kW/kg power density and 98.9% efficiency [75], [76]. This power density and efficiency numbers were updated to 16.0 kW/kg in [20]. It is considered partially superconducting with a cryogenically cooled rotor producing a 2.0 T field. A detailed description of the rotor design and analysis can be found in [77].

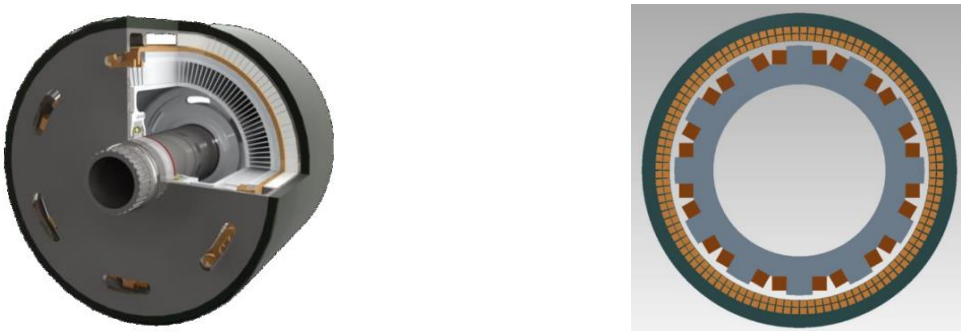

(a) (b)

Figure 2.2-1 Sample megawatt scale machines for aerospace propulsion applications: (a) University of Illinois Urbana-Champaign complete 1 MW machine concept with air-core stator and outer-SPM Halbach array rotor shown [17]**; (b) NASA HEMM partially superconducting WFSM with single-turn per winding stator and cryogenically cooled rotor** [75]**.**

The stator design is especially unique with a semi-toothless stator structure (i.e., extremely thin stator teeth) which is selected to provide mechanical structure and additional heat paths to the winding. Each coil has a single turn of rectangular litz wire consisting 6,000 strands of fine gauge wire [78]. The winding is encapsulated in a high thermal conductivity potting material to improve the thermal performance of the stator and to provide additional structure to the winding. The stator is then cooled by dielectric fluid, which interacts with the stator in two ways: cooling channels

placed in the stator back iron, and direct winding cooling with fluid flowing through the machine airgap.

Other megawatt scale high power density machines used in automotive and aerospace can be found in industry. Focusing on electrified propulsion, Honeywell developed a high-speed 1 MW WFSM achieving 7.9 kW/kg power density to be used in a hybrid electric concept [21]. General Electric recently completed testing of megawatt scale machine and drives for hybrid electric flight, though few details of the design are available to the public [79].

TABLE 2.2-1 SURVEYED MEGAWATT-SCALE MACHINES FOR AEROSPACE PROPULSION

Machine	Topology	Slot / Pole / Phase	Power [kW]	Speed [RPM]	Power Density [kW/kg]	Cooling Method	Ref.
UoI – High Speed	Halbach-array SPM	Slot-less / 20p / 3-ph.	1,000	18,000	14	Air-cooled	[17]
UoI – Direct Drive	Halbach-array SPM	Slot-less / 32p / 3-ph.	2,600	3,000	11	Air-cooled	[18]
OSU	Induction Machine	-	2,700	~5,000	> 13	-	[19]
NASA HEMM	Semi-Toothless WFSM	108s / 12p / 9-ph.	1,400	6,800	16	Direct liquid cooled stator windings, cryogenically cooled rotor	[20], [76]
Honeywell	WFSM	- / 8p/3-ph.	1,000	20,000	7.9	Oil-cooled	[21]

Further ongoing industry and academic efforts related to megawatt-scale propulsion can be found in the ARPA-E Aviation-class Synergistically Cooled Electric-motors with Integrated Drives (ASCEND) portfolio [23], highlighting the possible types of cooling technologies (superconducting, cryogenic, direct liquid cooling, air cooling, etc.) and machine topologies (radial- and axial-flux machines with Halbach magnet arrays, induction machines, and radial flux

air core designs, etc.) used to achieve power densities exceeding 12 kW/kg. A summary of the surveyed megawatt scale machines is provided in TABLE 2.2-1.

2.2.2. Multi-Kilowatt Scale Propulsion Electrical Machines and Drives

Multi-kilowatt electrical machines have been developed for aerospace propulsion applications with some examples listed here. These machines are more oriented towards smaller aircraft and VTOL concepts illustrated in Fig. 2.1-5, or as scaled-down demonstrators for future megawatt-scale machines.

2.2.2.1. Power Range: 100 kW to 1 MW

Recently researchers at Marquette University proposed a 250 kW 5,000 rev/min FSCW SPM demonstrator machine for a future megawatt level propulsor in [80], which features additively manufactured windings with hollow channels allowing for high-fill slot-copper fill-factors and direct cooling. Further, notches are removed from the stator back-iron to remove additional mass. On the rotor side, a Halbach magnet array is used to minimize rotor mass. Additional power density benefits are realized by integrating power electronics into the machine housing in an IMMD configuration [81], allowing for a shared thermal management system. This machine is estimated to reach an impressive active mass power density of 20.2 kW/kg.

Next, the design process and analysis of a 500 kW direct-drive SPM propulsion machine from the University of Nottingham is presented in [82]. The machine is designed to use only indirect liquid cooling (no liquid in direct contact with the machine winding) through a cooling jacket which is integrated into the machine housing. Like some of the previously mentioned designs, a Halbach magnet array is employed on the rotor and the windings use litz wire to minimize AC loss. An active mass power density ~5.0 kW/kg and efficiency of 97% is expected for this design.

Another propulsive fractional-slot machine was designed by the Universitaet der Bundeswehr Muenchen with the objective to replace the gas turbine used in existing German aircraft Do 128-6. The machine analysis also included the added mass associated to the speed-reduction gearbox, and a speed of 13,300 rev/min was selected for optimum power density [83]. A FSCW 12-slot 14-pole machine design with an interior permanent magnet (IPM) rotor was selected for the final design [84]. The most notable feature of the machine is the flux barriers added to the stator which provide an airgap flux focusing effect, improving machine performance. Ultimately the machine has a 10.6 kW/kg active mass power density and a 96.6% efficiency.

Researchers at the University of Bristol designed a fault-tolerant motor for helicopter application [30]. Fault tolerance is achieved by dividing the stator into four separately excited three-phase modules rated for 75 kW each (300 kW total). Each module is to be overrated to compensate for the loss of a module in the event of a fault. The stator uses a single layer winding (alternate tooth-wound) to limit the magnetic, electric, and thermal interactions between adjacent teeth. Further, the machine is designed with 1 per-unit inductance to limit the magnitude of short-circuit current. The machine was designed for a 4,000 rev/min peak speed and power density greater than 6 kW/kg.

Researchers at the Ohio State University Center for High-Performance Power Electronics (CHPPE) designed and built a 17,000 rev/min 300 kW machine [85] which has limited published test data available. The machine features an inner-rotor SPM topology with the magnets contained by a 3.75 mm-thick steel containment structure. Like the Illinois machine, the stator uses a toothless stator winding to reduce core mass. The machine is expected to achieve active mass power density of 14.4 kW/kg and 99.2% electromagnetic efficiency at full load.

TABLE 2.2-2 SURVEYED 100 KW TO 1 MW MACHINES FOR AEROSPACE PROPULSION

Machine	Topology	Slot / Pole / Phase	Power [kW]	Speed [RPM]	Power Density [kW/kg]	Cooling Method	Ref.
Marquette University	Halbach-array SPM	36s / 30p / 3-ph	250	5,000	20.2	Direct liquid hollow conductors	[80]
University of Nottingham	Halbach-array SPM	36s / 30p / 3-ph	500	3,000	~5.0	Indirect Liquid-cooled	[82]
Universitaet der Bundeswehr Muenchen	IPM	12s / 14p / 3-ph	300	13,300	10.6	Liquid-cooled	[84]
University of Bristol	Halbach-array SPM	24s / 28p / 3-ph	300	4,500	> 6.0	Air-cooled	[30]
OSU CHPPE	Toothless Stator SPM	Slot-less / 10p / 3-ph	300	17,000	14.4	-	[85]
magniX magni200	-	-	350	2,300	3.1 (total dry)	Liquid-cooled	[66]
magniX magni500	-	-	640	2,300	3.2 (total dry)	Liquid-cooled	[66]
Safran	-	-	500	1,900	3.5 (total)	-	[86]
H3X HPDM-250	-	-	250	20,000	12 kW/kg (total)	Liquid-cooled	[87]
Siemens	Halbach-array SPM	-	260	2,300	5.2	Direct liquid cooled stator windings	[88]
Siemens	SPM	-	170	6,250	7.0	Direct liquid cooled stator windings	[88]
ENSTROJ	Axial Flux PM	-	200	4,000	4.9	Indirect air and water cooling	[88]

Another example of propulsion machines found in industry is the company magniX producing the 350 kW magni350 and the 640 kW magni640 Electric Propulsion Units (EPU) for direct drive propulsion [66]. These machine's expected total (machine weight plus drive electronics) power densities equal to 3.1 and 3.2 kW/kg respectively. Next, Safran's ENGINeUS 500 (rated 500 kW) direct-drive option with 3.5 kW/kg continuous power density (combined machine and electronics mass) [86]. Last, integrated machine-drive startup H3X is pursuing multi-kilowatt and megawatt

propulsion [87]. Their upcoming 250 kW rated HPDM-250 is expected to exceed 12 kW/kg with integrated electronics. Other examples of aerospace propulsion power dense machines in industry are given [88] and summarized in TABLE 2.2-2.

TABLE 2.2-3 SURVEYED 10 KW TO 100 KW SCALE MACHINES FOR AEROSPACE PROPULSION

Machine	Topology	Slot / Pole / Phase	Power [kW]	Speed [RPM]	Power Density [kW/kg]	Cooling Method	Ref.
NASA X-57 Cruise Machines	Halbach-array SPM	48s / 40p / 3-ph	60	2,700	2.7	Air-cooled	[62]
NASA X-57 High Lift Machines	Halbach-array SPM	24s / 20p / 3-ph	13.7	5,470	5.6	Air-cooled	[89]
Safran ENGINeUS 50-100	-	-	50 / 100	2,500	3.5 (total)	-	[86]
Rotex-Czech Republic	SPM	-	50	2,200	2.5	Air or liquid cooled	[88]
Siemens and EADS-Germany	SPM	-	65	5,000	5.0	Direct oil cooled winding	[88]
ACENTISS-Germany	Dual Motor SPM	-	32	2200	2.9	Air cooled	[88]
Yuneec – China	SPM	-	20	2400	2.4	Air cooled	[88]

2.2.2.2. Power Range: 10 kW to 100 kW

Several reference designs for the NASA X-57 (Fig. 2.1-3) electric machine propulsors have been published. The selection-and-design process of wingtip cruise machines is described in [62], using an outer-rotor Halbach array SPM design is chosen with 60 kW and 2,700 rev/min peak ratings. The machine achieves an expected 96% efficiency and a relatively low active power density equal to 2.7 kW/kg. While the power density is low, the machine is air-cooled and does not require the extra systems needed for a liquid-cooled solution (pumps, dedicated cooling loops, etc.). Next, a reference design for the X-57 high lift propulsors is provided in [89] rated for 13.7

kW at 5470 rev/min and are to be used only during aircraft takeoff or inflight maneuvering. Like the cruise machine, a fractional-slot 24-slot 20-pole Halbach magnet array SPM was selected and uses air cooling. The machine is predicted to have 5.6 kW/kg power density with a minimum efficiency of 93%.

Other examples of lower power aerospace propulsion power dense machines in industry are given [88] and summarized in TABLE 2.2-3.

2.2.3. Review of Non-Propulsive Aerospace Electrical Machine and Drives

Numerous non-propulsive aerospace machines have been proposed in the literature [29], [31], [38], [40], [47]–[58], with notable examples shared here. First, a power-dense aircraft power generator design and test is presented in [56] and is rated for peak power and speeds of 175 kW and 12,000 rev/min. An outer-rotor SPM topology is selected in a FSCW 20-slot 24-pole configuration. Rectangular litz wire is used to suppress ac losses related to high operating frequency. A stepped-slot design is used, as shown in Fig. 2.2-2(a), to improve thermal performance and to maximize copper fill factor. The machine windings are directly cooled via in-slot cooling channels made of stainless steel. Last, this machine is design for fault tolerant operation utilizing magnetic slot wedges to boost the machine inductance and a single-layer winding configuration to minimize interactions between phases.

Next, [31] shares the design and test of an aerospace alternator, which is rated for a peak power and speed of approx. 120 kW and 14,000 rev/min. This machine features a fault-tolerant modular stator design, with spacer teeth inserted between three-phase modules allowing for modular isolation. This spacer tooth concept is illustrated in Fig. 2.2-2(b). On the rotor side, a 20-pole inner-rotor SPM topology is used.

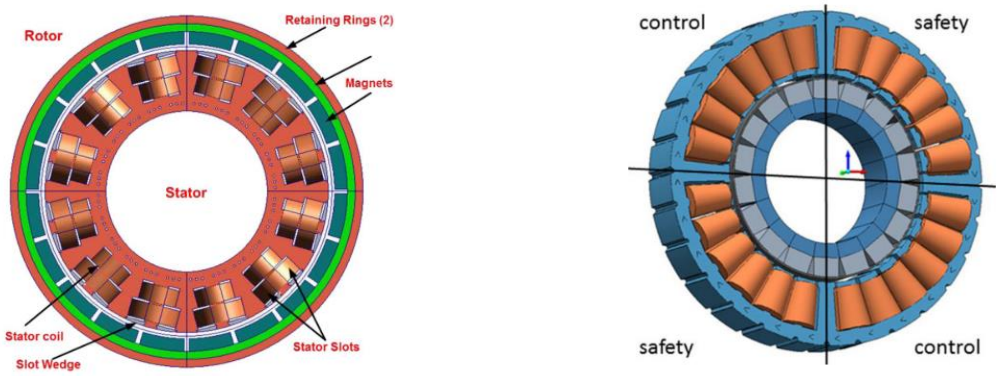

(a) (b)

Figure 2.2-2 Non-propulsive aerospace machines: (a) outer-rotor FSCW SPM generator [56]**; and (b) four-module fault-tolerance aerospace alternator with spacer teeth between modules** [31]**.**

An aerospace electric drive system consisting of a FSCW inner-rotor SPM machine is presented in [38]. A single-layer 12-slot 10-pole winding configuration is used, which is broken into six-phases. The stator is designed for fault-tolerance by modularizing the stator into two-groups, each with their own three-phase drive. Isolation between phases is achieved by utilizing a single-layer winding.

Last, an aerospace engine stator generator system is presented in [55] rated for a peak speed of 32,000 rev/min and power rating of 150 kW. The electromagnetic design features a 36-slot 6-pole design utilizing an inner-rotor SPM utilizing a Halbach magnet array. An aggressive stator flooded cooling concept is used to cool the stator to effectively cool the stator and lessen the effects of thermal aging. Specifically, oil is forced through channels located in the machine stator core and winding. This oil is contained to the stator by a stationary sleeve located in the machine airgap.

2.2.4. Trends in Aerospace Machines and Drives

A brief review of aerospace machines is shown. Several power-density trends for aerospace machines are observed:

- In general, Permanent Magnet Synchronous Machines (PMSM) are often utilized to improve machine power density. In particular, the SPM configuration is used frequently in combination with a Halbach magnet array.
- FSCW machines are commonly used due to compact end winding structure, though several designs use a slot-less stator design with distributed windings to eliminate stator core mass.
- Machine designs are generally skewed to either lower-speed (2,000 rev/min to 5,000 rev/min) and high-pole count, or higher-speed (13,000 rev/min to 20,000 rev/min) and low-pole count. In either case, high electrical fundamental frequencies can be expected (up to 2,000 kHz). The use of transposed litz wire is common to suppress excessive ac losses related to skin and proximity effects.
- Direct cooling of the stator windings is commonly used in power dense machines in order to push copper current density. The use of air-cooled designs is being considered, though tradeoffs between added machine mass and the associated Thermal Management System (TMS) mass are unclear.
- Fault tolerance features are commonly utilized due to the safety-criticality of the application. However, the associated reliability improvement associated to the chosen fault tolerance method is unclear, along with the associated mass, performance, and cost tradeoffs.

2.3. Characteristics of Power Dense Machines

The preceding aerospace survey describes state of the art aerospace machines and their associated features. This section expands on the previous discussion to highlight and stress characteristics power dense electrical machines, which can be utilized in future aerospace propulsion designs.

2.3.1. Rotor Topology

Candidate machine topologies for the quadrotor machine design include induction machines (IM), permanent magnet synchronous machines (PMSM), wound-field synchronous machines (WFSM), switched reluctance (SR), and synchronous reluctance (SynRM) topologies. First, the IM topology's asynchronous operation and robust rotor structure offer operation and construction advantages. However, the IM suffers from relatively high rotor loss due to imbedded rotor bars and asynchronous fields. Similar simple and robust rotor construction claims can be made for the SR and SynRM machines.

Next, both PMSMs and WFSMs produce torque via rotor-flux generated by rotor-embedded magnets or coils, respectively. Overall, the WFSM, SR, and SynRM topologies are desirable from a FT perspective due to the adjustability or absence of externally-applied rotor field, limiting fault currents in the stator winding in the event of a fault. In contrast, the PMSM topology cannot turn off their rotor magnet fields, so there exists the possibility for substantial fault currents if the machine excitation is not managed properly.

There are several published papers that present performance tradeoffs between these topologies [90], [91]. In general, the PMSM topology emerges as a leading candidate for power dense

applications due to its inherent low mass and efficiency advantages. The tradeoffs associated with managing the magnet flux in the event of a fault will be discussed in a subsequent section.

The PMSM category can be further differentiated based on magnet placement that typically leads to the definition of two major sub-categories. The first is surface permanent magnet (SPM) machines, which mount magnets on the surface of the rotor core as illustrated in Fig. 2.3-1(a). These magnets are held in place by an adhesive or containment sleeve. Alternatively, an outer rotor SPM configuration in which the magnets are mounted on the inside of a rotating cylinder can be used to eliminate the need for the containment ring as observed in [17], although this approach adds mechanical complexity to the rotor assembly and bearings.

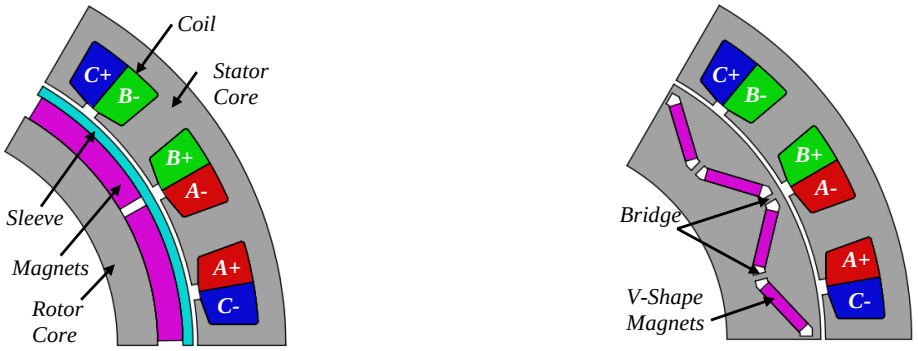

Figure 2.3-1 PMSM magnet arrangements classified by rotor configuration: (a) SPM; (b) IPM.

The second PMSM sub-category is interior permanent magnet (IPM) machines, which imbed magnets inside the rotor core as described in Fig. 2.3-1(b). A basic IPM arrangement is shown in Fig. 2.3-1(b), though the geometry of the magnets and core can be modified in many ways to improve torque performance by either concentrating the magnet flux in the airgap or enhancing the rotor magnetic saliency. However, thick magnet containment bridges identified in Fig. 2.3-1(b) are required for the IPM machine to maintain the rotor's structural integrity during high-speed operation. These bridges behave as magnetic short circuits that re-direct some of the magnet flux

away from the airgap, reducing the IPM machine's torque density. The use of dual-phase material (i.e., lamination materials which can "disable" localized magnetic properties) can be used to lessen the significance of these bridges [92], though questions about the availability and mechanical strength of this material remain.

Other more specialized PMSM arrangements can be found beyond those described in Fig. 2.3-1. An axial-flux configuration can be used, which has an axial airgap (compared to the radial airgap in Fig. 2.3-1). This type of machine can stack multiple rotor or stator stages axially, providing interesting opportunities for performance enhancement and fault tolerance. Examples of high-performance axial-flux machines can be found in [93], [94]. Alternatively, a flux-switching topology (with either a radial or axial airgap) can be used which removes the magnets from the rotor and places them in the stator. This simplifies the rotor structure which resembles the rotor of the SR machine topology, allowing for improved magnet cooling. However, the valuable stator space must now be shared by the stator windings and magnets, penalizing power density. Examples of FT flux switching machines can be found in [94]–[96].

2.3.2. Winding Topology

There are several types of stator windings which can be adopted for the selected rotor topology. Generally, the choice of windings is heavily influenced by the Slot-per-Pole-per-Phase (SPP) metric of each machine which is defined by:

$$SPP = \frac{S}{P \cdot m} \tag{2.3.1}$$

Where S is the number of stator slots, P is the number of machine poles, and m is the number of phases. Machine stator windings with SPP > 1 are characterized as distributed windings, resulting in machine windings that extend over a pole pitch as shown in Fig. 2.3-2(a). These

machines produce sinusoidal airgap flux density distributions in the airgap, but they have substantial end windings that contribute to increased machine loss and mass. Furthermore, the machine phase windings are in very close proximity to each other in the end winding regions which is undesirable for FT machines.

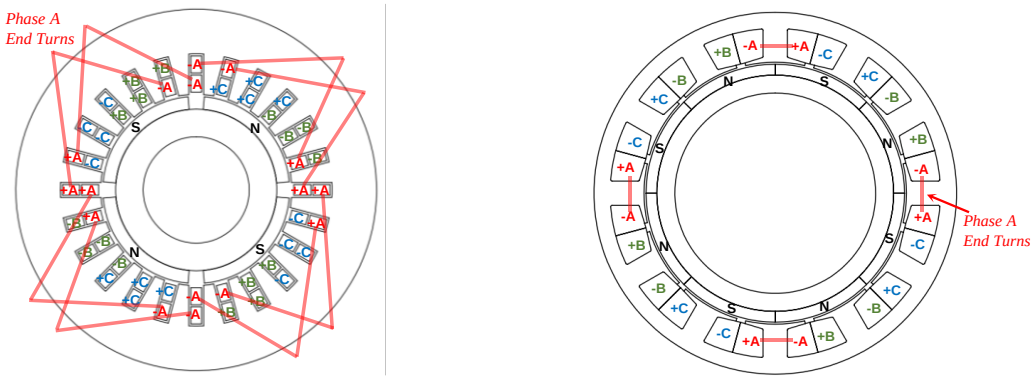

Figure 2.3-2 Machine stator examples with Phase A end windings highlighted: (a) 24-slot, 4-pole distributed windings; and (b) 12-slot, 8-pole fractional-slot concentrated windings (FSCW).

Fractional-slot concentrated winding (FSCW) machines have a SPP < 1 and deliver a number of benefits over distributed wound machines [97]. The phase coils are wound around each individual tooth in a double-layer (DL) winding as shown in Fig. 2.3-2(b), or around every second tooth in a single-layer (SL) winding. As suggested by Fig. 2.3-2(b), the FSCW configuration has short end windings compared to the distributed winding, contributing to lower winding loss and reduced end winding mass. Furthermore, the separated nature of the windings makes the FSCW configuration inherently advantageous for FT machine designs. The primary disadvantage of a FSCW is increased spatial harmonic content in the stator airgap flux which can contribute to increased rotor losses.

2.3.3. Sizing Considerations

Substantial power density insights can be gained from basic sizing equations, which can be used to guide the design of machines. Considerations for sizing characteristics are discussed in [6], [23], [71], [90], with main observations reiterated here. Simplified machine torque and power equations are shown in (2.3.2), where T_e is the shaft torque, P_e is shaft power, ω_r rotor mechanical speed, V_r is the rotor volume, and σ_m is the rotor shear stress.

$$\begin{aligned} T_e &= 2 \cdot V_r \cdot \sigma_m \\ P_e &= \omega_r \cdot T_e \end{aligned} \tag{2.3.2}$$

From (2.3.2) it is clear machine power density can be directly improved by increasing the rotor speed and fundamental frequency. Alternatively, the torque capability can be addressed directly by increasing the shear stress, while maintaining a constant rotor volume. Shear stress is defined in (2.3.3) and consists of two components: electric loading K_{s1} and magnetic loading B_{g1}.

$$\sigma_m = B_{g1} \cdot K_{s1} / 2 \tag{2.3.3}$$

In PMSM machines the magnetic loading is affected by the choice of rotor topology, magnet containment, magnet material, and overall machine magnetic design. Alternatively, increases to the electric loading will lead to increased stator loss densities and require higher operating temperatures or more aggressive cooling.

Related to electric loading is copper current density J, which is defined by

$$J = \pi \cdot K_{s1} \cdot D_{or} / (S \cdot A_{cu}) \tag{2.3.4}$$

with rotor diameter D_{or}, number of stator slots S, and copper area per slot A_{cu}. It is clear from (2.3.4) that higher current density can correspond to a smaller stator slot (smaller A_{cu}) and improved power density. However, higher current density corresponds to higher winding loss densities and

increased cooling requirements (hence the aggressive cooling implementations observed in the aerospace machine review).

Additional sizing considerations have to do with selection of the rotor tip-speed or surface-speed v_{tip} [m/s]:

$$v_{tip} = \frac{\pi}{60} \cdot n \cdot D_{or} \tag{2.3.5}$$

where n is the machine speed in rev/min. Tip-speed power density tradeoffs are discussed in [98] where higher tip speeds are associated to superior power density. However, diminishing power density benefits are observed with increased tip speed due to more demanding magnet containment as seen in Fig. 2.3-3. Further, a higher tip speed coalesces well for some propulsor-fan designs allowing for rim mounted integration. This is emphasized in [71] where a large-diameter toroidal-wound 7kW-rated axial-flux SPM is integrated with its propulsor as shown in Fig. 2.3-4.

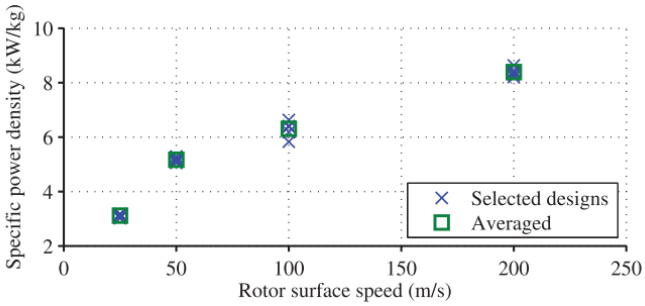

Figure 2.3-3 Rotor tip speed and active mass power density tradeoff [98]**.**

Figure 2.3-4 Integrated 7kW axial-flux SPM and propulsor-fan demonstration [71].

2.3.4. Enabling Technologies for Fault Tolerant Power Dense Machines and Drives

Numerous existing and emerging technology approaches can be used to enhance the power density of a motor-drive system. Promising technologies will be reviewed in this subsection.

2.3.4.1. Machine Materials and Manufacturing

The basic components of a PMSM are highlighted in Fig. 2.3-1. The materials for each of these components can be selected to improve the power density of the quadrotor IMD. First, there are several potential stator and rotor core lamination materials discussed in [99]. Cobalt-iron (CoFe) alloys are appealing since they offer magnetic saturation flux density values above 2.0 T which is valuable for minimizing the stator back-iron thickness. In addition, readily-available CoFe laminations with thin thicknesses offer appealingly low loss characteristics compared to other lamination materials [100]. Further, availability of lamination cutting techniques like wire Electrical Discharge Machining (EDM) can have significantly improve the loss characteristics of the core material compared to conventional stamping and laser-cutting methods [101].

Next, rare-earth Neodymium-Iron-Boron (NdFeB) and Samarium-Cobalt (SmCo) magnets are often used in power-dense machines due to their high remanent flux density B_r values [102]. In particular, SmCo magnets are appealing due to their high-temperature (> 200 ºC) capabilities, reducing the rotor cooling requirements while also maintaining their magnet demagnetization resistance during a fault event. Furthermore, these magnets can be segmented axially to minimize eddy current losses caused by airgap flux harmonics. The NASA University Leadership Initiative (ULI) megawatt machine described in [22] uses segmented SmCo magnets with 1 mm thickness in the axial direction. Further, the use of a Halbach magnet array can be used to minimize or eliminate the rotor core material and to enhance magnet airgap flux [90].

Consideration must also be given to the stator coil configuration and slot materials. The machine power density can be enhanced by raising the machine speed and the associated fundamental frequency of the machine. Transposed (i.e., twisted) litz wire with narrow wire strands is often adopted in power-dense aerospace machines to minimize ac losses associated with high-frequency operation as found in [17], [22], [56], [71], [90]. Additional performance and power density benefits can be gained if a segmented stator structure with compressed stator windings allowing for higher slot fill factors [103].

Beyond the winding coils themselves, the selected insulation system plays a critical role in power density. At a minimum, the insulation must handle the voltage and partial discharge requirements of the application. Additional thermal benefits are gained if the selected slot potting materials are thermally conducting, improving the overall cooling scheme. The NASA ULI machine in [22] uses thermally conductive Lord EP2000 which has a thermal conductivity of 1.9 W/m-K to improve the thermal characteristics of the machine. Other examples of thermally-

conducting insulating materials can be found in [104], [105]. In some instances, coolant channels can be placed in the potting material allowing for direct cooling of the stator winding [106].

Finally, emerging additive manufacturing techniques can enable novel approaches for reducing the mass and improving the performance of electric machines [107], [108]. In particular, additive manufacturing is opening potential paths for improving the machine cooling, which is critical for reaching the necessary power density [109]. One such path is the introduction of 3D printed cooling structures allowing for direct winding cooling. In [110] 3D printed ceramic heat exchangers are inserted between stator coils, allowing the coolant to come into close thermal contact with the stator windings. Alternatively, the ability to 3D-print the stator windings themselves can allow for novel cooling schemes. In [80], [81], [111] the machine windings are 3D printed allowing for the insertion of hollow conductor direct cooling.

2.3.4.2. Power Electronics Integration and Wide Bandgap Devices

A review of IMD technology found in industry applications and the academic literature is presented in [24], [112], [113]. Often power electronics are mounted axially on the machine end bell or radially into the machine housing as shown in Fig. 2.3-5.

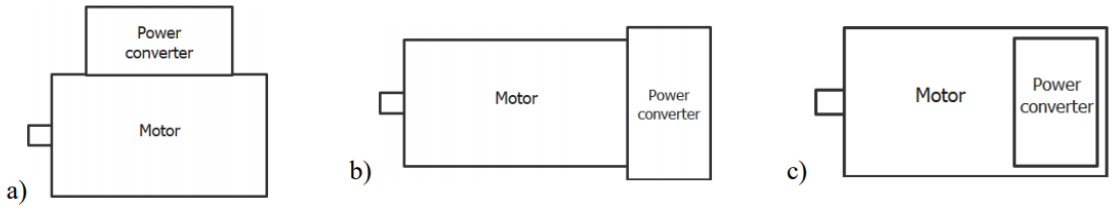

Figure 2.3-5 Types of power electronics integration [42]**: (a) radial integration, (b) axial integration, and (c) axially integrated into the housing.**

Some of the benefits provided by IMDs are summarized here. An IMD configuration can directly improve the power density of a motor-drive system by minimizing inverter cable lengths

and combining housing and cooling structures [114], [115]. Further, the reduction of cable lengths reduces the cable loss associated with the motor drive and helps to minimize overvoltage transients at the motor terminals attributed to very high *dv/dt* values caused by the switching of wide-bandgap power switches as discussed below [42].

Fault tolerance can be enhanced by modularizing the IMD using multiple semi-independent inverter modules (either single phase or multiphase modules) in a configuration denoted as an Integrated Modular Motor Drive (IMMD) as highlighted in Fig. 2.3-6. The use of IMMD is being pursued by the aerospace propulsor efforts described in [22], [81], [116].

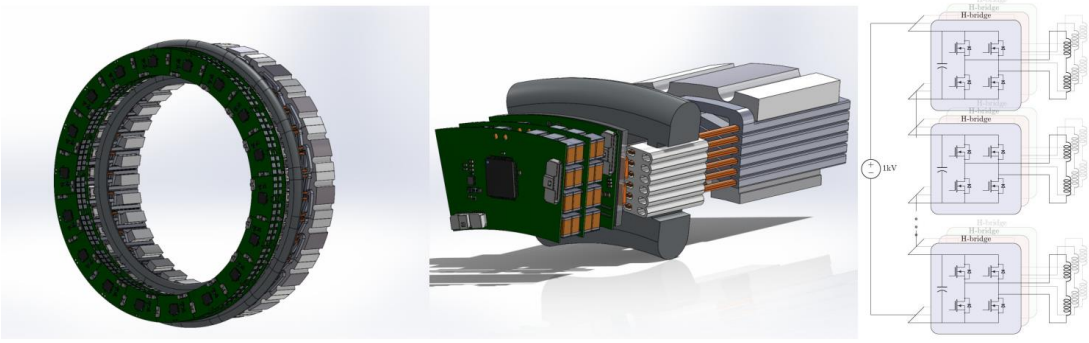

(a) Integrated modular motor drive. (b) Individual drive module. (c) Drive architecture.

Figure 2.3-6 Example aerospace axial-mounted IMMD drive architecture utilizing multiple full-bridge modules [116]**.**

The growing availability of wide bandgap (WBG) power semiconductor devices is an enabler for power-dense machines. A comparison of WBG devices with conventional Silicon devices is provided in [117]. In general, these WBG devices exhibit lower on-state resistance, allowing for substantially smaller devices compared to Si. These WBG devices switch much faster than their Si counterparts, result in reduced switching losses and higher switching frequencies. High switching frequency is particularly important for power-dense machines which often have high

fundamental frequencies between 1 to 2 kHz resulting from high pole counts and high operating speeds.

2.4. State of Fault Tolerant Electrical Machine and Power Electronics Design

High reliability is critical in demanding safety-critical applications like aerospace. The use of FT features is common method for improving reliability allowing for partial or full operation after a failure. The choice of FT machine and power electronics topology is dependent on the allowable fault conditions defined by the application. Often these FT considerations compete with the overall system requirements of the motor drive system, affecting motor-drive performance through the addition of new components, and/or component oversizing for derating purposes. This section reviews the failure modes of IMD systems and the current state of the art for fault tolerance design for both machines and power electronics.

2.4.1. Fault Tolerant PMSM Topologies

The considered FT machines must continue operation after a fault, implying that design features must be introduced to prevent faults from propagating within the motor-drive system. Fault propagation in multi-phase machines is addressed in [28] and guidelines are provided for isolating the machine phases. These guidelines can be broadened to apply to any FT machine with redundant pathways for delivering electrical power to the machine and producing torque, referred to hereafter as “power channels” (e.g., isolated single phase, multiphase, redundant three-phase modules, etc.):

1. Inherent short-circuit current limiting.
2. Power channel isolation:

a. Magnetic isolation between power channels.

b. Electric isolation between power channels.

c. Physical separation between power channels.

d. Thermal isolation between power channels.

3. Number of redundant power channels.

The required amount of isolation and the number of channels is largely dependent on the type of machine and application needs. Each of these guidelines will be addressed individually and novel FT approaches will be highlighted in the following subsections.

2.4.1.1. Short Circuit Limiting Features

Short-circuit current-limiting features are particularly important for FT PMSMs due to the fixed magnetization of the permanent magnets. If precautions are not taken, large fault currents can flow in the machine coils which can overheat the stator and/or lead to irreversible demagnetization of the rotor magnets. This is illustrated in the SPM machine equivalent circuit shown in Fig. 2.4-1, with phase resistance r_s, inductance L_s, back-emf voltage E_i, and machine mechanical frequency ω_r (related to the electrical frequency $\omega_e = \omega_r \cdot P/2$). The machine back-emf E_i is related to the magnet flux linkage λ_{pm} according to $E_i = \omega_e \cdot \lambda_{pm}$.

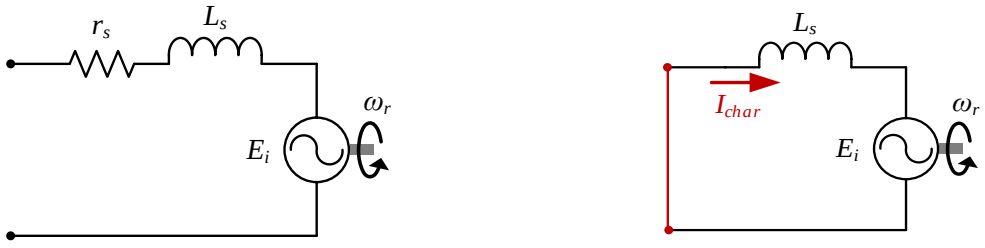

Figure 2.4-1 SPM machine equivalent circuit model (left) and short-circuit condition (right).

In the event of a three-phase terminal short circuit, shown in Fig. 2.4-1, the phase currents in the machine will be determined by the machine impedances and back-emf. Assuming negligible phase resistance, the amplitude of the steady-state short-circuit phase current is known as the characteristic current I_{char} defined by

$$I_{char} = \frac{\lambda_{PM}}{L_s} \tag{2.4.1}$$

FT machine short-circuit limiting features often include increasing the phase inductance of the machines, thereby reducing the characteristic current. Often these FT machines have design features creating sufficient inductances to make the machine's rated and characteristic currents equal (i.e., 1 per-unit characteristic current). There are many examples of how this is pursued in the literature.

Increasing the machine stator winding turn count is one method of boosting the phase inductance, but this approach is restricted by the maximum supply voltage limits. More often, increased inductance is pursued by increasing the machine coil flux leakage. In general, a FSCW stator winding is desirable for FT machines due to increased harmonic leakage flux and higher slot leakage flux compared to other stator winding configurations [97]. FT machines typically reach the desired inductance by manipulating the stator slot dimensions as highlighted in Fig. 2.4-2. One approach is to modify the slot height and width as described in [28].

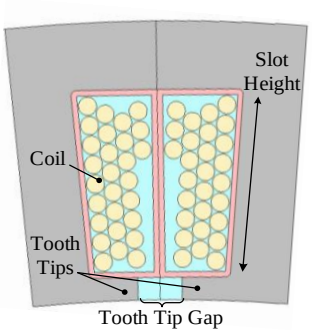

Figure 2.4-2 Stator slot features and dimensions used for manipulating stator slot leakage.

Alternatively, the leakage inductance can be manipulated by adjusting the slot tooth tip geometry and the corresponding tooth tip gap. Examples of FT machines using these types of features are described in [22], [31], [57], [118]. Notably, this tooth tip manipulation is taken to an extreme in [118] with the complete closing of the tooth tip gap and is shown in Fig. 2.4-3. Closing the slot assists with meeting the desired inductance goals and drastically decreases rotor-induced eddy current losses that are aggravated by the stator slot openings. However, some decrease in average torque capability is caused by totally closing the tooth tip gaps, creating design tradeoffs.

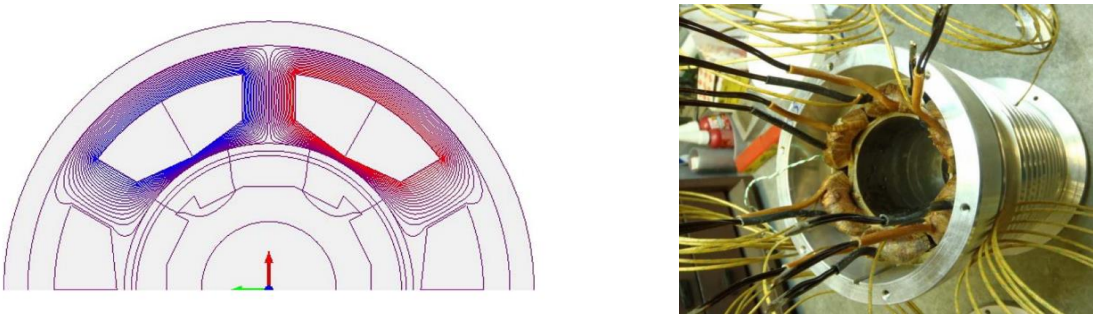

Figure 2.4-3 FT PMSM machine with closed slot design (flux contour left, assembled stator right) [118]**.**

A similar magnetic leakage effect is achieved by introducing magnetic wedges in the tooth tip gap as done in [56]. This approach makes it possible to retain sizeable slot openings that simplify coil insertion during stator fabrication. Choice of the wedge material and magnetic permeability provides additional degrees of design freedom for adjusting the machine phase inductance.

Other short-circuit current limiting approaches have been proposed outside of slot leakage maximization. In [119] a FT PMSM generator using a ring-motor winding is presented which orients coils in the same direction causing phase self and mutual fluxes to partially cancel during healthy balanced operation (Fig. 2.4-4). As a result, the phase self-inductance can be boosted without affecting the terminal characteristics of the machine, which limits short-circuit faults considerably in the event of a turn-to-turn failure.

Figure 2.4-4 FT PMSM generator designed for internal turn-to-turn FT [119]**.**

The criticality of short-circuit limiting features in aerospace-propulsion machines is exemplified in the axial-flux SPM integrated-propulsor in [71] and shown in Fig. 2.3-4. This machine achieves an impressive torque-density of 11 N-m/kg (the critical metric for its application) by utilizing a toroidally-wound slot-less stator design. On the rotor side, it utilizes a core-less Halbach magnet array with a total pole-count of 72. Due to its large diameter and pole count, each phase coil only had three turns leading to a very low inductance. Unfortunately, an internal short circuit occurred in the machine winding during testing leading to significant localized heating, preventing further demonstration. Although unfortunate, this winding-failure highlights the tradeoff between short-circuit limiting features and power-density.

2.4.1.2. Isolation Approaches

Isolation features can be added to machine-drive systems to prevent the propagation of faults. Power channel isolation features in FT systems can categorized into several interconnected subcategories:

- Magnetic isolation: Magnetic isolation features prevent magnetic interactions between power channels. In the context of FT machines, fault currents in failed windings should minimally couple with remaining healthy channels. Excessive coupling between channels can lead to potential unbalanced currents and torque ripple [120].
- Electrical isolation: This approach limits electrical interconnections between channels. For example, breaking the internally connected neutral in a wye-connected machine is a form of electrical isolation.
- Physical separation: The physical separation of channels prevents contact-related faults between channels. For example, two unseparated coils sharing the same stator slot can rub together due to machine vibration, leading to a potential insulation failure and interphase fault.
- Thermal isolation: The thermal state of a power channel must have negligible heat transfer effects on surrounding power channels.

A dual-redundant machine-drive with two power channels (Fig. 2.4-5) meets the isolation criteria previously described. However, this FT approach is suboptimal for simultaneously achieving the desired fault tolerance and overall low mass required for applications requiring high power density. Alternative forms of isolation have been investigated in the literature and are organized into general groupings here.

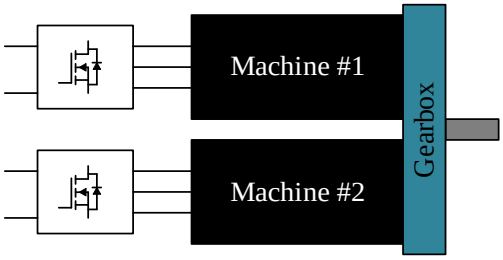

Figure 2.4-5 Dual-redundant motor-drive system with interconnecting gearbox or coupling.

This baseline dual-redundant machine-drive can be compacted by placing redundant stators on the same shaft as shown in Fig. 2.4-6. One stator can fail but system operation will be maintained by the remaining healthy stator. Isolation is maintained between stator modules due to the physical separation of the stators (although there will be mechanical interaction via the shared shaft). This type of FT approach has been applied to power steering in [121], assuring continued operation under conditions of a short-circuit fault.

The dual stator approach provides additional degrees of freedom by selecting the magnet arrangement for each stator. The dual stator implementation naturally applies to axial flux machines [94]. Other dual stator examples can be found in [122], [123]. While stator-redundancy can provide good isolation, it scales poorly for stator counts greater than two since each additional redundant stator adds significant mass and length to the machine shaft, as well as degrading the dynamic performance of the longer rotor assembly.

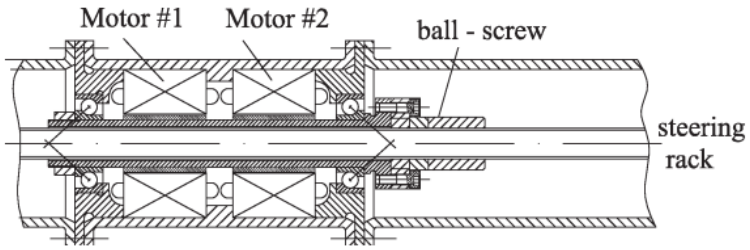

Figure 2.4-6 Dual stators sharing a single shaft example [121].

Often redundant power channels are built into the stator itself, requiring internal stator isolation features. These types of machines often use FSCW stator winding configurations to take advantage of their inherently separated phase end windings and good natural magnetic isolation assuming careful selection of the slot-pole combination [124], [125]. The use of SL FSCW machines physically separate stator coils and phases, which makes it a popular approach for achieving stator isolation in FT stators, with some notable examples identified here. As the first example, a multiphase 12-slot, 8-pole SPM machine is presented in [28]. The machine achieves electrical isolation by assigning a full-bridge converter to each phase. Furthermore, the choice of SL windings helps to thermally isolate coils after a short circuit in an adjacent failed phase.

For the second example, a SL winding is applied to fractional-slot 24-slot, 28-pole machines in [30], [126], which divides its stator into four three-phase modules. Similar thermal isolation between coils is observed after a module short circuit as shown in Fig. 2.4-7. As evident in Fig. 2.4-7, ideal thermal isolation is difficult for SL windings as there is some thermal interaction between modules through the spacer teeth.

For a third example, SL coil isolation and performance benefits can be gained by inserting flux barriers between teeth [127]. In general, the use of SL is one of the most common implementation of FT isolation based on the previously mentioned benefits. Other examples of notable SL winding FT machines not yet discussed in this review can be found in [128], [129].

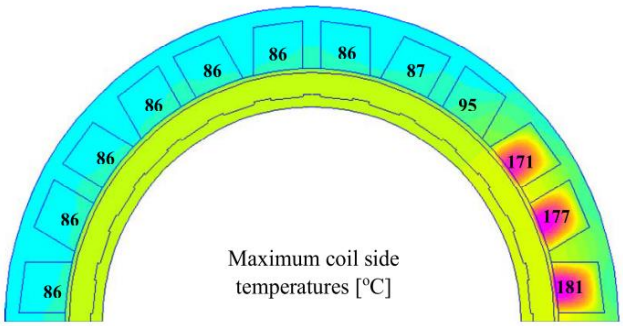

Figure 2.4-7 Machine cross-section thermal contour of SL winding under a fault condition with peak coil temperatures highlighted [30]**.**

FT machines with SL windings achieve high electromagnetic isolation, but this choice can degrade both power density and performance because of elevated harmonic flux components in the airgap that increases the rotor losses. Furthermore, the desire to achieve high power density for aerospace applications typically favors machines with a high rotor tip speed (and therefore rotor diameter) relative to the stack length, causing the impact of end windings to be significant. This can be observed when considering both SL and DL windings for the same stator geometry in Fig. 2.4-8. For the same stator core geometry, the SL winding alternative is estimated to have 25.2% higher coil volume, 26.7% higher mean-turn-length, and 33.4% higher axial length. Similar observations about SL windings are discussed in [130].

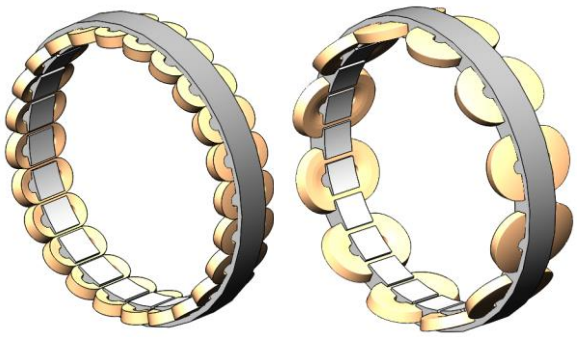

Figure 2.4-8 24-slot/28-pole modular stators using DL (left) and SL (right) FSCW winding configurations.

Modular FT machines with multiple three-phase channels can utilize other forms of isolation to prevent the propagation of faults. Specifically, isolation features can be inserted between modules allowing for greater module design flexibility (e.g., the use of DL windings). This approach was adopted in [31] where spacer teeth are inserted between modules as shown in Fig. 2.2-2(b). More recently, a five-phase 20-slot 22-pole modular design uses small spacer teeth between machine phases to reach the desired level of isolation during a turn-to-turn short circuit [131] as shown in Fig. 2.4-9. Alternatively, certain slot-pole combinations can be modularized on the phase level allowing for stator airgaps between phases as shown in Fig. 2.4-10 [132], or to concentrate machine phases reducing the number of contact point between modules in [133], [134].

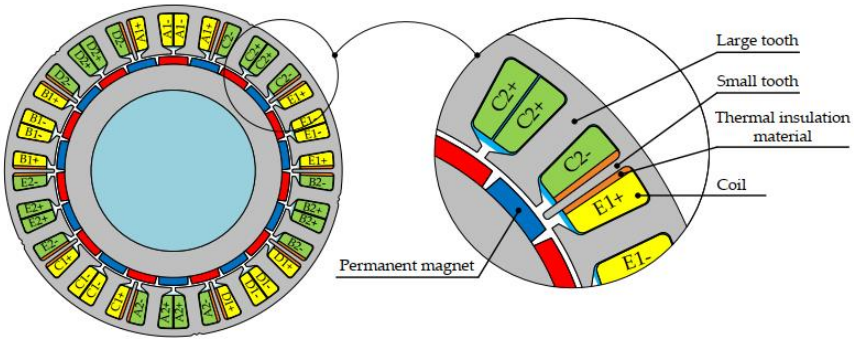

Figure 2.4-9 Modular 20-slot 22-pole machine with small spacer teeth located between phases [131].

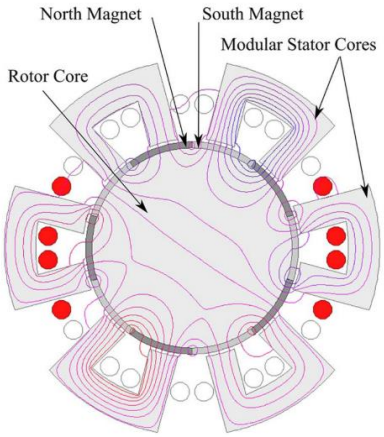

Figure 2.4-10 Phase modular stator core and coil flux lines [132].

2.4.1.3. Redundant Power Channels

It is necessary for FT machines to have enough power channels to allow for meaningful operation after one or more faults. For a system with *n* redundant power channels and *f* allowable failures, the required channel derating *F* can be described by

$$F = \frac{n}{n - f} \tag{2.4.2}$$

For example, a four-channel system with two allowable failures requires each channel to be derated by a factor of 2x to maintain full torque operation after the second failure. This derating factor can be reduced if degraded operation (i.e., reduced operating power) during fault modes is acceptable. A higher derating factor degrades the machine's power density by requiring oversizing of each of the stator windings, stator core, and the associated stator cooling to prevent machine overheating during post-fault operation.

As discussed in preceding subsections, FT machine power channels can take several forms, with pure machine redundancy being the simplest approach as described in Fig. 2.4-5 (i.e., each redundant machine acts as an independent power channel). Similar redundant power channels can be added using multiple stators on the same shaft as in Fig. 2.4-6. For electric aircraft this direct redundancy can be applied on the propulsor level utilizing DEP. For machines, stator-based redundancy can be achieved by dividing the stator coils into either single- or multi-phase modules.

The concept of independently exciting machine phase legs to improve overall system reliability extends back several decades to industrial IMs in [135]. Similar phase excitation concepts have been applied to PMSMs in [28], [29], [40], [48], [51], [81], [115], [116], where windings are excited by full-bridge converters as shown in Fig. 2.4-11. This approach is often used with multi-phase machines due to the flexibility it offers to the machine designer. Exciting each phase

separately as in Fig. 2.4-11 offers electrical isolation advantages by removing internal machine connections, but adds some challenges to the machine control problem.

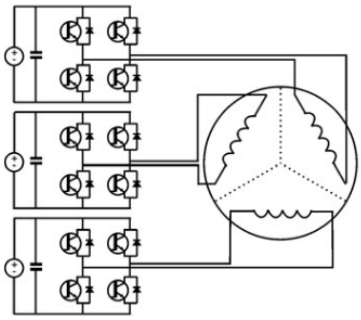

Figure 2.4-11 Single-phase power channel with isolated full-bridge converters [51]**.**

It should be noted multi-phase FT machines can be used without isolated full-bridge converters. A five-phase machine considering both SL and DL windings is presented in [39], which considers control strategies and impact of multiple phase open-circuit failures.

Modular machine drives (MMD) are distinguished by breaking the stator into multiple three-phase winding groups, each excited by its own inverter. This approach is being used in the NASA ULI program MW-scale propulsor machine, where the 18-slot, 12-pole machine is separated into three three-phase winding groups as shown in Fig. 2.4-12 [22]. Further this project aims to integrate the modular electronics in an IMMD configuration. As shown in the figure, the three groups, each with its own inverter, can be connected in series, reducing the required voltage rating of each of the three modules.

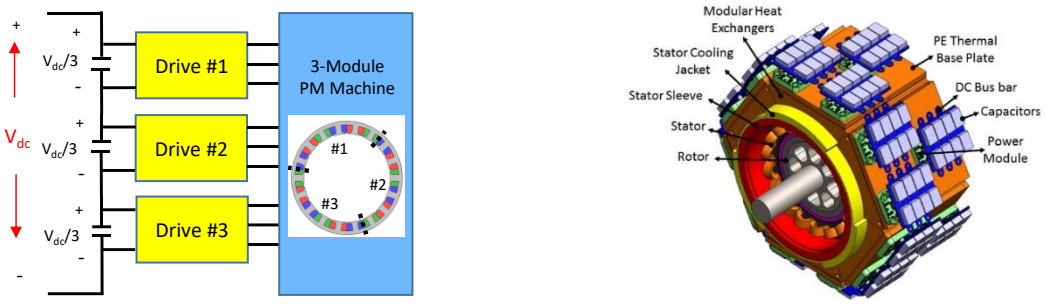

Figure 2.4-12 Modular 18-slot 12-pole machine with drives connected in series (left) with rendered machine and integrated power electronics (right) [22]**.**

Another example of a FT MMD PMSM is found in [136] for a safety-critical elevator application. Like the previously mentioned NASA machine, this machine is modularized into three winding groups constituting a total nine-phases as shown in Fig. 2.4-13. In this example, the modularity is expanded to consider the AC-DC converter. Detailed discussion on modular control strategy are also discussed. Other FT modular machines can be found in [30], [31], [51], [126], [136]–[139].

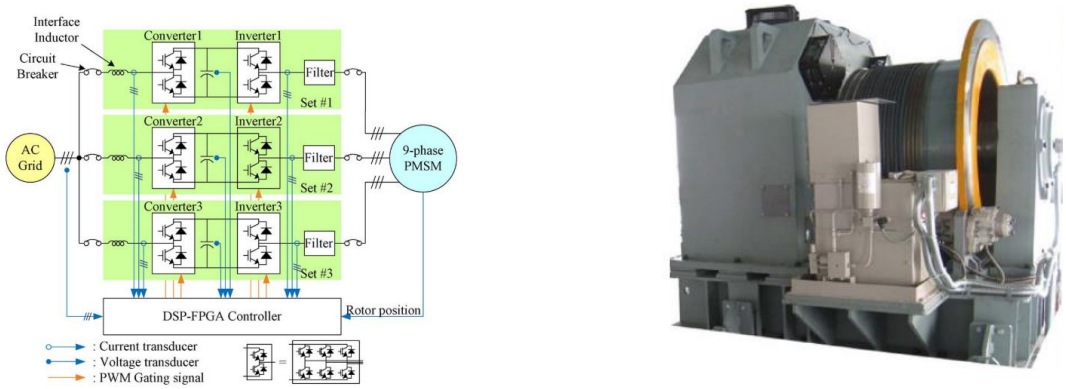

Figure 2.4-13 Nine-phase FT modular machine for an elevator application [136]**.**

2.4.2. Fault Tolerant Power Electronics Topologies

A similar literature review was performed for FT power electronics topologies. The same fault tolerance guidelines and observations related to power channel isolation and redundancy apply to power electronics as well. This review focuses on traditional two-level voltage-source inverters (VSI), although other converter types such as the matrix converter [40], [41] or the current-source inverter (CSI) can be used to eliminate unreliable components like dc-link capacitors [140].

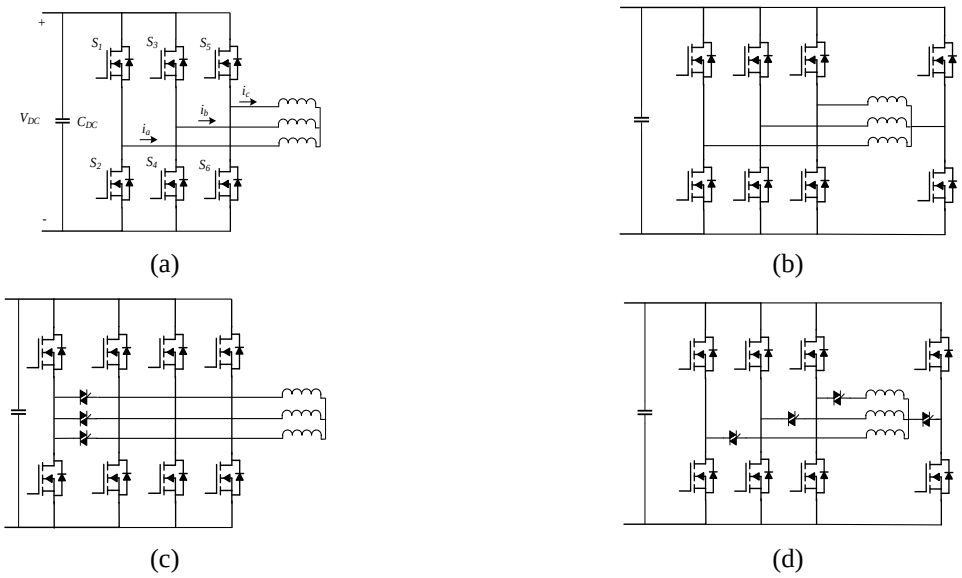

Figure 2.4-14 Two-level VSI configurations: (a) baseline non-FT; (b) redundant phase leg #1; (c) redundant phase leg #2; (d) redundant phase leg #3.

A basic two-level, three-phase VSI is shown in Fig. 2.4-14(a), which consists of a minimum of six switches and a dc link capacitor. Several FT VSI approaches exist, such as adding redundant phase legs [32] that provide opportunities for drive reconfiguration after a fault. The first connects a redundant phase leg to the machine neutral as described in Fig. 2.4-14(b), allowing for faulted operation after an open-circuit (OC) failure in a phase winding or device. Similar redundant phase legs topologies are described in Fig. 2.4-14(c) and Fig. 2-14(d) with triac devices added to electronically implement the reconfiguration, enabling operation after a short-circuit (SC) switch

failure. Variants of the described two-level, three-phase FT VSIs are discussed in [33], [34]. Similar FT strategies and limitations apply for multi-phase machines ($m > 3$) [35], [36].

The incorporation of direct converter redundancy can be used to avoid the complexities associated with drive reconfiguration. This approach coalesces with FT machine strategies using multiple single-phase, full-bridge converters in Fig. 2.4-11, or modular three-phase VSI drives in Fig. 2.4-12. The modular VSI approach can be modified to connect VSIs to both ends of the machine winding as described in Fig. 2.4-15 [33], [38], [39], also known as an open-winding configuration. FT operation during a switch OC or SC event is achieved by creating an artificial neutral in the faulted drive by activating all the upper or lower switches (depending on the location of the failed switch). Machine winding faults can be managed by isolating the faulted phase and operating the drive as a two-phase system. A detailed discussion on open-winding fault modes and post fault operation can be found in [38].

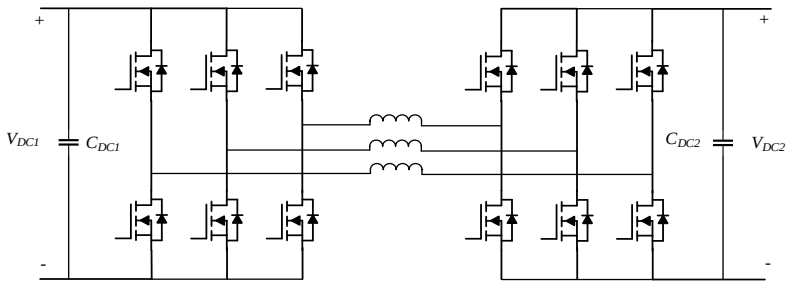

Figure 2.4-15 Three-phase modular VSI using an open-winding configuration.

Additional layers of fault tolerance can be added to modular strategies via the incorporation of redundant phase legs or increased phase count. Examples include the use of a redundant phase leg in a three-module, two-phase drive system in [141] shown in Fig. 2.4-16, or the five-phase open-winding system in [37] which is similar to the approach illustrated in Fig. 2.4-15.

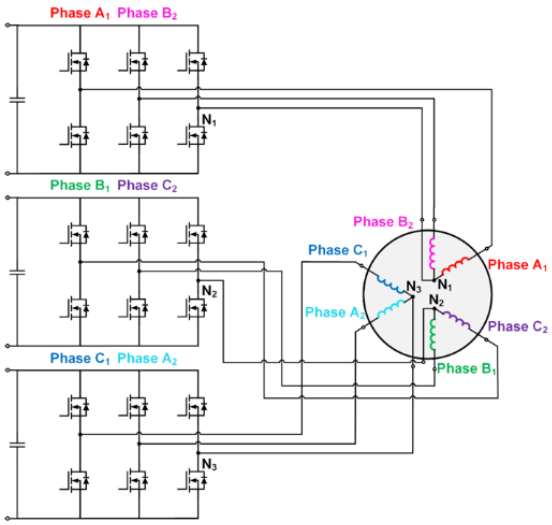

Figure 2.4-16 Six phase electrical machine divided into three two-phase modules [141]**.**

2.4.2.1. FT Current Source Inverters (CSI)

The use of Current Source Inverters (CSI) in aerospace applications has been identified as a strong candidate for aerospace propulsion due to potential machine power density benefits related to inherent voltage boosting capability [142]. Further, the availability of wide band-gap device enables the possibility of high switching frequencies and reduced passive components (e.g, dc link inductor) [42]. Other advantages include the removal of low reliability components like dc link capacitors as previously mentioned.

A major FT PMSM advantage of the CSI over the VSI is its transient response to switch-short circuits, scenarios where excitation is lost during flux-weakening operating leading to uncontrolled generator operation, and terminal short circuits [143]. Specifically, the presence of a stiff DC link current can suppress fault transient-currents which can be excessive for VSI faults contributing to significant transient torque ripple and possible demagnetization.

Beyond built-in FT advantages, FT features similar to the VSI can be implemented with many FT topologies summarized in [144]. In most cases these FT CSI topologies mirrors the VSI implementations discussed above (switch redundant, multi-phase, etc.).

2.4.2.2. Summary of FT VSI Power Electronics

A summary of major VSI power electronics FT configurations and their capabilities is summarized in TABLE 2.4-1. The use of redundant phase legs described in Fig. 2.4-14 offers FT capability for an OC device failure, and some FT capability for SC device failures. These redundant phase-leg configurations are not suitable for multiple switch failures or a capacitor failure. Similar observations can be made for an *m*-phase drive, with potential for continued operation after multiple OC switch failures. Next, FT approaches with redundant converters (like those shown in Fig. 2.4-11, Fig. 2.4-12, and Fig. 2.4-13) offer the greatest range of fault tolerance capability, allowing for multiple switch or capacitor failures. While each of these approaches offers some opportunities for continued operation following an OC machine winding fault event, SC winding fault events can be better addressed using a modular converter approach.

TABLE 2.4-1 SUMMARY OF MAJOR FT VSI CONFIGURATIONS AND CAPABILITIES

Fault / Topology	Redundant Leg #1	Redundant Leg #2	Redundant Leg #3	Multi H-Bridge	Open Wind. 3-Phase	Multi 3-Phase	M-Phase	Multi M-phase
Switch OC	Yes	Yes	Yes	Yes	Yes	Yes	Yes	Yes
Multiple Switch OC	No	No	No	Yes	No	Yes	Yes	Yes
Switch SC	No	Yes	Yes	Yes	Yes	Yes	No	Yes
Multiple Switch SC	No	No	No	Yes	No	Yes	No	Yes
Cap. Failure	No	No	No	Yes	Yes	Yes	No	Yes
Winding	Limited	Limited	Limited	Yes	Limited	Yes	Limited	Yes

Finally, there are cost and parts count tradeoffs associated with each of these FT power electronics approaches, as indicated in TABLE 2.4-2 that summarizes the expected component counts for each of the considered approaches. In general, the addition of redundant phase legs or increasing the number of phases requires a comparatively small increase in devices. In contrast, the use of modular systems can vastly increase the number of required components depending on the level of modularity. Further differentiation can be made among these topologies considering device utilization, sizing, losses, and operating stresses.

TABLE 2.4-2 PARTS COUNT FOR THE CONSIDERED FT VSI CONFIGURATIONS

Fault / Topology	Redundant Leg #1	Redundant Leg #2	Redundant Leg #3	Multi H-Bridge	Open Wind. 3-Phase	Multi 3-Phase	M-Phase	Multi M-Phase
Min. Switches	8	8	8	4*m	12	6*n	2*m	2*m*n
Triacs	0	3	4	0	0	0	0	0
Min. Caps	1	1	1	m	2	n	1	n

2.5. IMD Reliability Evaluation

Numerous techniques can be used to evaluate the reliability of motor-drive systems. This section first reviews IMD failure sources followed by common reliability calculation techniques and their application to electric machines and drives.

2.5.1. IMD Failure Sources

Identifying the failure modes and effects of IMDs is critical first step for a reliability evaluation. Numerous surveys of industrial motor-drives exist in the literature with summaries of key survey results provided in [145], [146]. Surveyed electrical machine failure distributions are summarized in Fig. 2.5-1(a) and shows bearing failures as predominant failure mode in electric machines

followed by stator failures. These stator failures primarily consist of winding failures located at the machine terminals (open or short circuit), or internal short circuits between coil turns. The rotor failures described in Fig. 2.5-1(a) predominantly relate to shaft and rotor bar failures in IM, though rotor failures related to magnet demagnetization and magnet containment bursting exist for PMSMs [147]. Surveyed power electronics failures are shown in Fig. 2.5-1(b), showing the VSI capacitor as the most unreliable components followed by PCB and semiconductor components.

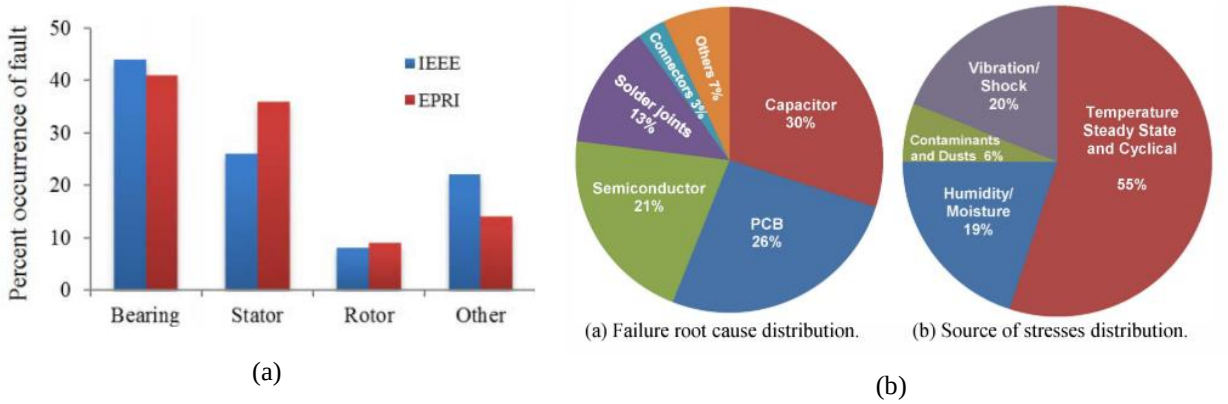

(a) (b)

Figure 2.5-1 Motor drive failure distributions based on industrial survey data: (a) electric machine failures [145]**; and (b) power electronics failures** [146]**.**

The stressors and processes of IMD failures are numerous. Environmental stresses operating temperature, vibration, humidity, and dust can all have an impact the expected reliability of a component [146], [148]. Particular to an IMD, the power electronics are particularly vulnerable to vibration due to close integration with the machine. Further, the operating characteristics of the electrical machine and power electronics influence device reliability. In particular, thermal over stresses related to the device loading and thermal duty cycle can lead to accelerated stator winding aging [52], or CTE-related fatigue failures in power electronics wire bonds and solder joints [149].

Voltage over stress also contribute to IMD component failures like dielectric breakdown in power electronics devices and electrical machine windings. The use of hard-switched Pulse Width

Modulated (PWM) drives with high *dv/dt* can further age the machine winding, contributing terminal voltage spikes, uneven winding voltage distributions, and increased partial discharge [150], [151]. Last, additional stresses can be introduced via manufacturing defects. For example, eccentricity in the machine stator or rotor introduce an Unbalanced Magnetic Pull (UMP) on the rotor contributing to increased bearing wear, and in some catastrophic cases causing contact between rotor and stator components [152].

2.5.2. Reliability Calculation Methods

There are numerous tools and standards available for assessing system and component reliabilities [153], [154]. Several reliability evaluation methods are shared here in combination with a brief introduction into reliability mathematics.

2.5.2.1. Reliability Mathematics

Primers into reliability mathematics can be found [153], [154] with relevant component failure rate distribution discussions reiterated here. The use of reliability statistics can be used to estimate system reliability and requires assumptions of the underlying component failure probability distributions. Specifically, the probability of component failure P between times t_1 and t_2 is determined by the component failure probability density function $f(t)$ in

$$P(t_1 < t < t_2) = \int_{t_1}^{t_2} f(t)dt \leq 1 \tag{2.5.1}$$

This can be modified into Cumulative Distribution Function (CDF) describing the probability of failure at a particular time $F(t)$. A more useful CDF is the reliability function $R(t)$, which gives the probability of healthy operation and can be calculated from $F(t)$:

$$F(t) = \int_{-\infty}^{t} f(t)dt = \int_{0}^{t} f(t)dt$$
$$R(t) = 1 - F(t) \tag{2.5.2}$$

The Mean Time to Failure (MTTF) of the system is a key metric to describe the reliability and can be derived from the reliability function in (2.5.3). A higher MTTF corresponds to a more reliable system.

$$MTTF = \int_{0}^{\infty} R(t)dt \tag{2.5.3}$$

An exponential failure distribution is commonly used to model electrical component failures with a constant failure rate λ (in failures per hour) and is shown

$$f(t) = \lambda \cdot e^{-\lambda \cdot t} \tag{2.5.4}$$

Inserting (2.5.4) into (2.5.3) and (2.5.2) yields an expected MTTF equal to $1/\lambda$.

A constant failure rate assumption like what is assumed in (2.5.4) is typically unrealistic. A component's failure rate can be broken into three-stages over its lifetime as described in Fig. 2.5-2. The first stage is the infant mortality stage in which failures can be attributed to the failure of weak items (e.g., defect parts), which decrease with time. The middle stage is the useful life portion of the component in which the failure rate can be considered constant due to randomly induced failures (e.g., overstress). The final stage is characterized by an increasing failure rate related to the natural wear-out of components.

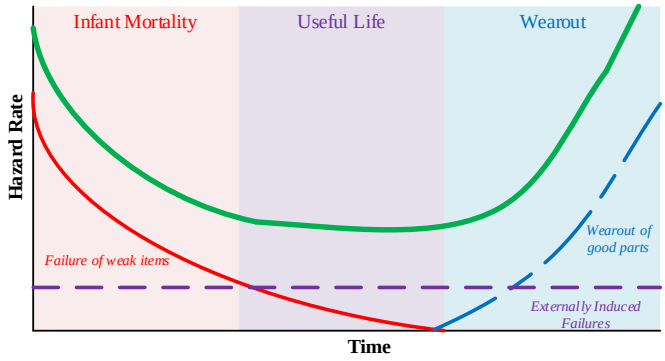

Figure 2.5-2 Component failure rate curve (bathtub curve) of components.

Next, systems are often made up of multiple components, each with their own reliability function. The reliability relationship between these components can affect the overall system reliability and can be represented graphically. A series connected system is shown in Fig. 2.5-3(a) with two components with reliabilities $R_1(t)$ and $R_2(t)$. The overall system is considered failed should either component fail with system reliability represented by

$$R_{sys}(t) = \prod_{k=1}^{n} R_k(t) \tag{2.5.5}$$

Alternatively, a parallel connected (redundant) system is shown in Fig. 2.5-3(b) with components connected in parallel. The system is only considered failed if both components fail. The corresponding two-component parallel system reliability is

$$R_{sys}(t) = R_1(t) + R_2(t) - R_1(t) \cdot R_2(t) \tag{2.5.6}$$

In general, a series connected system has lower reliability relative to its sub-components, and a parallel system has improved reliability. In other words, a parallel system would be considered redundant or fault tolerant.

The formulas described in (2.5.5) and (2.5.6) are useful for simple systems, though become cumbersome for large and more complex reliability problems. An example of this type of reliability evaluation method in combination with Fault Tree Analysis (FTA) is given in [155] which evaluates the thrust, reliability, and weight tradeoffs associated with turboelectric DEP aircraft-architecture concept. Other methods for estimating system reliability are shared here.

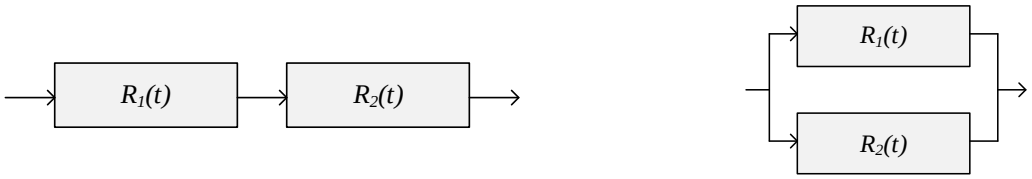

Figure 2.5-3 Series (a) and parallel (b) connected reliability representations.

2.5.2.2. Part Counts Methods and Fault Tree Analysis

Many standards exist that use a part count methods in combination with stress factors for determining component and system failure rates [148]. The MIL-HDBK-217F military standard dates back to the 90's [156] and is an example of one of these parts count methods. System failure rate λ is calculated using

$$\lambda = \sum_{i=1}^{n} N_i \cdot \pi_i \cdot \lambda_i \tag{2.5.7}$$

with n groups of components, group-i component failure rates λ_i, number of group-i components N_i, and component stress and environment factors π_i. Formulas and tables for calculating stresses and component failure rates are provided in MIL-HDBK-217F. Others standards like the NWSC-11 can be used to estimate stress factors [157].

This type of parts count approach for estimating reliability has been applied to [41], where a matrix converter is compared against traditional ac-to-ac converter topologies. In more recent years, the MIL-HDBK-217F is considered outdated, though is still referenced by many component

manufacturers. Further, (2.5.7) provides good intuitive value illustrating how increased part counts and higher system stresses will negatively impact reliability.

More sophisticated reliability evaluation methods can be applied to motor-drive systems. Fault Tree Analysis (FTA) is a graphical method with failure modes interconnected with logic gates, allowing for visualization of fault propagation paths. These logic gates follow a similar logic to the parallel and series system diagrams shown in Fig. 2.5-3. This type of evaluation has been applied in [51] for modular machines with the corresponding machine and power electronics graph shown in Fig. 2.5-4. Further, the previously mentioned UAM VTOL reliability studies in [26], [68] used a Fault Tree Analysis (FTA), which was used to identify components like electric machines and drives as limiting components for high reliability.

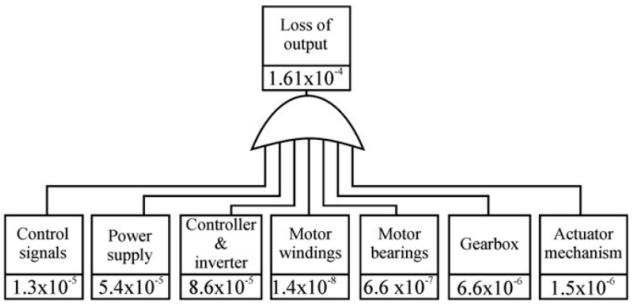

Figure 2.5-4 Example FTA of a motor-drive system [51]**.**

2.5.2.3. Markov Chain Analysis

Markov models provide a flexible tool for evaluating IMD systems and have been frequently applied to motor-drive systems. These Markov chains divide the system into interconnected healthy and failed states, and transitions between states are defined by component failure rates. State space techniques can be used to estimate failed state probabilities and system reliabilities. A deeper discussion of Markov chains and the underlying reliability mathematics can be found in [154].

There are numerous examples of Markov chains applied to electric machines and power electronics in the literature. Previously, discrete-time Markov chains have been used in [32] to develop comparisons among the FT power electronics topologies (neglecting machine components) in Fig. 2.4-11 and Fig. 2.4-14. The study shows repairs are critical to improve reliability and that the redundant full-bridge configuration in Fig. 2.5-5 has better potential for reliability improvement relative to other topologies due to its capacitor redundancy. A similar continuous-time approach was applied to FT machine drive configurations in [43]. A three-module configuration was studied in [43] and shown here in Fig. 2.5-6, further identifying modularity as a promising path for improving reliability numbers in combination with repairability.

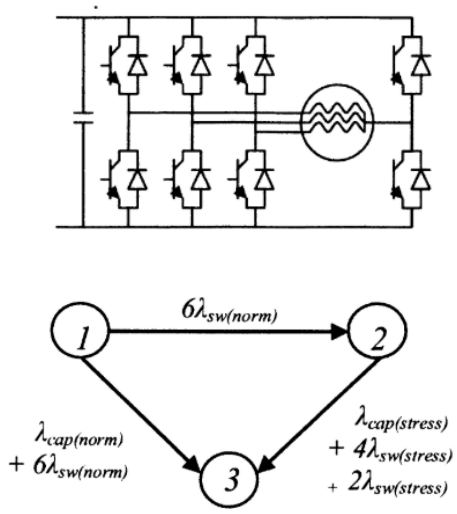

	MTTF (Hours)	
Topology	*No Repairs*	*Repairs*
Standard Inverter	869,000	869,000
Neutral	629,000	869,000
Redundant	784,000	869,000
Triac Phase & Neutral	845,000	3,998,000
Separate H-bridges/Caps	381,000	1,360,000,000

Figure 2.5-5 Example neutral phase leg Markov chain model and MTTF results for FT drive topologies [32]**.**

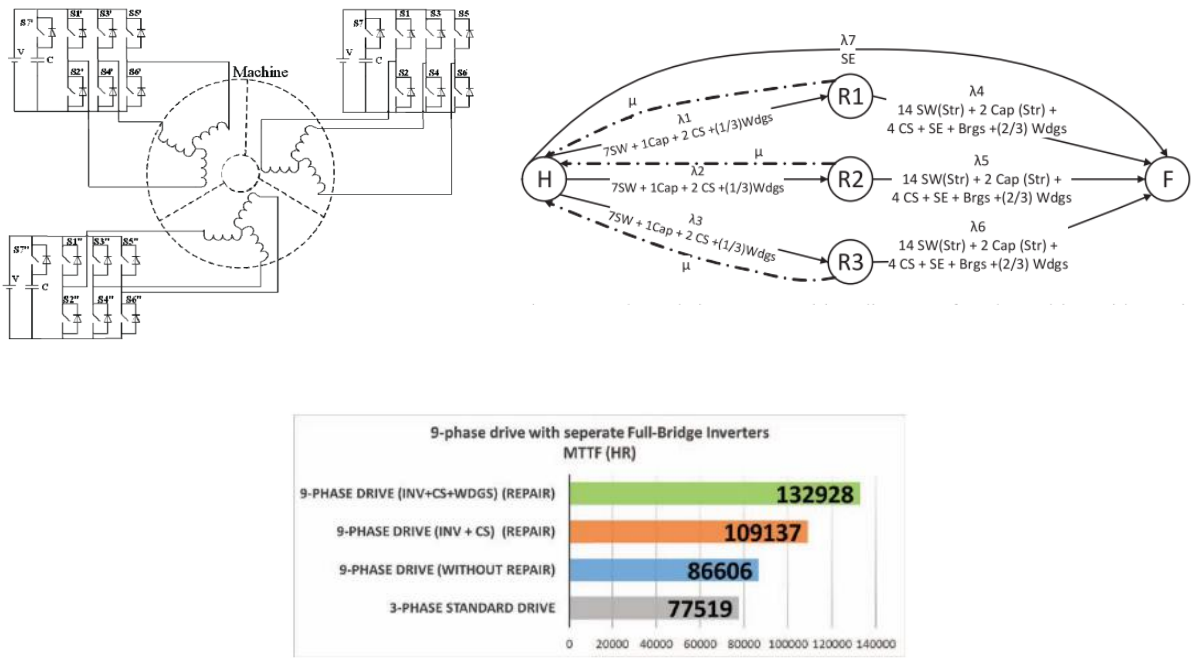

Fig. 12. MTTFsof 9-phase drive with and without repair compared to standard 3-phase drive

Figure 2.5-6 Three-module Markov chain model and MTTF results [43]**.**

Next, Markov chains were used in [158] to compare different types of winding structures in PMSMs (multi-phase, multi-three phase winding sets) and use analytical thermal to estimate the winding thermal stresses which were used to determine π-stress factors. Additional states and transitions can be added to these machine Markov models to investigate the impact of component aging, as has been done for the case of insulation deterioration in [159]. Other motor-drives Markov chain examples can be found in [160]–[166].

More recently the application of Markov chains has been applied to study the reliability relationship between a quadcopter UAV with FT power electronics utilizing a fourth inverter leg attached to the machine neutral shown in Fig. 2-14(b) allowing for two-phase operation after a switch failure [44]. Device failure rates are set following a physics-of-failure approach considering

the thermal cycling on drive devices following the expected mission profile (capturing both healthy and faulted stress).

2.5.2.4. Physics of Failure Modeling

In recent years, reliability evaluation has shifted towards a Physics of Failure (PoF) approached defined as a methodology based on an underlying failure mechanism analysis, considering the expected operating cycle of the component, and the associated physical-statistical model [146]. A summary of different types of PoF power electronics models is summarized in Fig. 2.5-7. Similar statistical models are identified for electrical machine failure modes in [167].

Failure mechanisms	**Failure sites**	**Relevant loads**	**Failure models**
Fatigue	Die attach, wire bond /TAB, solder leads, bond pads, interfaces	ΔT, T_{mean}, DT/dt, dwell time, ΔH, ΔV	Nonlinear Power law (Coffin-Manson)
Corrosion	Metallization	M, ΔV, T	Eyring (Howard)
Electromigration	Metallization	T, J	Eyring (black)
Conductive filament formation	Between Metallization	M, ΔV	Power law (Rudra)
Stress driven diffusion voiding	Metal traces	S, T	Eyring (Okabayashi)
Time dependent dielectric breakdown	Dielectric layers	V, T	Arrhenius (Fowler-Nordheim)

T: temperature; H: humidity; Δ: cyclic range; V: voltage; M: moisture; J: current density; ∇: gradient; S: stress.

Figure 2.5-7 Summary of failure mechanisms, loads, and statistical models for power electronics [146]**.**

In [168] estimated inverter lifetimes for an electrical vehicle application are estimated using the MIL-HDBK-217F calculated MTTF, which are compared to thermal lifetime models for power electronics. These physics-based lifetime models include an Arrhenius model to capture temperature level effects, and a modified transistor Coffin-Manson model which captures the impact of junction temperature cycling. Variables N refers to the number of temperature-cycles the transistor can handle for temperature variation ΔT. The results of this study show the limitations

of parts counts methods due to an inability to accurately account for application specific stresses, leading to an overestimation of system MTTF by a factor of 4.

Other power electronics PoF studies have been performed on WBG device packaging using Finite Element Analysis (FEA). The study in [169] compares WBG silicon-carbide (SiC) and silicon (Si) packaging for fatigue related to thermal cycling, and shows differences in SiC and Si CTE can lead to significant fatigue damage in device solder layer. Other examples of PoF modeling for power electronics can be found in [44], [146], [170], [171].

Similar PoF studies have been performed on electrical machines, with specific emphasis on stator winding insulation health. The impact of thermal overload and duty cycle for a SL PMSM aerospace machine is discussed in [52]. The effect of insulation aging due to overload temperature and cycling is investigated using motorettes (i.e., smaller versions of the stator core and winding). The results of this study were used to inform a modified Arrhenius model considering the impact of thermal cycling. A similar cyclic thermal insulation aging approach is described in [172]. The effects of electrical field stress on winding insulation is described in [173], with the impact of electrical stress included in a modified Arrhenius model.

2.6. Research Opportunities

This literature survey has reviewed a wide range of published techniques for designing fault-tolerant electric machines and drives for applications requiring high reliability. The need for reliable motor drives is exemplified by emerging electrified aircraft propulsion systems that have reliability needs far exceeding those of typical terrestrial applications in addition to their demands for the highest achievable power density. A review of aircraft electric propulsion concepts and their associated power-dense electric machines is presented, highlighting key electrical machine

development efforts and trends. In general, the adoption of SPM synchronous machine topologies to achieve the highest possible power density is a popular trend. In many cases, fault-tolerant features are incorporated into the machine and electronic drive designs to improve their reliability characteristics. In addition, the integration of drive power electronics into the electrical machine housing to form integrated machine drives (IMDs) makes it possible to further enhance the machine drive's power density and fault-tolerant performance characteristics.

The UAM VTOL reliability study in [26] identifies propulsor motors and their associated electronics as low-reliability components limiting the feasibility of these electric machines in VTOL propulsion applications. The use of FT features is a common methodology for improving reliability. Key trends are observed in this survey focusing on the papers addressing FT electric machines and drives:

- Most surveyed FT electric machine papers were selected for aerospace applications indicating their usefulness for improving system reliability for safety critical applications. The second most common use of FT is for automotive applications followed by industrial application
- Overall, the use of single-layer windings to increase the electromagnetic and physical isolation of individual phase windings is the most common feature used in FT machines. The implementation of specialized current limiting features in PMSM is also common.
- Adoption of modular machine drives with multiple three-phase (or more) windings appears in multiple papers, the addition of special electromagnetic, thermal, or physical isolation features such as spacer teeth between modules is quite rare, indicating that there are research opportunities to investigate new techniques to improve the modular isolation characteristics

- Many different approaches and implementations of fault-tolerant motor drives exist though difficulty exists in comparing their usefulness in improving system reliability against alternative FT implementations.

Based on this review of state-of-the-art FT electric machines and their associated drives, the following research opportunities have been identified:

1. **Comprehensive comparison of electric machine FT approaches highlighting tradeoffs of each approach and the impact of modularity:**

   Several studies exist that compare FT features in the motor drive power electronics. However, no study of this type has been found for FT electric machines. Numerous types of fault-tolerant features in electric machines are presented in the literature, but Figures of Merit (FoM) to evaluate and compare these techniques do not exist, making it difficult to determine preferred FT approaches for different applications. This is particularly important since the introduction of some FT modularity techniques leads to significant degradation of other key metrics such as machine power density or efficiency. This research will specifically address the impact of these tradeoffs in order to identify the most promising techniques for achieving isolation of the motor modules, with particular attention devoted to electromagnetic isolation.

2. **Investigate promising approaches to implementing modularity in electric machines and drives to improve fault tolerance, focusing on the challenges of achieving modular isolation when serious faults (e.g., short-circuit faults) appear in adjacent machine modules:**

   Surveyed FT machine designs primarily feature single-layer windings to achieve electromagnetic isolation between machine phases and modules, which can lead to suboptimal performance metrics including degraded power density. Alternative machine modularity

design approaches to enhance the machine's electromagnetic isolation capabilities while minimizing their negative impact on key performance metrics will be investigated. In addition, the use of in-slot cooling will be evaluated as a promising technique for providing improved cooling of the machine modules as well as assisting with thermal isolation of individual modules.

3. **Reliability estimation in modular electrical machines and drives identified for aerospace propulsion machines:**

   The design process for a FT modular PMSM with integrated power electronics will be explored to investigate the reliability challenges associated with propulsion machines in UAM VTOL aircraft. The developed models will be used as a starting point to investigate the expected machine stresses during both healthy and faulted operating modes that can be used as inputs into machine reliability analysis. Markov chain analysis will be used to investigate the predicted reliability of modular motor drive systems in order to identify strategies for significantly improving the machine drive's reliability. This FT evaluation will consider the harmful effects of internal winding short circuits, which can be especially dangerous for FT PMSMs.

Chapter 3

Achieving High Levels of Machine Power Density Using Modular Machine Drives

The previous chapter described different types of power dense machines used in aerospace applications. This section presents a methodology for developing initial machine designs for power dense applications, optimizing both winding loss and power density. This sizing tool is effective for exploring a machine design space for a given set of specifications considering speed, slot/pole combinations, etc., and will be used in subsequent chapters that discuss the development of modular power-dense machines for aerospace applications.

Next, the power density and fault tolerance characteristics of two machine designs developed by the author during a NASA University Led Initiative (ULI) project are discussed. These machine designs were designed to be technology demonstrators for future electrified aircraft propulsion applications [174]. More specifically, the design of a 1 MW Surface Permanent Magnet (SPM) machine is presented, which is divided into six sets of three-phase windings, each with its own dedicated power electronics. The design of a closely-related 200 kW demonstrator machine is also presented. Experimental test results for both machines are shared, showing good agreement with their design predictions.

The developed six-module machines share several features with the modular FT machine topologies discussed in Chapter 2, but they fail to provide sufficiently high electromagnetic isolation of their winding modules after a fault. A combination of simulations and experimental tests has been used to investigate the behavior of the 200 kW demonstrator machine during open- and short-circuit terminal faults, including post-fault operation. This investigation has provided valuable insights into the impact of the choice of modularity implementation (e.g., split into

machine halves or interleaved modules) on post-fault performance. In particular, it has highlighted tradeoffs between machine vibration caused by unbalanced magnetic pull (UMP) on the rotor, and electromagnetic interactions between adjacent winding modules that contribute to unbalanced currents.

3.1. Power Density Metrics and Design Philosophy

Key metrics associated with high performance and power dense designs are presented in Chapter 2 and summarized in Table 3.1-1 in the context of permanent magnet synchronous machines (PMSM). These metrics identified in [6], [23], [71], [90] include machine speed n [rev/min], shear stress σ_m [Pa] (consisting of the product of magnetic loading B_{g1} [T] and electric loading K_{s1} [A/m]), current density J [A/m^2], and rotor tip speed v_{tip} [m/s]. These equations are reiterated here

$$\begin{aligned} P_e &= \left(\frac{\pi}{30}\right)\cdot n \cdot V_r \cdot \sigma_m \cdot \cos\varphi \cdot \eta \\ \sigma_m &= B_{g1}\cdot K_{s1}/2 = \frac{T_e}{2\cdot V_r} \\ J &= \pi \cdot K_{s1}\cdot D_{or}/(S\cdot A_{cu}) \\ v_{tip} &= \frac{\pi}{60}\cdot n \cdot D_{or} \end{aligned} \tag{3.1.1}$$

with shaft power P_e [W], rotor volume V_r [m^3], airgap power factor $cos\varphi$, airgap efficiency η, rotor outer diameter D_{or} [m], shaft torque T_e [N-m], number of stator slots S, and copper area per coil A_{cu} [m^2]. For simplicity, the presented sizing tool assumes power factor and efficiency of 1.

Limiting factors each power density metrics are identified in Table 3.1-1, highlighting the tradeoffs associated with each approach for power density. Maximizing each of these metrics may

lead to undesirable levels of losses leading to poor efficiency or infeasible designs from a structural or thermal perspective.

As such, this sizing methodology does not seek to maximize each of the metrics defined in Table 3.1-1, rather use different combinations of key metrics to identify the lowest active mass design (core material, windings, magnets, etc.) at the lowest possible loss. In other words, these metrics will be used as inputs as opposed to a post-design determined quantities.

TABLE 3.1-1 KEY METRICS FOR POWER DENSE PMSMS

Metric	Design Impact	Limiting Factors
Machine speed n	Increase power output for same torque output and rotor volume.	• Machine pole count and fundamental frequency • Rotor structural integrity • AC losses
Shear stress σ_m	Increased torque capability via higher magnetic or electrical loading leading to shorter core stack length	• Lamination saturation limits • Magnet materials and retention • Increased losses and thermal rejection capability
Current density J	Smaller stator conductors and stator sizing	• Winding cooling • Machine efficiency
Rotor tip speed v_{tip}	Larger rotor diameters for the same rotor speed	• Rotor structural limits • Machine aspect ratio (core diameter/length)

3.2. Modular Machine Sizing

This chapter presents sizing equations which can be used for sizing power dense electrical machines. The intention of these equations is to be used for initial machine sizing with further optimization in electromagnetic Finite Element Analysis (FEA).

3.2.1. Sizing FSCW SPM machines for active mass power density

Sizing equations are often used to guide the design of electrical machines and are presented here in the context of modular PMSM machines. As identified in the Chapter 2 power density review, the radial-flux surface permanent magnet (SPM) rotor topology is selected due to its compact rotor construction. Last, a double-layer fractional slot concentrated winding (DL-FSCW) is assumed to minimize end winding losses. These equations can be easily modified to accommodate studies with single layer windings or distributed windings.

3.2.1.1. Machine Dimension Definitions

Sizing equations for SPM topologies are provided in [175] and can be configurated to assist with sizing SPM machines for high-power density. The basic stator and rotor dimensions are provided in Fig. 3.2-1. As indicated, the stator inner diameter D_{is} is assumed approximately equal to the rotor outer diameter D_{or} for algebraic simplicity. Other dimensions highlighted include stator outer diameter D_{os}, stator back iron thickness d_{cs} stator slot height d_{ts} and rotor thickness d_r. Next, the rotor and stator stack lengths are equal and identified as l_e (ignoring lamination stacking factors).

Also provided in Fig. 3.2-1 are dimensions related to the FSCW end turns which will need to be included in the winding loss and power density calculation. Highlighted dimensions include tooth width d_{th}, average end winding length l_{ew} per coil side, coil width w_c, and coil stick out l_{so}.

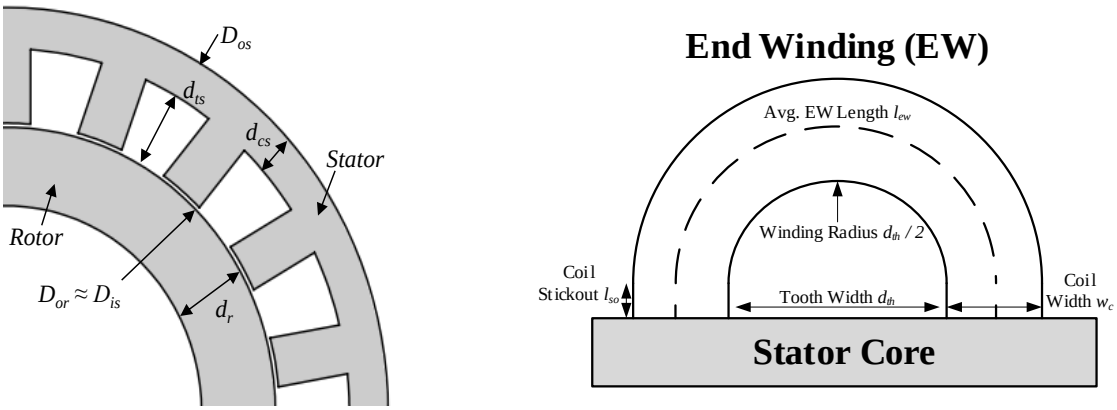

Figure 3.2-1 Sizing equation stator and rotor cross-section and end-winding dimensions.

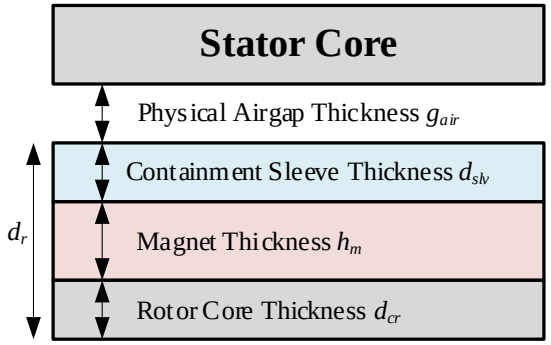

Figure 3.2-2 SPM rotor components and dimension definitions.

Since a SPM topology is selected, the rotor is comprised of three parts: laminated core material with thickness d_{cr} [m], permanent magnet material with thickness h_m [m], and a magnet containment sleeve with thickness d_{slv} [m] as highlighted in Fig. 3.2-2. For simplicity of calculation, the rotor back-iron thickness d_{cr} will be assumed equal to the stator back iron thickness d_{cs}. These comprise the total rotor thickness d_r

$$d_r = d_{cr} + h_m + d_{slv} \tag{3.2.1}$$

Based on the defined dimensions, the below geometric calculated quantities can be calculated:

$$\begin{aligned} V_r &= \pi \cdot D_{or}^2 \cdot l_e / 4 \\ g &= d_{slv} + g_{air} \end{aligned} \tag{3.2.2}$$

for rotor cylindrical volume V_r [m^3], physical airgap g_{air} [m], and effective airgap g [m].

TABLE 3.2-1 REQUIRED INPUTS FOR MACHINE SIZING

Variable Symbol	Description
P_e	Desired shaft power rating [W]
σ_m	Range of possible shear stress [Pa] (typically 20-100 kPa)
n	Range of possible machine speeds [rpm]
J	Range of possible current densities [A/m^2] (typically 10-30 A_{rms}/mm^2)
v_{tip}	Range of possible tip speeds [m/s] (typically 100-250 m/s for power dense machines)
q	Slot-per-pole-per-phase
k_1	Winding factor associated to q
P	Machine pole count (or range of pole counts to be studied). Selected pole counts must be compatible with selected q and the desired modular configuration (e.g., multiple three-phase winding sets).
m	Phase-number
g_{air}	Airgap thickness [m]
h_m	Magnet thickness (or range of magnet thicknesses) [m]
B_r	Magnet residual flux density [T] (typically 1.1 T for SmCo magnets and up to 1.3 T for NdFeB magnets)
l_{so}	Winding stick-out length [m]
LLM	Litz length multiplier accounting for wire transposition (~1.15 for type-1 litz and ~1.3 for type-8 litz)
k_{cu}	Conductor fill factor
ρ_1	Conductor resistivity [ohm-m] (Copper resistivity = 1.68e-8 Ω-m at 20 °C)
α	Resistivity adjustment factor for temperature [1/°C] (3.9e-3 1/°C for copper)
T_{op}	Expected average winding temperature [°C]
B_{cs}	Desired back-iron flux density [T] (up to 2.2T for CoFe)
B_{ts}	Desired stator tooth flux density [T]
ρ_{cu}	Winding density [kg/m^3] (typically 8960 kg/m^3 for copper)
ρ_{fe}	Core density [kg/m^3] (typically 8100 kg/m^3 for CoFe laminations)
ρ_{mag}	Magnet density [kg/m^3] (typically 7600 kg/m^3 for NdFeB magnets)
ρ_{slv}	Retention sleeve density [kg/m^3] (approximately 2000 kg/m^3 for carbon fiber composite containment)

3.2.1.2. Sizing Inputs

Machine specifications should be defined before beginning the machine sizing analysis. A list of necessary sizing inputs and their associated variable name is defined in Table 3.2-1. For winding

loss derivations, a litz winding is assumed to allow for AC effects to be neglected. Discussions related to more complicated winding layouts to be outlined in a later section.

Other input quantities like shaft torque T_e, number of stator slots S, and temperature corrected resistivity ρ_2 can be calculated from the below Table 3.2-1 inputs:

$$\begin{aligned} T_e &= \left(\frac{30}{\pi}\right) \cdot \frac{P_e}{n} \\ S &= m \cdot q \cdot P \\ \rho_2 &= \rho_1 \cdot (1 + \alpha \cdot (T_{op} - 20°C)) \end{aligned} \tag{3.2.3}$$

3.2.1.3. Sizing Equations

Based on the machine dimension definitions and sizing inputs, selected machine dimensions can be calculated as follows. Starting with rotor dimensions, the rotor outer diameter is directly calculated from the specified tip-speed and operating speed by rearranging (3.1.1):

$$D_{or} = \frac{60 \cdot v_{tip}}{\pi \cdot n} \tag{3.2.4}$$

Similarly, the machine stack length can be determined from the shear stress calculation in (3.1.1), torque calculation in (3.2.3), rotor volume in (3.2.2) and the specified shear stress in

$$l_e = \frac{2 \cdot T_e}{\sigma_m \cdot \pi \cdot D_{or}^2} \tag{3.2.5}$$

The magnet retaining sleeve thickness can be determined from D_{or}, h_m, n, and v_{tip} using the sleeve sizing methodology described in [147]. With sleeve thickness d_{slv} known, magnetic loading can be approximated for an SPM [175]:

$$B_{g1} = \frac{B_r}{1 + \frac{g}{h_m}} \tag{3.2.6}$$

leading to all rotor dimensions and operating quantities fully defined. On the stator side, electric loading can be determined from (3.2.6) and shear stress

$$K_{s1} = 2 \cdot \sigma_m / B_{g1} \tag{3.2.7}$$

Approximate stator back-iron and tooth thickness can be determined using [175] using the magnetic loading and the saturation limits defined in Table 3.2-1 leading to

$$\begin{aligned} d_{cs} &= \frac{D_{or} \cdot B_{g1}}{P \cdot B_{cs}} \\ d_{th} &= \frac{\pi \cdot Dor}{S} \cdot \frac{B_{g1}}{B_{ts}} \end{aligned} \tag{3.2.8}$$

The associated slot opening d_o [m] can be determined

$$d_o = \frac{\pi \cdot D_{or}}{S} - d_{th} \tag{3.2.9}$$

which can be used in the calculation of the slot opening ratio k_{sl}:

$$k_{sl} = \frac{d_o}{d_o + d_{th}} \tag{3.2.10}$$

Assuming a stator slot height of d_{ts}, the area of a single stator slot A_{slot} can be estimated using the slot opening ration and the machine rotor diameter:

$$A_{slot} = \frac{A_{cu}}{k_{cu}} = \frac{\pi}{4} \cdot \frac{k_{sl}}{S} \cdot \left[(D_{or} + 2 \cdot d_{ts})^2 - D_{or}^2 \right] \tag{3.2.11}$$

The stator slot height d_{ts} can be determined by inserting (3.2.11) and (3.2.7) into the current density equation in (3.1.1). Rearranging leads to the stator slot height d_{ts}

$$d_{ts} = \frac{D_{or}}{2} \cdot \left[-1 + \sqrt{1 + \frac{4 \cdot K_{s1}}{k_{sl} \cdot k_{cu} \cdot J \cdot D_{or}}} \right] \tag{3.2.12}$$

Last, the stator outer diameter is determined from the stator back-iron thickness and the stator slot height

$$D_{os} = D_{or} + 2 \cdot (d_{ts} + d_{cs}) \tag{3.2.13}$$

All stator and rotor dimensions are fully defined leaving only the end winding dimensions shown in Fig. 3.2-1 remaining. The width of the coil w_c for a DL winding is defined as

$$w_c = 0.5 \cdot A_{slot} / d_{ts} \tag{3.2.14}$$

and the overall coil copper area per coil A_{coil}

$$A_{coil} = 0.5 \cdot A_{slot} \cdot k_{cu} \tag{3.2.15}$$

Finally, the average end winding length l_{ew} is determined:

$$l_{ew} = 2 \cdot l_{so} + \pi \cdot (w_c + d_{th}) / 2 \tag{3.2.16}$$

3.2.1.4. SPM Component Volume and Mass Calculations

SPM volume and mass is calculated using the fully defined dimensions in the previous subsection. Winding conductor volume (insulation excluded) in the straight portion of the stator core V_w, end windings V_{ew}, and total winding volume $V_{w,tot}$ is given:

$$\begin{aligned} V_w &= k_{cu} \cdot l_e \cdot S \cdot A_{slot} \\ V_{ew} &= 2 \cdot S \cdot A_{coil} \cdot l_{ew} \\ V_{w,tot} &= V_w + V_{ew} \end{aligned} \tag{3.2.17}$$

Stator core volume is determined by calculating the overall volume of the stator core V_{sc} and subtracting out the core-section winding volume in

$$V_{sc} = \frac{\pi}{4} \cdot \left[D_{os}^2 - (D_{or} - 2 \cdot g)^2 \right] \cdot l_e - V_w / k_{cu} \tag{3.2.18}$$

Rotor sleeve volume V_{slv}, magnet volume V_{mag}, and core volume V_{rc} are given in

$$\begin{aligned} V_{slv} &= \frac{\pi}{4}\cdot l_e \cdot D_{or}^2 - \frac{\pi}{4}\cdot l_e \cdot (D_{or} - 2\cdot d_{slv})^2 \\ V_{mag} &= \frac{\pi}{4}\cdot l_e \cdot (D_{or} - 2\cdot d_{slv})^2 - \frac{\pi}{4}\cdot l_e \cdot (D_{or} - 2\cdot d_{slv} - 2\cdot h_m)^2 \\ V_{cr} &= \frac{\pi}{4}\cdot l_e \cdot (D_{or} - 2\cdot d_{slv} - 2\cdot h_m)^2 - \frac{\pi}{4}\cdot l_e \cdot (D_{or} - 2\cdot d_r)^2 \end{aligned} \tag{3.2.19}$$

Total SPM mass m_{tot} [kg] and active mass power density *AMPD* [kW/kg] is determined from the calculated volumes and material densities in Table 3.2-1:

$$\begin{aligned} m_{tot} &= \rho_{fe}\cdot(V_{cr} + V_{cs}) + \rho_{cu}\cdot V_{w,tot} + \rho_{mag}\cdot V_{mag} + \rho_{slv}\cdot V_{slv} \\ AMPD &= \frac{P_e}{1000\cdot m_{tot}} \end{aligned} \tag{3.2.20}$$

3.2.1.5. Winding Loss Calculation

Machine DC winding losses are calculated from the SPM dimensions, electric loading and current density parameters discussed above. As mentioned, the use of litz wire is assumed in order to ignore AC loss effects related to high frequency operation. To begin, the number of series turns-per-phase N_s is assumed to be equal to the number of phase coils:

$$N_s = S / m \tag{3.2.21}$$

The expected phase current I_s is calculated from the electric loading [175]:

$$I_s = \frac{K_{s1}\cdot\pi\cdot D_{or}}{2\cdot m\cdot N_s\cdot k_1} \tag{3.2.22}$$

The associated phase coil resistance R_{dc} is then calculated from the developed stator geometry

$$R_{dc} = \frac{N_s\cdot LLM\cdot\rho_2\cdot 2\cdot(l_{ew} + l_e)}{A_{coil}} \tag{3.2.23}$$

which can be used in combination with (3.2.22) to calculate the DC winding loss:

$$P_{dc} = m \cdot R_{dc} \cdot I_s^2 / 2 \tag{3.2.24}$$

3.2.1.6. SPM Sizing Equation Optimization

The presented sizing and loss equations can be used to optimize target speed, shear stress, current density, slot/pole combination, and magnet thickness, as suggested in Table 3.2-1. The above equations are implemented into MATLAB with a multi-objective genetic algorithm (MOGA) following [176]. A pareto front of designs with objectives related to maximizing power density (*AMPD*) and minimizing loss (P_{dc}) can be identified allowing users to choose better starting point designs before beginning time consuming FEA studies. A flow-diagram of the developed algorithm is shown in Fig. 3.2-3(a) with each step listed. A sample output of the algorithm is shown in Fig. 3.2-3(b) with initial and final design populations, and optimal designs shown.

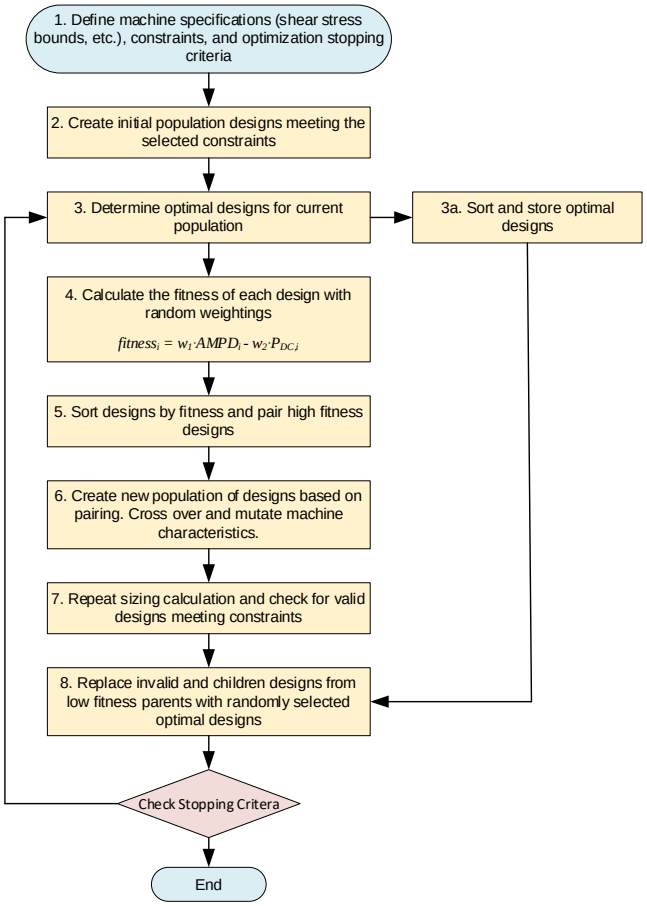

(a)

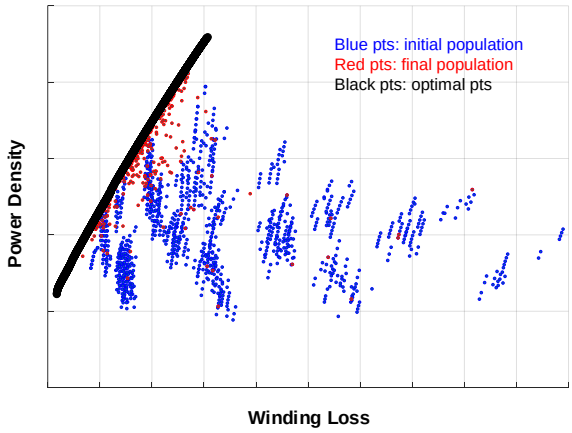

(b)

Figure 3.2-3 Sizing equation optimization algorithm flowchart (a), and sample tool output with initial and final population, and optimal designs highlighted.

3.2.1.7. Sizing Equation Improvements

The presented set of sizing equations and winding-loss calculations provide a general framework for exploring the power-dense PMSM design space with potential to be modified to fit the specific needs of the user. Possible modifications include the calculation of machine turns based on additional input parameters (e.g., dc bus voltage) or the estimation of machine inductance based on the calculated geometry [177]. The determination of the number of machine turns could be used to approximate a machine winding layout and the associated AC losses uses techniques described in [178], [179]. Additional complexity can be added to incorporate considerations related to the chosen machine thermal management system or desired propulsor fan [71].

In any case, the presented methodology highlights key metrics and their effects on machine power density and winding losses. These power density principals are used to guide the design of the aerospace demonstrators presented in the following section.

3.3. Description of Modular 1 MW and 200 kW Rated Aerospace Demonstrators

The NASA University Leadership Initiative (ULI) program is structured to give university-led project teams the opportunity to investigate advanced technical concepts that address the major component- and system-level challenges associated with a turbo-hybrid-electric aircraft concept [174]. One of the major tracks of this project is the development of a 1 MW Integrated Modular Motor Drive (IMMD) that pushes the state-of-the-art in terms of power density. A low-power demonstrator version of this machine with a 200 kW power rating has been fabricated and tested to reduce the technical risks for the final 1 MW machine. Specifications for both machines are provided in Table 3.3-1.

TABLE 3.3-1 NASA ULI MACHINE SPECIFICATIONS & PERFORMANCE METRICS

Spec.	Final 1 MW Design	Risk Reduction Demonstrator	Units
Max. Power	1,000	200	kW
Speed	20,000		RPM
Slot/Pole	18/12		-
Torque	477.5	95	N-m
DC Bus Volt.	2,000	600	V
Tip Speed	200		m/s
Current Density	35.6	4	A_{rms}/mm^2
Shear Stress	54.3	11.4	kPa
Magnet Loading	0.7		T
Electric Loading	155	32.6	kA/m
Physical Airgap (total with sleeving)	1.5 (4.7)	1.0 (5.2)	mm
Active Power Density	22.6	4.8	kW/kg

An 18-slot, 12-pole (SPP=1/2) SPM machine topology was selected for the IMMD configuration (e.g, six sets of three-phase windings). Machine features and high-level dimensions are highlighted in Fig. 3.3-1 which shows a single machine winding module. An in-depth discussion of the design optimization of these machines is beyond the scope of this thesis. Further details and analyses of the electromagnetic, thermal, and power electronics can be found in [22], [180]–[184].

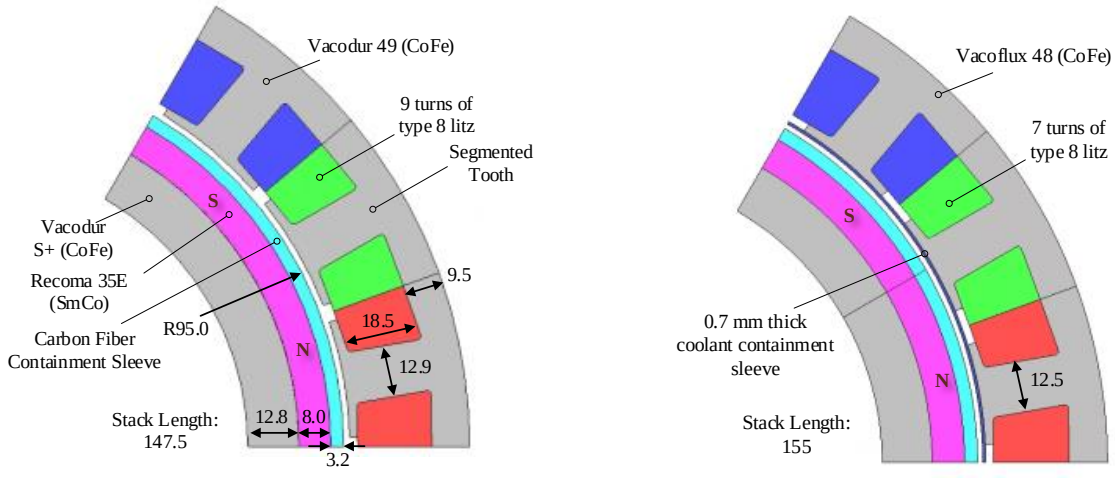

Figure 3.3-1 Single 1/6th cross-section of developed machines with key dimensions and features of developed 200 kW demonstrator (left) and 1 MW demonstrator (right) with 1 MW design differences highlighted.

3.3.1. Megawatt Machine Features

First, a summary of the higher power demonstrator features is given. For the stator core, 0.1 mm thick CoFe Vacoflux 48 laminations were selected due to their high saturation flux density (approx. 2.2 T) and appealing high-frequency loss performance. A segmented stator tooth configuration was selected to accommodate the stator concentrated windings and for implementation of the selected in-slot cooling design. More specifically, the stator is flooded with a dielectric fluid which is contained by a stationary carbon fiber sleeve shown in Fig. 3.3-1.

Each tooth is wound with seven turns of rectangular Type 8 litz wire consisting of 32-AWG strands, which are necessary because of the high fundamental frequency of the machine (2 kHz at 20,000 rpm). The concentrated winding achieves a 26% fill factor (i.e., ratio of copper area to total slot area) which is low to accommodate direct cooling channels between turns. Although in-slot cooling occupies valuable space otherwise filled by copper, being able to directly cool the winding makes up for elevated current densities observed in Table 3.3-1.

For the rotor core, 0.35 mm thick CoFe Vacodur S+ laminations were selected because of the excellent mechanical properties of this material, with yield strength capability up to 800 MPa. The rotor magnets have a parallel magnetization pattern. Each magnet is segmented axially using 1.0 mm thick segments to minimize the magnet losses. Finally, the magnets are held in place by a 3.2 mm-thick carbon fiber sleeve.

A key feature of the final 1 MW design is a modular stator compatible with multiple three-phase drives, and the same configuration was adopted for the 200 kW demonstrator machine. The use of multiple three-phase drives is an appealing approach for reducing the risk of partial discharge at high altitudes by reducing the maximum voltage differences appearing across each stator winding and inverter switch.

Electromagnetic Finite Element Analysis (FEA) calculated single module machine characteristics (1/6th of the total machine) are summarized in Table 3.3-2. Final photos of the 1MW rated machine before and after power electronics integration is given in Fig. 3.3-2.

TABLE 3.3-2 CALCULATED 1MW RATED MACHINE MODULE PARAMETERS

Machine Module Metric	Quantity
Rated Module Phase Current [A_{pk}]	445.1
Rated Module Phase Voltage [Vpk]	345.6
Module flux linkage with 200 °C Magnets [Wb]	0.021
Module Phase Inductance [μH]	39.9
Characteristic Current [A_{pk}]	489.0 (1.4 per unit)
Module DC Phase Resistance [mΩ]	9.4

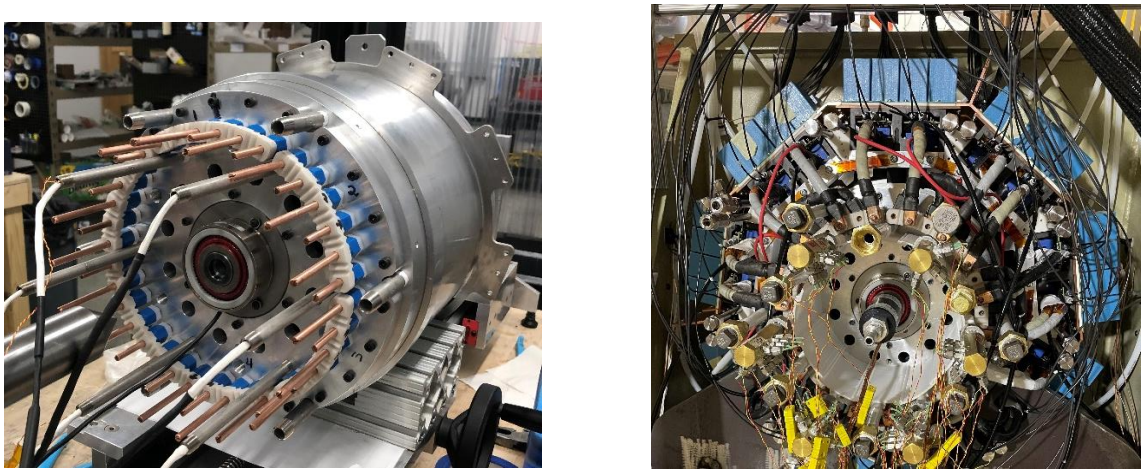

Figure 3.3-2 1MW demonstrator after final machine assembly with phase-rod connections shown (left) and final integrated modular power electronics mounted on the outer surface of the machine (right).

3.3.2. Reduced Power 200 kW Rated Demonstrator Features

As stated, both the 1MW and 200kW share many features in order to retire the most risk for the final 1MW design. Key differences between the two designs are briefly summarized here. For the stator core, 0.1 mm thick CoFe Vacodur 49 laminations were selected. The machine windings

feature an additional two-turns of type-8 litz wire, which consist of fine 36 AWG strands. A conventional cooling jacket is used to cool the stator, allowing for the slot to be filled with litz leading to a copper fill factor of 38%. The stator windings are subsequently potted using Lord EP2000 encapsulant material which has a high thermal conductivity of 1.9 W/m-K.

Although the same modular structure is common across designs, the 200 kW demonstrator is excited by two commercial 100 kW SiC motor drives that are housed in a separate enclosure. The dc input terminals of these two drives are connected in parallel to an adjustable 600 Vdc supply. Three of the six three-phase stator modules are excited in parallel by each of the two inverters.

Electromagnetic FEA calculated single module machine characteristics are summarized in Table 3.3-3. Note a higher characteristic current is expected for the demonstrator due to similar turn counts and magnet flux linkage compared to the final 1MW demonstrator.

TABLE 3.3-3 CALCULATED 200KW RATED MACHINE MODULE PARAMETERS

Machine Module Metric	Quantity
Rated Module Phase Current [A_{pk}]	67.5
Rated Module Phase Voltage [Vpk]	349.8
Module flux linkage with 200 °C Magnets [Wb]	0.027
Module Phase Inductance [μH]	72.5
Characteristic Current [A_{pk}]	329.3 (4.9 per unit)
Module DC Phase Resistance [mΩ]	8.6

3.3.3. Healthy Test Operation

Initial testing of the 1MW kW demonstrator machine has been carried out using the dynamometer facilities at the University of Wisconsin-Madison. The dynamometer is limited to 15,000 rev/min maximum speed at 170 kW shaft power, preventing testing at rated power and speed. At the time of this writing the 1 MW machine design is under test at the NASA NEAT facility located in Sandusky Ohio. Only the low-power test results from the University of

Wisconsin test initialization are shared here. These integrated results are limited to 4000 rpm and ~50% rated torque in order to minimize machine stresses before the primary NASA NEAT test, with integrated back-emf, current, and torque performance summarized here.

Primary data acquisition is performed by an HBK Gen7tA instrumentation rack and MX1609KB modules. Secondary measurements are captured using a Teledyne LeCroy MDA810A Motor Drive Analyzer. Measurements of the inverter phase currents (x6) are made using CWTMini HF3B Rogowski coils installed on select winding phases. Dc bus current, and dc voltage measurements are made in a separate enclosure. Inverter phase voltage measurements (x6) are made at select power electronics terminals. Torque measurements are made using an in-line HBK T40 torque transducer, and speed is measured using a shaft-mounted dynamometer encoder.

Initial no-load testing was carried out with the demonstrator machine coupled to the dynamometer before integrating power electronics around the machine. Fig. 3.3-3 shows a single-module phase back-emf waveform compared with the FEA prediction for 8000 rev/min operation (800 Hz fundamental frequency). The measured fundamental component of the back-EMF is approx. 5% lower than the FEA prediction, attributable to some combination of lower-than-expected magnet flux density and/or leakage flux components not captured with sufficient accuracy in the simulation. This difference is consistent with the back-emf measured in the other stator modules over the tested speed range.

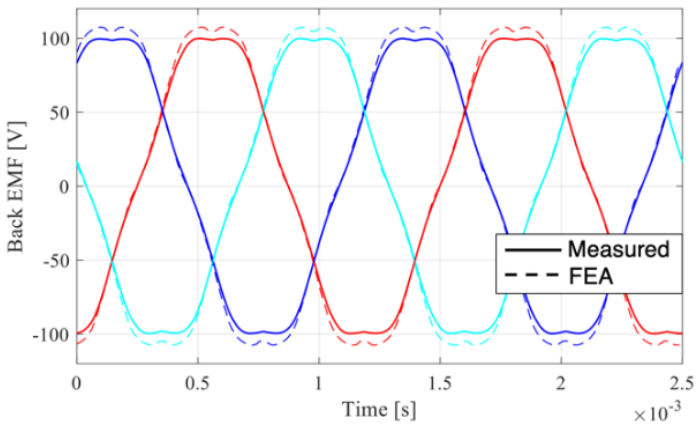

Figure 3.3-3 Measured back-emf voltage waveforms against FEA calculations at 8000 rpm.

After installing power electronics around the machine as shown in Fig. 3.3-2, machine is evaluated up to ~50% (~260 N-m) and 4,000 rpm operating speed. Single module phase currents at the maximum tested power are highlighted in Fig. 3.3-4(a). Measured machine torque against commanded q-axis current is shown in Fig. 3.3-4(b). As expected with the observed lower back-emf, the machine output torque is approximately 5% lower than the FEA model. This torque reduction aligns well with the observed lower back-emf. Based on the observed torque and speed, the developed demonstrator reached operating powers of 108.5 kW (~11% of its total rating) during the UW test checkout.

Considering the ongoing test of the 1MW machine at the NASA NEAT facility, the high-power and speed data will be shared in later publications along with its loss and thermal performance. More comprehensive test results are available in [180] for the lower power demonstrator using a similar test setup. A deeper review of these test results is not provided given the common magnetic features between the two designs. Overall, these results indicate good agreement for back-emf and torque performance measurements. Further, a deeper examination of the 200 kW rated machine losses is given showing analytical and FEA test results within 10% of measured.

This section provides a brief overview of ongoing efforts to achieve 1MW propulsive power, illustrating some of the specifications, parameters, and machine features used to reach high levels of power density. These include the use in-slot cooling to push machine current density and the integration of power electronics. These features are exemplified by contrasting against a lower power demonstrator with a similar package size.

The chosen modular structure offers benefits from a device sizing and partial discharge mitigation perspectives. Another major possibility for developed modular approach is the possibility for fault tolerant (FT) operation where a single module can fail without a total loss of torque production. This modular benefit and tradeoff is studied using the lower power 200 kW demonstrator in the next section.

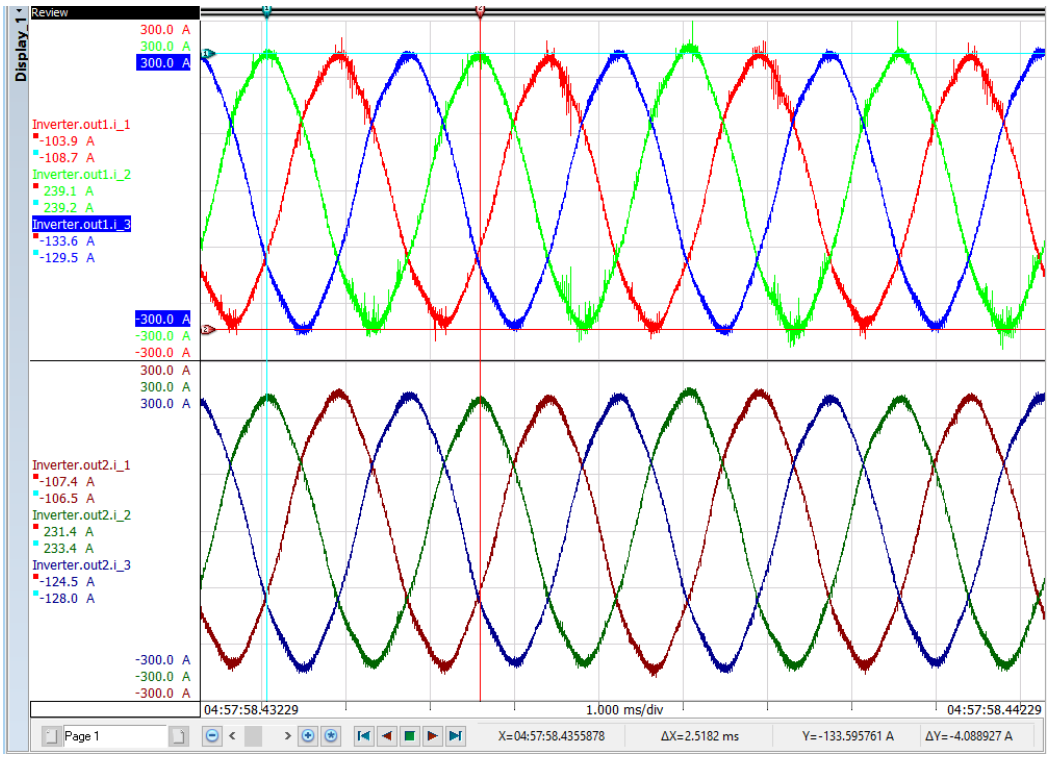

(a)

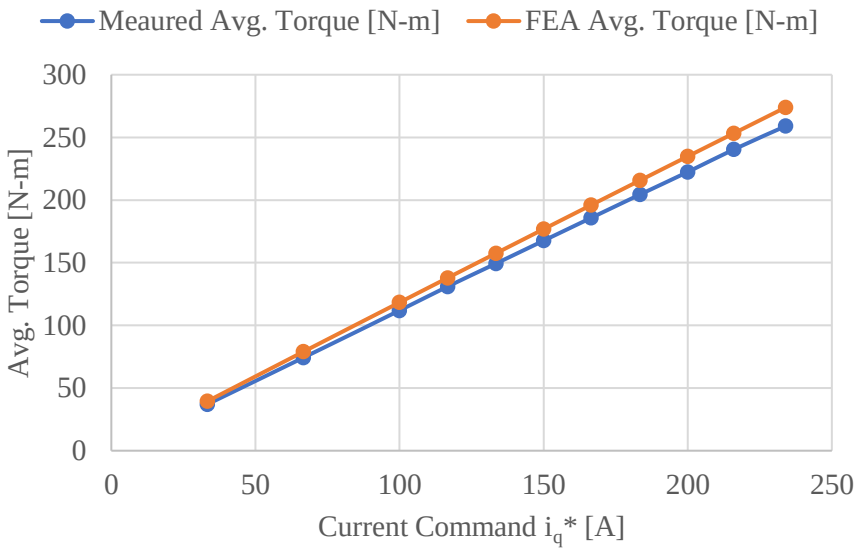

(b)

Figure 3.3-4 Megawatt rated machine initial test results: (a) module 1 (top) and module 6 (bottom) phase currents from the HBK Perception display for 259 N-m operating point and 4000 rpm machine speed operating points (108kW shaft power); and (b) measured machine torque against FEA at 4000 rpm.

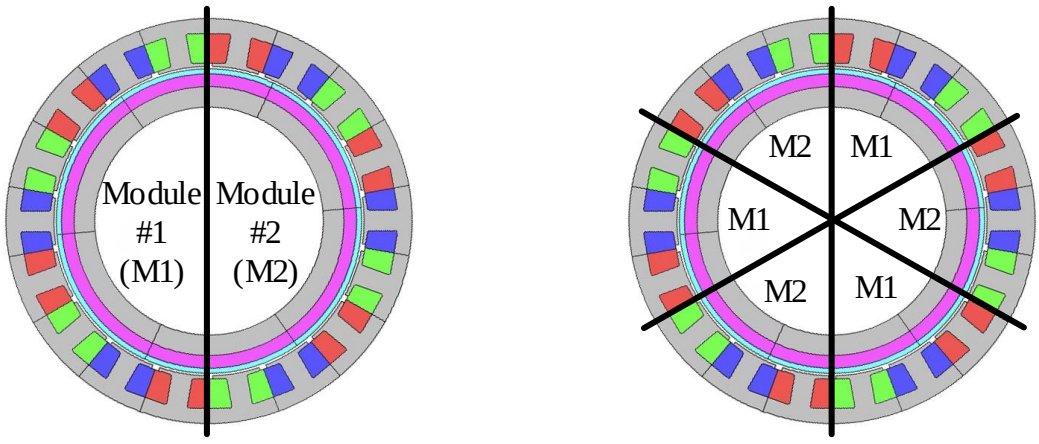

(a) (b)

Figure 3.4-1 Demonstrator machine cross-sections showing two alternative module arrangements: (a) module halves; and (b) interleaved modules.

3.4. Fault Tolerant Modular Machines Demonstration

As noted in the preceding discussion, the 200 kW demonstrator machine stator is divided into six three-phase windings sets, which are organized into two modules, each excited by a SiC inverter. Two modular winding arrangements are considered: one divides the machine into halves as in Fig. 3.4-1(a), and the other interleaves the coil modules around the stator as shown in Fig. 3.4-1(b) to improve the electromagnetic and resulting radial force symmetry around the machine's circumference.

3.4.1. Low-Speed Terminal-Fault Demonstration

The machine's fault-tolerance capability has been demonstrated experimentally by applying a three-phase simulated short-circuit fault to Module #1 at a 4,000 rev/min (20% rated speed) with a 40 N-m per module operating point (42.1% rated torque and module #2 command of 180A-pk). To simulate a partial three-phase short-circuit at the module's terminals, a *d*-axis current of -70 A (which is divided into three-parallel coils per module leading to 23.3A/coil or ~35% of the machine current rating) is supplied to counteract the magnet flux linkage in Module #1, suppressing the amplitude of its terminal voltages. This *d*-axis current amplitude is substantially lower than the machine's rated current and its characteristic current (given in Table 3.3-3) value to avoid any risk of damaging the machine.

The three measured phase current waveforms in healthy Module #2 are provided for the halved modular configuration in Fig. 3.4-2(a), exhibiting a maximum 20 A unbalanced phase current difference between the phase peak currents. This unbalanced current amplitude increases for the interleaved configuration, reaching a maximum 40 A phase current difference as shown in Fig. 3.4-2(b). Note a substantial fifth-harmonic current component is visible in all waveforms due to

its presence in the machine back-emf waveform (similar to the 1MW design back-emf if Fig. 3.3-3).

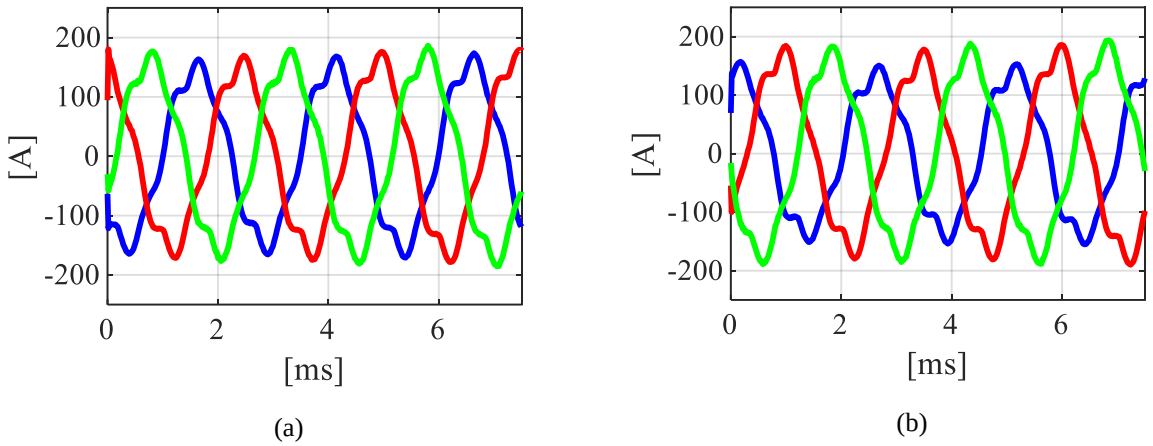

Figure 3.4-2 Measured module-2 phase currents after -70A d-axis current is applied to module-1 to simulate a short-circuit fault condition: (a) halved modular configuration and (b) interleaved module configuration.

These values seem relatively small for the selected speed, though are measured at relatively low speeds, low-amplitude artificial fault-currents, and the partial suppression by the implemented closed-loop current control. These imbalances can be better studied using standard machine equations discussed in the next subsection.

3.4.2. Module Magnetic Interactions During Fault Events

The source of the current unbalance observed in Figure 3.4-2 comes from two sources: (1) magnetic interactions between modules; and (2) inherent built-in inductance unbalance due to the selected modular structure (q = 0.5). This can be shown using standard machine equations as follows. Vectors for the phase variables in the n-module machine are presented in (3.4.1) for the phase currents $\boldsymbol{i}_s$, voltages $\boldsymbol{v}_s$, and PM magnet flux linkages $\boldsymbol{\lambda}_{pm,s}$.

$$\begin{aligned}
\mathbf{i}_s &= \begin{bmatrix} \mathbf{i}_{abc1} & \mathbf{i}_{abc2} & \mathbf{i}_{abc3} & \mathbf{i}_{abc4} & \mathbf{i}_{abc5} & \mathbf{i}_{abc6} \end{bmatrix}^T \\
\mathbf{v}_s &= \begin{bmatrix} \mathbf{v}_{abc1} & \mathbf{v}_{abc2} & \mathbf{v}_{abc3} & \mathbf{v}_{abc4} & \mathbf{v}_{abc5} & \mathbf{v}_{abc6} \end{bmatrix}^T \\
\boldsymbol{\lambda}_{pm,s} &= \begin{bmatrix} \boldsymbol{\lambda}_{pm1} & \boldsymbol{\lambda}_{pm2} & \boldsymbol{\lambda}_{pm3} & \boldsymbol{\lambda}_{pm4} & \boldsymbol{\lambda}_{pm5} & \boldsymbol{\lambda}_{pm6} \end{bmatrix}^T
\end{aligned} \tag{3.4.1}$$

Each vector consists of *n* three-phase vectors for the *n* modules including the phase currents $\boldsymbol{i_{abcn}}$, voltages $\boldsymbol{v_{abcn}}$, and magnet flux linkage $\boldsymbol{\lambda_{pmn}}$ vectors. For simplicity only the fundamental component of the magnet flux linkage is considered. This design has six possible modules ($\underline{n} = 6$) (three-phase winding sets). The choice to use two modules connected in parallel reduces these vector equations to:

$$\begin{aligned}
\mathbf{i}_s &= \begin{bmatrix} \mathbf{i}_1 & \mathbf{i}_2 \end{bmatrix}^T \\
\mathbf{v}_s &= \begin{bmatrix} \mathbf{v}_1 & \mathbf{v}_2 \end{bmatrix}^T \\
\boldsymbol{\lambda}_{pm,s} &= \begin{bmatrix} \boldsymbol{\lambda}_{pm} & \boldsymbol{\lambda}_{pm} \end{bmatrix}^T
\end{aligned} \tag{3.4.2}$$

where subscript 1 or 2 refers to the respective M-module shown in Fig. 3.4-2. A similar reduction is shown for the magnet flux linkage though only variable λ_{pm} is used to reflect equal flux linkages across three-phase winding sets. Current and voltage reductions are based on a parallel winding assumption and defined by

$$\begin{aligned}
\mathbf{i}_1 &= \mathbf{i}_{abc1} + \mathbf{i}_{abc2} + \mathbf{i}_{abc3} \\
\mathbf{i}_2 &= \mathbf{i}_{abc4} + \mathbf{i}_{abc5} + \mathbf{i}_{abc6} \\
\mathbf{v}_1 &= \mathbf{v}_{abc1} = \mathbf{v}_{abc2} = \mathbf{v}_{abc3} \\
\mathbf{v}_2 &= \mathbf{v}_{abc4} = \mathbf{v}_{abc5} = \mathbf{v}_{abc6}
\end{aligned} \tag{3.4.3}$$

These current and voltage vectors only consider the terminal characteristics of the machine. Due to the parallel connection, circulating currents are expected internally between phase coils due to magnetic interactions between modules and module unbalance.

Each machine grouping has a resistance r_{ph}, which can be represented in (3.4.4) for the entire machine where **I** is the identity matrix with order 2.

$$\mathbf{R} = r_{ph} \cdot \mathbf{I} \tag{3.4.4}$$

The coupling between modules is defined by the inductance matrix **L** shown in (3.4.5). This matrix consists of four diagonal 3x3 inductance submatrices where $\mathbf{L_{nn}}$ represents each module's internal magnetic coupling, and submatrices $\mathbf{L_{nm}}$ captures the electromagnetic interactions between module-*n* and module-*m*. These off-diagonal matrices in (3.4.5) are all zero matrices in an ideal machine with zero inter-module electromagnetic coupling.

$$\mathbf{L} = \begin{bmatrix} \mathbf{L_{11}} & \mathbf{L_{12}} \\ \mathbf{L_{21}} & \mathbf{L_{22}} \end{bmatrix} \tag{3.4.5}$$

The complete set of machine electrical differential equations is given using the vectors and matrices in (3.4.2) to (3.4.5) where the operator ρ signifies the time derivative *d/dt*.

$$\mathbf{v_s} = \mathbf{R} \cdot \mathbf{i_s} + \mathbf{L} \cdot \rho \cdot \mathbf{i_s} + \rho \cdot \boldsymbol{\lambda}_{\mathbf{pm,s}} \tag{3.4.6}$$

This evaluation focuses on a single module so that (3.4.6) is reduced to

$$\mathbf{v_1} = (\mathbf{R_{11}} + \rho \cdot \mathbf{L_{11}}) \cdot \mathbf{i_1} + \rho \cdot \boldsymbol{\lambda}_{\mathbf{pm}} + \mathbf{L_{12}} \cdot \rho \cdot \mathbf{i_2} \tag{3.4.7}$$

Some phase unbalance is observed in the diagonal $\mathbf{L_{nn}}$ matrices in Fig. 3.4-3, which is attributable to asymmetries in the mutual inductances inside each module caused by the interfaces between adjacent modules. This unbalance is most pronounced in the interleaved module configuration which has more points of contact between modules (i.e., increased magnetic leakage paths between modules). The magnet flux linkage λ_{pm} is also determined via FEA and assumed

sinusoidal for this analysis. Adjacent module currents $i_{abc,k}$ can be treated as disturbance terms in (3.4.7).

Phase	*a1*	*b1*	*c1*	*a2*	*b2*	*c2*
a1	24.8	-8.5	-6.3	-1.9	-1.9	-4.0
b1	-8.5	24.8	-8.5	-1.9	-1.9	-1.9
c1	-6.3	-8.5	24.8	-4.0	-1.9	-1.9
a2	-1.9	-1.9	-4.0	24.8	-8.5	-6.3
b2	-1.9	-1.9	-1.9	-8.5	24.8	-8.5
c2	-4.0	-1.9	-1.9	-6.3	-8.5	24.8

(a)

Phase	*a1*	*b1*	*c1*	*a2*	*b2*	*c2*
a1	24.9	-8.3	-2.0	-2.0	-2.0	-8.3
b1	-8.3	24.9	-8.3	-2.0	-2.0	-2.0
c1	-2.0	-8.3	24.9	-8.3	-2.0	-2.0
a2	-2.0	-2.0	-8.3	24.9	-8.3	-2.0
b2	-2.0	-2.0	-2.0	-8.3	24.9	-8.3
c2	-8.3	-2.0	-2.0	-2.0	-8.3	24.9

(b)

Figure 3.4-3 FEA calculated coil inductance matrices with module internal inductances L11 and L22 in green and mutual inductances L12 and L21 in yellow: (a) M1 halved modularity; and (b) M2 interleaved modularity.

Next, (3.4.7) has been implemented using MATLAB Simulink to assess the impact of module unbalance and module coupling during simulated short-circuit faults in one module. For simplicity, the rotor is assumed to operate at constant speed to match the mentioned test condition (4000 rev/min). Each healthy machine module is assumed to have an independent low-bandwidth synchronous reference-frame current regulator supplying sinusoidal module voltages.

Initial simulations are oriented towards replicating the observed unbalance shown in Fig. 3.4-2 where a *d*-axis current command of -70 A is supplied to M1 while M2 is operating at a healthy state of 180A. Healthy module M2 phase currents for are given for both the halved and interleaved configurations in Fig. 3.4-4(a) and (b). For the mentioned fault condition, a peak current difference of 9A (5% of operating current) is observed for the halved configuration compared to a difference of 30A (16.7% of operating current) for interleaved configuration. Although the magnitude of the unbalance differs from the experimental test, the general shape of the current waveforms matches quite well. Differences are likely attributed to the simplifying assumptions made for the machine parameters and control.

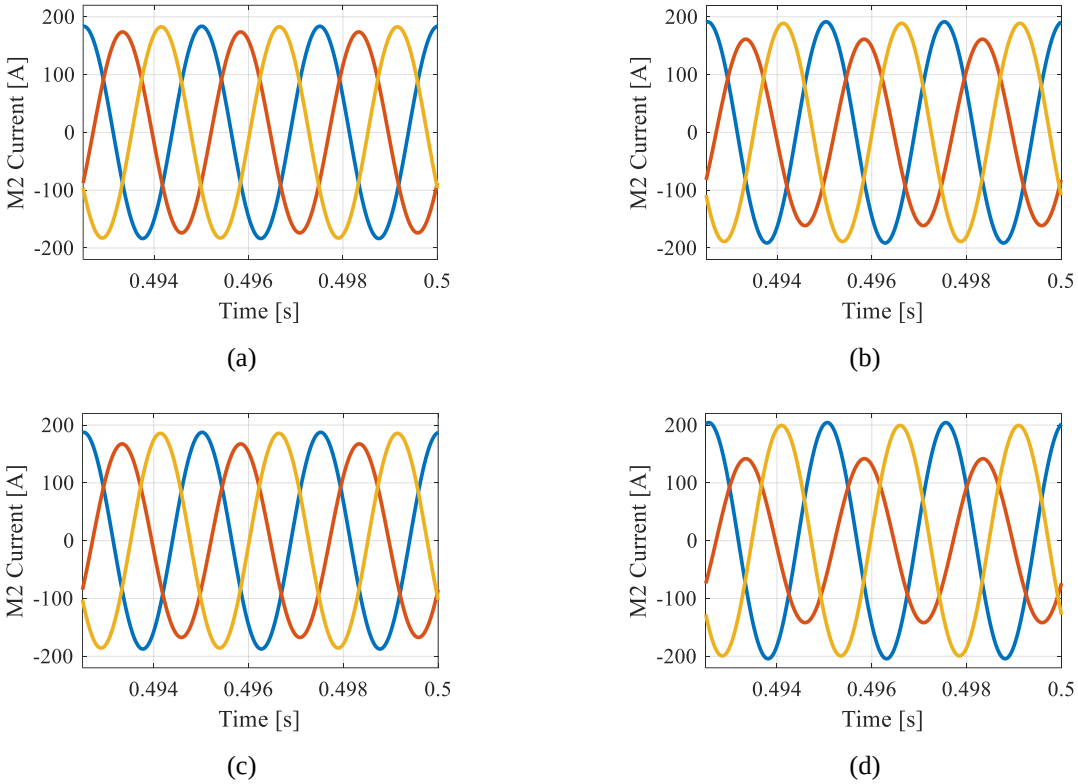

Figure 3.4-4 Two-module short-circuit fault simulation: (a) halved-configuration with 70A short circuit current M1, (b) interleaved-configuration with 70A short circuit supplied to M1, (c) halved configuration with 330A short circuit current supplied to M1, and (d) interleaved configuration with 330 short circuit current supplied to M1.

The simulation is repeated for higher levels of fault current at 330A matching the demonstrator fault current listed in Table 3.3-3. Steady state currents for healthy module M2 are provided for the halved and interleaved configurations in Fig. 3.4-4(b) and (c) respectively. For a 4.7x increase in the fault current, the halved configuration unbalance increases to 20.1A (a 2.2x increase and 11.1% of operating current). The interleaved current unbalance also increases by a factor of 2.1x to 62A between current peaks (34.4% of operating current).

Further observations can be made by examining the inductance matrices in shown Fig. 3.4-3. The values given can be divided into self-inductance L, mutual-inductance M, and mutual leakage components M_{lkg} as shown for an interleaved configuration:

$$L_{11} = \begin{bmatrix} L & M + M_{lkg} & M \\ M + M_{lkg} & L & M + M_{lkg} \\ M & M + M_{lkg} & L \end{bmatrix} \quad L_{12} = \begin{bmatrix} M & M & M + M_{lkg} \\ M & M & M \\ M + M_{lkg} & M & M \end{bmatrix} \tag{3.4.8}$$

Clearly from (3.4.8) the unbalance in the system is driven by the leakage inductance between phases. The effect of this unbalance can be mitigated by reducing leakage paths (tooth tip removal, etc.) within the machine, though this has a negative impact on the machine's overall inductance value which is undesirable for FT machines. The ratio of the mutual leakage M_{lkg} components from the interleaved configuration (-6.3 μH) against the halved configuration (-2.1 μH) yields 3.0 which matches the observed ratio of unbalance in Fig. 3.4-4. As such the mutual leakage inductance ratio (MLIR) critical metric is identified for comparing FT modular machines:

$$MLIR = \frac{M_{lkg1}}{M_{lkg2}} \tag{3.4.9}$$

Further, the relationship between the self-inductance L of a module-phase and the magnitude of leakage inductance will influence the impact of the observed unbalance. Clearly if M_{lkg} is small relative to L, then the observed unbalance will be smaller. This observation informs the leakage inductance isolation ratio (LIIR):

$$LIIR = \frac{M_{lkg}}{L} \tag{3.4.10}$$

The LIIR can be used as a rule of thumb for estimating the level of unbalanced current Δi_{pk} in a machine for fault current i_f when simulation tools are unavailable:

$$\Delta i_{pk} \propto LIIR \cdot i_f \tag{3.4.11}$$

This is illustrated for the above case study where the interleaved configuration has a LIIR ratio of 0.25 and the halved configuration has a LIIR of 0.09. These correspond to Δi_{pk} values of 17.5A and 6.0A for the 70A fault current scenario, and Δi_{pk} values of 82.5A and 28.1A for the 330A fault current scenario. Although not exact, these values current values track the impact of leakage mutual coupling between modules.

Similarly, a mutual inductance isolation ratio (MIIR) is proposed to capture effects of mutual inductance M components in L_{12}.

$$MIIR = \frac{M}{L} \tag{3.4.12}$$

Practically segregating the leakage inductance M_{lkg} from the mutual inductance M is difficult. Instead, the modular isolation ratio (MIR) is proposed to compare different FT modular machines. This ratio will be used in the Chapter 4's tradeoff study.

$$MIR = \frac{M_{lkg} + M}{L} \tag{3.4.13}$$

3.4.3. Halved-Modularity Open Circuit Fault Demonstration

The previous test results suggest a split stator modularity implementation is best due to superior magnetic isolation compared to an interleaved implementation. However, a split approach does contribute to mechanical stressor disadvantages during fault events.

An open-circuit fault condition was unintentionally demonstrated during the healthy machine test (with the halved modular configuration in Fig. 3.4-1(a)) when one of the two inverters shut

down unexpectedly. Before the fault, the machine operated at a higher speed and torque operating point compared to the preceding modularity test (95 N-m @ 8000 rev/min). As expected, the machine continued to deliver 50% rated torque after the fault as shown in Fig. 3.4-5. The large torque transient that followed the fault event can be reduced with improved control. It is also noteworthy that the bearing accelerometer reading increased after the fault due to rotor unbalanced magnetic forces.

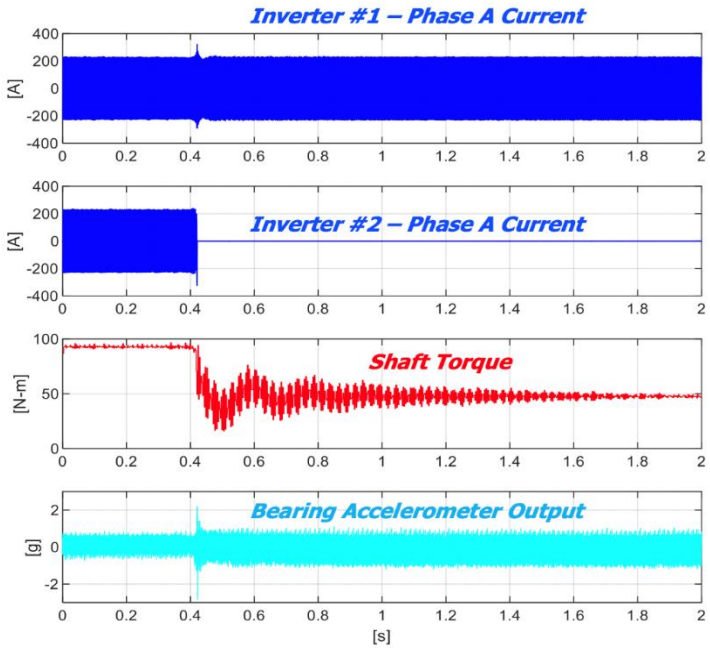

Figure 3.4-5 Fault tolerance demonstration with Drive #2 tripped to open-circuit condition near t =0.4 seconds.

The halved modular approach limits the amount of coupling between the modules and the resulting unbalanced phase current, as well as the amplitudes of the torque ripple and vibration caused by the unbalanced rotor pull during the fault event. In contrast, the interleaved approach increases the electromagnetic module coupling by doubling the number of module interfaces along the stator circumference. This elevated coupling raises the amplitude of the resulting current

unbalance during a fault event, but the amplitude of the unbalanced rotor pull is suppressed because of the improved electromagnetic symmetry compared to the halved configuration.

3.4.4. Magnetic Isolation Tradeoffs

Clear tradeoffs are highlighted in the modular isolation study between reasonable magnetic isolation between modules and level of unbalanced magnetic pull on the rotor. First, concentrating module phases results in a minimized number of contact points between modules and the associated unbalanced currents, and is a potential strategy for reducing coupling between modules to achieve better magnetic isolation. However, this comes with the tradeoff of potential unbalanced magnetic pull on the rotor which can lead to accelerated aging on components like bearings due to increased radial loads [185].

Switching to an interleaved implementation of coils remedies the unbalanced pole problems but comes with the issue of increased magnetic interactions between modules. This interaction manifests itself as unbalanced phase currents during fault events with its magnitude dependent on the built-in module unbalance, the level of magnetic coupling between modules, and magnitude of coil currents. Even if this unbalance is suppressed using control, the associated voltage unbalance would contribute to elevated winding aging [157]. In some cases, slight current unbalance may be acceptable, though does come with performance degradation in torque ripple and uneven machine heating.

3.5. Summary

Emerging safety-critical applications such as electrified aerospace propulsion require the realization of high performance electrical machines (e.g., high power density) while maintaining high levels of reliability for safe operation of the aircraft. In particular, the use of PMSMs is a

strong candidate machine topology for achieving the desired levels of power densities. Furthermore, the use of integrated modular motor drives (e.g., dividing a stator into multiple three-phase winding sets, each with its own dedicated inverter mounted inside the machine enclosure) is an appealing way to enhance the drive system power density while adding redundancy to the motor drive. This chapter has provided a methodology for sizing machines to achieve high levels of power density as well as highlighting the opportunities to enhance their fault tolerance using modular machine topologies that are accompanied by their own performance tradeoffs.

A methodology for designing power dense PMSMs is presented that uses conventional post-processed machine power density metrics (current density, shear stress, tip speed, machine speed) as optimization variables. Machine sizing equations are presented, allowing users to quickly determine dimensions and winding losses directly from these metrics. These equations can be implemented in an optimization algorithm to enable users to explore the design space more efficiently.

These identified power density principles are applied to the design of a 1 MW Integrated Modular Motor Drive (IMMD) and a lower power 200 kW demonstrator machine. Features of these machines, including in-slot direct cooling, are highlighted for their role in elevating the machine power density. Initial machine back-emf, phase-current, and torque measurements are shared, which exhibit good agreement with the model predictions.

The lower-power 200 kW demonstrator machine is investigated in more detail to evaluate its magnetic isolation capabilities. The stator is comprised of six 3-phase modules that can be arranged with a group of three adjacent modules forming each half of the machine or alternating the modules from the two groups around the stator circumference in an interleaved configuration. Machine experimental tests shows that the interleaved configuration exhibits higher levels of

electromagnetic coupling between the two module groups due to both its higher number of inter-group interfaces and the impact of the chosen slot-pole combination (18-slot, 12-pole). These electromagnetic interactions contribute to higher unbalanced phase currents in the healthy module during fault scenarios.

A set of analytical machine equations has also been developed that confirms the observed post-fault unbalance. These equations also highlight an inherent phase inductance unbalance associated with the chosen slot-combination. These equations have been implemented in a simulation that confirms these unbalanced currents. The simulation is then used to evaluate terminal short-circuit fault performance for high levels of characteristic current. For these elevated values of characteristic current, higher electromagnetic coupling between modules exacerbates the module current unbalance in the healthy module. Based on the developed simulation, electromagnetic isolation metrics are proposed for evaluating modular machines.

Although grouping the modules into two 3-module halves achieves higher levels of electromagnetic isolation, it is more vulnerable to unbalanced magnetic forces on the rotor during fault events than the interleaved configuration. This unbalanced force results in elevated machine vibration that has been experimentally observed following an open-circuit fault applied to the 200 kW demonstrator machine.

Results presented in this chapter have highlighted some of the tradeoffs that must be considered when evaluating alternative modular machine topologies for new applications. These observations and tradeoffs receive more attention in subsequent chapters including their impact on modular machine drive power density, thermal isolation, and reliability.

Chapter 4

Tradeoff Study of IMD Fault Tolerant Topologies and Strategies for Quadcopter Application

The previous chapters described common types of FT-IMD implementations using PM synchronous machines. A electrically-propelled quadrotor is a potential application for the use of FT-MMDs to help offset reliability shortcomings in existing motor-drive technologies. One approach for the quadrotor IMD is a FT modular machine with FSCW stator winding that divides the power electronics and machine windings into redundant power channels. However, the specific choice of slot-pole combination, the number of phases, and the implemented isolation features are undetermined. These important details of the machine design must be carefully selected in order to ensure that the machine's demanding meet quadrotor specifications.

This chapter examines the power density and loss tradeoffs between different modular isolation approaches. The types of isolation to be examined include: (1) single-layer (SL) windings; (2) five-phase modular machine; and (3) spacer-tooth modular isolation. These tradeoffs will be presented in the context of a double-layer (DL) 36-slot, 24-pole FSCW baseline SPM machine that shares some of the key design features of the NASA ULI machine described in [22] including FSCW windings with $SPP = 0.5$ and the modular structure illustrated in Fig. 2.4-12. In general, the choice of $SPP = 0.5$ offers a wide range of possible slot-pole combinations, making it applicable to a wide range of applications.

While the $SPP = 0.5$ topology is convenient for modular machines, it does have limitations due to high electromagnetic coupling between phases. This illustrated using metrics such as the Module Isolation Ratio (*MIR*). Alternative slot-pole combinations like the double-layer wound SPP = 2/7 are identified for their inherent isolation features and good power density. New

electromagnetic isolation features are developed that introduce back-iron flux barriers and remove interphase tooth tips. This technique is shown to achieve electromagnetic isolation on the same level as SL windings. The impact of electromagnetic coupling between phases is simulated, showing the impact of unbalanced mutual coupling between modules.

Additional considerations for modular isolation are discussed including criteria for determining the level of required isolation. Techniques and metrics are provided for assessing different types of slot pole combinations for their isolation capability. Finally, alternative slot-pole combinations compatible with the identified electromagnetic isolation technique are shared.

4.1. Quadcopter Requirements

This chapter focuses on the propulsion machines required for the six-passenger quadrotor described in [13] and shown in Fig. 4.1-1. The basic mission profile for this vehicle is provided in Fig. 4.1-1 which identifies mission segments, operating altitudes, and travel distances.

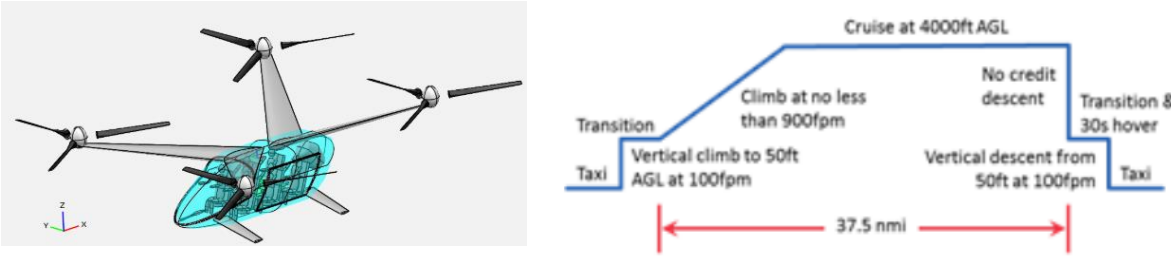

Figure 4.1- 1 Six-passenger quadrotor vehicle and associated mission profile [13].

The electric machine requirements selected for this investigation were developed in consultation with NASA researchers and are summarized in TABLE 4.1-1. Inputs from NASA indicated that the continuous power rating of the machine must fall in the range between 50 and 70 kW. For purposes of comparing multiple FT machine topologies, 70 kW was selected for this investigation. Future performance and thermal-design benefits can be realized by considering the

intermittent quadrotor operating cycle (i.e., power duty cycle) described by the aircraft mission profile in Fig. 4.1-1.

TABLE 4.1-1 QUADROTOR ELECTRIC PROPULSOR MACHINE REQUIREMENTS

Specification	Quantity	Units
Continuous Power Rating	70	kW
Corner Point Speed	8,000	RPM
Maximum Speed Limit (@ 70 kW)	9,600	RPM
DC Bus Voltage	700-810	V
Target Machine Efficiency (@ 70 kW, 8000 rpm)	95.0	%
Target Mass Power Density (@ 70 kW, 8000 rpm)	13.3	kW/kg
Target Volume Power Density (@ 70 kW, 8000 rpm)	36.8	kW/*l*

The machine corner point speed is assumed to be 8,000 RPM with a 20% overspeed range that corresponds to constant-power operation at 70 kW. A gearbox is required to step down the machine speed to drive the propulsor rotor. Next, the dc bus voltage is constrained to the range between 700 and 810 V. Finally, the proposed machine must achieve a minimum full-load efficiency of 95% and target minimum active material power density values (i.e., without housing) of 13.3 kW/kg and 36.8 kW/*l* during corner point operation at 70 kW, 8000 rpm.

As previously stated, the proposed machine is designed to incorporate FT features to improve the overall aircraft reliability. Specifically, the machine must be capable of full torque/power operation after a failure in either the machine windings or power electronics. Additionally, the machine must be capable of continued operation after a second failure, albeit at a lower maximum torque/power rating that is 67% of the machine's continuous power rating. A summary of the FT strategy is provided in the Fig. 4.1-2 state diagram.

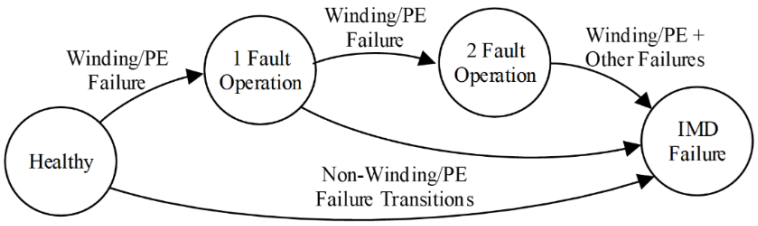

Figure 4.1-2 Specified fault tolerance operation state diagram.

This chapter is organized as follows. First, machine sizing equations are developed for power-dense machines and applied to the 36-slot, 24-pole baseline machine design. Next, this baseline machine design is compared to alternative machine designs that incorporate SL winding, multiphase configurations, and module isolation variants. In general, the examined FT isolation approaches degrade the predicted machine performance. Alternative DL winding magnetic isolation features are proposed, which have been ultimately selected for adoption in the final modular IMD design.

4.2. Modular Baseline Machine Sizing and Design

This chapter presents a power-dense baseline design for a quadrotor application to serve as a comparison point to other FT topologies. Sizing equations are used to establish initial machine dimensions, which are further optimized in electromagnetic FEA.

4.2.1. Sizing FSCW SPM machines for active mass power density

Sizing equations are often used to guide the design of electrical machines. A sizing methodology for power dense machine designs is presented in Chapter 3. These equations are then applied to a fractional slot concentrated wound (FSCW) 36s/24p machine, which will be the baseline machine for this tradeoff study. The baseline 36s-24p sizing parameters are provided in TABLE 4.2-1.

TABLE 4.2-1 BASELINE MACHINE SIZING ANALYSIS PARAMETERS

Sizing Spec	Quantity	Units
Power	70	kW
Base Speed	8,000	RPM
Slots	36	-
Pole Count	24	-
Fundamental Freq.	1.6	kHz
Shear Stress (σ_m)	45	kPa
Tip Speed (v_{tip})	110	m/s
Current Density (J)	20	A_{rms}/mm^2
Magnetic Loading (B_{g1})	0.9	T
Airgap	1.0	mm
Copper Fill Factor (k_{cu})	0.40	-

4.2.2. Baseline Electromagnetic Design

The sizing analysis dimensional outputs are implemented in 2D finite element analysis (FEA) using JMAG Designer. Machine loading, magnetization, and geometry are modified until the machine performance and losses converge to meet the power density and efficiency requirements defined in TABLE 4.2-1. Final baseline machine dimensions are provided in Fig. 4.2-1(a). This machine has a short stack length of 17.6 mm relative to its rotor diameter of 262.6 mm. This is a direct consequence of the sizing methodology which leads to machines with large diameters and short stack lengths to achieve the highest possible power density.

Stator and rotor core laminations use cobalt-iron because of its high saturation flux density. Each coil consists of 29-turns of litz wire, which is necessary to minimize ac losses associated with the 1.6 kHz fundamental frequency. The selected magnet material is samarium-cobalt for compatibility with high-temperature rotor operation. These magnets are segmented axially in 1 mm laminations to minimize eddy current losses, and are magnetized in a Halbach magnet array to minimize rotor core thickness to 2.4 mm. These magnets are contained by a high-strength 0.9 mm thick carbon fiber sleeve, which is sized according to [53]. The proposed machine achieves

an active mass power density of 16.1 kW/kg, exceeding the quadrotor objective defined in TABLE 4.1-1. Magnetic flux density contours are provided in Fig. 4.2-1(b) for the baseline machine at full-load.

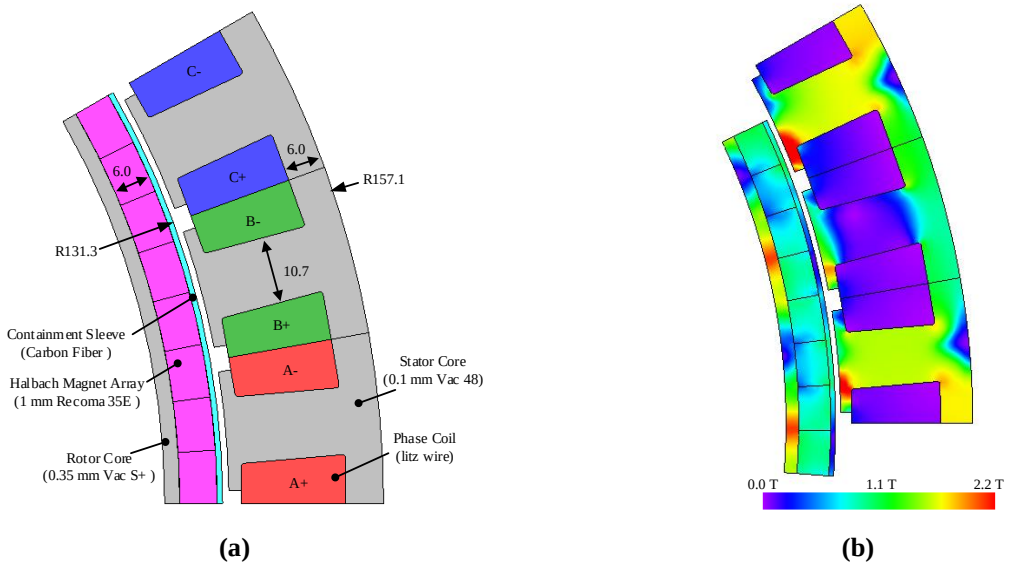

(a) **(b)**

Figure 4.2-1 Baseline machine details: (a) materials and dimensions; and (b) magnetic flux density contours at full load.

Performance and losses are estimated using JMAG Designer and analytical equations based on the stator geometry. A 30% ac loss factor is applied to estimate the losses associated with the high fundamental frequency of the machine. The proposed machine is predicted to meet the required 95% full-load efficiency requirement when estimates of the core, winding, magnet, sleeve and windage losses are all included. Fig. 4.2-2(a) provides predicted machine efficiency over its complete required speed-torque range, including the 20% overspeed region. Most of the loss comes from the stator core loss and winding loss, which are presented separately in Fig. 4.2-2(b) and Fig. 4.2-2(c), respectively. In general, core losses are influenced most heavily by the machine speed, and the winding loss is determined primarily by the torque level.

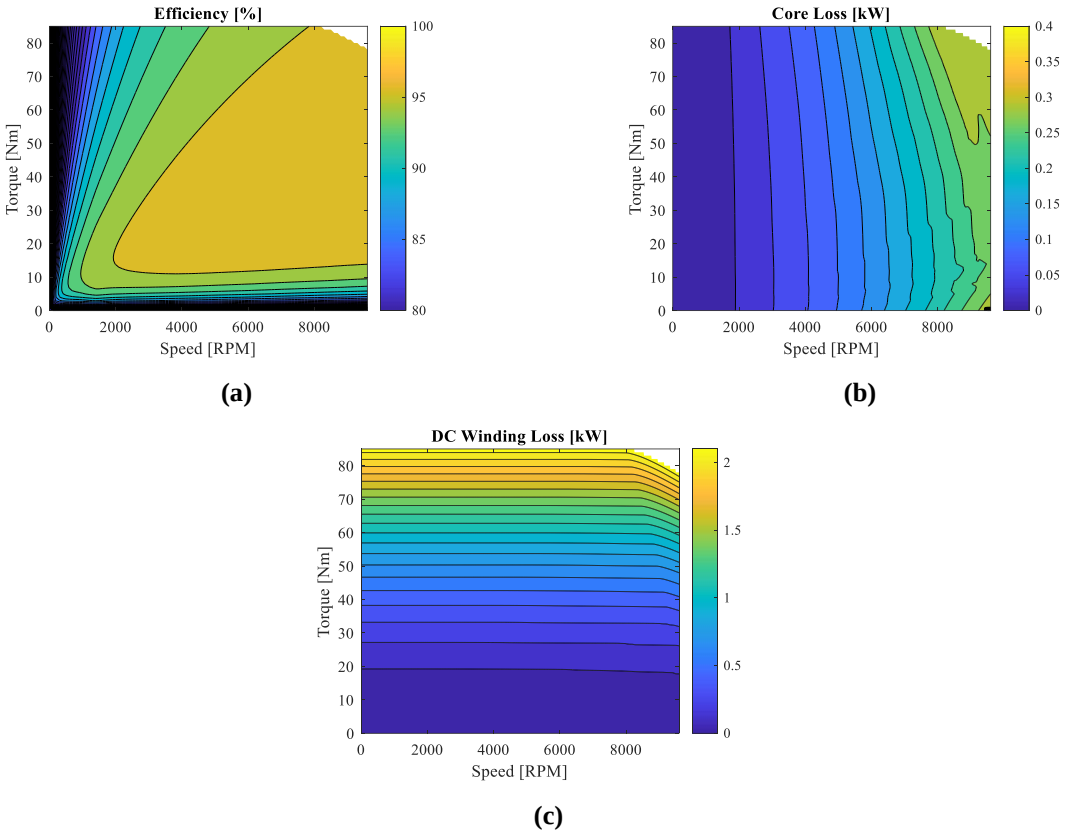

Figure 4.2-2 Baseline machine performance contours: (a) efficiency; (b) core loss; and (c) dc winding loss

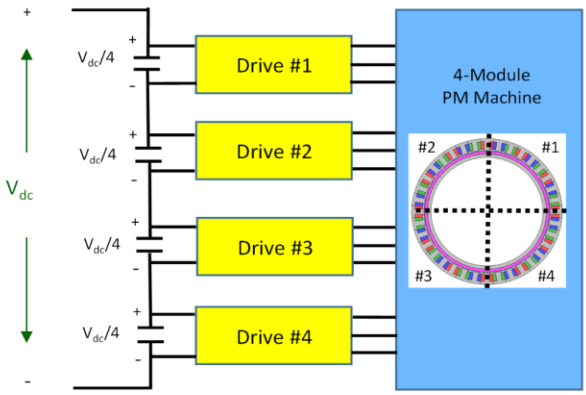

Figure 4.2-3 Baseline machine modular structure and series connection.

The FT configuration selected for the baseline machine is presented in Fig. 4.2-3, where the proposed machine is divided into four quadrants, each consisting of three-phase windings. Each of these modules has its own dedicated two-level VSI. These modules are then connected in series to the main dc bus voltage V_{dc} so that each module receives 25% of the total dc bus voltage.

In the event of a faulted winding or power electronics device, the faulted module is bypassed which increases the available module voltage by 33%. Remaining healthy modules can increase their current to restore rated torque levels. This is illustrated in Fig. 4.2-4 for a three-phase OC fault at the machine terminals, with healthy and faulted torque waveforms shown in Fig. 4.2-4(b). Average torque drops by 75% after the loss of a module with no change in the current supplied by the remaining 3 healthy phases. Full torque is restored by increasing each healthy module current by 33%. However, increased torque ripple is observed due to increased saturation in the healthy stator modules.

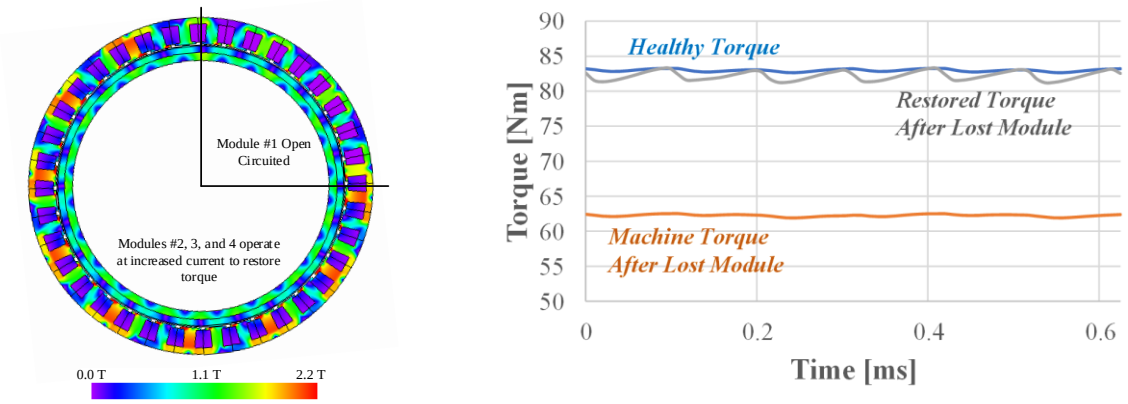

(a) **(b)**

Figure 4.2-4 Baseline machine single-module OC fault: (a) flux machine contour with full torque restored; and (b) torque performance under healthy and faulted conditions assuming sinusoidal excitation currents, including post-fault operation with both 100% and 133% rated current supplied to the three healthy machine phases.

The presented 36-slot, 24-pole baseline machine meets the performance and fault tolerance requirements defined for the quadrotor application. While the presented machine is capable of operation under faulted conditions, the choice of DL winding leaves opportunity for faults to propagate between modules. Furthermore, the presented base design is not derated (e.g., decreasing healthy operating current density) as required for full-torque operation after a fault.

4.2.3. Baseline Stator Thermal Concept

A high winding loss is a consequence of raising the machine power density to high values. In order to validate the feasibility of the baseline machine design, a preliminary stator cooling concept has been developed. As discussed in the literature review, it is common for electrical machines to be cooled indirectly through the stator back iron. A challenge posed by this approach is passing the coil heat through the slot lining material that typically acts as a high thermal resistance. Valuable thermal benefits can be realized by potting the stator winding in a high thermal conductivity potting material. Due to the short stack length of the machine, substantial cooling improvement can be achieved by using the potting material to form a thermally-conducting bridge between the end windings and the stator housing that is actively cooled on its exterior surface as illustrated in Fig. 4.2-4.

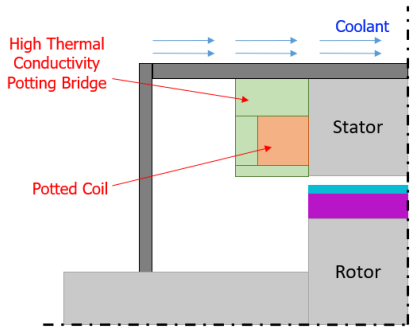

Figure 4.2-5 Potted channel cooling concept.

This potted channel cooling approach has been evaluated using JMAG 3D thermal FEA. Model assumptions and material properties are provided in Fig. 4.2-6. A single tooth is modeled for simplicity. Adiabatic boundary conditions are assumed between the adjacent stator teeth, and the outer surface of the housing is assumed to be actively cooled. Remaining surfaces are assumed to be exposed to stagnant ambient air. For further simplification, the coil model is homogenized with

thermal conductivity properties determined using [186]. Any contact resistances at the material surface interfaces are neglected in this preliminary analysis.

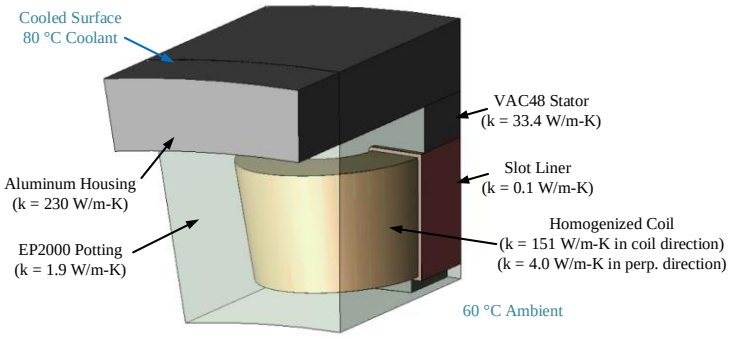

Figure 4.2-6 Thermal model material thermal conductivities

The heat transfer coefficient at the housing's outer surface have been conservatively varied between 500 to 5,000 W/m^2-K based on values found in the literature survey. A low constant heat transfer coefficient of 3 W/m^2-K is assumed for the ambient exposed surfaces. A constant total core loss heat load of 0.3 kW is assumed and is uniformly distributed throughout the stator core material. The total winding loss is varied between 2.9 kW (rated) and 3.6 kW (overload) condition and is uniformly distributed throughout the winding volume. Non-isotropic values of the thermal conductivities are assumed in the coil with a high value of 151 W/m-K in the direction of the coil wires and a much lower value of 4 W/m-K in the plane perpendicular to the coil using values calculated using [186].

The maximum predicted maximum coil temperatures are plotted vs. the cooling jacket heat transfer coefficient in Fig 4.2-7(a). In general, the maximum coil temperature is located in the coil portion inside the slot. These results show that a potted end-winding cooling approach is insufficient by itself to accomplish the necessary stator cooling, resulting in predicted coil temperatures exceeding 270°C for the more favorable lower (rated) winding loss condition with the highest stator housing cooling conditions, which is beyond the thermal limits of conventional

insulation systems. Fig. 4.2-7(b) shows a thermal color contour plot of the coil indicating a hot spot on the underside of the coil closest to the machine air gap.

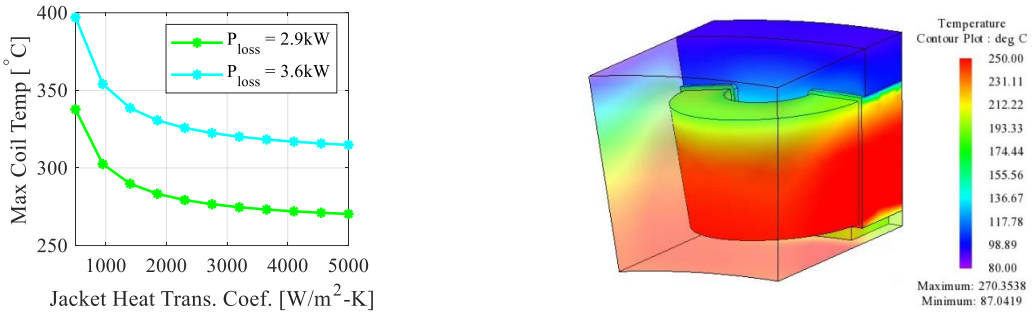

(a) (b)

Figure 4.2-7 Predicted thermal performance for the cooling conditions with potted end windings (only): (a) predicted maximum coil temperature for two loss conditions as a function of the cooling jacket heat transfer coefficient; and (b) thermal FEA color contour plot of the coil end winding region for 5,000 W/m^2-K water jacket cooling condition and 2.9 kW of winding loss (rated).

The performance of the Fig. 4.2-6 thermal system can be improved with an alternative potting compound with a higher thermal conductivity. Replacing the EP2000 material in Fig. 4.2-6 with a potting with thermal conductivities exceeding 10 W/m-K allows for the feasibility of this concept. However, availability of these types of materials is limited [104] and often comes with negative tradeoffs like high viscosity which will affect the quality of the potted winding. Beyond this, direct cooling approaches to extract the heat from the coils can be applied. For example, the use of an in-slot 3D printed structures has been shown to enable significantly higher current densities to be achieved in [110] and are considered here. The Fig. 4.2-6 system has been updated to consider an alumina ceramic cooling structure cradling the bottom side of the coil as shown in Fig. 4.2-8(a), allowing for the previous hot spot to be addressed while having only a marginal negative impact on the coil slot fill.

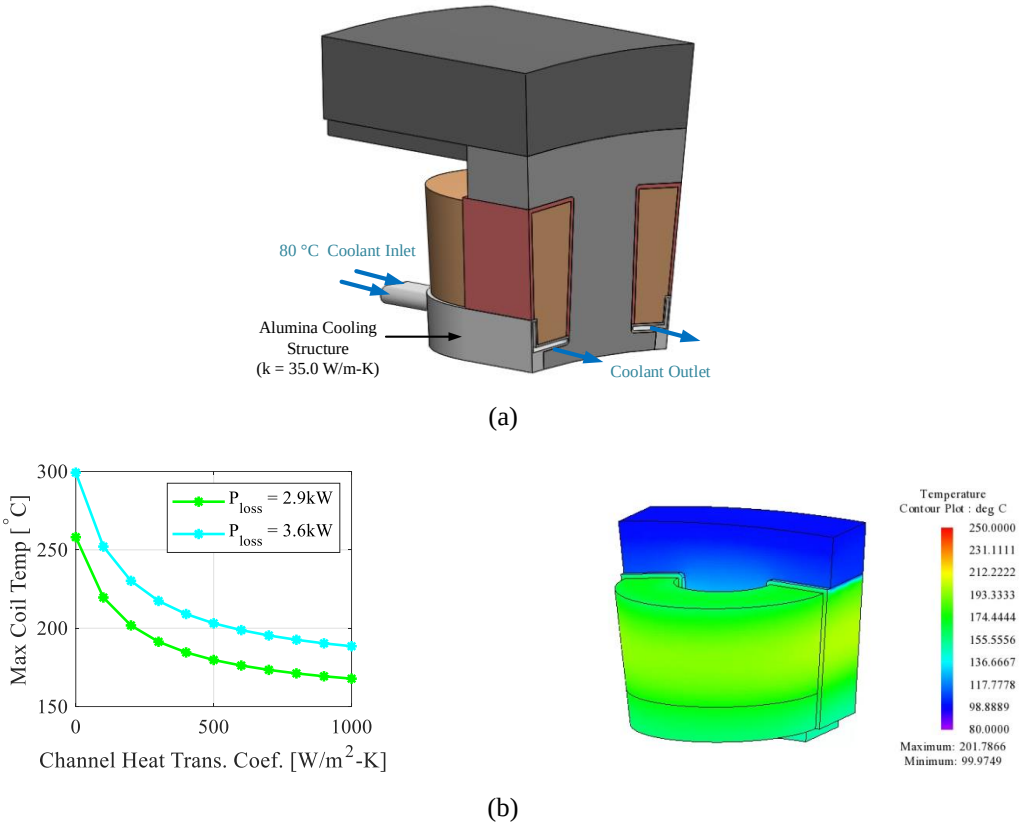

Figure 4.2-8 Direct in-slot cooling: (a) concept; and (b) FEA color contour plot results for rated winding losses (2.9 kW) for a fixed stator cooling jacket heat transfer coefficient value of 5000 W/m^2-K and a heat coefficient value of 200 W/m^2-K for the in-slot cooling structure.

The analysis using 3D thermal FEA has been repeated considering the same rated and overloaded losses, and a fixed cooling-jacket heat transfer coefficient of 5,000 W/m^2-K at the high end of the considered range. The heat transfer coefficient on the new in-slot cooling structure surface has been varied between 0 to 1000 W/m^2-K based on published results in [110]. The maximum predicted coil temperature and a temperature contour plot are provided in Fig. 4.2-8(b). These results indicate that this cooling concept can limit the maximum coil temperature sufficiently for cooling channel heat transfer coefficient values above 200 W/m^2-K (rated loss) and 500 W/m^2-K (overloaded loss). Furthermore, the coil exhibits a more uniform temperature distribution compared to the previous results in Fig. 4.2-7(b) without the in-slot cooling structure.

This combination of direct in-slot cooling and indirect cooling using an outer stator cooling jacket has been adopted for the proposed FT quadrotor machines. One important advantage of the integrated motor drive architecture is that the stator housing cooling jacket can be used to assist with cooling of the drive power electronics if the inverter is mounted around the outer circumference of the stator housing. More detailed discussion of the power electronics integration and cooling analysis are provided in Chapter 4.

4.3. Tradeoff Study of Conventional FT Modular Machines

Electromagnetic isolation features between stator modules is critical for preventing fault propagation between modules. Several alternative isolation approaches presented in Chapter 2 examined further in this section. To do so, 2D FEA designs are produced for promising strategies and compared against the baseline design. These strategies include the SL winding, multiphase, and spacer teeth isolation approaches.

4.3.1. Single-Layer 36-Slot 24-pole Variant Topology

The use of a SL FSCW winding configuration is a popular method for providing physical isolation between machine coils and modules. The presented baseline DL winding can be modified to be a SL winding as shown in Fig. 4.3-1(a) and Fig. 4.3-1(b). Also shown in Fig. 4.3-1 are the winding functions (which represent the winding's airgap flux density waveshape and magnitude), and the corresponding winding function spatial harmonic spectrum (which can be used to assess torque capability and rotor harmonic losses).

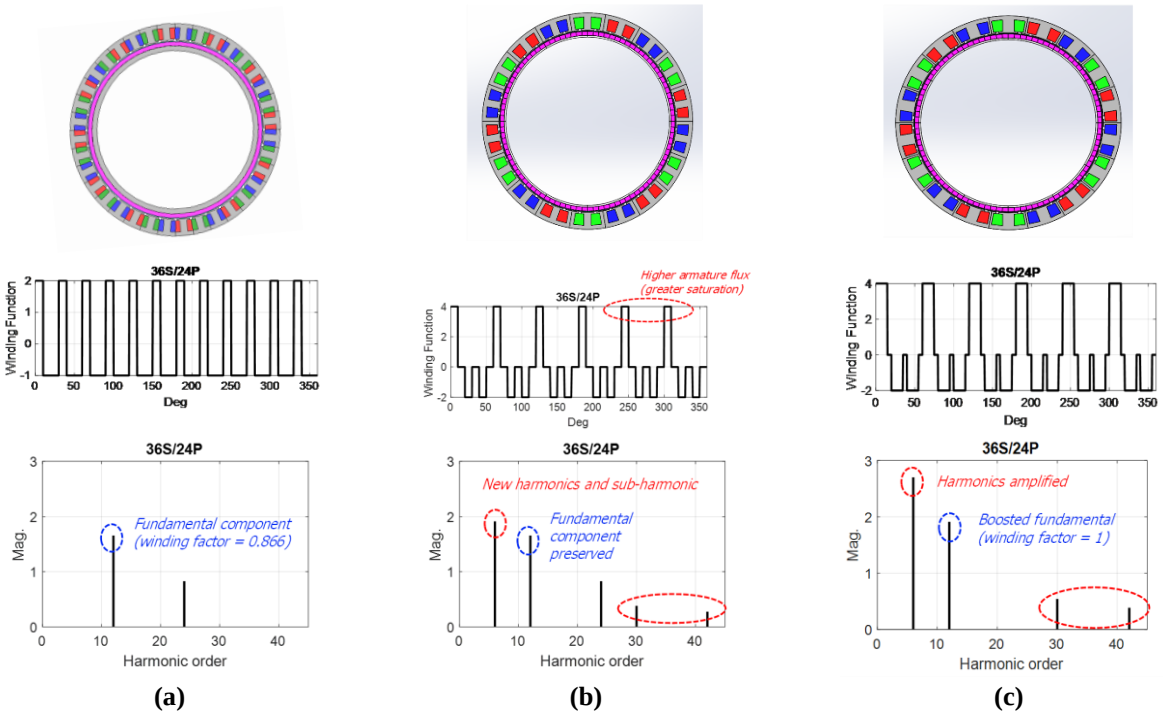

Figure 4.3-1 36-slot, 24-pole winding variants, winding factors, and winding factor spatial harmonic content: (a) DL baseline; (b) SL variant; and (c) SL variant with modified tooth thicknesses.

Comparing the SL and DL winding functions, it is apparent the SL variants have higher peak winding functions, indicating higher levels of expected steel saturation and core loss for the same current levels. Decomposing these winding functions into their spatial harmonic components shows the SL variant having substantially higher spatial harmonic content compared to the DL baseline. These harmonics are asynchronous with the rotor speed and contribute to increased rotor eddy current loss.

The basic SL variant can be modified further by adjusting tooth thicknesses, as shown in Fig. 4.3-1(c). Specifically, teeth located between phases can be narrowed in combination with widening of the wound teeth. Examining the harmonic content of the winding function shows an increased fundamental component, indicating improved torque capability. However, this approach amplifies some of the winding function spatial harmonics which further increase the rotor losses.

Both SL variants have been analyzed using 2D FEA to evaluate torque performance and core loss. Main machine dimensions (rotor radius, etc.) are held constant for all three winding designs, although the modified tooth geometry halves the narrowed tooth thickness and increases the wound-tooth thickness by 50%. Winding loss is estimated from the stator geometry and includes a 30% ac loss factor accounting for high frequency losses. A comparison of the 36s/24p baseline and variants is provided in TABLE 4.3-1.

TABLE 4.3-1 36-SLOT, 24-POLE SL TRADEOFF STUDY RESULTS

Criteria	36S/24P DL	36S/24P SL #1	36S/24P SL #2
Power [kW]	70		
Torque Ripple [%]	1.6	3.8	3.2
Core Loss [kW]	0.4 (S), 0.1 (R)	0.4 (S), 1.7 (R)	0.4 (S), 1.7 (R)
DC Winding Loss (+ AC) [kW]	2.2 (+ 0.7)	2.8 (+ 0.8)	2.5 (+ 0.8)
Winding Mass [kg]	1.4	1.7	2.0
Remaining Active Mass [kg]	3.0	3.0	2.9
Power Density [kW/kg]	16.1	15.0	14.2

In general, the DL variant outperforms both SL variants in terms of torque ripple, losses, and active mass power density. Both SL variants have substantially higher saturation, contributing to increased torque ripple. Furthermore, the increased stator airgap spatial harmonics contribute massive increases in rotor core losses. Winding losses increase for both SL variants due to large end windings. However, the modified stator tooth SL geometry version (#2) has a somewhat lower winding loss than version #1 due to its improved fundamental winding factor. However, thickening the wound-teeth increases the length and overall size of the end winding, reducing its expected power density compared to the other two designs.

Overall, the SL winding configuration is a useful method for introducing modular stator isolation features, but it results in higher winding and rotor loss, as well as lower power density. These tradeoffs are exacerbated by the large diameter and short stack length of the baseline machine.

4.3.2. Five-Phase 20-slot, 22-pole Machine

Multiphase machines are a viable option for increasing the FT capability of modular machines. The five-phase 20-slot, 22-pole design is attractive for FT isolated designs due to its localized stator winding flux characteristics. This machine can be divided into two channels as indicated in Fig. 4.3-2. These drives can be connected in series like the baseline machine in Fig. 4.2-3, or in an open-winding configuration as described in Fig. 2.4-15 or [37]. Furthermore, the number of switches in a dual five-phase system is less than that of the baseline four-module three-phase design, while maintaining much of the required FT capability.

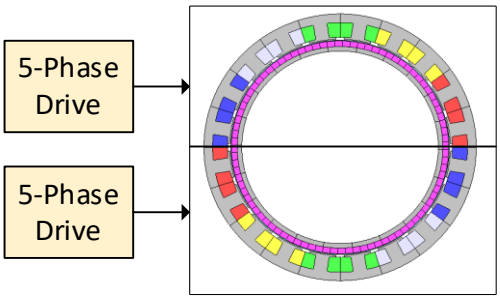

Figure 4.3-2 Dual-module five-phase 20-slot, 22-pole FT configuration.

Fault-tolerant 20-slot, 22-pole machine designs have been developed using the previously mentioned sizing equations and 2D FEA to assess performance. This investigation has evaluated three winding configurations that parallel those considered in Fig. 4.3-1 for the 36-slot, 24-pole quad three-phase machine: DL, SL, and SL with flux barrier variants that are shown in Fig. 4.3-3. Compared to the baseline machine, the five-phase designs have a smaller rotor radius and longer

stack length. This has been done to account for expected larger end windings associated with the lower number of slots (i.e., added end-turn length associated with thicker teeth). FEA-calculated magnetic flux contours are also provided in Fig. 4.3-3. The SL variant has substantially higher stator and rotor core saturation for the same geometry, which is consistent with the previous SL baseline study. The second SL variant introduces flux barriers between phases as discussed in [127]. The introduction of the flux barriers required an increase in outer radius and slot height to maintain the coil copper current density. Further thickening of the stator and rotor back iron is necessary to account for added saturation relative to the DL design. This saturation is caused by the concentration of winding flux produced by the flux barriers.

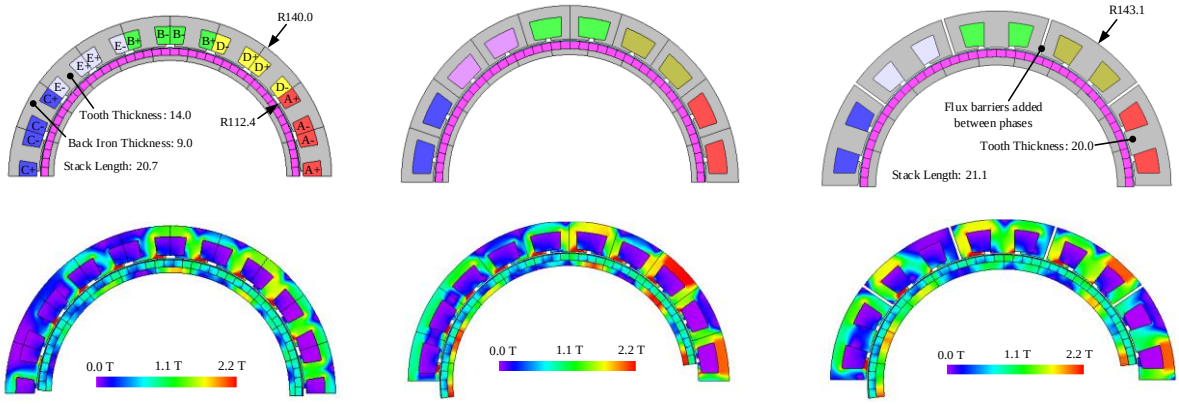

Figure 4.3-3 Five-phase 20-slot 22-pole machine variants and FEA-calculated predicted full-load magnetic flux contour plots: (a) DL winding; (b) SL winding variant; and (c) SL winding variant with flux barriers.

A performance summary of the three five-phase designs is provided in TABLE 4.3-2. Once again, it is observed the DL winding configuration outperforms the two SL variants in terms of loss and power density. In both SL cases, the torque ripple and core loss of the SL machines increases due to higher levels of saturation. Furthermore, the SL winding losses are higher than the DL version due to larger end windings. This loss impact is reduced by the improved torque characteristics associated with the flux barrier design. Both SL variants have degraded power densities due to

larger end windings. The flux barrier design is further penalized by a larger core mass related to integrating the flux barriers and managing increased saturation related to the concentrated flux.

TABLE 4.3-2 FIVE-PHASE 20-SLOT, 22-POLE PERFORMANCE TRADEOFF RESULTS

Criteria	20S/22P DL	20S/22P SL	20S/22P SL + FB
Power [kW]	70		
Torque Ripple [%]	0.3	1.0	1.7
Core Loss [kW]	0.2 (S), 0.4 (R)	0.4 (S), 0.7 (R)	0.3 (S), 0.9 (R)
DC Winding Loss (+ AC) [kW]	2.6 (+ 0.8)	3.4 (+ 1.0)	3.0 (+ 0.9)
Winding Mass [kg]	1.7	2.2	1.9
Remaining Active Mass [kg]	3.5	3.5	4.3
Power Density [kW/kg]	13.6	12.3	11.3

Compared to the three-phase 36-slot, 24-pole baseline machine designs, the presented five-phase designs underperform in terms of power density and losses. Furthermore, only the DL five-phase design meets the required performance requirements presented in TABLE 4.1-1. Additional intensive geometry optimization would be required to improve the competitiveness and applicability of the five-phase variants.

4.3.3. Modular Spacer Teeth Isolation Features

The introduction of spacer teeth between module windings is an alternative approach for providing electromagnetic isolation in FT modular machines. This approach is presented in [31] where stator spacer teeth are inserted between three-phase winding channels. On the simplest level, these features can be added between each of the four quadrants of the 36s/24p baseline machine windings as shown in Fig. 4.3-4(a), which maintains the same stator outer diameter and trims the widths of the stator slots and teeth to accommodate the added four teeth. FEA-calculated full-load

magnetic flux density contours are provided in Fig. 4.3-4(b) which indicate substantially higher stator magnetic saturation due to the compressed stator features. In addition, the introduction of the spacer teeth reduces the torque capability of the machine by reducing the magnet flux linkage and introducing inductance unbalances. These unbalances result in substantially higher torque ripple as observed in Fig. 4.3-4(c) for balanced three-phase sinusoidal current excitation.

Simply adding spacer teeth to the stator as described is an ineffective method for implementing modular isolation. Alternative approaches have also been evaluated. First, isolation between modules can be increased by removing stator windings instead of adding spacer teeth. This has been investigated for the *SPP* = 0.5 stator design by removing one set of three-phase windings between modules as shown in Fig. 4.3-5. The space previously occupied by these coils can be used for cooling or rotor position sensing coils.

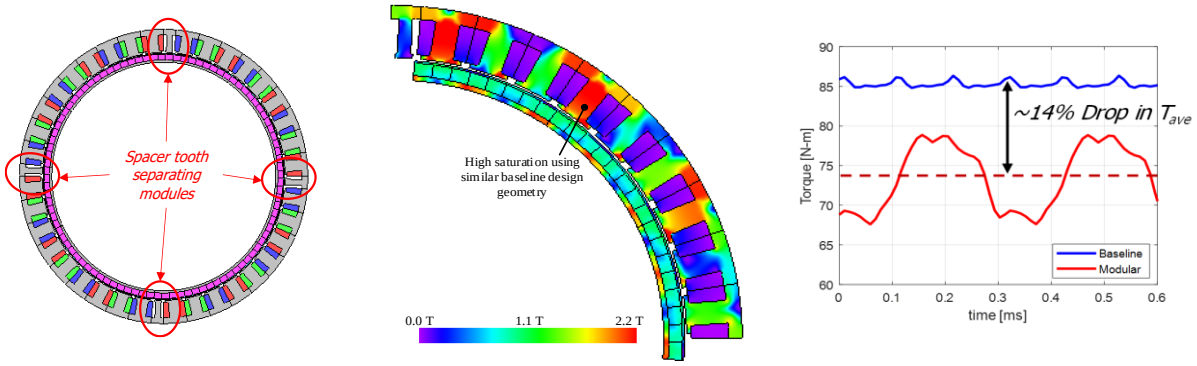

(a) **(b)** **(c)**

Figure 4.3-4 Simple spacer tooth module isolation approach: (a) concept; (b) full load magnetic flux density contours; and (c) torque performance impact compared to baseline assuming sinusoidal current excitation.

Machine torque can be maintained at the required full-load value by increasing the current density of the remaining coils by 50% from 20 to 30 A_{rms}/mm^2, which significantly increases the winding loss. Furthermore, it is apparent in Fig. 4.3-5(b) that the calculated flux density contour exhibits increased stator saturation caused by the increased coil currents. The winding loss can be

reduced back to baseline levels by increasing the slot height as shown in Fig. 4.3-5(c) which reduces the current density back to 30 A_{rms}/mm^2.

Performance and power density comparisons between these two implementations are summarized in TABLE 4.3-3. Without adjusting the slot height, the modular isolation version #1a has substantially higher winding loss caused by its much higher current density. However, the power density of this approach improves due to the removal of stator coils. Torque ripple in the modular structure increases, but to a lesser extent than the Fig. 4.3-4(c) case with the spacer teeth.

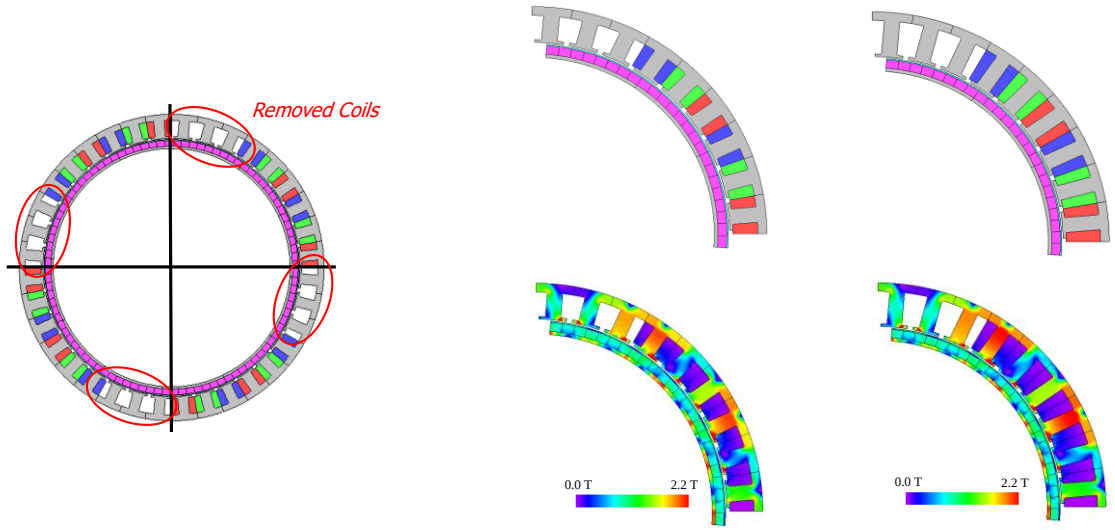

(a) **(b)** **(c)**

Figure 4.3-5 Modular isolation by removing coil phase groups between modules: (a) concept; (b) module isolation version #1a with high current density; and (c) module isolation version #1b with reduced current density.

Returning to 20 A_{rms}/mm^2 current density with a larger stator diameter and deeper slots in version #1b returns the coil loss level to baseline levels at the expense of power density. Specifically, a 9.9% reduction in power density is predicted, although the stator core mass can likely be decreased somewhat by modifying the stator teeth in the coil-less sections of the machine.

Finally, higher magnetic saturation is observed in the modular structure #1b compared to that in #1a, contributing to higher torque ripple with version #1b.

TABLE 4.3-3 MODULE ISOLATION BY REMOVING COIL: PERFORMANCE SUMMARY

Criteria	Baseline	Modular #1a	Modular #1b
Power [kW]	70		
Current Density [A/mm^2]	20	30	20
Core Loss [kW]	0.3 (S), 0.1 (R)	0.4 (S), 0.2 (R)	0.4 (S), 0.2 (R)
DC Winding Loss (+ AC) [kW]	2.2 (+ 0.7)	3.4 (+ 1.0)	2.2 (+ 0.7)
Power Density [kW/kg]	16.1	17.9	14.5

In summary, removing module coils can assist with achieving isolation, but the power density values presented in Table 4.3-3 are lower than those predicted for the SL winding approach presented in TABLE 4.3-1 for the same 20 A_{rms}/mm^2 current density. This leads to the conclusion that removing coils from the stator is an ineffective means of improving isolation between the modules.

The coil removal approach in Fig. 4.3-5 can be modified in combination with rotor changes to increase the viability of this approach. Specifically, each spacer tooth is added in combination with a new rotor pole. Doing so maintains the *SPP* = 0.5 characteristic of one pole pair per three stator teeth. This is shown in Fig. 4.3-6(a) where four spacer teeth are added to the baseline design, increasing the machine pole count from 24 to 28. An FEA-calculated full-load magnetic flux density contour of this alternative spacer tooth approach is shown in Fig. 4.3-6(b), indicating similar saturation levels to the baseline design.

The baseline design performance and the modified spacer tooth isolation approach is summarized in TABLE 4.3-4. The first disadvantage to this approach is the ~17% increase in fundamental frequency caused by the increased number of rotor poles. This alternative spacer tooth approach with 4 additional rotor poles has substantially higher torque ripple related to unbalanced phase flux linkages and inductances caused by the spacer teeth. Beyond this, losses associated with the machine are comparable, with winding losses being reduced modestly due to compacted end windings. A modest decrease in power density by approx. 6% is also observed. These results suggest that further machine design optimization efforts to minimize the torque ripple would be required to make this isolation approach more appealing.

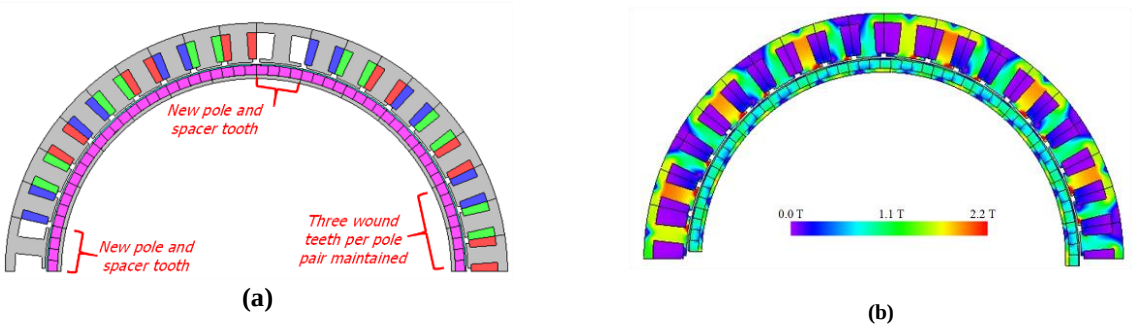

Figure 4.3-6 Spacer tooth isolation approach with modified rotor pole count: (a) concept; and (b) full load magnetic flux contour plot.

TABLE 4.3-4 MODULAR ISOLATION STUDY WITH SPACER TOOTH AND INCREASED POLE COUNT

Criteria	Baseline	Modular #2
Power [kW]	70	
Fundamental [Hz]	1600	1866
Torque Ripple [%]	1.6	8.5
Core Loss [kW]	0.3 (S), 0.1 (R)	0.4 (S), 0.1 (R)
DC Winding Loss (+ AC) [kW]	2.2 (+ 0.7)	2.0 (+ 0.6)
Power Density [kW/kg]	16.1	15.6

4.3.4. Electromagnetic Isolation Tradeoff Study Summary

Several modular isolated designs have been analyzed using 2D FEA to better evaluate performance and power density tradeoffs compared to the 36-slot, 24-pole baseline. Specific metrics are captured for each design including the active mass power density, core and winding losses, and torque ripple, which are summarized in Fig 4.3-7.

First, SL variants of the 36s/24p machine are investigated. In general, switching to a SL winding degraded the active mass power density compared to the DL baseline due to larger end windings. Furthermore, the SL winding increased losses that are also attributable to the larger end windings and increased saturation in the stator and rotor core. This saturation also contributes to nearly doubling the amount of torque ripple. Similar observations can be made for the five-phase 20s/22p designs after evaluating both the DL and SL variants. Overall, the five-phase design underperforms in all categories compared to the considered three-phase designs. Further geometric optimization of the five-phase design will be necessary to find a design that meets the quadrotor machine requirements.

Alternative modular isolation approaches were also considered that physically separate modules by removing coils or inserting spacer teeth. In general, the introduction of these modular features makes this type of isolation approach competitive with the DL baseline in terms of power density and losses by avoiding bulky end windings observed in SL variants. The main disadvantage of a modular isolation approach is the increased torque ripple, which is related to phase and magnet flux linkage unbalances due to the inserted isolation features.

It is apparent conventional modular isolation approaches produce competing tradeoffs in terms of meeting both the quadrotor performance and FT requirements. The next section discusses an alternative method of modular isolation utilizing a DL winding in order to seek an approach that

improves the isolation of the baseline DL winding configuration without losing the desirable performance characteristics of that winding type.

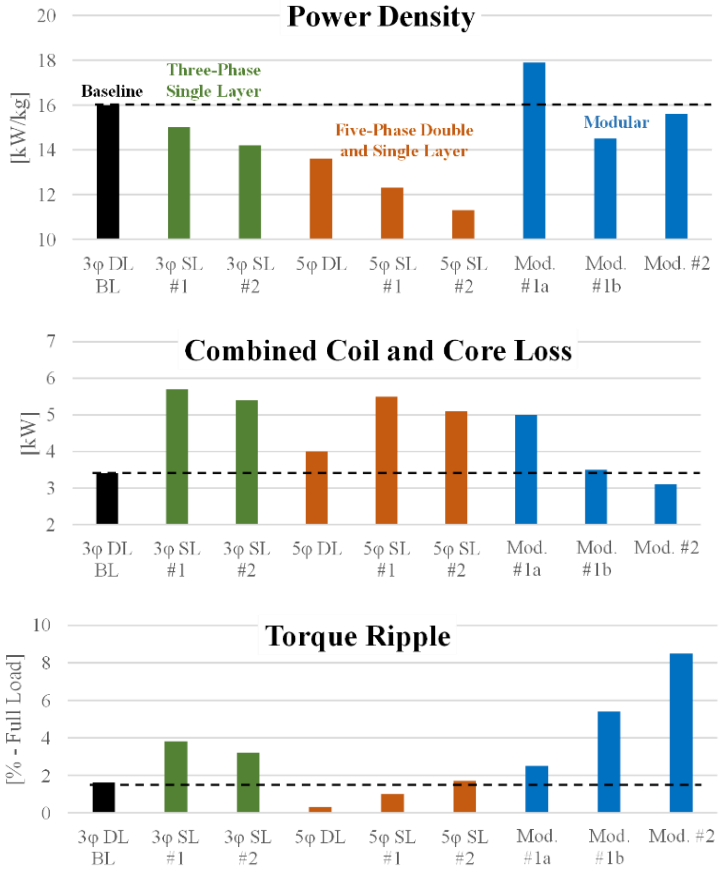

Figure 4.3-7 Summary of modular isolation tradeoff study.

4.4. Enhanced Magnetic Isolation Strategy and Modular Machine Modeling

The modular isolation approaches discussed in the preceding section use the stator core structure to provide electromagnetic and thermal isolation between modules (e.g., spacer teeth or SL winding). This section explores an alternative isolation approach using DL windings that utilize spacing and insulating materials between coils that share the same slot. Furthermore, the use of in-slot cooling methods can also assist with thermal isolation. This type of DL winding

isolation approach has been applied to the final quadrotor machine, which is discussed in the next section.

Electromagnetic isolation is an important concern for the baseline DL winding machine. However, the stator core can be modified to reduce or block linkage flux between adjacent modules. One technique is the introduction of cavities in the stator back-iron and/or the removal of tooth tips between modules. Complete removal of stator tooth tips from all of the stator teeth would eliminate a major source of leakage flux at the price of eliminating a design handle for reaching high machine inductance.

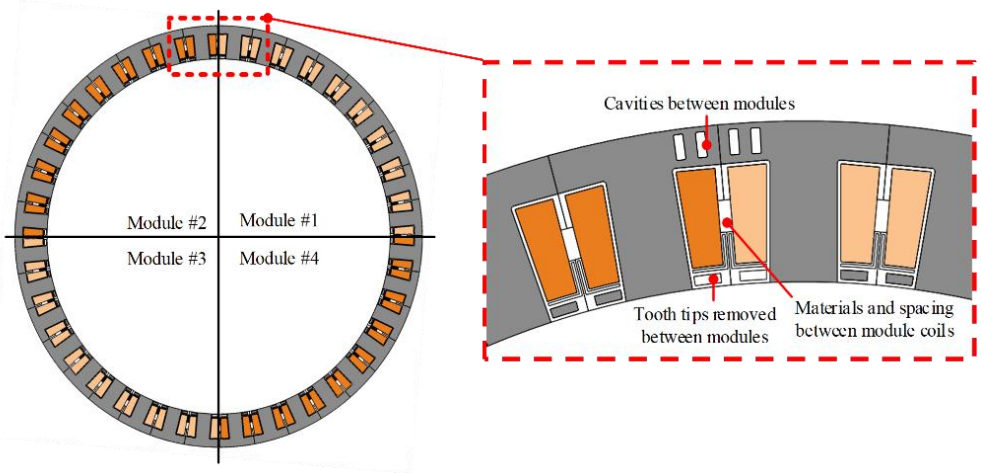

Figure 4.4-1 Alternative modular isolation approach for baseline stator.

This type of modular isolation approach can be applied to the baseline 36-slot, 24-pole machine, as shown in Fig. 4.4-1. Compared to the previous spacer tooth approach, the power density and loss tradeoffs are less severe due to minimal changes in the stator structure. However, electromagnetic unbalances still exist in the stator magnet flux linkage and inductances, leading to large torque ripple and the potential for nonuniform heating in the machine. Furthermore, this type of machine design may be vulnerable to lower reliability characteristics, as new stresses are introduced into this type of FT machine.

Alternatively, this type of stator cavity and tooth tip removal process can also be applied on a phase level to limit the effects of unbalance. In particular, FSCW machines with slot-per-phase-per-pole (SPP) values of 2/7 or 2/5 are appealing due to their inherently localized phase winding flux paths allowing for simple application of the previously described techniques. Other slot-pole combinations and techniques for assessing modular stators is discussed later in this chapter.

A single phase of one these windings consisting of two adjacent stator teeth with two windings is depicted in Fig. 4.4-2(a), with the phase winding's main flux path highlighted. This drawing shows that the inner tooth tips between the two teeth can be adjusted to meet the necessary current-limiting inductance value required for the machine.

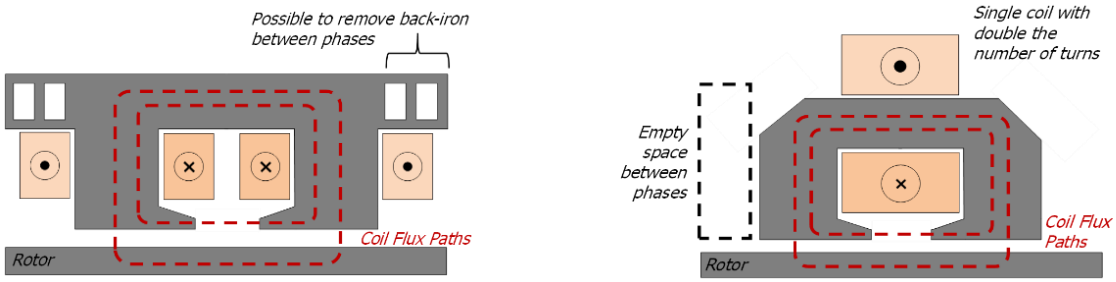

Figure 4.4-2 SPP = 2/7 or 2/5 isolation approach applied on phase level: (a) conventional winding; and (b) toroidal winding.

The proposed isolation structure can be taken a step further by utilizing a toroidal winding allowing for complete physical isolation of phases. This is shown in Fig. 4.4-2(b) with a similar electromagnetic flux path highlighted. Electromagnetic flux leakage paths passing through adjacent phases can be nearly eliminated by removing core material between the phases. Overall, this type of winding could utilize simplified direct cooling and manufacturing methods. While this is an interesting prospect, this report will focus on a conventional FSCW winding configuration due to is wider applicability.

This isolation approach has been applied to a four-module DL 24-slot, 28-pole (*SPP* = 2/7) machine for comparison with the baseline DL winding machine design. First, results of an FEA analysis of a conventional 24-slot, 28-pole FSCW machine with DL windings is presented. Next, back-iron cavities and tooth tip removal features are introduced to the conventional machine, and isolation tradeoffs are evaluated. A machine simulation has been performed on both the conventional and isolated configurations in MATLAB Simulink to assess the impact of module electromagnetic isolation on key performance characteristics, considering a three-phase short-circuit fault scenario.

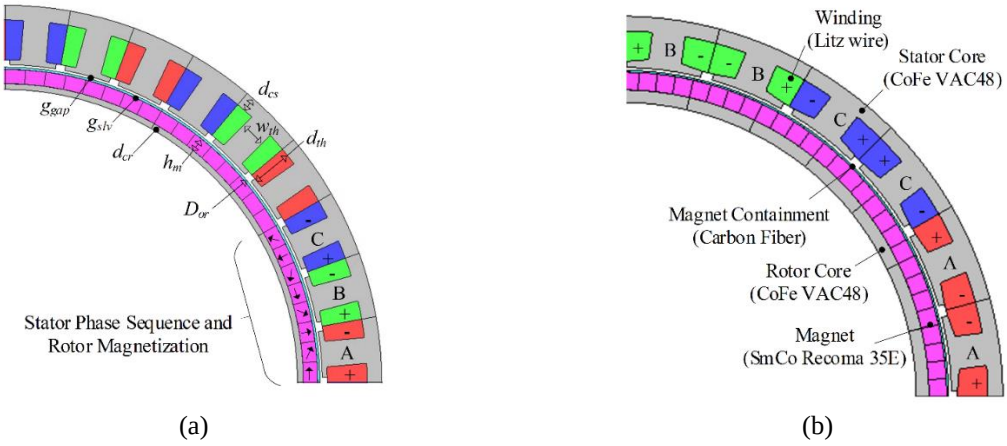

Figure 4.4-3 Cross-sections of DL 4-module FSCW machine topology candidates: (a) 36s/24p topology with key machine dimension variables highlighted; and (b) 24s/28p topology with machine materials highlighted.

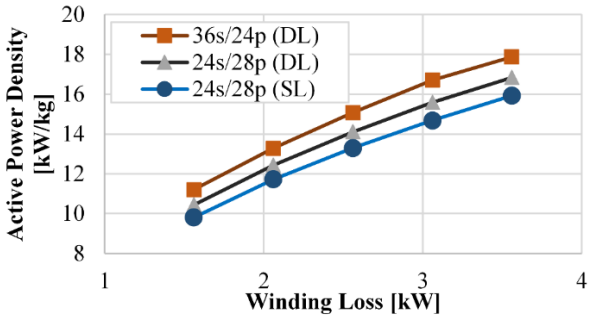

Figure 4.4-4 Sizing analysis optimal design points for inputs σ_m between 30 to 50 kPa, v_{tip} between 70 to 130 m/s, and J between 10 to 25 A-rms/mm^2.

4.4.1. Sizing Equation Comparisons

The sizing equation analysis shared in Chapter 3 is revisited to guide the design on the 24s/28p machine. Instead of assigning set specifications (e.g., tip speed, etc.) an optimization process is followed to explore the design space more thoroughly. Specifically, the winding loss is identified as a dominant loss component in the tradeoff study, which can be calculated using sizing equations. To validate the results of the previous section, a comparative SL 24s/28p machine is studied using sizing equations and this analysis is repeated on the 36s/24p topology.

TABLE 4.4-1 SIZING ANALYSIS OPTIMAL DESIGN POINTS FOR 3.1 KW WINDING LOSS LEVEL

Metric	36s/24p (DL)	24s/28p (DL)	24s/28p (SL)
Winding Factor	0.866	0.933	0.966
Power Density [kW/kg]	16.7	15.6	14.7
Tip Speed [m/s]	98.1	93.1	87.1
Shear Stress [kPa]	39.9	35.1	34.6
Current Density [A-rms/mm^2]	24.6	23.8	23.1
Electric Loading [kA-m]	88.8	77.6	75.9
Rotor Diameter [mm]	234.2	222.3	207.9
Core Stack Length [mm]	24.3	30.7	35.6

A brute-force optimization that explored a grid of candidate designs varying key machine dimensions has been carried out to identify designs that minimize the active mass and winding loss for the two DL concentrated-winding machine configurations in Fig. 4.4-3, plus a SL 24s/28p topology for comparison. A grid of design points was generated for ranges of shear stress, tip speed, and current density. The predicted power density vs. winding loss for the best designs are plotted in Fig. 4.4-4 for these 3 machine topologies. Overall, the 36s/24p topology exhibits superior power density compared to the two 24s/28p topologies due to its compact end windings. Similar end winding differences degrade the SL 24s/28p power density relative to the DL 24s/28p configuration, as expected from the initial tradeoff study.

The predicted machine characteristics for an assumed 3.1 kW winding loss are presented in TABLE 4.4-1 for all three machines. In all cases, the power density requirement is met, with the 36s/24p design achieving an estimated power density of 16.7 kW/kg. This 36s/24p design also has the highest target tip-speed (v_{tip} = 98.1 m/s), shear stress (σ_m = 39.9 kPa), and current density (J = 24.6 A-rms/mm^2) compared to the other topologies. All three machines optimize with a large rotor diameter relative to its stack length, resulting in diameter-to-length ratios values in the range between 5.8 to 9.6. Last, the results from TABLE 4.4-1 indicate some potential improvements exist for the baseline design in terms of power density. Specifically, the power density can be increased by 0.6 kW/kg at a 3.1 kW winding loss level.

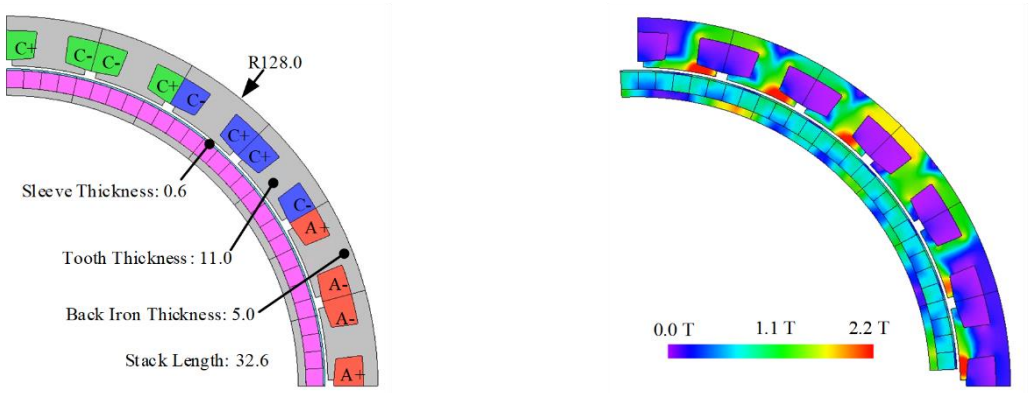

Figure 4.4-5 New modular 24-slot, 28-pole machine design study: machine dimensions and full-load flux density contours of the selected design.

24s-28p DL and SL modular machine designs are selected to exceed the 13.3 kW/kg requirement with minimum winding loss. Models of this modular machines have been analyzed and validated via 2D finite element analysis (FEA) using JMAG Designer. Final dimensions of the DL 24s/28p machine are provided in in Fig. 4.4-5 along with the corresponding full-load flux density contour. A summary of machine performances compared to 36s/24p baseline are shown in TABLE 4.4-2.

First, the results in the table show that the new modular 24s/28p machine has slightly lower average output torque characteristics and marginally higher torque ripple compared to the original baseline 36s/24p machine. Further optimization of the Halbach array magnetization angles and tooth tips geometry will likely make the torque ripple values more comparable for the two machines. Furthermore, this new 24s/28p design has a 17% higher fundamental frequency due to its increased pole count.

TABLE 4.4-2 BASELINE MACHINE DESIGNS COMPARISONS

Criteria	Old Baseline (36S/24P)	New Baseline (24S/28P)
Avg. Torque (N-m)	85.3	84.6
Torque Ripple (N-m pk-pk)	1.4	1.8
Fundamental [Hz]	1600	1866.7
Rotor Core Material	0.35mm VAC S+	0.10mm VAC 48
Core Loss [kW]	0.3 (S), 0.1 (R)	0.3 (S), 0.1 (R)
DC Winding Loss (+ AC) [kW]	2.2 (+ 0.7)	2.0 (+ 0.6)
Power Density [kW/kg] (Goal: 13.3)	16.1	14.6

Next, this 24s/28p design needs to use higher-performance CoFe laminations in the rotor to suppress the rotor core losses to a low level. This is necessary because the airgap MMF of the SPP = 2/7 winding has substantial spatial harmonics compared to the baseline 36s/24p design, which can lead to substantial rotor core losses unless special provisions are made to suppress them. The new baseline 24s/28p machine has ~10% lower winding losses than the original 36s/24p baseline machine.

Finally, the new baseline 24s/28p machine has 9.3% lower power density compared to original baseline 36s/24p design. Increasing the current amplitudes in the 24s/28p machine design to

equalize the winding losses in the two machines would reduce the power density difference between the two machines.

4.4.2. Electromagnetic Isolation Design and Enhancement

The baseline DL 36s/24p and 24s/28p machines have been evaluated using 2D FEA to assess their electromagnetic isolation. Single-phase active magnetic flux contours are provided in Fig. 4.4-6 for scenario where one phase is excited, and magnets are treated as air. Adjacent (non-active) coil flux is compared with the excited phase flux to assess phase isolation. Isolation metric Module Isolation Ratio (*MIR*) metric that is defined in (4.4.1), comparing the mutual coupling λ_m between phases with the self-flux linkage of each individual module λ_s.

$$MIR = \frac{\max(\lambda_m)}{\lambda_s} \tag{4.4.1}$$

The *MIR* can also be expressed as the ratio of mutual *M*, mutual-leakage M_{lkg} and self-inductance *L* components as discussed in Chapter 2.

$$MIR = \frac{M_{lkg} + M}{L} \tag{4.4.2}$$

The DL 36s/24p exhibits *MIR* = 28.0% coupling with adjacent phases compared to 7.5% observed in the DL 24s/28p machine. In both cases, substantial leakage flux is observed through the stator tooth tips. This leakage can be minimized by removing the tooth tips entirely, but this removal reduces the machine inductance and increases its characteristic current, degrading the machine's short-circuit current-limiting capability. In contrast, a SL equivalent of the 24s/28p design exhibits *MIR* <1.0% coupling with adjacent phases.

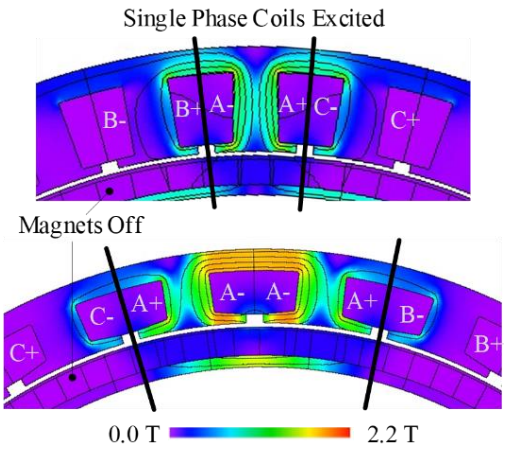

Figure 4.4-6 Comparison of magnetic flux contour maps for 36s/24p DL (top) and 24s/28p DL (bottom) winding configurations with only phase A active.

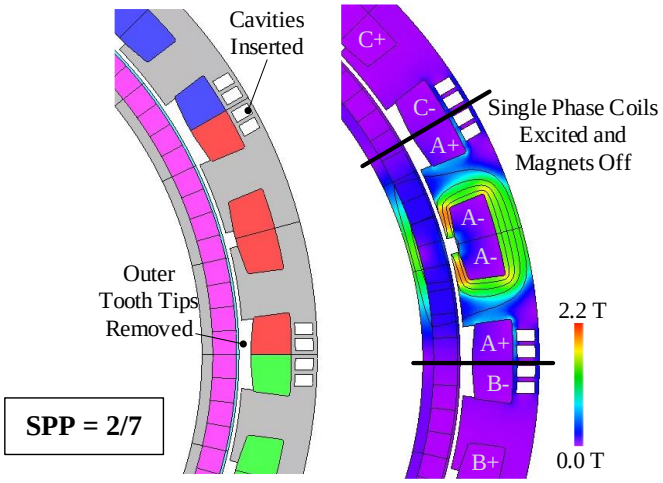

Figure 4.4-7 24s/28s stator configuration using DL windings with added electro-magnetic isolation features and resulting single-phase magnetic flux contour.

TABLE 4.4-3 ISOLATED 24-SLOT 28-POLE PERFORMANCE COMPARISON

Criteria	New Baseline (24S/28P)	Isolated 24S/28P (large cavities)
Avg. Torque (N-m)	84.6	86.7
Torque Ripple (pk-pk N-m)	1.8	2.9
Core Loss [kW]	0.3 (S), 0.1 (R)	
DC Winding Loss (+ AC) [kW]	2.0 (+ 0.6)	
Power Density [kW/kg]	14.6	15.0

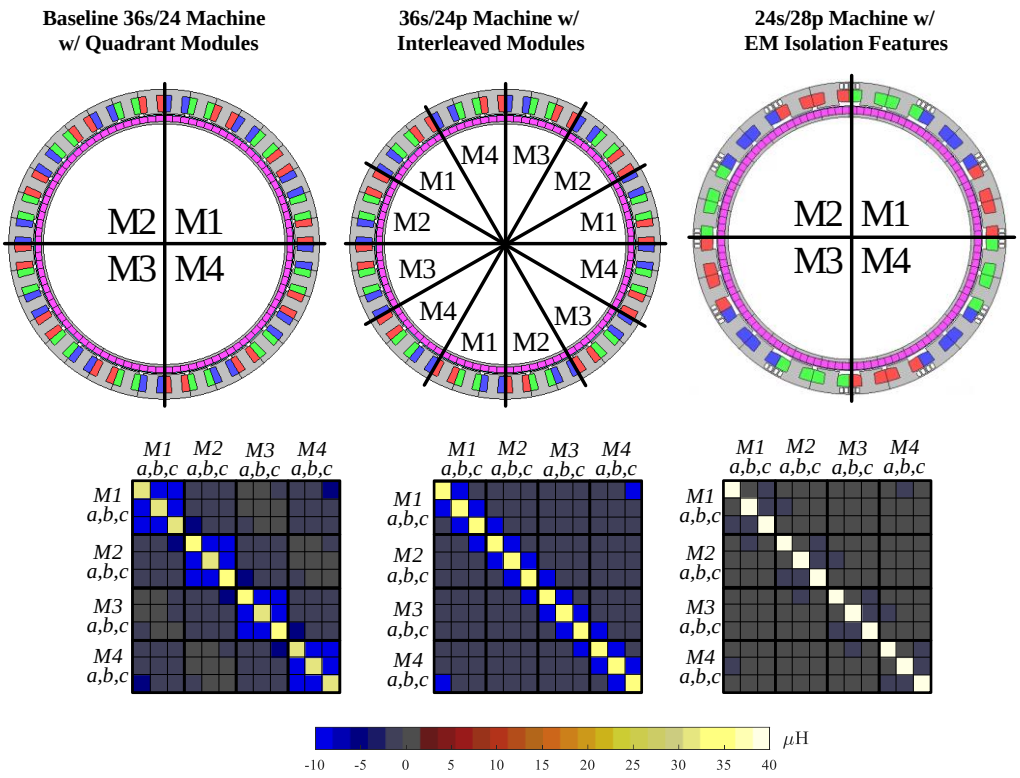

Figure 4.4-8 Quadrant and interleaved four-module machine arrangements and corresponding inductance matrices highlighting coupling between modules.

The DL design can be modified to significantly improve its electromagnetic isolation by removing interphase tooth-tips and inserting cavities in the stator back iron, as shown in Fig. 4.4-7. Applying this isolation approach to the Fig. 4.4-5 DL design reduces phase coupling by 4x to *MIR* = 1.6%. Furthermore, the dimensions of the remaining inner tooth tips can be adjusted to raise the inductance to the values required in FT machines. The resulting machine performance compared to the standard DL design is shown in TABLE 4.4-3.

It is interesting to note that the average torque increases modestly for the two designs with enhanced electromagnetic isolation due to a small flux-focusing effect created by the isolation features. However, the removal of the stator tooth tips caused an increase in torque ripple, which can be suppressed with further design adjustments. Losses for all three designs are nearly identical

due to similar geometries and magnetic saturation levels. Finally, the enhanced-isolation designs have higher power density due to the removal of core material (offsetting the impact of the larger outer radius and back-iron thickness).

4.4.3. Modular Machine Modeling

The impact of electromagnetic isolation on the module performance has been evaluated for the Fig. 4.4-8 arrangements following the methodology described in Chapter 3, which are briefly reintroduced below. These models have been developed to assess magnetic coupling (level of isolation) between modules and the impact of terminal short-circuit faults. The machine equation for a single three-phase module (module-1 below) is defined as

$$\mathbf{v}_{\mathbf{abc1}} = (\mathbf{R}_{\mathbf{11}} + \rho \cdot \mathbf{L}_{\mathbf{11}}) \cdot \mathbf{i}_{\mathbf{abc1}} + \rho \cdot \boldsymbol{\lambda}_{\mathbf{pm}} + \sum_{k=2}^{4} (\mathbf{L}_{\mathbf{1k}} \cdot \rho \cdot \mathbf{i}_{\mathbf{abc,k}}) \tag{4.4.3}$$

where $\boldsymbol{v}_{abc1}$, $\boldsymbol{i}_{abc1}$, and $\boldsymbol{\lambda}_{pm}$ vectors (with dimension 3x1) contain phase voltage, current, and magnet flux linkage vectors. Vector $\boldsymbol{i}_{abc,k}$ refer to currents in module-k phases. Operator ρ signifies the time derivative *d/dt*. The $\mathbf{R}_{11}$ matrix contains phase resistances for module-1 and $\mathbf{L}_{11}$ and $\mathbf{L}_{1k}$ inductance terms belong to the overall machine inductance matrix **L** defined as

$$\mathbf{L} = \begin{bmatrix} \mathbf{L}_{11} & \mathbf{L}_{12} & \mathbf{L}_{13} & \mathbf{L}_{14} \\ \mathbf{L}_{21} & \mathbf{L}_{22} & \mathbf{L}_{23} & \mathbf{L}_{24} \\ \mathbf{L}_{31} & \mathbf{L}_{32} & \mathbf{L}_{33} & \mathbf{L}_{34} \\ \mathbf{L}_{41} & \mathbf{L}_{42} & \mathbf{L}_{43} & \mathbf{L}_{44} \end{bmatrix} \tag{4.4.4}$$

The coupling between modules is defined by the inductance matrix **L** shown in (4.4.3). This matrix consists of n^2 diagonal 3x3 inductance submatrices where $\mathbf{L}_{nn}$ represents each module's internal magnetic coupling, and submatrices $\mathbf{L}_{nm}$ captures the electromagnetic interactions

between module-*n* and module-*m*. These off-diagonal matrices in (4.4.3) are all zero matrices in an ideal machine with zero inter-module electromagnetic coupling.

Like the Chapter 3 demonstration, some phase unbalance is observed in the diagonal $\mathbf{L_{nn}}$ matrices in Fig. 4.4-8, which is attributable to asymmetries in the mutual inductances inside each module caused by the interfaces between adjacent modules. This unbalance is most pronounced in the interleaved 36s/24p machine, and it is significantly smaller for the isolated 24s/28p design.

Next, (4.4.2) has been implemented using MATLAB Simulink to assess the impact of module unbalance and module coupling during a three-phase terminal short-circuit fault in one module. For simplicity, the rotor is assumed to operate at constant speed (8000 rev/min rated speed or 9600 rev/min peak speed). Each healthy machine module is assumed to have an independent synchronous reference-frame current regulator supplying sinusoidal module voltages.

The module arrangements in Fig. 4.4-8 have been simulated for the case of a three-phase terminal short circuit applied to module-2 followed by a three-phase short circuit applied to module-4. Machine currents and voltages are converted to the *dq* synchronous-reference frame using the Park transformation defined as:

$$\begin{bmatrix} f_q \\ f_d \end{bmatrix} = \left(\frac{2}{3}\right) \cdot \begin{bmatrix} \cos(\theta_e) & \cos(\theta_e - 2\pi/3) & \cos(\theta_e + 2\pi/3) \\ \sin(\theta_e) & \sin(\theta_e - 2\pi/3) & \sin(\theta_e + 2\pi/3) \end{bmatrix} \cdot \begin{bmatrix} f_a \\ f_b \\ f_c \end{bmatrix} \tag{4.4.5}$$

where θ_e equals product of electrical frequency and time $\omega_e \cdot t$, and the zero-sequence current component is ignored. Further, magnet flux linkage is assumed aligned with the machine -*d*-axis.

Module-*n* $T_{e,n}$ and total torque T_e is calculated using

$$T_{e,n} = \frac{3 \cdot P}{4} \cdot i_{q,n} \cdot \lambda_{pm,n}$$
$$T_e = T_{e,1} + T_{e,2} + T_{e,3} + T_{e,4} \tag{4.4.6}$$

Healthy module synchronous reference frame *dq*-voltages and *dq*-currents are shown in Fig. 4.4-9 during this fault sequence, along with the faulted module-2 phase current waveforms and total machine torque for the highly-coupled interleaved 36s/24p configuration. Bar-chart plots of the voltage, current, and torque ripple amplitudes for all 3 configurations are presented in Fig. 4.4-10 for three fault conditions. The observed ripple frequency is observed at 2x the electrical frequency. These plots show that ripple amplitudes roughly double when the second fault is introduced, and the ripple amplitudes increase approximately in proportion to the speed increase from 8000 to 9600 rev/min.

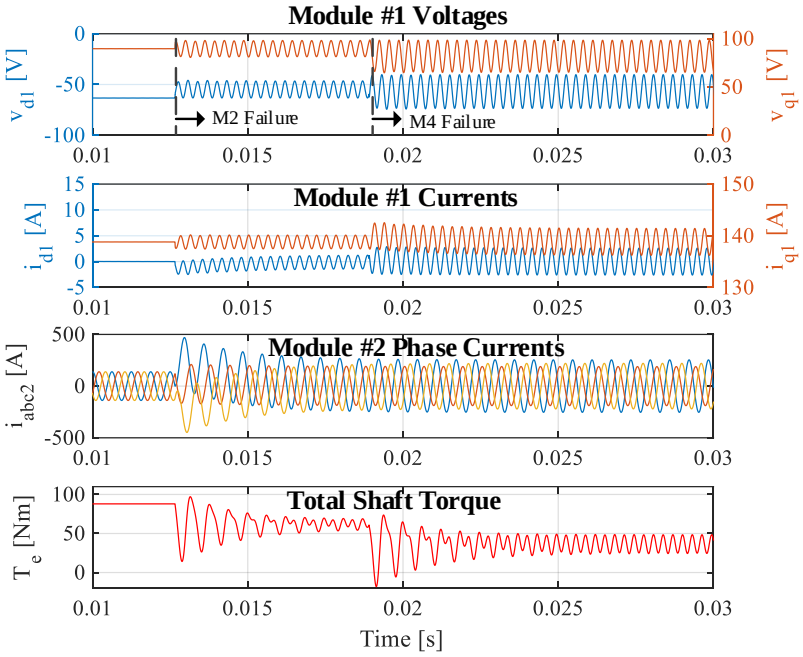

Figure 4.4-9 Module-1 dq-voltages, dq-currents, module-2 phase-currents, and total shaft torque results after 3-phase faults for interleaved 36s/24p design.

Substantial *dq*-ripple current can be observed for both 36s/24p module arrangements, with the interleaved module arrangement most affected by the faults due to the high inter-module coupling. A notable unbalance can be observed in the module-2 short-circuit current waveform, which is attributable to the module's unbalanced mutual inductances noted earlier (i.e., the $\mathbf{L}_{22}$ matrix). In all cases, a large transient torque is observed at the time instant when each three-phase fault is applied, accompanied by a 25% reduction in steady-state torque for each faulted module. A steady-state post-fault torque ripple can be observed, which is attributable to the *q*-axis current ripple. In contrast, the isolated 24s/28p healthy modules are largely unaffected after faults in adjacent modules as indicated by the low ripple in the post-fault *dq* current and voltage waveforms.

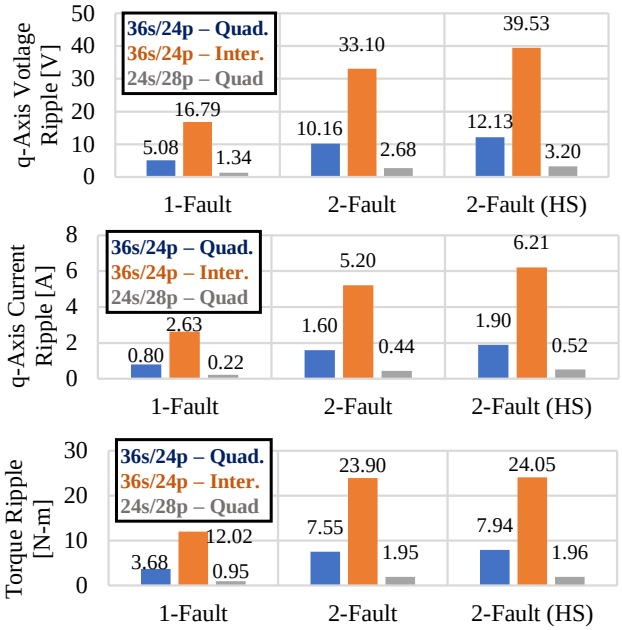

Figure 4.4-10 Healthy module voltage, current, and total torque ripple following module faults at rated 8,000 rev/min and at peak speed 9,600 rev/min (HS).

The SPP=2/7 stator isolation technique in Fig. 4.4-7 provides an appealing alternative approach for achieving high modular electromagnetic isolation with a DL winding configuration without

using spacer teeth. The simulation results show that the negative performance impact of increasing the electromagnetic isolation is substantially diminished using this approach.

4.5. Extended Magnetic Isolation Considerations

The previous sections in this chapter focus on performance tradeoffs for alternative four-module machines topologies and the impact of poor magnetic isolation is demonstrated for the 36S/24P machine design. Further considerations for modular machines are discussed here including stator modularity due to its ideal magnetic isolation and overall metrics for assessing whether additional magnetic isolation features. These features can include the developed modified tooth tip scheme introduced above.

4.5.1. Modular Stator FT Implementation

The implementation of multiple-stators on a common shaft (modular stator topology) has been explored for use in FT applications in [121]–[123]. From a magnetic isolation perspective, this type of approach is ideal as magnetic coupling between stator modules is negligible (*MIR* = 0%) since the FT modules reside in separate packages. Furthermore, this modular stator approach has additional benefits from thermal and electrical isolation standpoints. Other benefits include ability to offset stators to minimize machine cogging. Due to these stated benefits, two-module radial-flux SPM modular-stator designs are examined following a similar methodology (ratings, sizing equation approach, etc.) presented above. Ultimately, the 36s/24p machine is used for the stator modules for this study due to its observed power density benefits, aligning with the results of the previous tradeoff study.

The studied modular-stator structure, optimized dimensions, and full-load flux density contours are provided in Fig. 4.5-1. Full-load performance metrics are shared in Table 5.1-1 along with the

original 36s/24p baseline and proposed 24s/28p isolated design. Overall, the presented dual-stator design realizes higher torque-ripple and similar loss performance metrics compared to the baseline and isolated design.

Focusing on the machine dimensions, the dual-stator has a notably lower tip-speed compared to the unitary designs resulting in a lower-machine diameter and longer stack length. This highlights the primary negative tradeoff associated with a radial-flux modular stator topology: inherent mass and loss penalties associated with 2x the number of end-windings. In this optimization, the rotor diameter is decreased to offset the loss-impact associated with end windings resulting in reduced power density. A modular stator approach would likely find improved competitiveness to a unitary implementation for an axial flux implementation or in situations where the machine overall diameter is constrained.

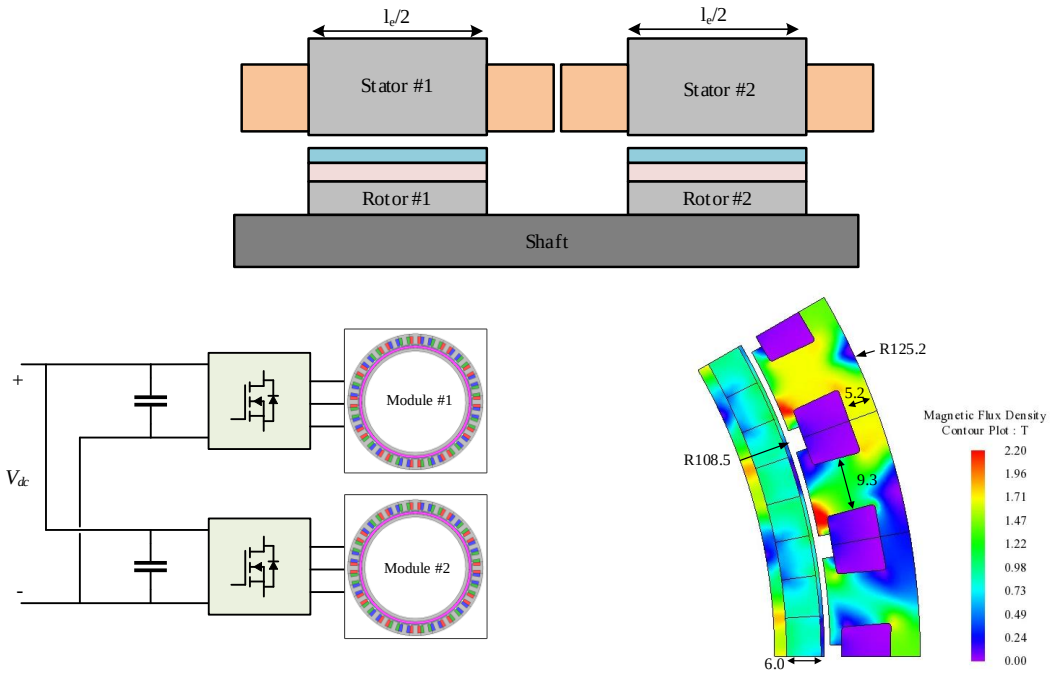

Figure 4.5-1 Dual-stator tradeoff study topology (top), considered modular configuration (bottom left), and dimensions and full load flux density contours (bottom right).

TABLE 4.5-1 DUAL-STATOR FEA RESULTS AGAINST UNITARY BASELINE AND ISOLATED DESIGNS

Metric	36s/24p (Baseline)	24s/28p (Isolated)	36s/24p (Dual)
Power [kW]		70	
Torque Ripple [%]	1.6	3.3	4.8
Core Loss [kW]	0.30 (s)/0.10 (r)	0.30 (s)/0.10 (r)	0.35 (s)/0.10 (r)
DC Winding Loss (+ AC) [kW]	2.2 (+0.7)	2.0 (+0.6)	2.0 (+0.6)
Core Length / Overall Axial Length [mm]	17.6 / 48.3	32.6 / 62.6	41.1 / 83.7
Tip Speed [m/s]	110	110	88.8
Rotor Diameter [mm]	262.6	262.6	217.0
Mass [kg]	4.3	4.7	5.8
Power Density [kW/kg]	16.1	15.0	12.1

4.5.2. Magnetic Isolation Criteria

The impact of magnetic isolation is illustrated in Fig. 4.4-10 for modular isolation techniques with varying levels magnetic isolation based on choice of slot-per-pole-per-phase and selected module integration techniques (concentrated vs. interleaved), resulting in varying levels of current unbalance.

Based on these results and those shared in Chapter 2, this current unbalance is related to:

a. Amount of magnetic coupling between modules and its product to the magnitude of the adjacent module fault current (e.g., $\mathbf{L}_{12}\cdot\mathbf{i}_{abc,k}$ above);
b. Inherent internal mutual-inductance unbalance internal to a module (e.g., inside $\mathbf{L}_{11}$ above) related to level of mutual leakage inductances between module phases
c. Number of contact points between modules and therefor increased leakage paths
d. Machine speed and fundamental operating frequency.

The use of the Modular Isolation Ratio (*MIR*) metric introduced in (4.4.1) and (4.4.2) can be used as a guide to determine whether a modular machine has a reasonable amount of isolation between modules. Following a similar logic to the leakage inductance isolation ratio (*LIIR*)

introduced in Chapter 3, the level of unbalanced current observed is proportionate to the *MIR*. The level of unacceptable unbalanced current is dependent on the user's needs, though is ideally kept below 3% compared to a machine's rated current I_s during a modular fault event with current I_f (likely the characteristic current). This leads to the below criteria

$$MIR \cdot \frac{I_f}{I_s} \cdot 100 < 3\% \tag{4.5.1}$$

The above constraint can be adjusted based on the user's needs. Stricter criteria may be necessary for machines at higher speed where the impact of unbalance is more severe. In some cases, a modular machine without any sort of specialized isolation features may be acceptable due to minimal mutual leakage between modules or low expected fault currents. Borderline cases for the (4.5.1) constraint perhaps can manage current unbalance using closed loop control with unbalanced terminal voltages. In more severe cases a change in topology is required.

4.6. Assessing Slot-Pole Topology Magnetic Isolation

The SL windings has been the natural choice for isolating machine phases as highlighted in the Chapter 2 literature review. However, this comes with a power density penalty as discussed in the tradeoff study above. As suggested in (4.5.1), a small amount of coupling between phases may be acceptable for a modular machine. Several papers in the literature have been published suggesting slot-pole combinations with low-phase interactions [132], [133], [187]. This section proposes a methodology and metrics for investigating these slot-pole topologies and evaluating whether additional isolation features are required. Further, topologies compatible with the flux-barrier and modified tooth tip design are discussed.

4.6.1. Evaluating Magnetic Isolation Capability of Modular Stators

Numerous slot-pole combinations exist for three-phase (or multi-phase) FSCW designs [188]. A subset of these can be considered modular if the stator can be divided into multiple three-phase winding sets or modules. A further reduced subset is suitable for FT modular motor drives due to inherent low magnetic isolation between phases. A methodology for accessing different types of slot-pole combinations is presented which can be applied to different modularity implementations using winding functions.

Winding functions are a spatial description of stator winding turns around the stator and their associated mmf. These are often used in the determination of the synchronous and harmonic inductance components of electric machines [189], and as such will be a useful tool for determining magnetic interactions between phases and modules. Example FSCW machines (SPP = 1/2, 3/8, 4/11) and their associated three-phase winding functions ($N_a(\theta)$, $N_b(\theta)$, $N_c(\theta)$) are provided in Fig. 4.6-1.

The mutual inductance isolation ratio (*MIIR*), introduced in Chapter 2 as the ratio of non-leakage mutual-inductance *M* and self-inductance *L*, can be directly calculated from these winding functions:

$$MIIR = \frac{M}{L} = \frac{\int N_a(\theta) \cdot N_b(\theta) d\theta}{\int N_a(\theta)^2 d\theta} \tag{4.6.1}$$

The MIIR metric is calculated for the Fig. 4.6-1 topologies: the SPP=1/2 topology has a *MIIR* value of 0.5. This high *MIIR* ratio is consistent with previous observations in the above tradeoff study. Next, the SPP=3/8 topology has an *MIIR* value of 0.0385 indicating reasonably low coupling between phases and a good candidate for two-module applications where perfect isolation isn't

required. The final SPP = 4/11 topology has ideal isolation characteristics with an *MIIR* equal 0. The shown 24s/22p combination is suitable for a four-module stator, though the concentration of phases does complicate the phase connections. This SPP = 4/11 topology is in the same class of machine as the previously studied SPP=2/7 and SPP=2/5 which share an *MIIR* metric of 0.

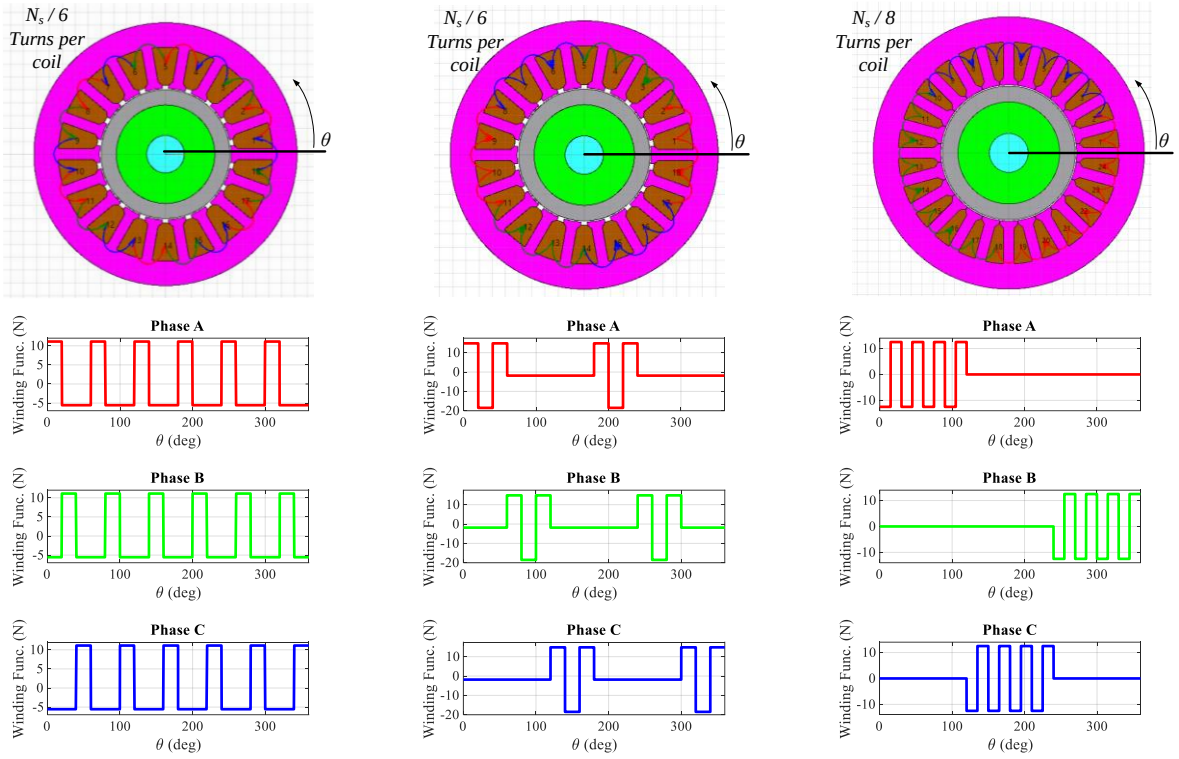

Figure 4.6-1 Candidate modular FSCW stators and their associated phase winding functions assuming 100 series turns per phase (N_s = 100): (a) 18s/12p, SPP=0.5, *MIIR*=0.5; (b) 18s/16p, SPP=3/8, *MIIR*=0.0385; and (c) 24s/22p, SPP=4/1, *MIIR*=0.

The *MIIR* calculation in (4.6.1) considers all of the stator phase coils in its calculations and can be further tailored to consider winding functions for individual module coils (i.e., winding N_{a1} for module-1 phase-a, etc.), which could yield different *MIIR* results depending on the phase coil distribution than what is shared in Fig. 4.6-1. For example, consider a two-module SL 12s/14p topology winding functions in Fig. 4.6-2.

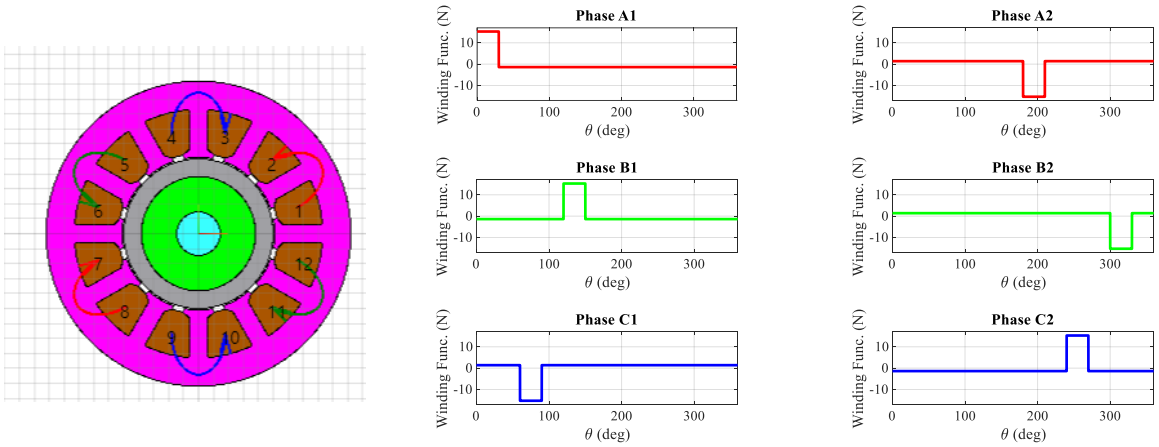

Figure 4.6-2 Two module single-layer 12s/14p (SPP=2/7) stator and its associated winding factors (assuming 17 turns per coil) based on module coil groupings. This topology achieves an *MIIR* of 0.091 indicating imperfect isolation.

The SL 12s/14p non-modular *MIIR* metric is 0, which is commonly why this SL configuration considered fully magnetically isolated. However, repeating the *MIIR* calculation by separating winding functions by modularity like Fig. 4.6-2, then the *MIIR* metric increases to 0.091. While still a low number, this highlights a misconception that SL windings have superior magnetic isolation characteristics. The SL winding still has isolation advantages as it does not have the unbalanced mutual flux linkage observed in the other DL FT topologies.

A limiting omission of the *MIIR* metric is the impact of the slot-leakage inductance that plays a substantial role in the observed unbalance in the above trade-study and the Chapter 2 demonstration. This leakage has an even larger role for DL SPM machines that have large electromagnetic airgap, lowering the associated synchronous inductance relative to slot-geometry related leakage components. Further leakage concerns exist for interleaved module configurations, increasing points of contacts and number of leakage paths between modules. Analytical estimates of leakage inductance can be determined using [177], and can be used to in the more comprehensive module isolation metric *MIR* (not to be confused with the *MIIR* metric above) that

includes leakage. In any case, the *MIIR* metric is useful in identifying candidate isolated machines for FT modular designs.

4.6.2. Slot-Pole Combinations Compatible with Proposed Enhanced Isolation Features

Removing features like tooth tips or magnetic wedges will alleviate mutual-leakage concerns somewhat, though at the direct consequence of a loss of a valuable inductance component in a FT machine. Concerns for DL winding mutual-leakage can be reduced by employing the suggested enhanced isolation strategy of modified tooth-tips and stator flux barriers like those shown in Fig. 4.4-7, giving the machine designer another handle for achieving the necessary inductance to limit fault currents.

Critical for the implementation of these isolation features is the selection of compatible slot-pole combinations. Specifically, the identified slot-pole combination must have anti-periodic adjacent phase-coils resulting in inherent closed loop flux characteristics highlighted in Fig. 4.4-2. This allows for isolation features to be placed between coils without interrupting the phase flux path. This characteristic is most apparent the 2/5 and 2/7 SPP families as identified in the tradeoff study. However, this characteristic can be found in other SPP families like the SPP=4/11 shown in Fig. 4.6-1. The SPP=4/11 family is unique in that it concentrates phase groups in 120° sectors, forcing the designer interleave module coils.

Last, variants of the proposed isolation scheme can be applied the SPP=3/8 family shown in 4.6-1. This group of slot-pole combinations is not inherently isolated (*MIIR* = 0.0385) though possess the antiperiodic winding pattern necessary for the implementation of flux barriers between

phases. These flux barriers and modified tooth tips can be applied to groups of three phase coils compared to only two in the 2/5 and 2/7 SPP families.

4.7. Chapter Summary

This chapter has presented key results of a tradeoff study of fault-tolerant modular machines for a UAM aircraft that requires machine power rating of 70 kW at 8,000 rev/min. The proposed fault tolerance approach divides the machine and power electronics into four three-phase modules that is designed for continued operation after the loss of one or more modules.

This tradeoff study compares various modular machine designs against a power-dense conventional double-layer (DL) winding configuration to evaluate the impact of alternative FT approaches. The study results show that the introduction of conventional FT isolation features degrades the machine power density and losses compared to a baseline machine design without the FT features. Results are presented for an investigation of alternative electromagnetic isolation concepts that require minimal performance sacrifice. Based on these results, a promising approach that introduces stator yoke cavities and modified tooth tips is proposed for a four-module 24-slot, 28-pole fractional-slot concentrated-winding (FSCW) machine. Simulations of the proposed machine configuration demonstrate effective electromagnetic isolation of the machine modules under demanding operating conditions, including a short-circuit event in an adjacent module that is particularly challenging for FT machines.

An analytical module-level model has been developed to evaluate the performance impact of electromagnetic coupling. Faults were applied to one and two modules, resulting in substantial current and torque ripple in the poorly-isolated 36s/24p baseline design. This ripple worsened in the interleaved module arrangement due to its higher electromagnetic coupling between modules.

In contrast, the healthy modules in the highly-isolated 24s/28p design are largely unaffected by adjacent module failures, confirming the appealing fault-tolerant performance characteristics of this machine topology.

The nuances of FT electromagnetic isolation are discussed including the presentation of the Modular Isolation Ratio (*MIR*), a measure of the level of unbalanced coupling between modules, and the Mutual Inductance Isolation Ratio (*MIIR*) which is a measure of mutual synchronous coupling between modules. These metrics are used to define criteria for assessing acceptable levels of electromagnetic coupling between modules for expected fault currents. A calculation method for the *MIIR* metric using winding functions has been presented, enabling further differentiation of modular stator SPP combinations. Finally, guidelines for identifying compatible slot-pole combinations with the proposed enhanced isolation techniques are shared, together with examples including the SPP=4/11 and SPP=3/8 families.

Chapter 5

Fault-Tolerant IMD Design Analysis for a Six-Passenger Quadcopter

The enhanced electromagnetic isolation scheme on the 24-slot 28-pole machine described in Chapter 4 has been expanded to consider machine thermal, structural, and fault-mode performance characteristics for a quadrotor machine. As a result, the physical and thermal isolation characteristics have been enhanced by appropriately choosing the cooling approach and slot materials. An iterative design approach was used as described in Fig. 5.1-1, and the final electromagnetic, thermal, and mechanical performance predictions are presented in this chapter. This performance evaluation extends to considering both healthy and faulted operating conditions. This machine has been for designed for an IMMD configuration and the design of the modular power electronics is also described in this chapter. The results of this analysis will be used as inputs into a reliability study in Chapter 6.

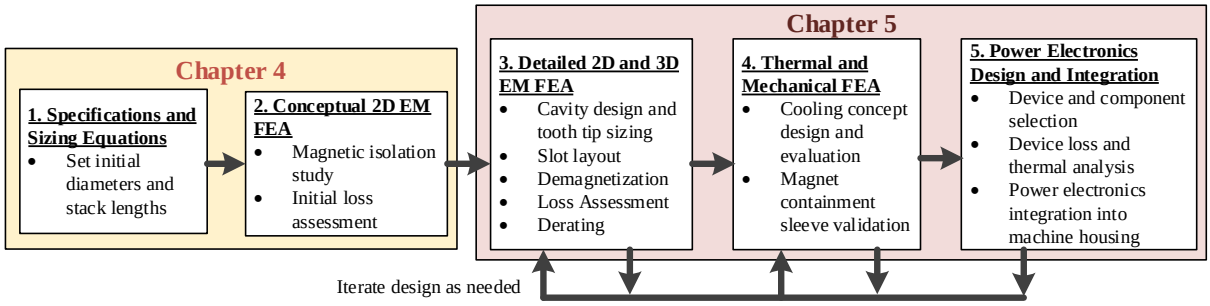

Figure 5.1-1 Quadrotor electric machine and power electronics design process.

5.1. Electromagnetic Design and Analysis

In the previous chapter, a 24s/28p machine design is presented as a possible candidate for a Vertical Takeoff and Landing (VTOL) quadrotor application due to its minimal electromagnetic isolation between phases and high-power density. This machine concept design is further

developed following the design process described in Fig. 5.1-1. Initial design steps related to machine sizing and core isolation concept details are provided in Chapter 4. This section focuses on the finalized electromagnetic design shown in Fig. 5.1-2 and the corresponding loss analysis.

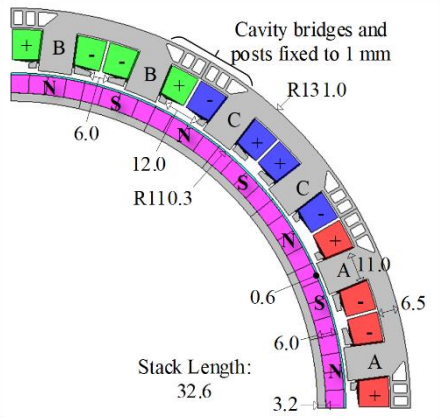

Figure 5.1-2 Final single-module stator design for FT 24s/28p machine with magnetic enhanced isolation.

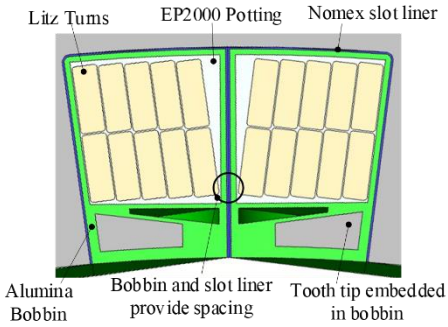

Figure 5.1-3 Stator slot design incorporating a bobbin design with in-slot cooling channel and embedded stator teeth.

High-performance materials are required to reach the target power density and efficiency values. The proposed machine with a power rating of 70 kW at 8000 rpm uses CoFe VAC 48 laminations for the rotor and stator. The rotor magnets use SmCo Recoma 35E, which are segmented into 1 mm laminations. The segments are magnetized in a Halbach array to minimize the rotor core material. The magnetization angle of each Halbach segment is set to maximize the average torque and minimize torque ripple. Each stator coil uses 10 turns of rectangular litz wire (Fig. 5.1-3) to minimize the ac losses.

The proposed machine achieves an active mass power density of 14.1 kW/kg, exceeding the power density target by 0.8 kW/kg. The stator core mass dominates overall, contributing 2.2 kg to the active mass. Further optimization of machine cavities can likely reduce this mass. Stator

windings contribute 1.3 kg excluding insulating materials. Rotor component masses are minimal with 1.1 kg of magnets, 0.5 kg of rotor core material, and 0.03 kg for the carbon fiber sleeve.

The machine is designed to continue operating after the loss of a single module. Full torque can be restored by increasing the current in the healthy module by approx. 33%. The machine is derated to compensate for the increased current after a fault event, penalizing the expected power density by 0.3 kW/kg. Providing this margin requires reducing the target current density for healthy operation and accepting smaller thermal margins during a fault event. FT machine performance will be discussed in detail later in this section.

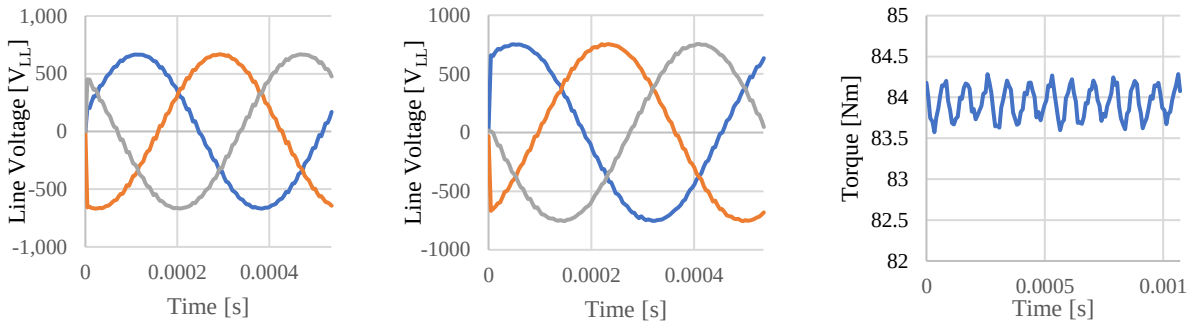

(a) **(b)** **(c)**

Figure 5.1-4 Three-phase machine voltage and torque waveforms generated from 3D FEA using sinusoidal current excitation: (a) no-load (back-emf) line-to-line voltages at rated speed (i.e., zero current); (b) full-load line-to-line voltage waveforms at rated speed; and (c) full-load torque waveform with sinusoidal current excitation.

5.1.1. Performance Characteristics and Loss Analysis

The proposed quadrotor machine performance and losses have been estimated using JMAG Designer 3D electromagnetic FEA. Machine voltage and torque characteristics are given in Fig. 5.1-4. A sinusoidal back-emf waveform is achieved via selection of the rotor magnetization and

tooth tip design. Full-load voltage waveforms are provided in Fig. 5.1-4 and corresponds to a total dc bus voltage of 750V, which is less than the maximum 800V requirement given in Chapter 3. The full-load torque waveform is also provided in Fig. 5.1-4, indicating less than 1 N-m of peak-to-peak torque ripple (~ 1%) with sinusoidal current excitation.

5.1.1.1. Core Losses

Full-load flux density and core loss density contours are provided in Fig. 5.1-5. Significant saturation is observed in the stator cavity section. Similarly, end effects result in stator and rotor core saturation at the two ends of the machine core. This increased saturation contributes to the highest observed loss value in the Fig. 5.1-5 loss contours. The calculated total stator core loss is 440 W, with substantial losses resulting from cavity saturation. Geometric optimization or removal of these cavities can directly reduce machine core loss. A total rotor core loss of 80 W is observed, with significant losses located at the ends of the machine.

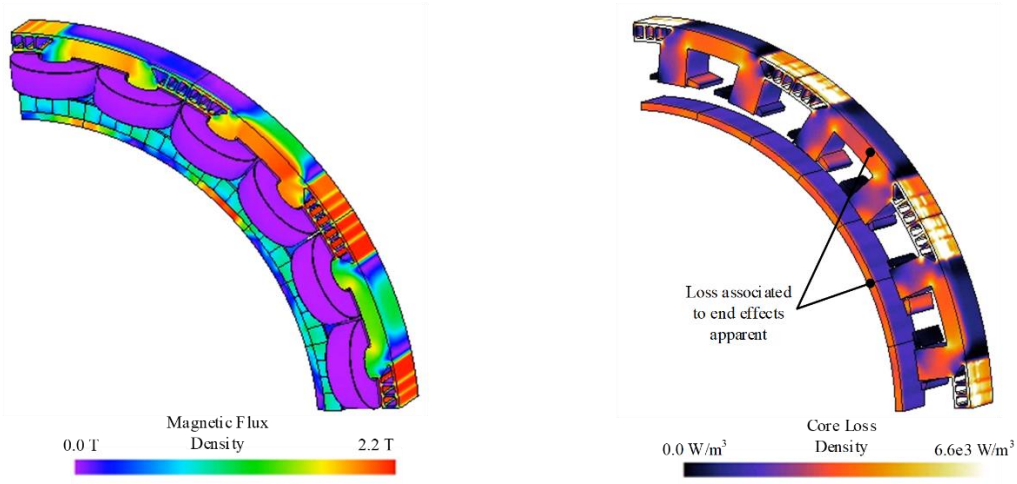

Figure 5.1-5 Full-load 3D electromagnetic FEA results.

5.1.1.2. Sleeve Loss Modeling

A carbon fiber sleeve with 0.6 mm thickness is used for magnet containment based on the Chapter 4 sizing analysis. Sleeve and magnet losses have also been estimated using 3D FEA.

Specifically, the carbon fiber sleeve material is modeled with anisotropic electrical conductivities as described in [190], [191]. These electrical conductivities can be modeled using cylindrical coordinates defined in Fig. 5.1-6(a). Conductivities σ_z, σ_θ and σ_r are dependent on the direction of the fiber, the fiber material conductivity, and the fiber volume fraction. For many SPM machines like the Fig. 5.1-6(a) example, the carbon fibers are wrapped in the hoop direction as defined in Fig. 5.1-6(b). There may be instances where fibers are oriented in both hoop and axial directions as shown in Fig. 5.1-6(c), which requires a more complex derivation of conductivities.

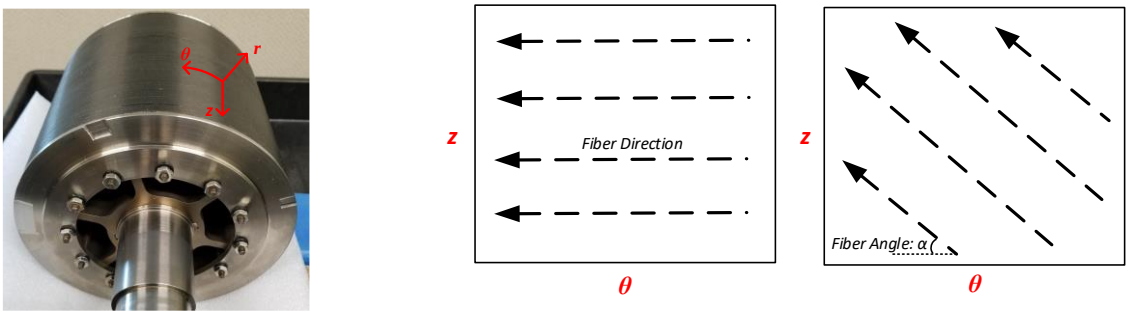

(a) (b) (c)

Figure 5.1-6 Carbon fiber sleeve containment loss modeling: (a) sleeve coordinate system on example rotor; (b) rolled out carbon fiber sleeve with fiber direction in the hoop direction; and (c) rolled out carbon fiber sleeve with sleeve fibers oriented in direction α.

For a hoop wound sleeve, the hoop direction conductivity σ_θ is directly calculated from the carbon fiber conductivity σ_{cf} and the fiber volume fraction k_{cf}. The axial direction conductivity σ_z is proportionate to the hoop conductivity by factor β, which is typically less than 0.1. Last, the radial conductivity σ_r approximates the axial conductivity and can be treated as equal for initial analyses:

$$\begin{Bmatrix} \sigma_\theta = k_{cf} \cdot \sigma_{cf} \\ \sigma_z = \beta \cdot \sigma_\theta \\ \sigma_r \simeq \sigma_z \end{Bmatrix} \tag{5.1.1}$$

A hoop conductivity of 33,000 S/m and axial conductivity of 3,300 S/m is used for the sleeve loss simulation assuming a Toray T300 tow. Due to difficulties to model anisotropic materials in the simulation software, the radial conductivity is assigned equal to hoop conductivity for this loss calculation. This corresponds to eddy current losses of 11.1 W for no-load operation and 22.8 W for full-load operation. Full-load sleeve loss density contours are shown in Fig. 5.1-7.

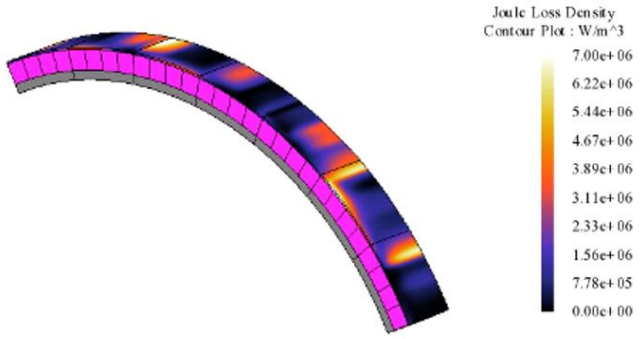

Figure 5.1-7 Sleeve loss density contours at full load condition.

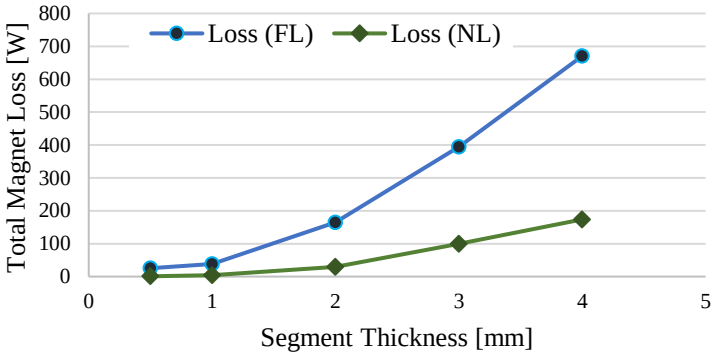

Figure 5.1-8 Full-load and no-load magnet eddy current loss depending on magnet segmentation thickness.

5.1.1.3. Magnet Losses

Next, magnet losses were estimated by modeling a single magnet segment with specified thickness in the axial direction and then extrapolating to the full machine stack length. Predicted magnet no-load and full-load eddy current losses vs. segment thickness are plotted in Fig. 5.1-8.

As expected, magnet losses decrease with lower segment thickness, although a point of diminishing returns appears at the low end of the thickness range. The greatest magnet loss density occurs at the magnet outer radius, near the stator slot openings. A segment thickness of 1.0 mm has been selected corresponding to full-load magnet loss of 38 W.

5.1.1.4. Winding Losses

Analytical equations are used to estimate the dc and ac winding losses. Module-phase dc resistance R_s is calculated using (5.1.2), with coil cross-section area A_{coil} taken from the FEA model, average turn length l_c estimated from the stator geometry, and the selected number of turns n_c per coil. The copper fill factor k_{cu} is estimated from the slot layout in Fig. 5.1-3. A litz wire copper fill factors of 65% and litz length multipliers k_{llm} of 1.3 (capturing the additional strand length from wire transposition) are based on quotes from a litz wire manufacturer. The copper resistivity ρ_{cu} assumes a full-load operating temperature of 156 ºC. A module dc resistance of 0.0192 Ω is estimated corresponding to a total dc winding loss of 1.83 kW.

$$R_s = \frac{2 \cdot \rho_{cu} \cdot n_c^2 \cdot k_{llm} \cdot l_c}{k_{cu} \cdot A_{coil}} \tag{5.1.2}$$

The tradeoff study in Chapter 4 assumed a 30% ac loss factor to capture skin and proximity effects associated with the machine's high operating frequency. This is likely a conservative estimate and is reevaluated for the final machine design. Litz wire eddy current loss estimates have been published for transformers in [192] and have been applied to electrical machine litz wire in [193]. A similar approach is applied here to estimate the impact of ac losses, with the turn eddy current loss $P_{turn,ac}$ estimated in (5.1.3).

$$P_{turn,ac} = \frac{\pi \cdot \omega_e^2 \cdot \bar{\hat{B}}^2 \cdot d_s^4 \cdot n_s \cdot k_{llm} \cdot l_s}{128 \cdot \rho_{cu}} \tag{5.1.3}$$

This formula assumes that each rectangular litz turn consists of n_s strands with diameters d_s. It is also assumed that the greatest eddy current losses occurs inside the slot (due to the rotating airgap magnetic flux), so the average strand length per turn l_s is equal to twice the machine stack length l_e. An upper bound on eddy current loss can be estimated by assuming that the peak flux ($\hat{B}$) through the turn strands equals the peak airgap flux density B_{g1} (i.e., 0.9 T).

A range of wire sizes is considered with estimated AC losses shown in TABLE 5.1-1. Selecting a litz wire with strand size of 32 AWG corresponds to a total eddy current loss of 470 W (to be rounded to 500 W for additional ac loss margin). This corresponds to an updated ac loss factor of 27.3% for a 500 W ac loss value.

TABLE 5.1-1 STATOR WINDING AC LOSS ESTIMATION FOR VARYING STRAND SIZES

Strand Gauge	d_s [mm]	Area/strand [mm^2]	n (approx.) per turn	Total Loss [W]
30	0.254	0.0507	82	733
32	0.2032	0.0324	128	470
34	0.16002	0.0201	207	291

5.1.1.5. Windage Loss Estimation

A common concern for high-speed machines is windage loss which can drastically affect the machine efficiency and thermal performance. (5.1.4) provides an estimate for airgap windage loss (P_{wind}) caused by the relative motion between the stator and rotor ignoring axial airflow in gap [194].

$$P_{wind} = C_f \cdot \pi \cdot \rho \cdot l_e \cdot D_{is} / 2 \tag{5.1.4}$$

Variables in (5.1.4) not previously encountered include the rotor skin friction coefficient C_f and air density ρ. An important assumption in this calculation is that the carbon fiber sleeve can be modeled as a smooth cylindrical surface, resulting in a significant reduction in the windage loss,

even if the stator bore is not perfectly smooth because of the stator teeth. The resulting windage loss is calculated to be 50 W at ground level. More advanced calculation methods and simulation may be needed depending on the choice of the machine cooling (e.g. forced axial airflow through the gap, etc.).

A summary of healthy full-load performance metrics are provided in TABLE 5.1-2. The machine power density and efficiency meet the quadrotor requirements defined in Chapter 4. Overall, winding loss is the largest loss contributor to the machine, which is a direct consequence of the aggressive power density target. Furthermore, elevated stator core loss is observed due to the saturated stator cavities.

TABLE 5.1-2 FINAL QUADROTOR MACHINE PERFORMANCE PREDICTIONS DURING FULL-LOAD (70 KW, 8000 RPM) OPERATION

Spec.	Value	Units
Torque	83.8	Nm
Active Mass Power Density	14.1	kW/kg
Winding Loss	2.33	kW
Stator Core Loss	0.44	kW
Rotor Core Loss	0.08	kW
Magnet Loss	0.04	kW
Sleeve Loss	0.02	kW
Est. Windage	0.05	kW
Efficiency	96.0	%

5.1.2. Tooth Tip Sizing and Inductance Calculation

The proposed machine exhibits the FT machine characteristics described in Chapter 4. Limiting the machine's short-circuit current by increasing the stator inductance is critical for achieving fault tolerance. Standard techniques for calculating FSCW machine inductance can be applied to estimate these quantities analytically [177]. The machine interphase tooth tips are sized to produce enough inductance to limit the 3-phase steady-state fault currents to less than 133% (i.e., 4/3rds)

of the rated current. This level of current corresponds to the expected overload condition on a healthy module after a fault, which falls within the capability of the developed stator cooling.

Manipulating the inner-most tooth tips is the primary means of increasing the stator slot leakage, though substantial inductance contribution comes from leakage associated with the end windings. This contribution is estimated in 3D FEA by varying the core stack length and extrapolating the machine inductance for a 0 mm core length (end windings only). This is shown in Fig. 5.1-9, where a 41.6 µH leakage contribution is expected for the machine inductance.

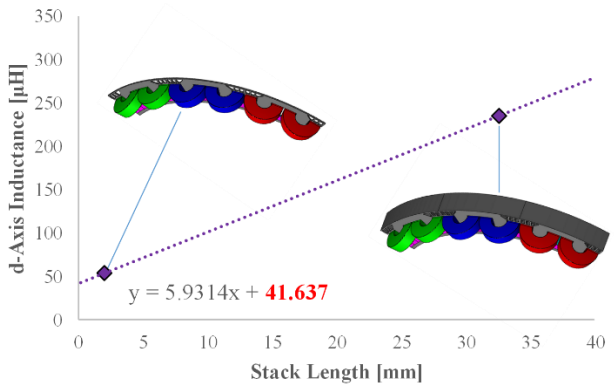

Figure 5.1-9 End winding leakage inductance FEA estimation of an earlier design iteration considering machine stack lengths of 32.3 and 2.0 mm.

With the impact of the end effect leakage defined, the remaining machine leakage inductance is set using the inner most tooth tips. This analysis also considers the impact of the tooth tips on the machine torque performance. This is highlighted in Fig. 5.1-10 where different machine average torques are shown for varying tooth tip gap thickness. The torque capability of the machine is reduced as the gap between the tooth tips closes, though a similar trend is observed for a complete removal of tooth tips. A tooth tip gap of 6 mm is selected to meet the inductance requirement of the machine, while also maintaining the torque performance of this machine. For this torque reason, a small stub tooth is added between machine phases as shown in Fig. 5.1-2.

Final tooth tip geometries are shown in Fig. 5.1-10, where the developed design achieves a total *d*-axis inductance of 197 μH during light-load conditions. Finally, each machine module is effectively isolated due to the stator core cavities and removed stator tooth tips, resulting in a low Module Isolation Ratio (*MIR*) value of 2.7%.

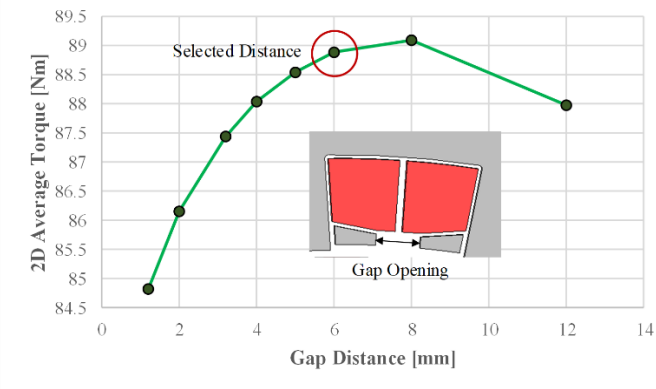

Figure 5.1-10 Inner-most tooth tip sizing analysis and impact on torque.

5.1.3. Slot Design and Electrostatic Analysis

The selected stator slot materials serve many roles in the overall machine design. At a minimum, these materials must provide voltage standoff capability to minimize the possibility of phase-to-ground, phase-to-phase, and turn-to-turn faults. Furthermore, these materials also play a vital role in the thermal design of the machine. Importantly for this FT modular machine, the selected materials need to support the FT design objectives, providing spacing between module coils and assisting with module thermal isolation.

5.1.3.1. Slot Materials and Layout

The basic layout of the slot is shown in Fig. 4-3. Materials to be selected include the strand insulation of the litz wire, a slot liner wrapped around the coil, a 3D printed ceramic structure, and potting material. A survey of materials was completed, with final material candidates summarized

in TABLE 5.1-3. Many of the material properties are taken from [104] and the material properties of CoorsTek ceramic consisting of 94% to 97% alumina have been assumed for the ceramic bobbin.

TABLE 5.1-3 QUADROTOR MACHINE SELECTED SLOT MATERIAL PROPERTIES

Function	Material	Max. Temp [ºC]	Dielectric Strength [kV/mm]	Therm. Cond. [W/m-K]	Viscosity [cps]	Relative Perm. (ε_r) [Unitless]
Strand Insulation	Polyester Amide-Imide	200	170	0.26 – 0.5	-	3.9
Slot Liner	Nomex 410	210	25	0.139	-	1.6
Ceramic Bobbin	CoorsTek Alumina	1200 - 1800	8.3 – 8.7	15 - 27	-	9.3
Potting	Lord EP2000	204	18.5	1.9	1300	3.6

Overall, the materials were selected to provide an insulation system rated at 200 ºC. Both the slot liner and alumina bobbin serve to standoff the coil voltage from the grounded stator. Additionally, these components provide physical separation between module coils and assist with the module thermal isolation by acting as a thermal barrier between coils. Furthermore, the alumina bobbin contains cooling channels allowing for direct cooling of the stator windings. A potting material with high thermal conductivity is used to assist the coil cooling and to prevent adjacent coils from rubbing due to vibration. Additionally, this potting assists with winding partial discharge mitigation during high-altitude operation by filling all winding voids.

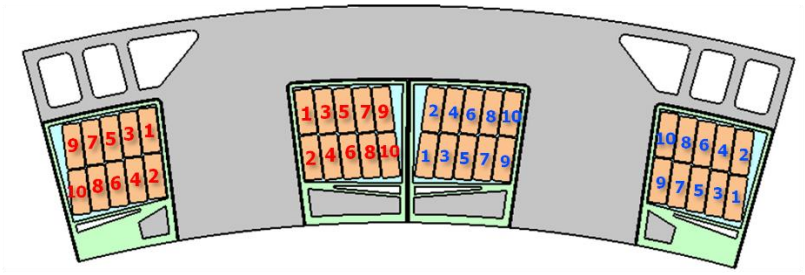

(a)

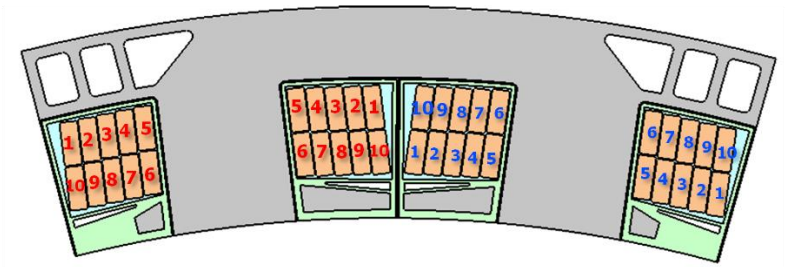

(b)

Figure 5.1-11 Possible winding arrangements for the proposed machine: (a) winding #1 and (b) winding #2.

5.1.3.2. Electrostatic Analysis

The choice of the winding layout can have a substantial impact on the manufacturability, end winding bulk, and operating voltage stress. Two phase winding layouts are considered for the proposed machine, as shown in Fig. 5.1-11. The first winding pattern (Fig. 5.1-11(a)) begins with the first coil-turn nearest the stator tooth, and winds outward, crossing over between the upper and lower layers after each turn. The second winding pattern (Fig. 5.1-11(b)) consists of upper and lower layer windings that crossover only once where the two innermost turns meet (#5-#6). This tooth-winding method is more complicated from a fabrication standpoint, although it produces a more compact end winding with many fewer crossovers between layers.

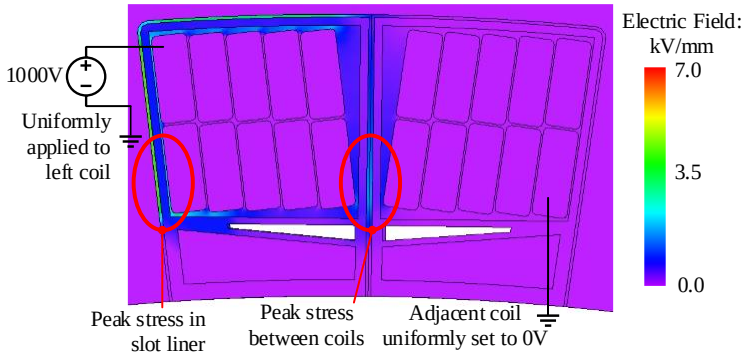

Figure 5.1- 12 Color contours showing phase-to-ground and phase-to-phase electric field stress predicted by electrostatic FEA.

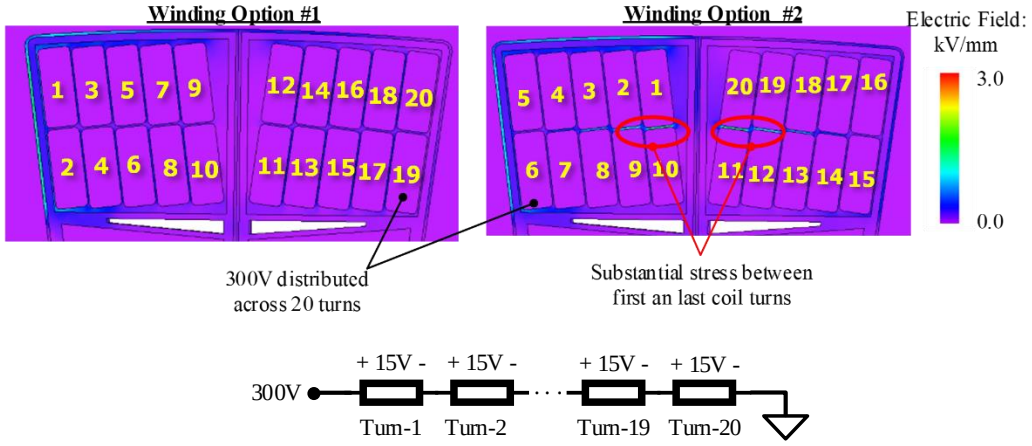

Figure 5.1-13 Color contours for two winding options showing turn-to-turn electric field stress predicted by electrostatic FEA results (above) and voltage distribution (below).

Each winding configuration has been implemented in JMAG electrostatic FEA to evaluate the expected material voltage stress using the material properties in TABLE 5.1-3. For simplicity, the complex litz turn geometry is treated as a solid conductor. Phase-to-ground and phase-to-phase insulation stress has been evaluated by applying 1000V to all of the turns in one coil and grounding the other coil and the stator core, with predicted stress results shown using color contours in Fig. 5.1-12. A peak electric field stress of 6.4 kV/mm is observed in the slot liner near the core which

is substantially lower than the liner material's rated dielectric strength. A similar peak field stress is observed in the slot liner between coils which is again well below the liner material's limits.

The turn-to-turn electric field stress was evaluated by distributing 300V (approximately one machine module) across the turns in accordance with the winding patterns in Fig. 5.1-11. Predicted electric field stress results are shown in Fig. 5.1-13. Overall, the predicted electric field stresses between turns are substantially less than the potting material's dielectric strength limit for both winding methodologies. However, the second winding approach results in substantial field stress the between the first and last winding turns that are separated by the full winding potential of 300 V in this FEA analysis. It should be noted the even voltage distribution described in the Fig. 5.1-13 circuit is for a steady state situation, and uneven turn voltages can be expected related to the *dv/dt* of the PWM pulse.

5.2. Thermal Design and Analysis

Two self-contained liquid cooling approaches have been evaluated to cool the stator to acceptable limits. Motivations for this type of cooling approach are discussed in Chapter 4.2. The first takes advantage of thermally-conducting potting material, creating a thermal bridge from the machine end windings to the stator housing cylinder that contains cooling channels on its outer surface as shown in Fig. 5.2-1. The second approach uses cooling channels designed into the stator tooth winding bobbin, as illustrated in Fig. 5.2-1 and 5.2-2. The channels embedded in the bobbin encircle the entire coil, including the end windings as shown in 5.2-2.

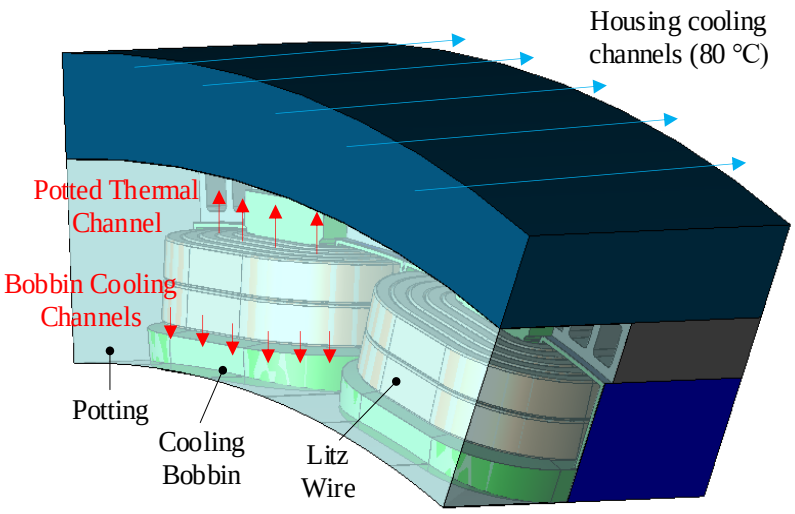

Figure 5.2-1 Stator cooling approach using housing channels and in-slot cooling channels in the winding bobbin.

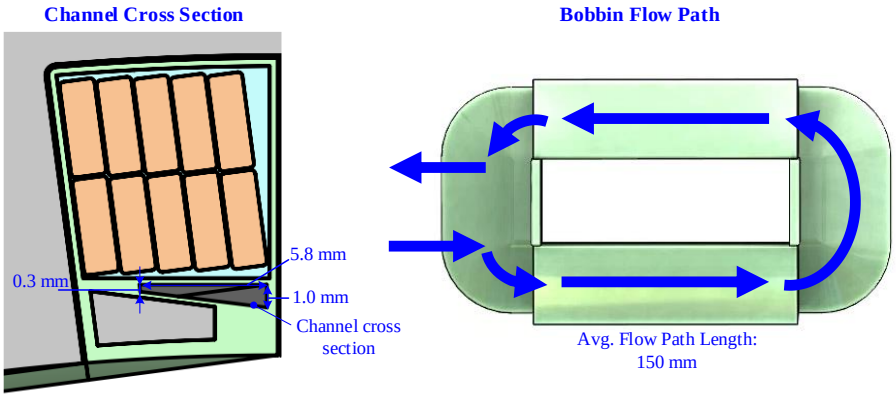

Figure 5.2-2 Winding cooling bobbin channel dimensions and flow path.

The bobbin is assumed to be 3D-printed alumina, which has been shown to be capable of effective in-slot cooling [110]. The bobbin also plays a role in the slot layout, surrounding the coil cross-section inside the slot as shown in the simplified Fig. 5.2-2 slot drawing. In an actual implementation, one of the sides of this casing will need to be removable in order to form the winding. Using this approach, the bobbin assists with coil physical separation, winding cooling, and thermal isolation between windings. The stator tooth-tips are embedded in the bobbins as

shown in Fig. 5.2-2 to simplify the bobbin installation process. If the use of separated tooth tips is not feasible, alternative magnetic materials such as magnetic wedges can be used to achieve the same electromagnetic effect.

JMAG Designer 3D thermal FEA software was used to assess the stator thermal performance including these bobbins. Heat transfer coefficients have been applied to the cooled surfaces based on values in [110], [195], with 5000 W/m^2-K selected for the housing outer jacket cooling channels and 1000 W/m^2-K selected for the bobbin cooling channels. Homogenization techniques were used to model the net thermal conductivity of the litz wire using material assumptions defined in TABLE 5.1-3 and the 32 AWG strand size and count presented in TABLE 5.1-1. Thermal contact resistances between material interfaces are neglected for this analysis.

Steady-state thermal FEA results are shown as color contour plots in Fig. 5.2-3 for rated loss conditions with 2.33 kW loss and a 33% overload condition with 2.90 kW winding loss. Under healthy conditions, the peak expected winding temperature is 156ºC, providing a 44 ºC temperature margin based on the 200ºC insulation system. For the overload condition, this thermal margin is eliminated with a peak predicted coil temperature of 204ºC. However, this overload only occurs during rare fault-mode operation conditions that are assumed to have short durations. Overall, the proposed stator cooling strategy effectively manages the substantial loss from the stator windings.

Thermal isolation between healthy and faulted modules has also been investigated using 3D thermal FEA. Specifically, the two-coil model is depicted in Fig. 5.2-4(a), including a healthy module coil, with losses associated with healthy operation (approx. 95.8 W per coil), and a faulted module coil with variable losses. Predicted peak steady-state turn and slot liner temperatures have been collected for several values of losses in the faulted coil up to 2x the healthy coil loss, with results plotted in Fig. 5.2-4(b).

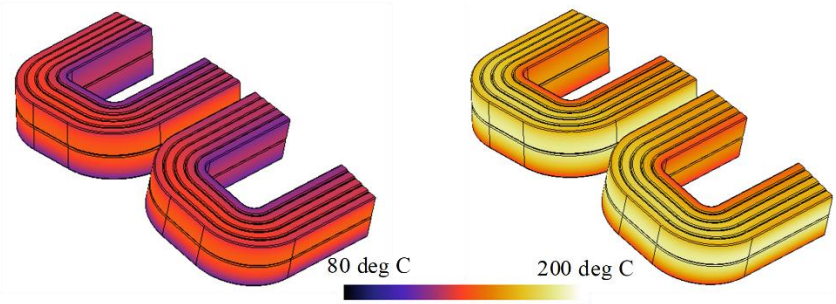

Figure 5.2-3 Predicted steady-state coil temperature color contours for healthy (2.3 kW loss) and 33% overload conditions (2.9 kW loss). The predicted maximum coil temperature is 156ºC during rated condition and 204ºC during overload condition.

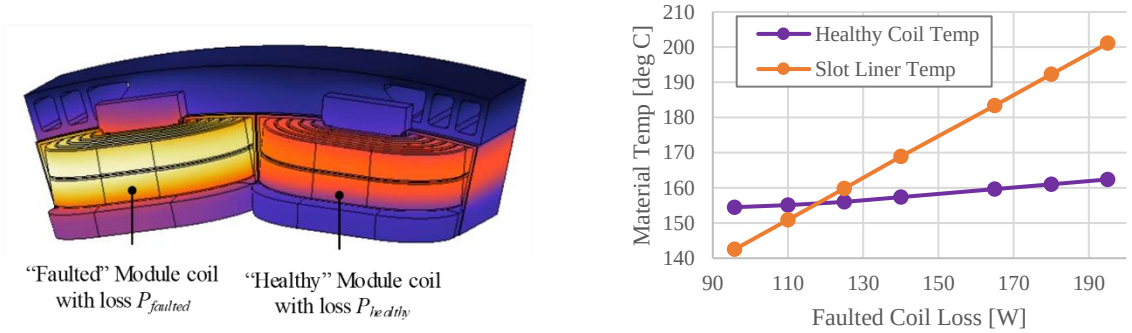

(a) **(b)**

Figure 5.2-4 Thermal isolation study model and predicted peak steady-state temperatures vs. losses in the faulted coil.

A maximum healthy module coil temperature of 162ºC for a 2x faulted coil loss (approx. 195 W per faulted coil) corresponding to a modest 6.4ºC temperature rise in the healthy coil above its normal rated operating temperature. However, a more substantial steady-state temperature increase is observed in the slot liner, which separates the healthy and faulted modules. A slot liner temperature rise of 58.6ºC is observed—nearly 9.2x higher than the healthy coil temperature rise.

Although the modules share slots, the proposed slot structure in Fig. 5.2-1 isolates the coils quite effectively, where a layer of slot liner insulation material between adjacent phases acts as a thermal barrier and the alumina bobbin casing redirects heat to the cooling channel. The concept of thermal isolation and its extension to the entire thermal management system is discussed in Chapter 7.

5.2.1. Internal Flow Calculation for Stator Cooling Concept

The preceding 3D thermal FEA analysis made several assumptions related to the heat transfer coefficients associated with the proposed stator cooling concept. Specifically, constant heat transfer coefficients of 5000 and 1000 W/m^2-K were applied to the housing and bobbin cooling channel surfaces, respectively. This subsection uses internal flow correlations to evaluate the thermal feasibility of these assumptions along with corresponding pressure, flow, and fluid property tradeoffs.

Discussions around internal flow correlations can be found in [196], [197] with key concepts listed here. The Engineering Equation Solver (EES) has built-in internal flow correlations that are used for the actual flow calculations. Each flow channel has a hydraulic diameter D_H defined in (5.2.1), which is related to the channel area A_{ch} and perimeter *per*.

$$D_H = \frac{4 \cdot A_{ch}}{per} \tag{5.2.1}$$

The hydraulic diameter is used in combination with the fluid density ρ, mean fluid velocity u_m, and the fluid dynamic viscosity μ to calculate the hydraulic Reynolds number Re_{DH} in

$$Re_{DH} = \frac{\rho \cdot D_H \cdot u_m}{\mu} \tag{5.2.2}$$

The Reynolds number describes the fluid flow condition with $Re_{DH} < 2300$ indicating laminar flow and $Re_{DH} > 2300$ indicating turbulent flow. The flow condition affects the selected correlation

and the associated thermal and flow characteristics. For the thermal analysis, these correlations can be used to evaluate the average Nusselt numbers (*Nu*), which, in turn, makes it possible to calculate the average heat transfer coefficient $\bar{h}$ given a fluid thermal conductivity *k* using

$$\bar{N}u = \frac{\bar{h} \cdot D_H}{k} \tag{5.2.3}$$

Similar correlations can be used to estimate the average friction factor $\bar{f}$, which can be applied to (5.2.4) to determine the pressure drop ΔP across the overall channel length *L*. Additional pressure drops are associated with the bends in the bobbin and cooling jacket, which are neglected in this initial analysis.

$$\Delta P = \frac{f \cdot \rho \cdot u_m^2}{2 \cdot D_H} \tag{5.2.4}$$

Finally, the overall fluid temperature rise ΔT can be calculated from the total heat load *Q* and the specific heat of the fluid c_p.

$$\Delta T = \frac{Q}{\dot{m} \cdot c_p} \tag{5.2.5}$$

Two fluids are considered as possible candidates for coolant in the quadrotor application. The first is Automatic Transmission Fluid (ATF) due to its expected availability on the quadrotor aircraft. The second is a Water Ethylene Glycol (WEG) mixture, which is a common heat-transfer fluid. Thermal properties for both ATF and WEG are provided in TABLE 5.2-1.

TABLE 5.2-1 FLUID PROPERTIES USED IN INTERNAL FLOW CALCULATION.

Fluid Property	ATF	WEG	Unit
Dyn. Viscosity (μ)	9.57	1.75	mPa-s
Kinematic Viscosity (v)	11.58	1.72	mm^2/s
Density (ρ)	0.827	1.017	g/cm^3
Specific Heat (c_p)	2100	3688	J/kg-K
Thermal Cond. (k)	0.155	0.377	W/m-K

5.2.1.1. Coil bobbin channel flow characteristics

Initial correlations are used to estimate the pressure and thermal characteristics of the bobbin shown in Fig. 5.2-2. For simplicity, a rectangular channel is assumed with dimension 0.7 mm by 5.8 mm. The average heat transfer coefficients and bobbin pressure drops are determined using the built-in correlations in EES, and plotted against flow rate in Fig. 5.2-5. For laminar flow conditions, two sets of heat transfer coefficients are provided corresponding to either constant temperature or constant heat flux boundary conditions.

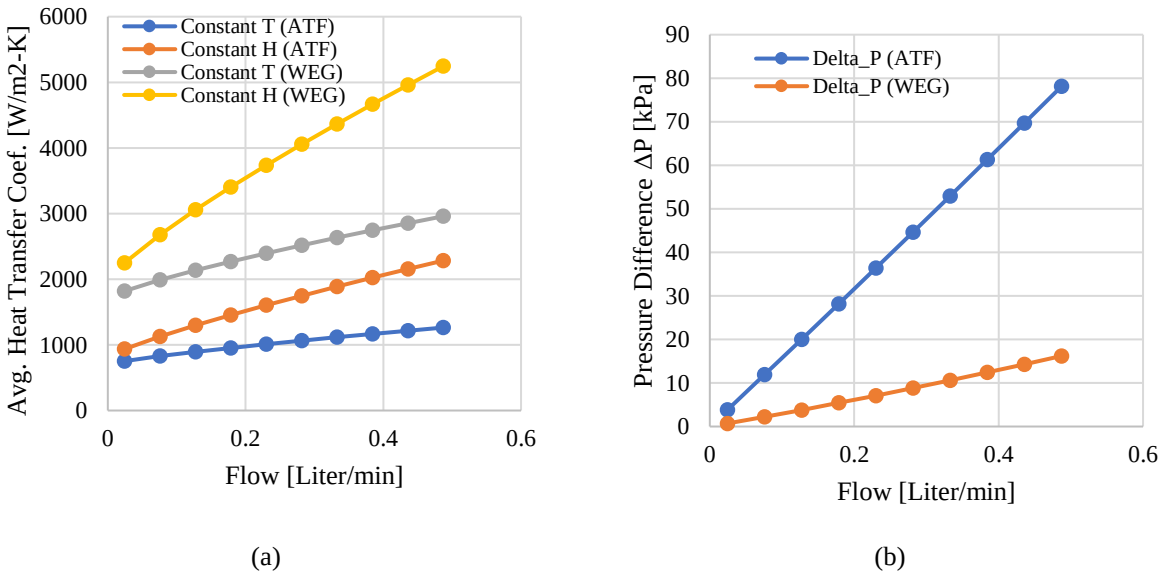

(a) (b)

Figure 5.2-5 Estimated heat transfer coefficients and frictional pressure drops for the proposed cooling bobbin.

The results in Fig. 5.2-5(a) show that both fluids are capable of meeting and exceeding the target heat transfer coefficient of 1000 W/m^2-K. However, in both cases, substantial pressure drops are expected due to the small channel size. The pressure drop is substantially higher for the case of ATF due to its higher viscosity.

5.2.1.2. Stator Cooling Jacket Design and Analysis

It has been assumed that coolant channels are inserted into the outer surface of the stator housing to provide cooling for the stator core and the potted end windings. In addition, this cooling jacket is intended to provide the primary cooling means for the integrated drive power electronics that is discussed in a subsequent section. A conceptual cooling jacket design has been developed as shown in Fig. 5.2-6 to evaluate the feasibility of the 5000 W/m^2-K heat transfer coefficient used in the FEA evaluation. These cooling channels are modularized into 12 sections (corresponding to the three phases associated with each of the four motor drive modules), providing a flat platform on which the power electronics phase modules can be mounted. A serpentine coolant path is used in each module with channel dimensions provided in Fig. 5.2-6.

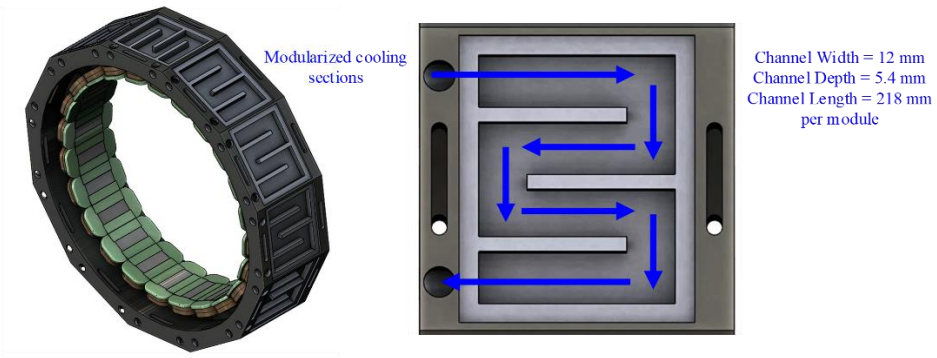

Figure 5.2-6 Cooling jacket conceptual design with modularized cooling sections to be utilized with power electronics integration. A serpentine channel is proposed in each cooling module with channel dimensions shown.

Using correlations to analyze a single cooling section, the pressure and flows necessary to reach the target heat transfer coefficients have been determined. For ATF, a massive flow rate at 60.4 L/min at a pressure of 98.9 kPa per cooling module is necessary, indicating alternative cooling jacket design approaches are necessary to make this cooling concept feasible. Numerous examples of cooling jacket designs can be referenced in the literature for future design iterations [198].

Alternatively, the pressure and flow requirements are much less severe with WEG, requiring 7.4 L/min flow rate at 1.9 kPa per cooling module.

5.2.2. Rotor Thermal Analysis

A similar steady-state temperature evaluation using thermal FEA has been performed on the rotor. On the rotor side, substantially less cooling capability is available. According to the baseline configuration, the losses produced in the carbon fiber containment sleeve, magnet, and rotor core cooling will be removed via ambient air convection in the housing (assuming an internal housing temperature of 120ºC), combined with heat conduction through the machine shaft and bearings (Fig. 5.2-7(a)). As a result, rejecting the rotor losses is quite challenging because of the limited cooling capability despite the seemingly low rotor loss value of 140 W. Preliminary calculations have shown that this proposed cooling method can maintain the carbon fiber sleeve below its 200ºC maximum limit with minimal margin. This margin disappears in the event of an overload condition or a faulted module.

In general, this minimal rotor cooling approach is feasible only with very low rotor losses or the utilization of high-temperature materials. In this proposed design, the composite carbon fiber sleeve is the temperature-limiting component, with a maximum operating capability expected to be less than 200ºC. Other high-temperature magnet containment materials such as the Inconel alloy can be used, but this approach will result in both increased rotor loss and a thicker containment shell which is undesirable.

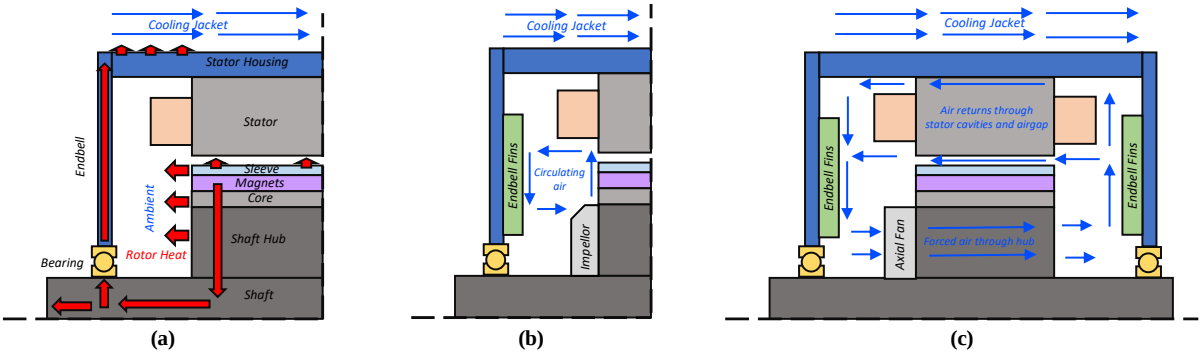

Figure 5.2-7 Rotor cooling approaches: (a) baseline passive cooling approach using housing ambient air convection and conduction through the rotor bearings as shown; (b) self-contained rotor forced-air convection cooling using radial impellors to stir air in housing cavities at both ends of the machine; and (c) self-contained rotor forced-air convection cooling using rotor-mounted axial fan(s).

The use of shaft-mounted fans can be an effective self-contained alternative to the baseline passive cooling approach. The viability of fan rotor cooling is increased if the quadcopter rotors operate at constant speed with pitched-blade control. Furthermore, the presence of airflow in the housing can assist with stator cooling, allowing for simplification of the stator cooling approach. Specifically, impellors can be added at both ends of the machine as in Fig. 5.2-7(b) which stir the housing air, or an axial fan can be added to force air to flow axially through the rotor hub and airgap as illustrated in Fig. 5.2-7(c). The stator core cavities can be used as channels that serve as heat exchangers for cooling the air as it flows between the two ends of the machine.

However, the design and evaluation of a compact self-contained fan-based rotor cooling approach is beyond the scope of this work. For this preliminary analysis, it is assumed that the selected carbon fiber sleeve has a maximum temperature limit that is sufficiently high to allow the baseline passive rotor cooling approach in 5.2-7(a) to be used.

5.3. Rotor Sleeve Sizing Confirmation

A structural analysis of the electrical machine rotor has been completed to validate the carbon fiber sleeve sizing analysis described in Chapter 4 that led to the choice of a 0.6 mm sleeve thickness. The rotor model and boundary conditions described in Fig. 5.3-1 were implemented in the ANSYS Static Structural package. Similar to its electric conductivity, the Young's Modulus of the sleeve varies with direction. For simplicity, an isotropic material characterized by the hoop-direction Young's Modulus is assumed for this analysis based on the properties described in [147].

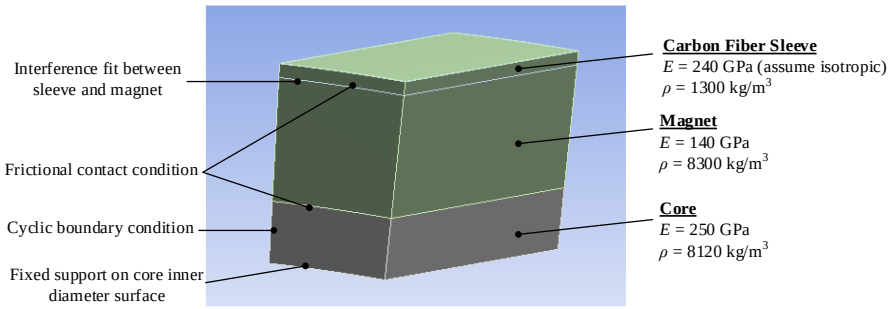

Figure 5.3-1 Magnet containment sleeve analysis conditions and material properties.

The simulation itself was carried out in two steps. In the first step, pre-stress is applied to the sleeve by modeling an interference fit to the magnet (i.e., decreasing the sleeve inner diameter relative to the magnet outer diameter). In the second step, an inertial condition is applied corresponding to the 9,600 rev/min peak speed. Peak equivalent stresses and contact pressures are shown in Fig. 5.3-2 for sleeve interferences of 0.3 and 0.6 mm.

For both interference values, the peak stress is highest in the sleeve, and significantly higher for the larger interference condition. This peak stress at 0.6 mm interference pushes the limits of the yield strength for the sleeve material described in [147], although there may be newer sleeve technologies with higher yield strength values. However, the 0.3 mm lighter interference condition is likely acceptable due to appreciable contact pressure between the sleeve and magnet. It should

be noted that the thermal expansion of the magnets and rotor core will also contribute significant stress to the sleeve at the rated speed. In any case, the structural analysis confirms that 0.6 mm is a reasonable choice for the carbon fiber sleeve thickness for this preliminary machine design exercise.

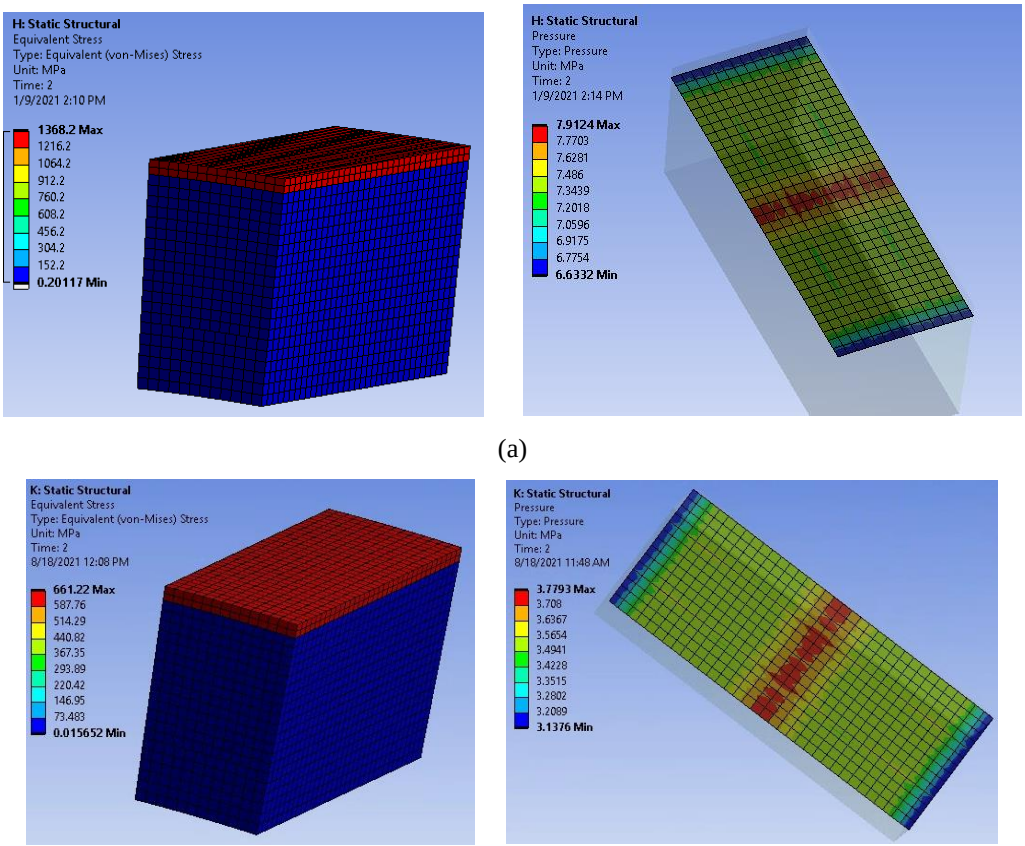

Figure 5.3-2 Calculated equivalent stress (left) and magnet contact pressures (right) from FEA structural analysis at 9,600 rev/min for: (a) 0.6 mm sleeve interference; and (b) 0.3 mm sleeve interference.

5.4. Power Electronics Design, Analysis and Integration

Each of the four 3-phase electric machine modules defined in Fig. 5.1-2 is excited by a two-level VSI. These modules are connected in series, reducing the module power electronics voltage requirements by a factor of four (V_{dc} = 200 V). The use of WBG switches is necessary to

accommodate the high fundamental frequency (1867 Hz) required by the machine at maximum speed (8000 rev/min). The low-voltage, high-current nature of the modules requires the use of discrete devices. The Wolfspeed SiC C3M0016120K MOSFET has been selected due to its low-on state resistance. It is assumed that these devices are connected in parallel to maintain the conduction loss in each device within a safe maximum limit as shown in Fig. 5.4-1.

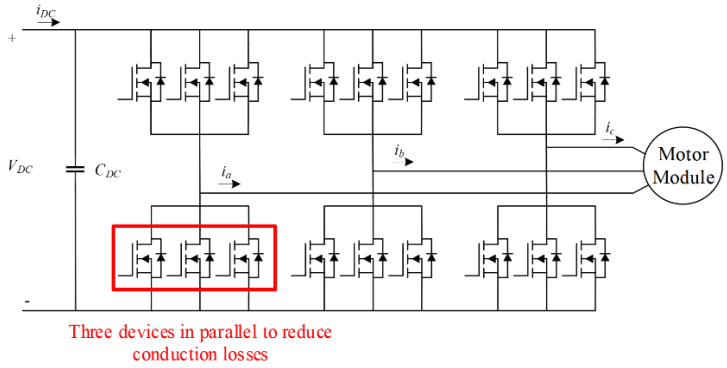

Figure 5.4-1 Single-module VSI with three devices in parallel to minimize conduction losses.

A single power electronics module has been implemented in PLECS (see Fig. 5.4-2) to estimate the device losses, to size the module capacitance, and to assess the machine's current ripple. Device and body diode loss models are downloaded from the manufacturer's website. The machine has been modeled as an inductance and flux linkage lookup table generated from FEA. The module current is regulated using an ideal synchronous-frame current regulator. Device deadtimes equal to 1% of the switching period are assumed. Non-idealities associated with the parallel device current balancing and the series-connected capacitor voltage balancing are neglected during this analysis. Finally, it is assumed that the devices are cooled by the same 80ºC coolant supplied to the machine with a convection cooling thermal resistance of 0.1 W/m-K.

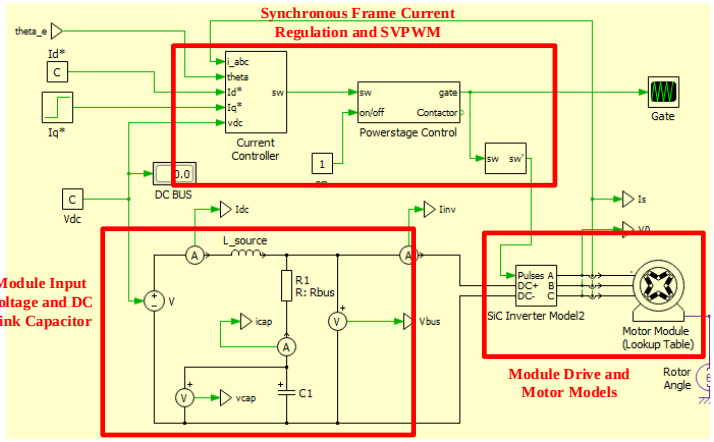

Figure 5.4-2 Single motor-drive module PLECS model.

A switching frequency of 27 kHz was selected to be suitable for the dc link capacitor inside the machine housing. A 450V 480 μF TDK B32778J448K000 film capacitor was selected for each module due to its compact design. A maximum healthy voltage ripple of 2.4 $V_{pk\text{-}pk}$ and rms capacitor current of 37.3 A_{rms} is estimated, meeting the selected capacitor specifications.

TABLE 5.4-1 summarizes the predicted module power electronics losses and efficiencies under various operating conditions. During healthy operation, the proposed four-module drive reaches 98.4% predicted efficiency, with conduction losses dominating. The switching losses are substantially lower due to the low dc bus voltage for each module. The device temperature rise is minimal due to the distribution of the loss across 18 module devices. The predicted module three phase currents including the PWM current ripple are shown in Fig. 5.4-3. The predicted current ripple amplitude is limited to 30 $A_{pk\text{-}pk}$ due to the large machine inductance (a benefit of the machine's FT current-limiting feature) and the high switching frequency.

The loss distribution for the IMD system during healthy operation is summarized in Fig. 5.4-4. Over 50% of the machine loss is dissipated in the machine windings. Next, device and body diode losses contribute over 25% of the overall loss. Overall, the proposed IMD is predicted to have a 94.3% efficiency during healthy operation at full-load and rotor speed (70 kW, 8000 rpm).

TABLE 5.4-1 PREDICTED HEALTHY MODULE PERFORMANCE FOR NORMAL AND FAULTED OPERATION

Module Spec.	Normal (All Modules Healthy)	Faulted		Units
Operating Condition	*None (full torque)*	*1-Module Lost (full torque)*	*2-Module Lost (degraded torque)*	-
Module Voltage	200	267	400	V
MOSFET Conduction Loss	162	270	244	W
MOSFET Switching Loss	26	44	66	W
MOSFET Junction Temp.	84.0	86.0	86.0	°C
Diode Conduction Loss	98	265	397	W
Four-Module Efficiency	98.4	--	--	%

Note: All loss values are provided on a per-healthy-module basis

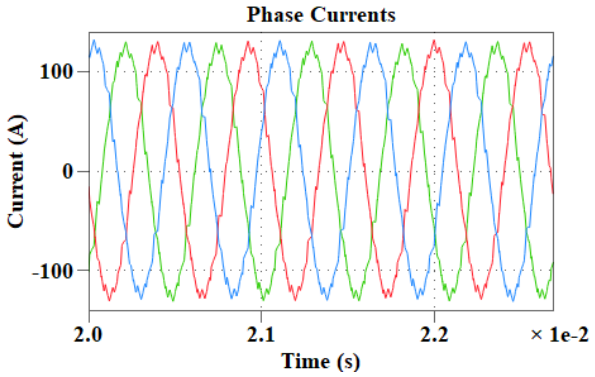

Figure 5.4-3 Predicted module phase currents during normal healthy full-load operation (70 kW, 8000 rpm)

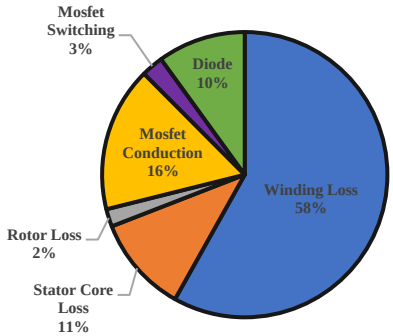

Figure 5.4-4 Predicted distribution of full-load IMD losses during normal healthy operation.

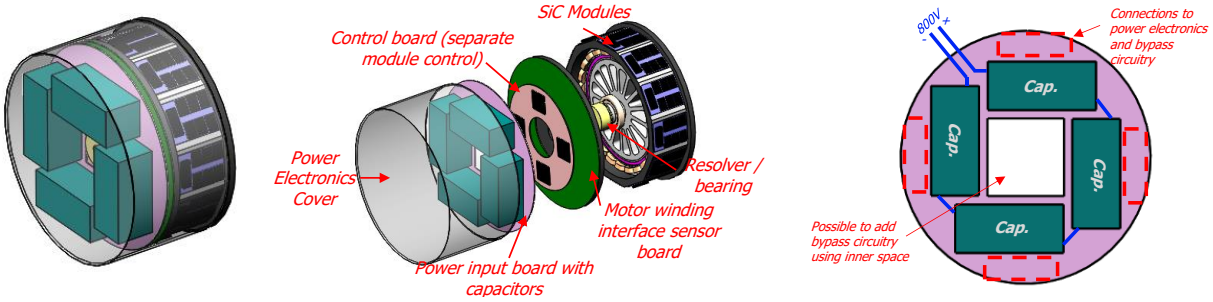

Figure 5.4-5 Conceptual IMD power electronics integration: (a) assembled IMD and exploded view showing major components; (b) power input board showing series capacitor connections.

A conceptual power electronics integration concept is depicted in Fig. 5.4-5(a), where the power switch modules are mounted around the stator outer circumference (allowing for shared machine housing cooling), and the capacitors and module control units are mounted axially inside the machine end bell. The power input board and series capacitor connections are highlighted in Fig. 5.4-5(b). An estimated IMD volumetric power density of 5.38 kW/liter is calculated from this conceptual model.

5.5. Post-Fault Operation and Analysis

The designed machine must be capable of full-torque operation after a power electronics fault, and degraded torque following a second module failure. In general, the IMD's response to a fault will be to short the faulted module dc link to bypass the faulted module and to either: 1) open circuit its three machine windings; or 2) short circuit its three machine windings, depending on the nature of the module fault. The remaining healthy modules will restore torque to the limit of their capabilities by increasing their phase currents.

5.5.1. Three-Phase Terminal Faults

Steady-state faulted operation of the machine has been assessed using a full machine model in 2D FEA with losses adjusted to be consistent with the 3D model. Flux contours under a single module loss scenario are provided in Fig. 5.5-1. Steady-state performance summaries for full-torque operation with one faulted module for both 3-phase open-circuit and short-circuit terminal conditions are summarized in TABLE 5.5-1. These results show that rated torque can nearly be restored following a module loss by increasing the healthy module currents by 33% at the price of higher losses and degraded thermal margins, particularly for the short-circuit conditions. It should

be noted the shorted modules have lower winding loss than the healthy modules due to the suppressed fault current amplitudes attributable to the designed value of the phase inductance.

Similar trends for the predicted power electronics performance are shown in TABLE 5.5-1 for the healthy modules during normal and fault-mode operation. Increased losses are observed in the healthy module components due to the increased load after faults, but the associated temperature increases are less severe than what is predicted in the machine.

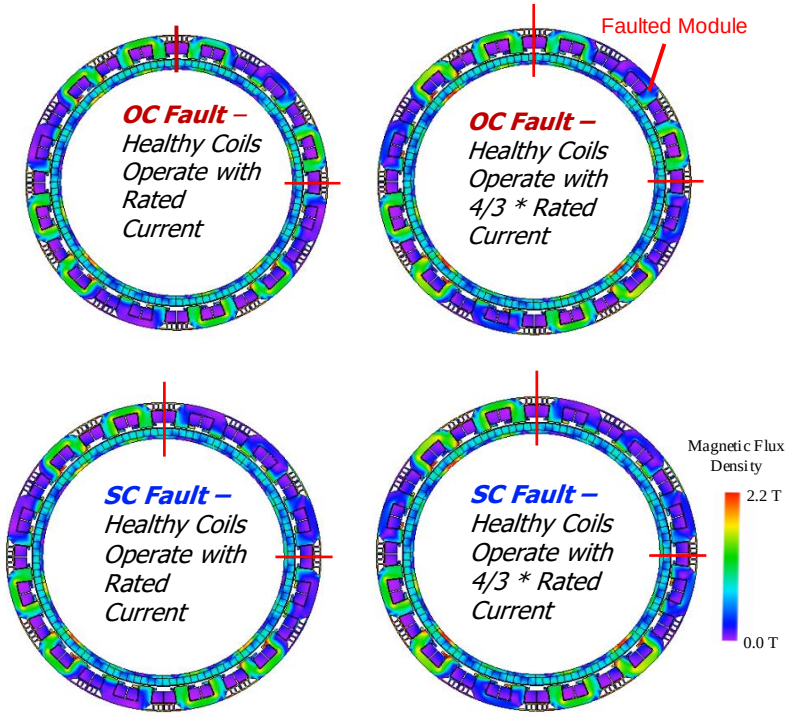

Figure 5.5-1 Predicted magnetic flux color contours for single-module open-circuit and short-circuit fault conditions with two current amplitudes in the healthy modules.

TABLE 5.5-1 PREDICTED MACHINE PERFORMANCE AFTER ONE MODULE IS LOST

Criteria	Normal (All Modules Healthy)	Module Open Ckt	Module Short Ckt
Healthy Module Current [A_{pk}]	126.2	4/3*126.2	4/3*126.2
Faulted Module Current [A_{pk}]	-	-	156.5
Torque [Nm]	83.8	83.2	80.9
Loss Per Healthy Tooth Coil [W]	95.8	161.1	161.1
Healthy Module Tooth Coil Peak Temperature [°C]	156	204	204
Loss Per Faulted Tooth Coil [W]	-	21.6	140.0
Faulted Tooth Coil Pk Temp [°C]	-	119	189

5.5.1.1. Unbalanced Magnetic Pull

A quadrant arrangement in assumed for the modular FT machine as shown in Fig. 5.5-2. This type of modularity has benefits related to modular electromagnetic isolation (discussed in Chapter 4) and for simplified power electronics integration, although it comes with post-fault tradeoffs. Specifically, an unbalanced magnetic pull (UMP) is developed due to the asymmetry introduced by a lost module. The impact of UMP has been studied for stator and rotor eccentricities, which can lead to increased wear on bearings, as well as negatively affecting the rotor dynamics and vibration [152], [199].

The full machine model previously utilized in the electromagnetic fault study is reused to assess the level of rotor force after one or two module failures. A force calculation condition for forces in cartesian coordinates shown in Fig. 5.5-2 is assigned to the rotor. Three phase terminal faults are applied to modules and rotor forces are calculated.

First, negligible rotor forces are observed during a healthy condition as shown in Fig. 5.5-3(a). In contrast, the rotor experiences substantial forces when a three-phase short-circuit is applied to module #1 also shown in Fig. 5.5-3(a). The magnitude of these forces is increased due to a 33%

higher current in the remaining healthy modules to restore the original machine torque. In both orthogonal directions, these x- and y-axis forces consist of a dc offset together with a 2x electrical fundamental frequency component.

Next, a second three-phase short circuit fault is applied to either an adjacent (module #2) or opposite (module #3) module with resultant forces shown in Fig. 5.5-3(b). For an adjacent fault, a significant increase in the average x-direction force and harmonic amplitudes is observed relative to the single-module failure case. Alternatively, an opposite module failure results in a symmetrical force cancellation much like a healthy operating condition.

These analytical results highlight the need for a reinforced shaft and bearings for a FT machine using a quadrant module integration scheme. This analysis also shows one of the benefits of having a higher number of modules if the module phases are concentrated together in one sector like the quadrant arrangement. Specifically, the adjacent fault scenario in Fig 5.5-3(b) can be viewed as a two-module machine with a single faulted module. Clearly the rotor forces for a single-module failure in a quadrant machine are less severe than the expected forces for a single-module failure in a two-module machine.

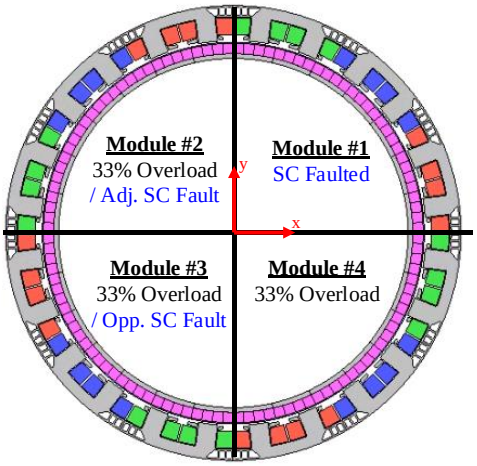

Figure 5.5-2 Quadrant modular arrangement and operating conditions for UMP simulation.

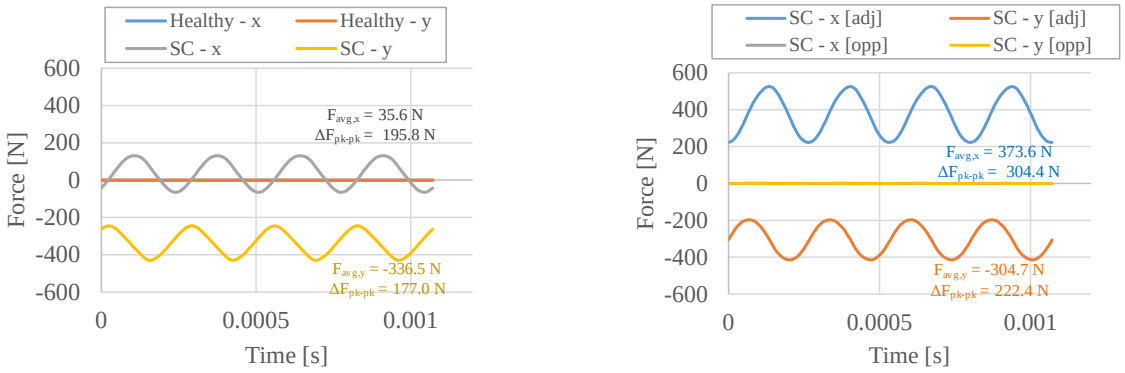

(a) **(b)**

Figure 5.5-3 Rotor forces after short circuit faults: (a) Single module short; and (b) second module short circuit.

5.5.1.2. Demagnetization Evaluation

Another fault mode of the developed FT quadrotor machine is demagnetization of the rotor magnets after a fault. To simulate a fault scenario, FEA was used to apply simulated fault currents of 2x rated current to the negative d-axis of the machine, and the resulting magnet demagnetization was observed and compared to a healthy operation scenario. Fig. 5.5-4 compares minimum magnet flux densities in localized areas across the magnet cross-sectional surface over the course of a fundamental cycle in the direction of the magnetization for both healthy and faulted scenarios. If the flux density is less than the knee point of the magnet (approx. -0.2 T for Recoma 35E magnet at 200°C) then the associated element is considered partially demagnetized.

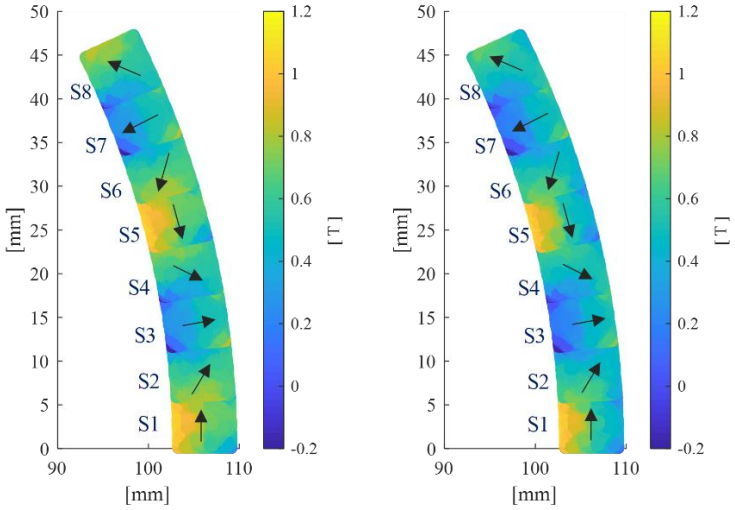

Figure 5.5-4 Demagnetization study results with minimum magnet flux density contours shown in the direction of the magnet-segment magnetization for a Recoma 35E magnet at 200°C: (a) healthy conditions with i_q = 126.2A and i_d = 0.0A; and (b) faulted conditions with i_q = 0.0 A and i_d = -252.4 A.

Even under healthy conditions, a small amount demagnetization is observed at the inner corners of the S3 and S7 magnet segment shown in Fig. 5.5-4(a). This demagnetization region increases slightly during the fault scenario, although the demagnetized area is small compared to the total magnet cross-sectional area.

5.5.2. Turn-to-Turn Fault Modeling

The previous section focused on relatively benign terminal faults, but there are other machine fault modes that can lead to catastrophic failures. In particular, internal turn-to-turn faults in the stator windings can be especially damaging to PMSMs. It is necessary to develop turn-to-turn fault models for the quadrotor FT machine to assess the possibility of fault propagation and to establish fault detection requirements for a turn-to-turn fault scenario.

Due to the severity of the turn-to-turn failure, numerous papers have been published on the modeling of this type of fault [145], [200]–[203]. An analytical turn-level model of the developed quadrotor machine is presented to aid with the evaluation process. This model has been validated using electromagnetic FEA.

5.5.2.1. Analytical Turn-to-Turn Fault Model

Based on the developed design, only a single machine phase needs to be analyzed due to the electromagnetic isolation between the phases. Each machine coil and phase can be modeled based on turn, sub-turns, and fault paths as shown in Fig. 5.5-5(a). Each turn segment has a back-emf,

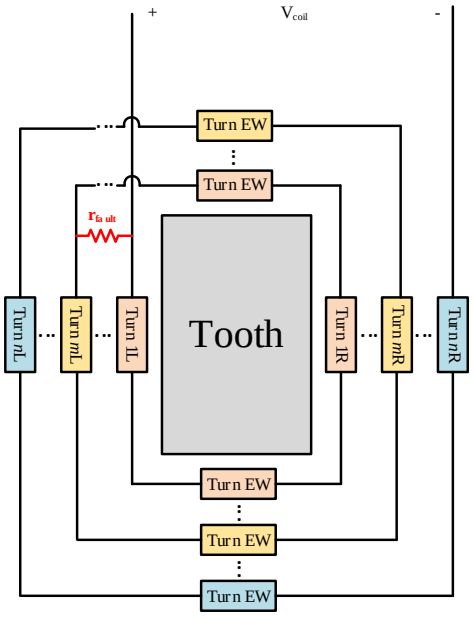

(a)

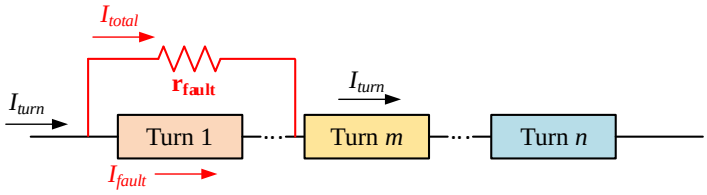

(b)

Figure 5.5-5 Isolated phase model with a turn-to-turn fault: (a) phase model with coils modeled on the turn and sub-turn level; and (b) rolled out model with lumped turns and fault currents defined.

inductance, and resistance associated with it. This coil can be rolled out to form a developed model with each turn modeled as a lumped element as shown in Fig. 5.5-5(b). An internal turn-to-turn fault occurs when a connection is formed between turns, which can result in substantial current in the faulted turns and localized heating.

Many of the surveyed turn-to-turn fault papers use lumped turn and coil models, like the one shown in Fig. 5.5-5, to estimate fault current levels. This type of approach is inflexible as new models need to be developed for different faulted turn locations. The model used to study turn-to-turn faults in the quadrotor machine shares similarities with the model in Fig. 5.5-5(b), but it has been generalized to provide greater flexibility for analyzing different fault locations and winding configurations. Specifically, fault resistances are inserted between every turn-node as shown in Fig. 5.5-6. The value of these resistances can be adjusted to assess the winding during both healthy or turn-to-turn fault conditions.

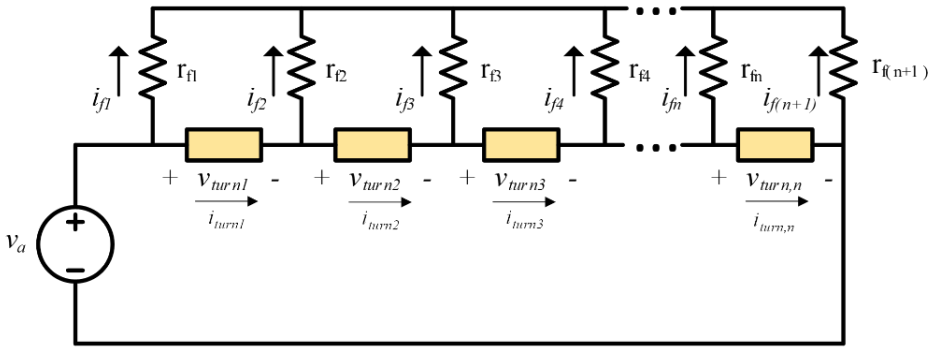

Figure 5.5-6 Isolated phase turn-to-turn fault model.

A system of equations can be developed to describe the Fig. 5.5-6 circuit. There are *n* voltage-loop equations resulting from Kirchoff's Voltage Law (KVL), one associated with each of the *n* turns in the machine in (5.5.1), which resemble a traditional machine model with turn resistance r_s, turn inductances L_{mk}, and turn magnet flux linkage λ_{pm}. The quadrotor machine has 20 turns per

phase with each turn being modeled as a 0.935 mΩ resistance with approximately 0.41 mWb magnet flux linkage. In addition, each turn has a self and mutual inductance of approximately 2.5 μH. Once again, the ρ operator represents the time derivative *d/dt*.

$$v_{turn,m} = r_s \cdot i_{turn,m} + \sum_{k=1}^{n} \left(L_{mk} \cdot \rho \cdot i_{turn,k} \right) + \rho \cdot \lambda_{pm,m} \tag{5.5.1}$$

Another *n-1* equations are needed to express Kirchhoff's Current Law (KCL) at each of the turn nodes consisting of turn currents i_{turn} and fault current i_f:

$$0 = i_{fm} + i_{turn,m} + ... + i_{turn,m-1} \tag{5.5.2}$$

And one final equation is generating by applying KCL at the common fault-path node:

$$0 = i_{f1} + i_{f2} + ... + i_{f(n+1)} \tag{5.5.3}$$

These equations have been implemented in MATLAB Simulink and results for a single-turn fault are shown here (specifically, shorting turn-1 via r_{f1} and r_{f2} in Fig. 5.5-6). Fault resistances for healthy turns are set to 1 MΩ. In this single-turn fault example, the total fault resistance R_f is defined by

$$R_f = r_{f1} + r_{f2} \tag{5.5.4}$$

Steady-state healthy (e.g. i_{turn2}) and faulted (i_{turn1}) turn currents for given fault path resistances are shown in Fig. 5.5-7. For sufficiently high fault resistance (R_f = 10 kΩ), there is little difference in current between healthy and faulted sections. Interestingly, the faulted-turn current drops relative to the healthy current for a 100 mΩ fault resistance R_f, but the fault current increasingly exceeds the healthy turn current as the fault resistance is progressively reduced. This result

reaffirms previous observations in the literature that the fault resistance has a significant impact on the expected fault current.

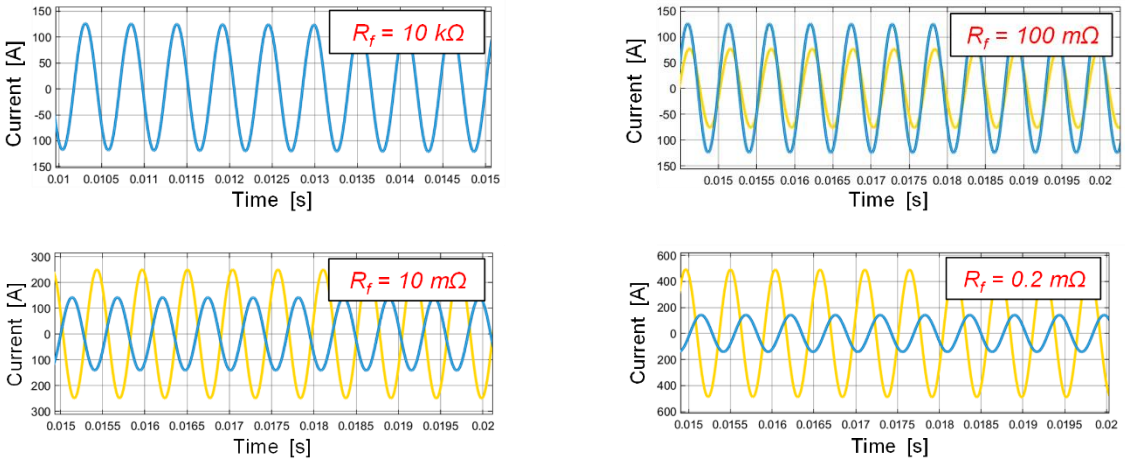

Figure 5.5-7 Simulated healthy (blue, i_{turn2}) and faulted (yellow, i_{turn1}) currents for varying fault resistance levels for single turn fault.

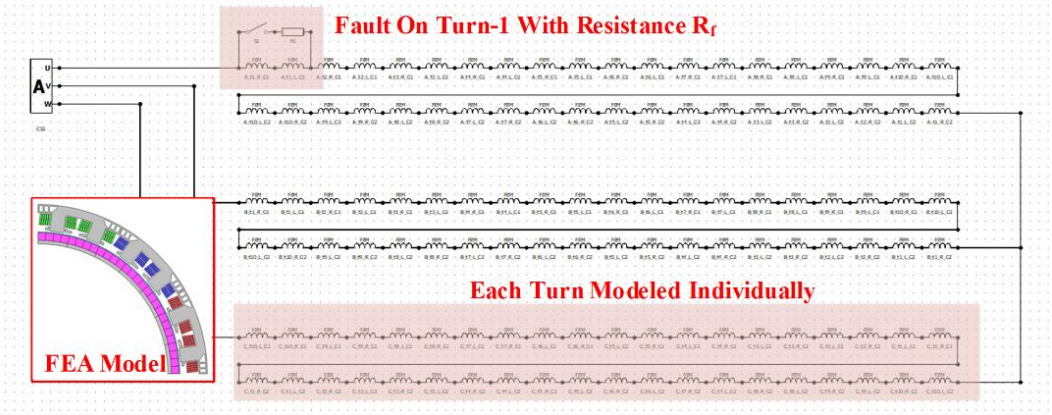

Figure 5.5-8 Turn-level electromagnetic FEA circuit model showing turn-1 fault.

5.5.2.2. FEA Validation of Turn-to-Turn Fault Model

A turn-level electromagnetic FEA model of the quadrotor machine has been developed to validate the analytical turn-to-turn fault model as shown in Fig. 5.5-8. A single fault resistance R_f is placed in parallel to turn-1 in the FEA model circuit. This resistance is varied and the turn-fault

(i_{turn1}) and fault resistance current (i_{f1}) is calculated. Results from the FEA are compared against the developed model calculation in Fig 5.5-9.

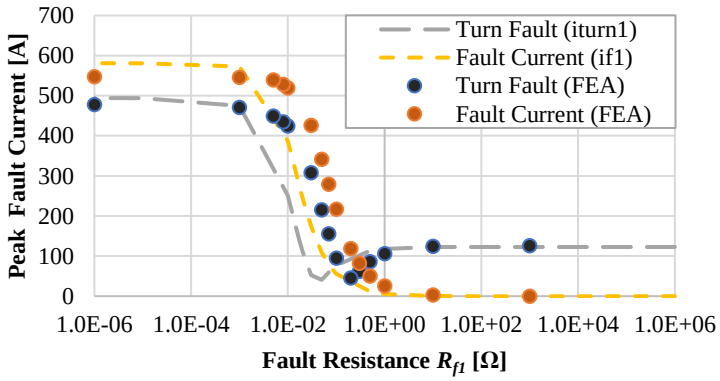

Figure 5.5-9 Developed single-turn fault model with variable resistance fault currents compared against FEA model for a single turn short circuit.

The results show reasonable agreement for high levels of fault resistance (i.e., under healthy conditions). For small fault resistance values (e.g., 1e-6Ω), the developed analytical model underestimates the fault resistance current by 34 A or 5.9% compared to the FEA model. For medium fault resistances (1e-3 to 1Ω), the Fig 5.5-9 curves agree in terms of shape and both models show a dip in turn-fault currents. However, the FEA model results appear shifted compared to the analytical model. The differences in results can likely be attributed to approximated machine parameters.

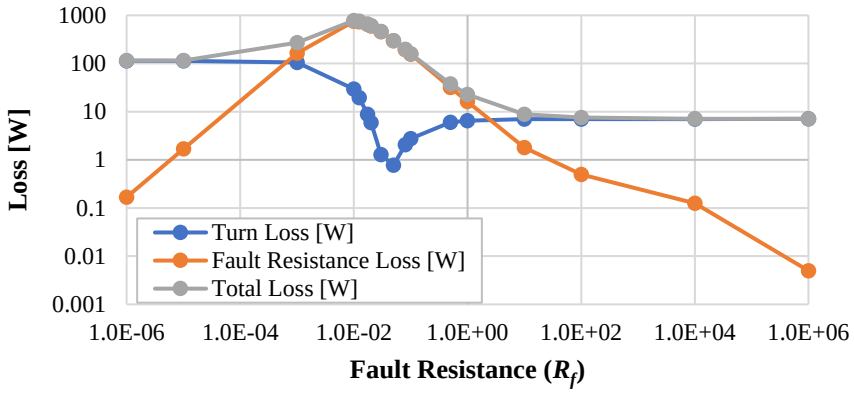

Figure 5.5-10 Faulted turn and fault resistance losses for varying fault resistances R_f

5.5.2.3. Thermal Isolation During Turn-to-Turn Fault Event

I^2R losses in the faulted turn and resistance can be estimated using the calculated currents and the specified resistances. Calculated losses associated to the analytical model for a single-turn short circuit fault are plotted in Fig. 5.5-10 and show that the losses in the fault-resistance can be considerable. Specifically, a fault-resistance loss of around 1000W is expected at a 10 mΩ fault resistance level. Significant losses are expected in the faulted turn during a complete short scenario (i.e., $R_f = 0$ Ω) with losses exceeding 100W.

The developed stator thermal models described in a previous section can be reapplied and modified to assess the turn losses during a complete turn-to-turn short scenario. The model has been modified to carry out a transient thermal analysis, and increased losses are applied to a single turn as shown in Fig. 5.5-11. A more complicated model is required to include the concentrated heat flux associated with the fault-resistance.

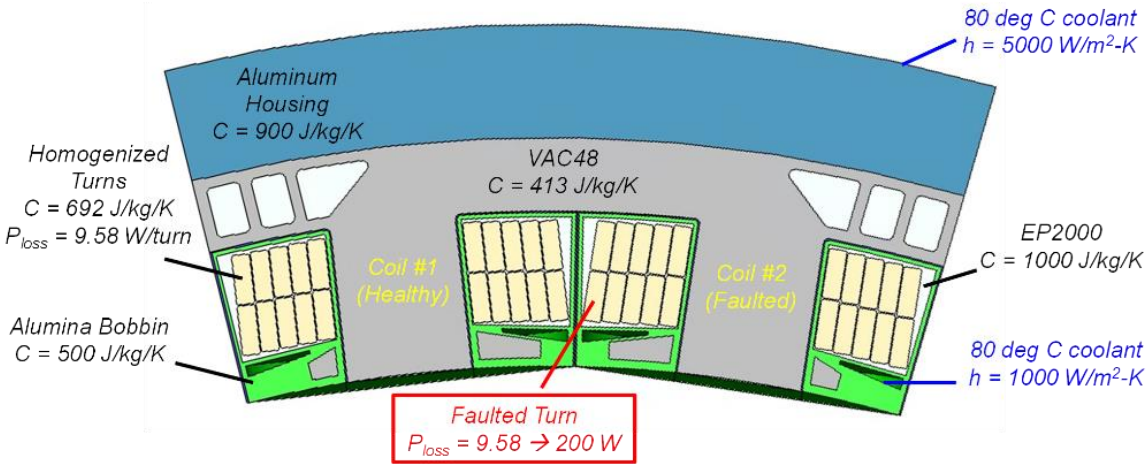

Figure 5.5-11 Transient thermal study model parameters.

As suggested by Fig. 5.5-11, the loss in the assigned faulted turn was varied from its loss value during rated healthy operation (~9 W) up to 200W to simulate the faulted turn loss in a dead-short scenario. Transient maximum coil temperatures for faulted turn losses values of 40W (~4x rated), 100W (~10x rated), and 200W (~20x rated) are provided in Fig. 5.5-12. For a 40W turn-loss condition, both the healthy and faulted coil maximum temperatures reach steady state below the 200°C insulation limit, although the faulted coil peak temperature is near 180°C which places it in the vicinity of the maximum safe operating temperature for the wire insulation.

Next, the 100W turn-loss condition shows the faulted-coil maximum-temperature exceeding the insulation temperature rating of the machine by approximately 40°C after a minute, which may be acceptable for short-time durations. A gradual increase in the healthy coil temperature is also observed, but it is below the insulation temperature limit for the plotted time scale up to 60 seconds. Similar observations can be made for the 200W turn-loss condition, albeit on a shorter timescale. Specifically, the maximum faulted coil temperature approaches 290°C at 20 seconds, while the temperature of the healthy coil reaches approx. 165°C after 20 seconds, still within the insulation's maximum temperature limit.

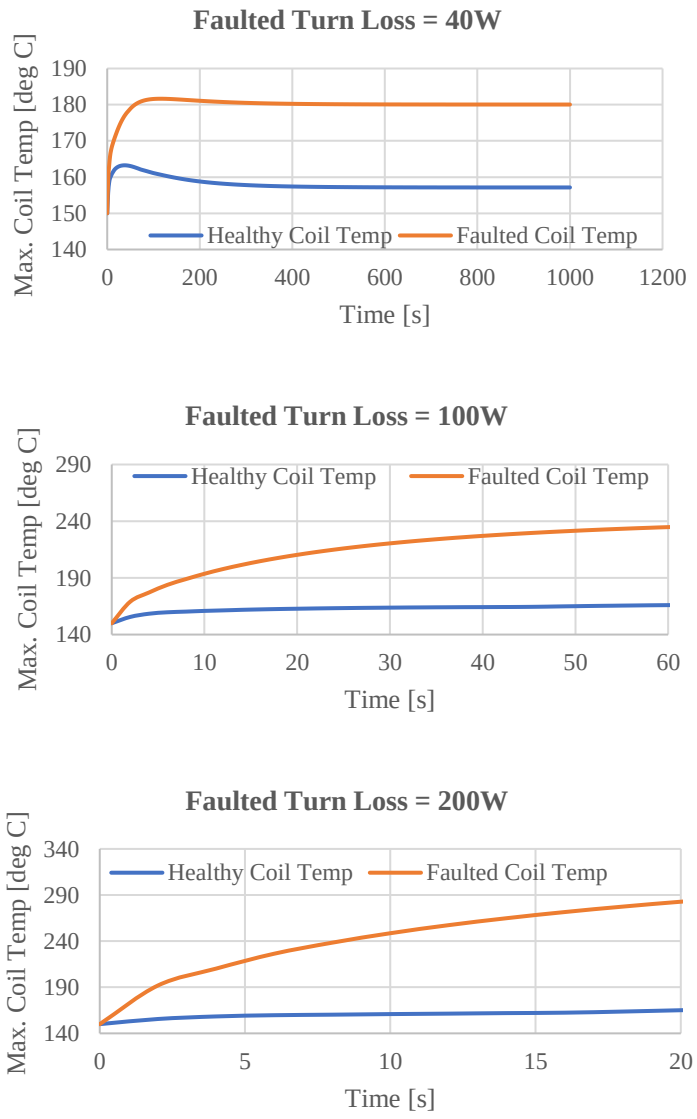

Figure 5.5-12 Transient thermal study for varying levels of faulted turn losses.

The results in Fig. 5.5-12 suggest that the developed stator slot structure and cooling method can thermally isolate healthy coils on short timescales, providing time for triggering a turn-to-turn fault detection scheme and remedial response (e.g., three-phase short circuit application to the faulted module terminals). However, the large change in the faulted coil temperature will raise the value of the faulted turn resistance and the expected heat load. More complex models are needed

to account for the changing temperature of the faulted turn and to incorporate the concentrated loss associated with the fault resistance.

5.6. Summary of Chapter

The results of a multi-physics design and analysis exercise for a quadrotor propulsor permanent magnet synchronous machine rated at 70 kW, 8,000 rev/min are presented. The developed machine has modular electromagnetic isolation features (modified tooth tips and flux barriers), a rotor with a surface-mounted Halbach magnet array, and integrated modular power electronics. Calculated machine performance and loss characteristics are reviewed, indicating a predicted full-load machine efficiency of 96.0% with an active-mass power density of 14.0 kW/kg.

A consequence of the high power density metrics is significant winding loss, and a special 3D-printed in-slot cooling structure has been developed that enables direct winding cooling. Thermal analysis of the proposed machine is presented that confirms the effectiveness of the direct cooling approach and its beneficial role for thermally isolating the machine modules. Predicted machine performance under faulted module conditions is also presented which shows that the proposed machine retains its ability to deliver rated torque and power after the module loss, while also maintaining substantial thermal isolation between the machine modules. The presented machine design provides sufficient healthy and faulted stressor information in order to inform the reliability analysis presented in Chapter 6.

Chapter 6

Reliability Assessment of Fault Tolerant IMD for Six-Passenger Quadcopter

The FT IMMD machine described in Chapter 5 has been subjected to a preliminary study to evaluate its reliability as well as its potential for improving the quadrotor aircraft reliability. Specifically, the details of the proposed design presented in preceding sections are used to supply the input for a first-pass reliability study. There are numerous tools available for assessing system and component reliabilities [153], [154]. For example, the UAM VTOL reliability study in [26] used a Fault Tree Analysis (FTA), which graphically shows the relationship between components and failures, as well as identifying the potential fault propagation paths. The development of FTA diagrams can be time consuming, and the FTA approach has limited capability to take into consideration system repairs, which is extremely important for FT machines.

Alternatively, Markov models provide a flexible tool for evaluating the proposed IMD as well as alternative IMD variants. These Markov chains divide the system into interconnected healthy and failed states. State space techniques can be used to estimate failed state probabilities and system reliabilities. This chapter introduces Markov chains and develops a Markov chain model for the proposed four-module IMD. A deeper discussion of Markov chains and the underlying reliability mathematics can be found in [154].

This study expands on previously reported modular machine results to consider the underlying machine and electronics and their associated stresses during healthy and faulted operation. The critical role of single-point failure rate in determining the IMMD failure rate is highlighted. The impacts of multiple module failures and total elimination of single-point failures are examined. Key parameters are identified and pathways for improving FT modular motor drives are discussed.

Further, simplified analytical reliability models are developed to compare the number of modules and the post-fault stresses, assessing the extent modularity can improve system reliability in the absence of repair. Overall, a general strategy for improving the quadcopter application reliability is proposed, though the conclusions can be applied to any FT system.

The lessons developed in the IMMD section are extended to the development of generalized FT figures of merit (FoMs) allowing for improved quantified comparisons of different implementations of FT. Specifically these FoM measure the overall reliability improvement of a FT system, the dependence on key variables like repair, and the relative reliability improvement against cost. This chapter concludes with a discussion of key reliability observations drawn from this study.

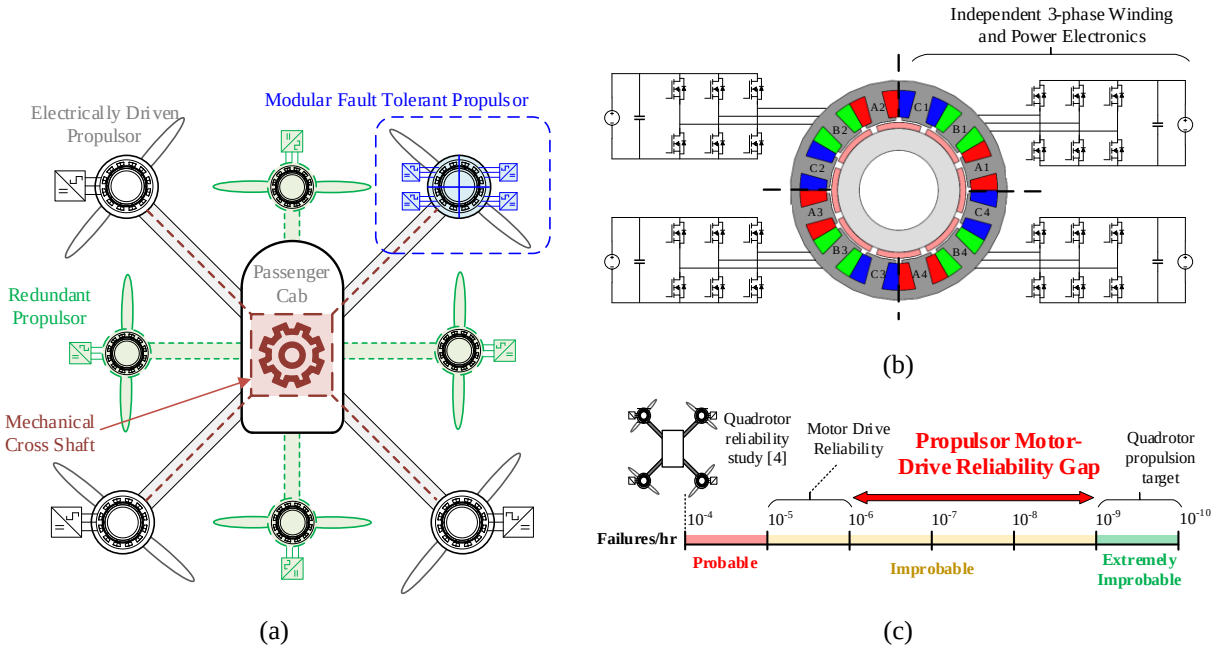

Figure 6.1-1 (a) Baseline quadrotor propulsor architecture with variants highlighted: propulsor cross shafting (red), redundant propulsor (green), and modular fault-tolerant propulsors (blue); (b) expanded modular motor-drive used in fault-tolerant propulsor; (c) Failure rate continuum with propulsor motor drive reliability gap highlighted.

6.1. Quadrotor Reliability Requirements

Electrified vertical takeoff and landing (VTOL) urban air mobility (UAM) vehicles are a potential solution for reducing greenhouse gas emissions and providing an alternative means of transportation in congested cities [6]. Several UAM conceptual reference vehicles are presented in [13] including a baseline quadcopter concept shown in Fig. 6.1-1(a) that consists of an electric motor and drive for each of the four propulsors. The reliability of these propulsors is critical to safe operation, with any propulsor failure leading to catastrophic consequences. In general, the catastrophic failure rate for these vehicles is targeted to be below 10^{-9} failures per flight hour [25] as illustrated in Fig. 6.1.-1(c).

The catastrophic failure rate for the UAM concept vehicles defined in [13] are assessed in [26] where the Fig. 6.1-1(a) quadrotor vehicle is estimated to have a catastrophic failure rate of ~8.0×10^{-4} per flight hour which is several orders of magnitude higher than the 10^{-9} per flight hour target. This study [26] shows that the aircraft catastrophic failure rate (including *all* components in the aircraft propulsion system) can be improved to 2.1×10^{-4} hr^{-1} by introducing a mechanical cross-shaft that links propulsors as shown in Fig. 6.1-1(a), still falling far short of the 10^{-9} hr^{-1} failure rate requirement. The power electronics and machines used in this UAM aircraft are identified in [26] as primary sources of the reliability shortcomings, with expected motor drive failure rates of 10^{-6} to 10^{-5} failures per hour using existing technologies. Major advances in motor drive components, manufacturing, and cooling are all critical to close the daunting reliability gap identified in Fig. 6.1-1(c), but they are not likely to be sufficient alone.

There are other system-level approaches for improving UAM vehicle reliability using existing technology. The addition of redundant propulsors in a multi-rotor vehicle system is one possibility

as shown in Fig. 6.1-1(a). This same propulsor redundancy concept can be incorporated into Distributed Electric Propulsion (DEP) architectures that provide additional aircraft performance benefits [9]. Alternatively, the power electronics and machine reliability can be addressed directly by aggressively introducing fault-tolerant (FT) features into their designs, enabling continued propulsor operation after a fault in either the machine or power electronics.

The purpose of this chapter is to investigate the potential of fault-tolerant motor drive configurations to contribute to significantly reducing the catastrophic failure of UAM propulsion systems. Although FT features can be applied by the addition of reconfigurable phases, or by modularizing one or more phases into independent drive units [204], [205], attention in this paper will be focused on achieving fault tolerance by dividing the machine into several redundant three-phase modular channels as shown in Fig. 6.1-1(a) and 1(b). This approach has been applied previously to surface permanent magnet (SPM) propulsion machines in [22], [30] to provide both FT features and high power density. Specific to the quadrotor application in Fig. 6.1-1(a), a four-module FT integrated modular motor drive (IMMD) is proposed in Chapter 5 to evaluate its potential for improving propulsor reliability. The IMMD is capable of delivering full-torque operation after loss of a single module, and it can operate with reduced torque after the loss of a second module. This machine will serve as the baseline for UAM motor drive reliability evaluations in this paper.

The results of the proposed design are used to supply the input for a reliability study using Markov chains as the primary tool. A brief introduction to Markov chains and reliability mathematics is provided in the context of fault tolerance and the quadrotor application. Previously, Markov chains have been used to develop comparisons of FT power electronics topologies in [32] and FT machine drives in [43]. A three-module configuration was studied in [43], identifying

modularity in combination with repairability as a promising path for significantly improving reliability. Additionally, Markov chains were used in [158] to compare different types of winding structures in permanent magnet synchronous machines (multi-phase, multi-three phase winding sets) combined with thermal analysis to estimate the winding thermal stresses. Additional states and transitions can be added to these machine Markov models to investigate the impact of component aging, as has been done for the case of insulation deterioration in [159]. Other motor drive and control reliability studies using Markov chain analysis can be found in [160]–[163].

6.1.1. Fault-Tolerant Modular Motor Drives

The use of FT modular machine drives (MMDs) is a promising candidate solution for enhancing UAM VTOL propulsor reliability. A FT modular motor drive can continue operation (i.e., supplying torque to the propulsor) after a failure in either the machine or power electronics. This approach makes it possible to achieve a low aircraft catastrophic failure rate that far exceeds the reliability of the individual components used in the motor drives. Using permanent magnet synchronous machines (PMSMs) as the example for this discussion, fault-tolerant PMSM motor drives using must possess three key characteristics in order to insure continued operation after a failure:

- *Redundant Phases, Modules, or Components* – The system must be designed to allow for continued operation after a failed module. If full-power operation is required after the failure of q modules in a motor drive containing n modules, each module must be oversized (e.g., increased device current rating) by the derating factor F given by

$$F = \frac{n}{n-q} \tag{6.1.1}$$

- *Isolation Between Phases or Modules* – Each of the redundant phases or modules must be sufficiently isolated from other modules to eliminate the possibility of inter-module failure propagation. Specifically, isolation features must be implemented to minimize and, if possible, eliminate electrical, electromagnetic, and thermal interactions between modules.
- *Fault Current Limiting Features* – The presence of the constant rotor flux linkage contributed by the spinning permanent magnets can induce excessive phase currents in the event of short-circuit failures initiated in either the power electronics or the machine itself. These fault currents must be limited to tolerable levels by designing the machine to sufficiently increase its winding inductance. This is often accomplished via stator slot geometry manipulation that increases the slot leakage flux via modifications of the slot height or tooth tips.

As noted in Section I, one of most appealing approaches for implementing FT modular motor drives is to design the modular machine with multiple isolated three-phase windings, each supplied by its own independent three-phase drive as suggested in Fig. 6.1-1(b). Design considerations for FT MMDs are discussed here in the context of the Fig. 6.1-1(a) quadcopter. Greater discussion related to FT MMD design can be found in the preceding Chapters.

6.1.2. FT MMD Component Rating and Isolation Concept

A single module of a four-module FT MMD system is shown in Fig. 6.1-2, consisting of a machine stator quadrant designed with its isolated 3-phase winding, excited by a dedicated two-level, 3-phase voltage-source inverter (VSI), and a dedicated module controller. In the event of a failure inside a module, the faulted module intentionally applies three-phase open- or short-circuit conditions to the module's machine terminals in order to suppress adverse fault effects inside that

module. The module failure detection schemes play a critical role in the success of this strategy, including the fault detection time and the mitigation-action response time, but a discussion of this rich topic extends beyond the scope of this thesis [152]. For purposes of this discussion, it is assumed that the failure detection and mitigation responses are fast enough to prevent catastrophic cascading failures, and they do not require the remaining healthy phases to be disabled even momentarily. Once reconfigured, the remaining healthy modules increase their phase current by the appropriate ratio to restore rated output torque. As a result, it is necessary to oversize the current rating of each device and to design in sufficient voltage headroom to supply the increased post-fault current.

The thermal management system for FT MMD power electronics and machine must be designed with sufficient excess capacity to tolerate increased thermal loads during post-fault operation. This may entail accepting decreased thermal margins during faulted operation, oversizing components to give them higher thermal capacities needed during faulted operation, or some combination of the two. Other special machine design adjustments must be made based on design-specific post-fault stressors. For example, rotor magnets must be thick enough to prevent irreversible demagnetization during a fault transient, and the rotor shaft must be sized to minimize deflections caused by unbalanced magnetic pull on the rotor following the failure of a stator module.

Designing machine stators to provide the necessary isolation characteristics while minimizing mass penalties is a serious challenge when developing MMDs. Electromagnetic and thermal isolation are particularly challenging in an MMD since the module windings are in close physical proximity in their shared stator core. Single-layer windings are often adopted to enhance these isolation characteristics in fractional-slot concentrated winding (FSCW) machines because each

stator slot contains coils of a single machine phase, making it simpler to minimize interphase magnetic field coupling and to provide thermal barriers between adjacent phase windings [30]. However, it should be noted that double-layer windings with two winding coil sides per slot are also being developed for FT FSCW machines in an effort to retain as many of the isolation advantages of single-layer windings while simultaneously avoiding their mass, volume, and loss disadvantages [206].

It should be noted that FT MMDs can deliver reliability benefits beyond their post-fault operating characteristics. For example, oversizing of components for FT motor drives reduces their stress during healthy operation due to lower temperature operation compared to a similarly rated conventional motor drive. If the motor modules are connected in series rather than in parallel, the voltage rating of each module is reduced inversely with the number of modules.

6.1.3. Reference Quadrotor IMMD Design

The considerations summarized in the preceding discussion were applied to a four-module Integrated Modular Motor Drive (IMMD) designed for a UAM quadrotor application. One of the key purposes of the IMMD has been to assess machine component stressors during both healthy and faulted operation. The peak power and rated speed of each propulsor IMMD has been set at 70 kW, 8,000 rev/min for a six-passenger aircraft. A brief description of the resulting IMMD design is presented in this section, providing key details that will be used in the reliability analysis. A more detailed discussion of the reference machine design can be found in Chapter 5.

The four-module machine achieves electromagnetic isolation via a combination of features including: a) selection of a 24-slot, 28-pole concentrated winding configuration; 2) the introduction of cavities in the stator yoke; and 3) the partial removal of interphase tooth tips as shown in Fig.

6.1-2. Physical and thermal isolation is enhanced by the careful selection of in-slot materials and the stator cooling approach.

The four IMMD drive modules are connected in series where each module receives 25% of the total 800V bus voltage. In the event of a failure, the faulted module is bypassed, increasing the excitation voltage for the remaining healthy modules by 33%. The proposed machine is capable of full-torque operation after the loss of one module, and partial-torque operation after the loss of a second module. Specifically, the remaining healthy modules are designed to handle ~33% higher current to enable the IMMD to deliver full torque after the loss of a single module. If a second module fails, the IMMD is capable of delivering 67% of its original full torque. Machine electromagnetic and thermal performance under healthy and faulted conditions has been evaluated using JMAG Designer. Similar drive performance calculations were made using PLECS. A summary of the predicted module-level performance for healthy and faulted conditions, including both winding and power electronics stresses, is provided in TABLE 6.1-1.

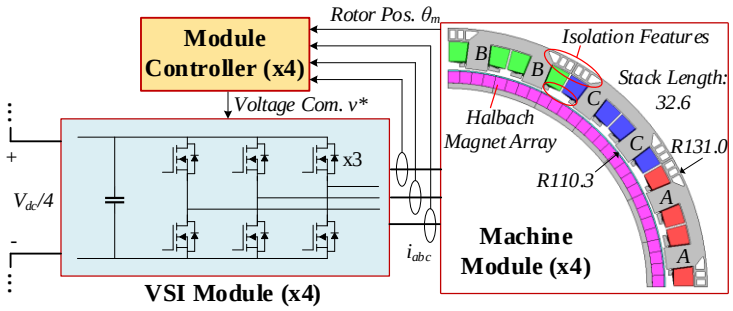

Figure 6.1-2 Developed quadrotor IMMD single module with isolation features and machine dimensions in millimeters.

TABLE 6.1-1 PREDICTED HEALTHY MODULE PERFORMANCE DURING NORMAL AND FAULTED OPERATION

Healthy Module Criteria	Healthy	1-Module Lost	2-Module Lost
Number Faulted Modules	0	1	2
Module Current [A_{pk}]	126.2	168.3	168.3
Loss Per Coil [W]	95.8	161.0	161.0
Coil Max. Temp [°C]	156	204	204
Module DC Voltage [V]	200	267	400
Drive Loss [W]	286	576	707
Max. MOSFET/Diode Junction Temp [°C]	83.8	85.6	86.9
Capacitor Current [A_{rms}]	37.3	67.4	73.8
Capacitor Volt. Ripple [ΔV]	2.4	5.2	5.7

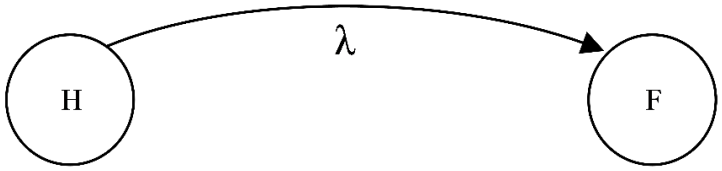

Figure 6.2-1 Elementary two-state Markov chain model with failed state absorbing.

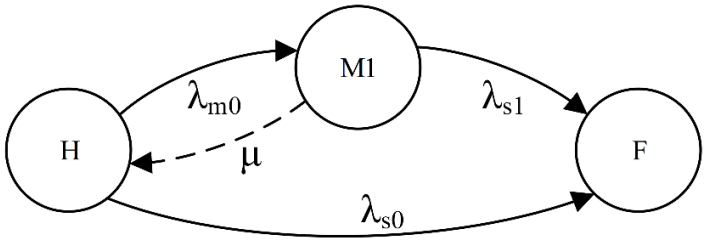

Figure 6.2-2 Three-state Markov chain with FT remedial state M1 with repair rate μ.

6.2. Markov Chains and Fault Tolerance Introduction

A brief introduction to Markov chains is provided here to give a mathematical overview for the FT MMD reliability study.

6.2.1. Two-State Markov Chains

Continuous time Markov chain analysis was selected as the preferred technique for assessing the reliability of the proposed four-module FT machine. In its simplest form, a system operates in

a healthy state with probability *H(t)* and failed state with probability *F(t)* as shown in Fig. 6.2-1. For a quadrotor vehicle, the failed state is defined to be any machine or power electronics failure leading to a hard landing or catastrophic event. These two states are connected by a failure transition probability λ [failures/hr], derived from the failure rates of the underlying components.

The basic system can be represented in matrix form as shown in

$$\begin{bmatrix} \dot{H} \\ \dot{F} \end{bmatrix} = T \begin{bmatrix} H \\ F \end{bmatrix} = \begin{bmatrix} -\lambda & 0 \\ \lambda & 0 \end{bmatrix} \begin{bmatrix} H \\ F \end{bmatrix} \tag{6.2.1}$$

where transition probabilities are placed in the transition probability matrix *T*. Both healthy and failed state probabilities can be solved using (6.2.1), allowing the Mean Time to Failure (MTTF) of the system to be determined using

$$MTTF = \int_0^\infty (1 - F)dt = \frac{1}{\lambda} \tag{6.2.2}$$

As indicated, the MTTF is simply $1/\lambda$ for the basic two-state system in Fig. 6.2-1

6.2.2. Three-State FT Markov Chains

The addition of FT capability adds new states to the system. Fig. 6.2-2 provides a basic representation of a FT system with a new faulted (but not failed) state $M_1(t)$. Fault transitions from *H(t)* to the faulted state $M_1(t)$ are defined by failure rate λ_{m0}, and transitions from this faulted state to the failed state *F(t)* are defined by λ_{s1} which is expected to be higher than λ_{m0} because of the higher stresses on the remaining healthy modules. Single-point failures from *H(t)* directly to *F(t)* associated with other failures in the propulsor unit outside of the individual modules (e.g., a centralized controller) are determined by λ_{s0}. If the system is repairable, the repair rate transition variable μ is added to transition from the $M_1(t)$ state back to the healthy *H(t)* state. The reciprocal

of μ (i.e., 1/ μ) corresponds to the mean time to repair (MTTR). In the context of a quadrotor vehicle, μ is the frequency of vehicle service and inspection (i.e., repair rate) with units of repairs per hour. The corresponding transfer matrix for the system in Fig. 6.2-2 is provided in

$$\begin{bmatrix} \dot{H} \\ \dot{M}_1 \\ \dot{F} \end{bmatrix} = \begin{bmatrix} -\lambda_{m0} - \lambda_{s0} & \mu & 0 \\ \lambda_{m0} & -\lambda_{s1} - \mu & 0 \\ \lambda_{s0} & \lambda_{s1} & 0 \end{bmatrix} \begin{bmatrix} H \\ M_1 \\ F \end{bmatrix} \tag{6.2.3}$$

along with the derived MTTF in

$$MTTF = \frac{\lambda_{m0} + \lambda_{s1} + \mu}{\lambda_{m0} \cdot \lambda_{s1} + \lambda_{s0} \cdot \lambda_{s1} + \lambda_{s0} \cdot \mu} \tag{6.2.4}$$

A procedure for deriving analytical MTTF expressions from state diagrams is provided later during the FT figures of merit subsection.

Both (6.2.3) and (6.2.4) have been implemented in MATLAB to perform the failure analysis of FT systems. For this analysis, the failure transition probabilities have been normalized by the module's single-point failure rate λ_{s0}. Fig. 6.2-3 shows the predicted system MTTF (using (6.2.4)) as a function of the $\lambda_{m0}/\lambda_{s0}$ failure rate ratio for both repairable (μ =10^{-2} hr^{-1}) and zero-repair (μ = 0) systems assuming a fixed value of λ_{s0} and λ_{s1} (i.e., λ_{m0} is the changing variable). Several important observations from these results include:

- The normalized module failure rate value $\lambda_{m0}/\lambda_{s0}$ significantly influences the predicted MTTF and repairability-effectiveness as observed in the approximate 10:1 MTTF drop in Fig. 6.2-3 as the value of $\lambda_{m0}/\lambda_{s0}$ is increased.
- The repair rate has a substantial impact on MTTF when the λ_{m0} and λ_{s0} failure transition probabilities are comparable. For example, when $\lambda_{m0}/\lambda_{s0}$ equals 10, the introduction of repairs improves the MTTF by 3x.

- The upper bound on the achievable MTTF equals the reciprocal of the single-point failure rate λ_{s0} when the $\lambda_{m0}/\lambda_{s0}$ failure rate ratio drops to zero (i.e., no module failures).

These observations define a general strategy for improving the FT machine drive reliability. The impact of failure rates associated with the M_1 state (λ_{m0} and λ_{s1}) can be significantly suppressed by maximizing the repair rate (μ) relative to these failure rates by frequent servicing, and the drive system MTTF can be significantly raised by aggressively minimizing the single-point failure rate (λ_{s0}).

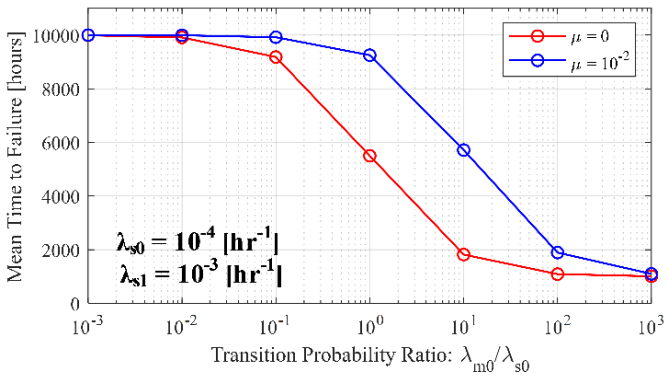

Figure 6.2-3 Predicted Mean Time to Failure (MTTF) for a fault-tolerant system as a function of the failure rate ratio $\lambda_{m0}/\lambda_{s0}$ for $\lambda_{s0} = 10^{-4}$ [hr^{-1}] and $\lambda_{s1}/\lambda_{s0} = 10$.

6.2.3. Strength and Limitations of Markov Chains

Markov chains are a powerful tool for performing reliability analyses of complex multi-state systems, but they are subject to limitations. These include an underlying assumption of exponential failure probability density functions, which may not hold for all components or repair scenarios. In addition, each state is only affected by itself and the immediate previous state as evident in (6.2.3) and it lacks memory of previous transitions between states. For example, frequent transitions between healthy and faulted states (i.e., transitions between *H* and M_1 in Fig. 6.2-2)

could contribute to increased wear that is not captured in the failure rates calculated from the model in (6.2.3).

In either case, additional states can be added to the system to better represent non-exponential distributions or to incorporate non-idealities such as aging [154]. For the purposes of this evaluation, simplified representations of the motor drive system using configurations such as the one in Fig. 6.2-2 are used to highlight overarching trends influencing the reliability of modular motor drive rather than seeking high quantitative accuracy.

6.3. Fault Modes and Stressors of IMD Components

The failure modes of any component can be described with Markov models, as illustrated in Fig. 6.3-1. Each failure mode has its own failure rate λ associated with it, with the total component failure rate being the sum of the underlying failure modes. Addressing or eliminating select failure modes directly affects the overall component reliability. Furthermore, these failure modes probabilities are dependent on the operating conditions of the component, which can improve or exacerbate component failure rates. Methods for quantifying the impact of component stresses can be estimated using standards like MIL-HDBK-217F and NSWC-11 [156], [157], or via a Physics of Failure (PoF) approach [146] that assesses component lifetimes based on physical models. Failure modes and stresses affecting the major IMD components are summarized in the following subsections.

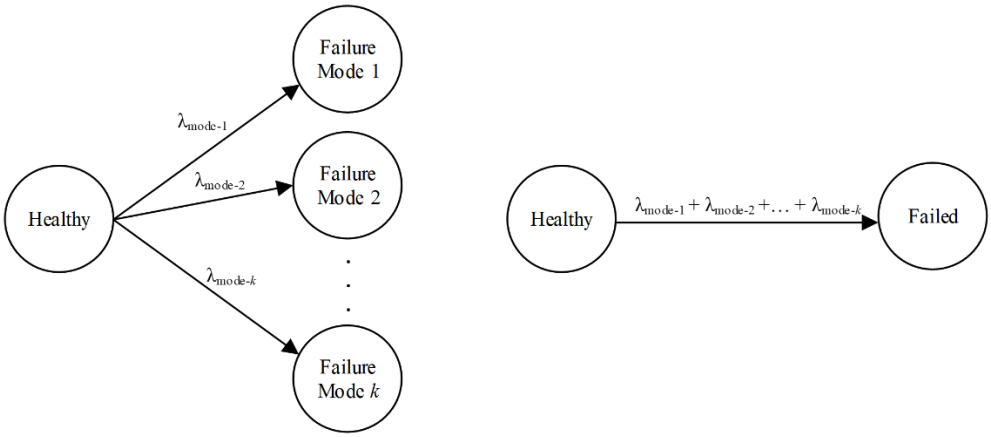

Figure 6.3-1 Markov representation of component failure modes and associated state reduction.

6.3.1. Stator Components, Fault Modes, and Stresses

The machine stator consists of a stator core and windings, each with its own failure modes. The stator core can experience delamination due to extreme temperatures, thermal cycling, or mechanical vibration. It is assumed for this reliability study that the stator core failure rate is sufficiently low to be neglected and that proper measures have been taken to avoid excessive stresses.

Failures in the stator windings are more common and have been documented extensively. Published failure rate values vary considerably over a range between 10^{-5} to 10^{-7} failures per hour [3], [43], [207]. These failure modes can be categorized as follows:

1. Winding open-circuit fault.
2. Terminal/connection open-circuit fault.
3. Short-circuit fault between phases or turns.
4. Short-circuit fault to stator core/ground.
5. Terminal/connection short-circuit fault.

It is assumed that the proposed IMD configuration is capable of detecting and responding to these failure modes. The common root cause of these failure modes can be ascribed to insulation failures. Insulation stressors and failure processes are described in [159], including:

- Temperature and voltage stress levels.
- Cycling rate of stresses.
- Choice of winding type and insulation materials.
- Manufacturing quality.
- Quality of maintenance.
- Random events such as voltage surges or foreign objects.

Considerations for temperature and voltage level stresses are quantifiable using the developed machine model in Chapter 4. However, the impact of the quadrotor mission duty cycle has not been captured in the machine analysis presented heretofore. Discussions related to UAM component reliability capturing mission profiles are discussed in [44], [208], [209]. It has been shown that repetitive short-duration thermal cycling can have cumulative adverse effects on the winding insulation life [52]. Furthermore, high dv/dt values associated with unfiltered VSI outputs are likely to have a determinantal impact on the insulation life as well. Although these stressors are not captured in the Chapter 5 machine analysis, a conservative winding failure rate will be selected accounting for these effects.

Next, the processes leading to failure include:

- Thermal aging that degrades mechanical and electrical properties.
- Insulation damage due to wire motion related to mechanical forces.

- Thermal expansion resulting in cracked insulation.
- Partial discharge in insulation gaps and voids.
- Electrical tracking.

Features incorporated into the proposed machine design presented in preceding sections mitigate some of these failure processes and modes. The proposed slot design and bobbin structure contributes to reducing opportunities for failures-to-ground or to other adjacent phases, and supplies sufficient cooling to the winding to prevent excessive insulation thermal aging. Furthermore, the selected winding potting helps to mitigate failure processes associated with wire movement and partial discharge. Specifically, eliminating gaps and voids in the potting material surrounding the windings is essential for reducing the effects of partial discharge, which is exacerbated by high-altitude operation in aerospace machines [70].

6.3.2. Power Electronics Component, Fault Modes, and Stresses

The core components of the power electronics modules are the SiC devices themselves, dc link capacitors, and the associated components such as gate drivers and printed circuit boards (PCB) boards. From a system and FT point of view, the primary failure modes of power electronics components can be summarized as: (1) open-circuit failures of the component; or (2) short-circuit failures of the component. It is assumed that both failure modes are detectable and that the proposed machine system can respond to these failures. The underlying causes of the failures in these components and the associated stress is more complex.

Power electronics reliability is discussed in [146], including a survey of power electronics failure root causes and stresses shown in Fig. 2.5-1(b). Overall, capacitors are identified as leading causes of failures followed by the PCB and the power semiconductor devices. The primary stressor

leading to failure is the steady-state temperature and thermal cycling of the electronics, resulting in mechanical fatigue of soldered leads and interfaces, corrosion, and degradation of dielectric materials. Furthermore, voltage is identified as a stressor contributing to dielectric breakdown and the formation of conductive filaments that can short traces and components. It is also expected that partial discharge associated with the quadrotor operation can contribute to power electronics failures.

The selection of capacitor type has reliability implications. Film capacitors, in particular, are notable for their desirable reliability characteristics, with capacitor failure component rates calculated using the curves provided in the TDK capacitor datasheet [210]. Additional capacitor lifetime models can be found in [211]. Primary stressors that were considered are capacitor voltage and temperature levels. It should be recalled that the capacitor voltage levels in the proposed FT IMD configuration increase with the number of faulted modules as described in TABLE 6.1-1. It is assumed that the capacitor temperature is held below 70 ºC in this evaluation.

Substantial historical failure data is available for mature Si IGBT power devices, which is not directly translatable to the selected emerging SiC power devices. For example, SiC devices have coefficients of thermal expansion (CTEs) and temperature capabilities that differ from those of IGBTs, resulting in differences in thermal cycling fatigue [169]. SiC packaging reliability limitations are examined in [171]. Some SiC device reliability data is provided by the selected device supplier in [212], reporting field reliability data of 2.3×10^{-9} failures per hour, although little context is provided about the nature of the considered failures. Like the selected capacitor, temperature and derating curves are supplied for the selected SiC device and used to estimate failure rates. Further discussions related to SiC device reliability can be found in [213]. In general,

the selected device has low stress due to effective cooling, low-amplitude thermal cycling, and low module voltage (relative to 1200V rating) as observed in TABLE 6.1-1.

6.3.3. Mechanical and Miscellaneous Component Considerations

Beyond the stator windings and power electronics, there are numerous other components incorporated into the proposed IMD that can fail. Stresses and failures in mechanical component (shafts, couplings, bearings, etc.) are discussed in NSWC-11. Bearings, in particular, have been identified as a common machine failure source and are included in this evaluation. The stresses on the bearings are assumed to be amplified by the loss of a stator module, resulting in an unbalanced radial load that is applied to the rotor shaft. Standard equations are provided in NSWC-11 or from bearing manufacturers [185] for bearing life which are used to account for additional radial loads on the bearing during fault events. Furthermore, it is assumed that the bearings are insulated or use ceramic rolling elements to minimize shaft circulating currents induced by the high VSI switching frequency.

Other fault modes can be attributed to the rotor core, magnets, and carbon fiber containment sleeve. Rotor core failures related to delamination are like those discussed above for the stator core and are neglected in this analysis. Next, magnets present a risk of demagnetization during a fault transient or other high-current events. The presented machine experiences minimal demagnetization during a short-circuit fault, so this fault mode is neglected. Finally, the failure modes associated with the carbon fiber containment sleeve are not well documented, and, therefore, are not included in this evaluation.

Failures associated with the module controller, gate drivers, current sensors, resolvers (rotor position sensor), and cooling systems are included in this analysis. It is assumed that failures in a

module controller, gate drivers, or current sensors result in open-circuit failures of the associated module due to an inability to deliver or implement current commands. Next, the resolver shares similarities to the proposed machine with its stator and rotor windings, which are susceptible to the winding failures described above. It is assumed that loss of position feedback represents a single-point failure that results in inability to operate the entire machine. Similarly, a loss in cooling caused by a failed pump, blocked channel, or leak prevents continuous operation of the machine due to overheating.

6.4. Reliability Analysis of a Four-Module IMMD

The Markov chain analysis introduced above has been applied to the proposed four-module FT machine. The objective is to evaluate the *relative* reliability impact of a modular FT architecture rather than to derive *absolute* reliability numbers.

6.4.1. Component Failure Data and Assumptions

The Markov chain analysis introduced in the preceding section has been applied to the four-module FT machine drive. Component failure data has been collected from the literature and component data sheets. These values have been adjusted to account for design features, stresses, and failure data source application, as well as technological advancements and maturity. Initial component lists and associated stressors are provided in TABLE 6.4-1. All module failure modes are assumed to be detectable and mitigatable (i.e., no single point failures related to the power electronics or windings).

The resolver failure data has been secured from MIL-HDBK-217F [156] as recommended by the resolver engineering handbook [214]. Capacitor failure rates are estimated using the selected capacitor technical datasheet [210] that incorporates voltage and thermal stresses. Baseline current

sensor, gate drivers, module controller, and cooling system rates are taken from previous reliability studies [26], [41], [43]. A 10x reduction in the failure rate is assumed for these components to reflect the impact of powerful market forces that are driving reliability improvements for demanding applications including aerospace and renewable energy (e.g., photovoltaic). Selected SiC MOSFET device failure rates discussed in [212] have been used to estimate device reliability. The operating voltage of these devices is substantially lower than their 1200 V rated value due to the IMMD structure (Fig. 6.1-2), and device temperature rises are expected to be low based on the chosen cooling method. Further discussion of SiC device reliability characteristics for aerospace applications can be found in [209].

Baseline winding and bearing failure rates are adopted from [43] with stressor multipliers determined using NSWC-11 [157]. Winding stressors include elevated temperature and module voltage. The winding failure rate has been adjusted to account for the selected stator design that reduces the likelihood of phase-to-ground and phase-to-phase faults, and for the low module voltages. Bearing stressors capture the expected impact of unbalanced magnetic radial load following a module loss. The bearing failure rate assumes that the stresses associated with misalignment and rotor unbalance have been minimized.

Components such as the machine housing, stator core, or rotor components are assumed to have low failure rates compared to the other components and are neglected in this simplified analysis. Furthermore, the dc power supply and machine gearbox are excluded from this analysis and treated separately from the IMMD subsystem reliability.

TABLE 6.4-1 COMPONENT FAILURE RATES UNDER HEALTHY AND STRESSED CONDITIONS ADOPTED FOR ANALYSIS

Component (Symbol)	Considered Stressors	Healthy λ [hours^{-1}]	Stressed λ [hours^{-1}] (1 module / 2 module lost)
Resolver (λ_{res})	-	$1.6\text{x}10^{-7}$	-
DC Link Capacitor (λ_{cap})	Temp., Volt.	$1.7\text{x}10^{-6}$	$2.5\text{x}10^{-6}$ / $6.7\text{x}10^{-6}$
Current Sensors (λ_{cs})	-	$2.0\text{x}10^{-8}$	-
Gate Driver (λ_{gd})	-	$1.9\text{x}10^{-7}$	-
SiC MOSFET Device (λ_{sw})	Temp., Volt.	$1.0\text{x}10^{-8}$	$5.0\text{x}10^{-8}$
Total Winding Coils (λ_{cls})	Temp., Volt.	$1.1\text{x}10^{-6}$	$4.7\text{x}10^{-6}$ / $8.0\text{x}10^{-6}$
Bearings (λ_{brg})	Unbalanced mag. forces	$3.2\text{x}10^{-6}$	$2.6\text{x}10^{-5}$
Cooling System (λ_{hex})	-	$5.2\text{x}10^{-6}$	-
Module Controller (λ_{ctrl})	-	$1.4\text{x}10^{-6}$	-

The expected lifetime for a conventional integrated motor drive (IMD) with a single module (i.e., no modularity) has been calculated using the values in TABLE 6.4-1 to establish a baseline for the multi-module analysis. It should be noted that the values in TABLE 6.4-1 were selected for the four-module case, and some differences in failure rate values are expected for a single-module configuration. Ignoring these differences in order to focus on overall trends, the TABLE 6.4-1 component failure rate values result in predicted inverter and motor failure rates of $4.5\text{x}10^{-6}$ and $9.7\text{x}10^{-6}$ failures per hour, respectively, leading to a predicted total single-module IMD failure rate of $1.4\text{x}10^{-5}$ failures per hour and a MTTF of 70,721 hours (8.073 years).

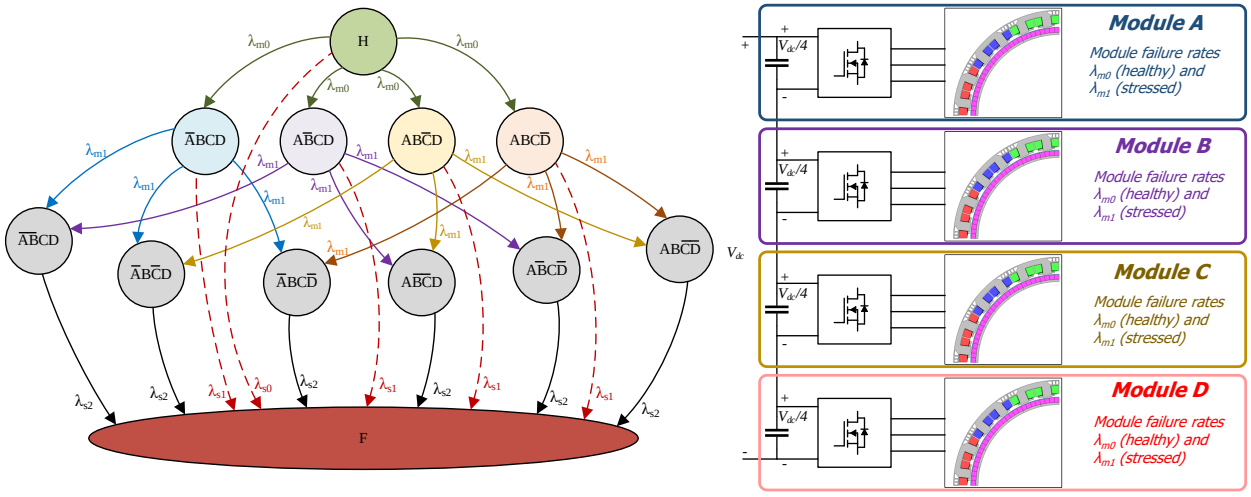

Figure 6.4-1 Four-module Markov chain diagram that allows two failed modules before IMMD failure. Repair transitions are not shown to minimize diagram complexity.

6.4.2. Four-Module Reliability Analysis

The TABLE 6.4-1 component failure rates have been applied to a four-module IMMD, leading to the Markov chain diagram in Fig. 6.4-1. The failure transitions include the single-module failure rate λ_{m0}, second-module (stressed) failure rate λ_{m1}, healthy single-point failure rate λ_{s0}, one module lost (stressed) single-point failure rate λ_{s1}, and third (final) failure rate λ_{s2}. These failure rates (in units of failures/hr) are calculated in

$$\left\{\begin{array}{l}\lambda_{m0}=\lambda_{cap}+n_{cs}\cdot\lambda_{cs}+n_{gd}\cdot\lambda_{gd}+n_{sw}\cdot\lambda_{sw}+0.25\cdot\lambda_{cls}+\lambda_{ctrl}=4.8\times10^{-6}\\ \lambda_{m1}=\lambda_{m0,stressed1}=6.0\times10^{-6}\\ \lambda_{s0}=\lambda_{hex}+\lambda_{brg}+\lambda_{res}=8.6\times10^{-6}\\ \lambda_{s1}=\lambda_{s0,stressed}=3.1\times10^{-5}\\ \lambda_{s2}=\lambda_{s0,stressed}+2\cdot\lambda_{m0,stressed2}=5.1\times10^{-5}\end{array}\right\} \quad (6.4.1)$$

with the number of components per module defined by n. Each module is assumed to have three current sensors (n_{cs} = 3), six gate drivers (n_{gd} = 6), and eighteen discrete switches (n_{sw} = 18) as shown in Fig. 6.1-2. A factor of 0.25 has been applied to the coil failure rate to reflect the reduced number of winding coils per module compared to a complete machine.

The resulting transition matrix and system has been implemented in MATLAB Simulink for the four-module drive system in Fig. 6.4-1. An analytical solution for the Fig. 6.4-1 Markov chain can be determined using the methodology in Section 6.5. Predicted MTTF results are provided in Fig. 6.4-2 for varying repair rate μ values. For low repair rates near 10^{-6} hr^{-1} (i.e., no repair), the MTTF is lower than that of the single module due to the much higher number of parts in the modular drive. However, when viewed on an expanded time scale in Fig 6.4-3, the probability of healthy operation *R(t)* for the no-repair four-module system is modestly better than that of the single-module case during the first 30,000 hours of operation. More significantly, the MTTF of the four-module drive surpasses that of the single-module drive when the repair rate reaches 2.5 x 10^{-5} hr^{-1}, corresponding to a high MTTR of approx. 4.6 years. For much higher repair rate values, the MTTF reaches 116,800 hours, a 65.2% increase over the value for the single-module drive.

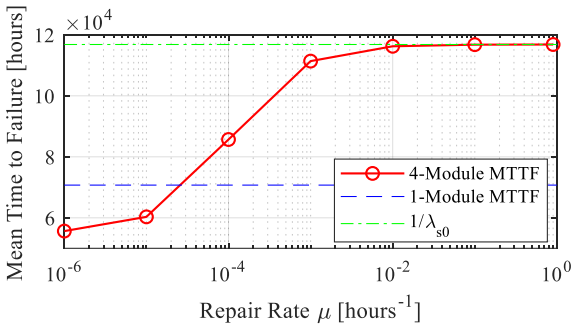

Figure 6.4-2 Predicted MTTF for four-module IMMD for varying repair rate μ. See (6.4.1) for failure rate λ_{s0}, λ_{s1}, and λ_{m0} values.

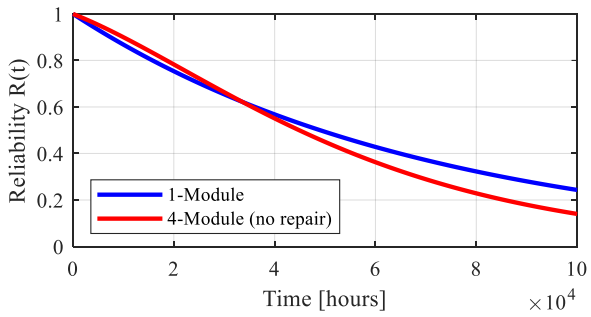

Figure 6.4-3 Predicted reliability probability curves for single-module and 4-module IMMD with zero repair rate (μ=0).

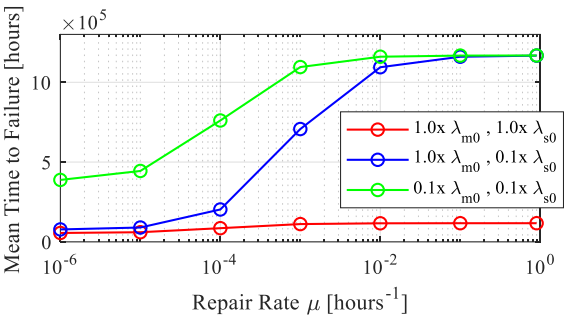

Figure 6.4-4 Predicted MTTF for 4-module IMMD vs. repair rate μ showing the impact of three combinations of single-module and healthy single-point failure rates λ_{s0} and λ_{m0}. See (6.4.1) for λ values.

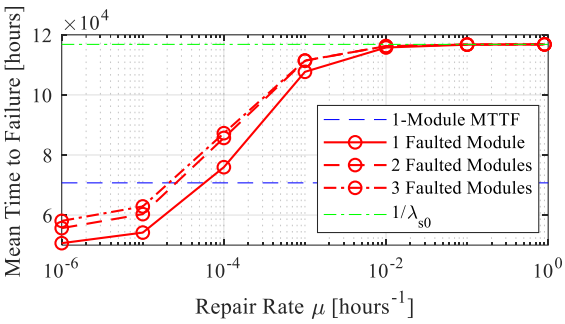

Figure 6.4-5 Four-module system showing the predicted impact of IMMD designs with 1, 2, and 3 faulted modules before IMMD failure. See (6.4.1) for failure rate λ values.

The Markov chain analysis can be used to perform failure rate sensitivity analyses for the four-module IMMD. Fig. 6.4-4 shows the impact of reducing the single-point failure rate (λ_{s0}) from its baseline value by a factor of 10, followed by a 10x reduction in the healthy module failure rate (λ_{m0}). Reducing the single-point failure rate by 10x increases the MTTF upper bound for high repair rates by a factor of 10, highlighting the powerful impact of λ_{s0} on the achievable drive reliability.

Reducing the healthy module failure rate λ_{m0} is unlikely to change the maximum reachable MTTF that is set by the single-point failure rate λ_{s0}, but lowering λ_{m0} significantly increases the reliability for lower repair rates or, alternatively, reduces the amount of repair service (i.e., reduces the repair rate μ) required to achieve high MTTF values. This is a significant observation because it emphasizes the importance and value of pursuing bold advances in the power electronics field that will make it possible to achieve much higher levels of integration in each power converter module that will dramatically reduce the value of the healthy module failure rate λ_{m0}. If the future of power semiconductor electronics leads to major improvements in the level of integration

comparable to that achieved in signal electronics by the leap from discrete semiconductor chips to integrated circuits, there is a real basis for optimism that spectacular improvements in the module's reliability will someday be achieved. Parallel advances in the ability to integrate power converters and machine windings into the same physical assembly will further expand the opportunities for major module reliability improvements.

The number of module faults that can be tolerated preceding IMMD failure affects the predicted MTTF of the four-module IMMD. To illustrate the impact of the number of faulted modules, the model in Fig. 6.4-1 was modified to also consider one and three faulted modules preceding IMMD failure. The additional states associated with the three-faulted-module case use the same stressed failure rate λ_{s1} as the two-faulted-module case. The predicted modular drive MTTF results for the three cases are presented in Fig. 6.4-5. Increasing the number of faulted modules preceding IMMD failure improves the IMMD's MTTF, particularly for low repair rate values. However, there are diminishing benefits as the number of tolerated module faults is incrementally increased from 1 to 3. That is, the MTTF improvement gained from incrementing the number of tolerated module faults preceding failure from one to two modules is substantially larger than the MTTF benefit provided by the subsequent increment from two to three tolerated module failures. The upper bound for the predicted MTTF for high repair rates continues to be the reciprocal of the healthy single-point failure rate λ_{s0} for each of the three cases.

6.4.3. Single Point Failure Rate Reduction and Source Elimination

The results of the preceding analysis demonstrated the potency of addressing the system single-point failures and increasing the repair rate to boost the MTTF. For that analysis, the single-point failures included the cooling system, resolver, and machine bearings, each of which is a candidate for single-point failure mitigation or elimination. The impact of sequentially mitigating or

eliminating these single-point failure sources (i.e., redundancy of non-module components) results in major MTTF improvements that are discussed here.

For example, the resolver stator can be modularized into four isolated sections like the proposed 4-module machine, allowing the resolver stator failure rate to be captured in the module failure transitions λ_{m0}. Similar modularization approaches can be applied to the cooling system, albeit with mass and volume tradeoffs. Significantly suppressing the probability that the bearings will cause a single-point failure results in a major improvement of the upper-bound MTTF value to 312,400 hours, achieving a 4.4x improvement over the baseline case.

The remaining bearing single-point failure can be mitigated by introducing active bearing monitoring (e.g., vibration or lubrication analysis) [215]. That is, active monitoring is used to recognize bearing degradation before a failure occurs so that the bearings will be replaced before a catastrophic failure occurs that would qualify as a single-point failure. This scenario is addressed in [43] where an aged bearing state ("Bearing Failure Imminent") is added to the system as shown in Fig. 6.4-6 to significantly reduce the ability of the bearings to become a dangerous source of single-point failures in the motor drive. For this exercise, the new state is modeled to conservatively recognize that the bearing has reached its half-life point, corresponding to a Markov transition rate of $2 \cdot \lambda_{brg}$. The same value of repair rate μ used for the modules has been assigned to the bearings for this analysis.

Adding this bearing active monitoring to the IMMD modularization of the resolver and cooling system discussed above causes the effective single-point failure rate in this exercise to drop to nearly zero, resulting in impressive improvements of the MTTF for the four-module IMMD. The impact of raising the repair rate μ is plotted in Fig. 6.4-7 for the limiting case of $\lambda_{s0}=0$ (i.e., elimination of all single-point failures). This plot indicates that an expected MTTF of 1.32×10^8

hours (i.e., failure rate = $7.6\text{x}10^{-9}$ hr^{-1}) is estimated for the four-module IMMD for an aggressive repair rate of $\mu=10^{-1}$ repairs/hr. This is a dramatic increase in the predicted MTTF for the four-module IMMD over that of the baseline single-module drive by a factor of 1866x.

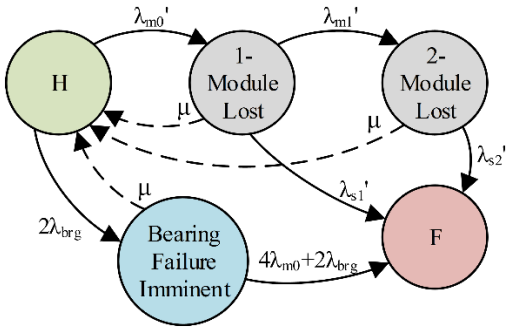

Figure 6.4-6 Markov chain diagram for a four-quadrant IMMD system that incorporates bearing health monitoring and early replacement, significantly reducing bearing single-point failures.

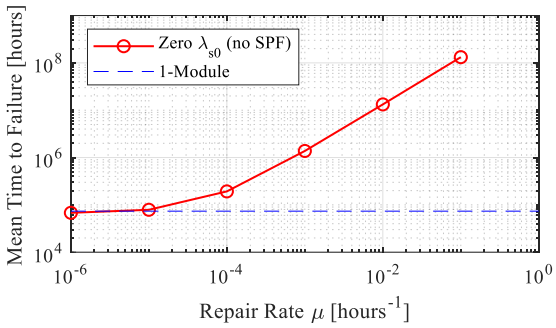

Figure 6.4-7 Predicted IMMD system MTTF vs. repair rate μ for the limiting case of complete elimination of single-point failures (i.e., $\lambda_{s0}=0$). The baseline values of λ_{m0} and λ_{m1} are in (6.4.1).

This dramatic MTTF boost is only aspirational because of the daunting challenge of eliminating *all* single-point failure sources. For example, the success of the bearing active monitoring system depends on the ability to confidently detect bearing degradation before failure, a critical feature that is not shared by many of the other key motor drive components. In addition, there are many other legitimate sources of single-point failures including the machine rotor, or the reliability of the proposed bearing health detection system itself, that have not been addressed in this analysis. Major effort including comprehensive failure modes and effects criticality analysis (FMECA) [26], [216] will be required to identify as many of the single-point failure sources as possible and then to find the most effective ways to eliminate or suppress them without having a major negative impact on the IMMD mass, volume, and cost.

These study results have provided valuable insights into the key factors influencing the reliability characteristics of fault-tolerant modular motor drives, as well as identifying fertile research opportunities for improving their reliability. The study results make it clear that modularity can only deliver major reliability benefits if it is combined with high repair/service rates that encompass advanced health monitoring techniques. In addition, the results have highlighted the critical importance of suppressing every possible source of single-point failures to harvest the full potential of the IMMD technology for improving the drive system reliability.

6.4.4. Parametric Study of Reliability Characteristics of Modular Motor Drives with Zero Repair

The importance of the repair rate μ for achieving major reliability improvements in modular motor drive systems can be further emphasized and clarified by investigating the reliability characteristics of modular drives with no repairs (μ=0). The previous analysis studied a four-module IMMD, although any number of modules greater than one can be used in this type of FT drive system. In order to minimize derating effects following a fault, increasing the number of modules is desirable as reflected in the definition of the derating factor F in (6.1-1). However, increasing the number of modules inevitably results in increased total part count, lowering the MTTF values in nearly all cases for low repair rate scenarios, assuming similar module component failure rates.

The impact of the number of modules and the remedial operation stress on the no-repair MTTF for an IMMD has been studied parametrically by considering a generic n-module system with one faulted module state. The effect of faulted operation stress can be evaluated by applying a variable stress factor α ($\geq$1) to the failure transition between the remedial *M1* state and the failed *F* state

(i.e., $\lambda_{s1} = \alpha \cdot (n\text{-}1) \cdot \lambda_{m0} + \alpha \cdot \lambda_{s0}$) in Fig. 6.2-2. A parametric study varying the number of modules n, the module stress factor α, and the ratio of the single-point failure rate λ_{s0} to the module failure rate λ_{m0} has been carried out. The MTTF calculation in (6.2.4) for the IMMD has been modified for this parametric study to incorporate the number of modules, post-fault stresses, and the zero-repair assumption, leading to

$$MTTF = \frac{(n + \alpha \cdot (n-1)) \cdot \lambda_{m0} + \alpha \cdot \lambda_{s0}}{\alpha \cdot n \cdot (n-1) \cdot \lambda_{m0}^2 + \alpha \cdot (2 \cdot n - 1) \cdot \lambda_{m0} \cdot \lambda_{s0} + \alpha \cdot \lambda_{s0}^2} \tag{6.4.2}$$

for $n > 1$.

For simplicity, the healthy module failure rate λ_{m0} has been fixed at 10^{-6} hr^{-1}regardless of the number of modules, and zero repair rate (μ=0) is assumed. Three values of the variable stress factor α are evaluated (α = 1, 2, and 10), as well as three values of the single-point failure rate λ_{s0} (λ_{s0} = 10^{-7}, 10^{-6}, and 10^{-5} hr^{-1}). The predicted MTTF values of the modular IMMD are then normalized by the MTTF of an equivalent single-module system (n = 1) with the same module failure rate value λ_{m0}.

The results of this parametric study are presented in Fig. 6.4-8 for this simplified analysis with constant failure and repair parameters. The two-module case with no stress impact on the module failure rate (n=2, α=1) achieves an improved MTTF with zero repairs for all three cases. A maximum improvement of 47.6% with α=1 is observed when $\lambda_{m0} > \lambda_{s0}$, which shrinks to an 8.3% improvement when $\lambda_{m0} < \lambda_{s0}$, again highlighting the major benefits of reducing the single-point failure rate λ_{s0}. However, the normalized drive MTTF drops below unity monotonically as the number of modules n is increased above 2 for almost all considered cases when the other variables α and λ_{s0} are held constant. In particular, the presence of elevated faulted operation stress (α > 1) tends to overwhelm any no-repair MTTF gains provided by modularity.

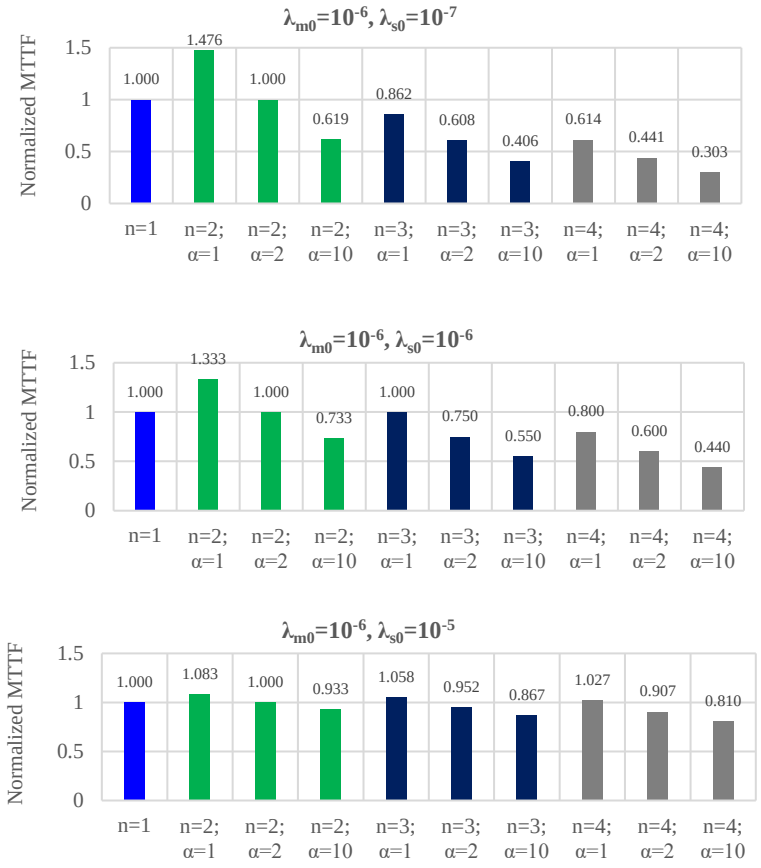

Figure 6.4-8 Predicted normalized MTTF results for a no-repair (μ=0) parametric study using *n* modules with $\lambda_{s1} = \alpha \cdot (n-1) \cdot \lambda_{m0} + \alpha \cdot \lambda_{s0}$.

If the MTTF formula in (6.4.2) is evaluated for the most favorable idealized case when the single-point failure rate is zero (λ_{s0} = 0) and the variable stress factor is unity (α=1), the equation for the normalized MTTF simplifies to:

$$MTTF_{norm} = \frac{MTTF(n)}{MTTF(n=1)} = \lambda_{m0} \cdot MTTF(n) = \frac{2n-1}{n \cdot (n-1)} \tag{6.4.3}$$

for n > 1, λ_{s0} = 0, and α = 1.

There are two important observations that can be drawn from this equation. First, the value of $MTTF_{norm}$ is independent of the healthy module failure rate λ_{m0} and, second, the value of $MTTF_{norm}$ has a peak value of 1.5 for two modules (*n*=2) and drops below unity for all higher numbers of

modules (n>2). The only reason that $MTTF_{norm}$ rises above unity even for n=2 is the starting assumption that two module failures are required for system failure of the IMMD modeled in Figure 6.4-1. Based on the simplifying assumptions that were made for this analysis, (6.4.3) indicates that modularity will not provide any value for increasing the IMMD's system reliability beyond that of a single module in the absence of repair, regardless of the number of modules (above 2) or the value of the healthy module failure rate λ_{m0}, provided that the value of the healthy module failure rate is independent of the number of modules.

However, there are a variety of reasons why the healthy module failure rate λ_{m0} may *not* be independent of the number of modules in practice. For example, increasing the number of modules may improve the module failure rate by reducing module operating stresses (e.g., lower voltages) or by enabling the use of smaller components with better reliability compared to a non-modular design. These opportunities can be exploited by designers to realize no-repair MTTF values higher than those illustrated in Fig. 6.4-8. Despite this important caveat, the presented parametric study has highlighted the importance of rapid repair for maximizing the reliability potential of any fault-tolerant modular motor drive system.

6.4.5. Four-Module IMMD Reliability Analysis Conclusions

This section summarizes key results from studying the reliability of a fault-tolerant integrated modular motor drive using Markov chain analysis. The analysis has been completed in the context of a power-dense four-module PM synchronous machine, but the analytical techniques can be extended to any type of machine configured as a modular motor drive. This simplified study has demonstrated that modularity by itself cannot provide substantial reliability gains to close the identified UAM reliability gap. However, the analytical results have clearly shown that modularity

combined with rapid fault detection and repair greatly improve the potential of the modular drive to achieve major system-level aircraft reliability improvements.

Further, the investigation has clearly demonstrated that this potential can only be fully realized if the single-source failure rates are suppressed to the greatest possible extent. The results have shown that the IMMD system MTTF could be increased by a factor >1000x if all single-point failures were mitigated by either the added redundancy of non-module components or by active health-monitoring, providing an aspirational target for future modular drive researchers and developers. Improved understanding and mitigation of all probable single-point failure sources in these IMMDs provides a potent pathway for future research that can contribute significantly to reaching the challenging failure rates required to qualify the quadrotor aircraft's propulsion system for commercial flight.

In addition to highlighting the importance of prompt repair and suppressing single-point failures, this work has also demonstrated the value and importance of accelerating efforts to dramatically reduce the healthy module failure rate via increased emphasis on improving the reliability of power electronics and its physical integration with electric machines. The wide chasm between the failure rates of today's state-of-the-art motor drive power electronics and the multiple orders-of-magnitude higher levels required for airworthy electrified aircraft propulsion drives can only be closed if major leaps can be made in the achievable reliability of this backbone technology. Higher repair rates and lower single-point failure rates will not be able to close the daunting chasm alone.

Finally, it should be noted that the fault-tolerant modular motor drive reliability analysis presented here has a level of generality that extends well beyond aerospace applications and the PM machines discussed in this paper, providing MMD designers with tools and insights that can

be applied to a much wider range of industrial, commercial, and transportation applications. Although many of these other applications do not have the same high level of reliability requirements that are found in aerospace systems, the techniques discussed here can be adapted for exploring the usefulness of modular motor drive technology in a wide variety of drive configurations with any type of motor topologies. For example, these techniques can be used to evaluate the expected MTTF improvement achievable with different levels of component derating and the resulting cost increase; or deciding whether to focus engineering effort on improving module reliability or single-point failure mode mitigation. The future success of modular motor drives in any application depends on having the necessary engineering tools to quantitatively evaluate their potential for improving the overall drive system reliability, and this study has attempted to strengthen the set of analytical tools available to accomplish that objective.

6.5. Figure of Merits for Comparing FT Motor Drives

The above analysis presents a reliability analysis with a predominate focus on modular machines with multiple independent sets of three-phase windings. However, there are numerous FT topologies for power electronics and electrical machines but an established methodology for selecting a preferred motor drive FT approach for a given application does not exist. To illustrate, the FT motor drive concepts shown in Fig. 6.5-1(a) all can operate in a remedial state such as the one identified in Fig 6.5-1(b). Each Fig. 6.5-1(a) FT system is capable of continued operation after a motor drive failure, but the preferred approach for a given application is not readily determined without clear criteria for making the selection.

Figures of Merit (FoMs) provide a useful method to evaluate the goodness of electrical machines and drives for achieving performance objectives. For example, FoMs such as machine

shear stress and winding current density are commonly used to evaluate the electromagnetic and thermal performance of electrical machines [175]. For power electronics components, Baliga FoMs in [217], [218] are used to compare the capabilities of power semiconductor switch devices at high switching frequencies. For FT machine drives, FT performance/degradation FoMs have been proposed in the literature including the Silicon Overrating Cost Factor (SOCF) and the Fault Power Rating Factor (FPRF) in [33].

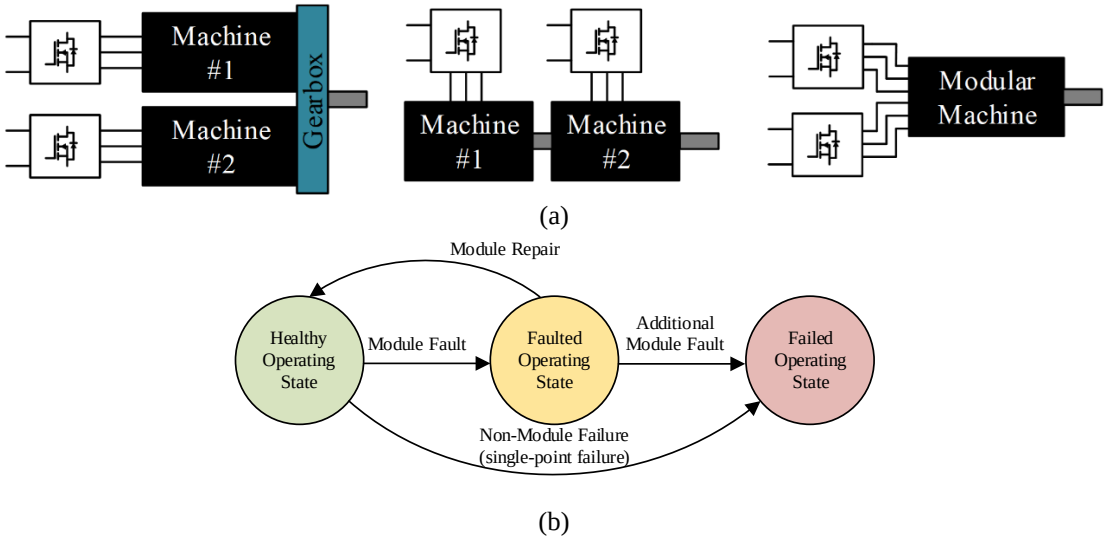

Figure 6.5- 1 (a) Examples of FT machine drive topologies: direct redundancy using two machines and a shared gearbox (left), two stators on a common shaft (center), and modular machine drives (right); (b) State diagram showing operating states (healthy, faulted, and failed) of a FT system and corresponding transitions

This section proposes a set of fault tolerance FoMs (FT-FoMs) to better quantify and compare the achievable system reliability benefits of candidate motor drive topologies, including the impact of undesired performance penalties (e.g., component overrating) in an attempt to expand and enhance the performance-oriented metrics defined in [33]. The intent of these metrics is to provide users some new tools to perform high-level quantitative comparisons between candidate FT topologies that can be helpful for carrying out down-selection exercises. This thesis also provides

a proposed procedure for calculating and applying these metrics using Markov Chains, as well as discussion on how to use the proposed metrics with FT machine drive topologies.

Before introducing the definitions of these FT-FoMs, some guidelines are provided to help inform potential users about some of the key characteristics of these metrics, the parameters that affect their values, and, finally, their design value and limitations.

1. The units of these FoM metrics vary widely and depend entirely on their definitions. While several are unitless because they are ratios of two parameters with the same units, others have unusual units such as hr/kg.
2. The quantitative values of the FoM metrics vary widely among the metrics, and any attempt to compare the quantitative values of two different FoM metrics is a futile exercise. The value of these figures of merit comes from comparing the quantitative values of the *same* FT-FoM metric for different candidate fault-tolerant motor drive topologies.
3. All of the FoM metrics in this report have been defined so that higher values are better when comparing their values among different candidate topologies for the same FT-FoM metric.
4. Each FoM metrics is defined so that its value for a candidate topology depends on the ratio of the topology's mean time to failure (*MTTF*) to one of the other performance metrics such as the MTTF of the motor drive modules, the frequency of repairs, the likelihood of single-point failures, etc. As a result, the "winning" topology for one of the FT-FoM metrics among a group of topologies that all share the same set of parameters may no longer be the winner for a different FT-FoM where the performance metric used to evaluate the FoM metric is changed.

5. Since the definition of each of the FT-FoM metrics is designed to highlight a different aspect of the candidate's attractiveness for fault-tolerant motor drive applications, a topology that rates the highest among the group of candidates evaluated for one FT-FoM metric may rank much lower for another FT-FoM metric, even when the same basic parameters are used to evaluate all of the candidate topologies for both FT-FoM metrics. This common situation gives designers the opportunity to evaluate engineering tradeoffs among the candidate topologies based on their FT-FoM values in order to determine which topology is "best" overall for a particular application

6.5.1. Proposed Fault Tolerance Figures of Merit (FT-FoMs)

The goal of the developed FoMs is to provide quantifiable metrics to simultaneously evaluate the reliability improvement delivered by a candidate FT motor drive topology and the degree to which these improvements are offset by selected performance penalties associated with the topology (e.g., number of parts, component derating, frequency of service, etc.). In general, these Fault Tolerance FoMs take the form

$$\text{FT-FOM} = f(\Delta\text{Reliability, Performance Impact}) \tag{6.5.1}$$

when the reliability and performance impacts are estimated and quantified using analytical formulas. This allows the user to perform quantifiable high-level comparisons of candidate topologies in order to perform down-selections for specific application.

In real applications, it is impractical to define a single universal FT-FoM that can be trusted to carry out the down selection process due to the complexities and nuances of the candidate FT motor drive topologies and the intended application. Given this reality, three sub-classes of FT-FoM metrics are proposed in this report to help evaluate and distinguish FT topologies in terms of

their reliability improvements and offsetting performance penalties. In total, seven distinct FT-FoM metrics are presented that can be used to draw comparisons between FT topologies, or customized to better fit the user's needs. These includes two FoM metrics focused on evaluating the topology's reliability improvement features, two highlighting the candidate topology's single-point failure (SPF) and repairability characteristics, and three designed to evaluate the topology's reliability-performance tradeoffs

6.5.1.1. System Reliability Metrics

The first sub-class of FoM metrics is focused on assessing the reliability improvement of candidate FT motor drive topologies. The first metric $FTFOM_1$ is defined as

$$FTFOM_1 = MTTF / MTTF_{std} \quad \text{[unitless]} \tag{6.5.2}$$

Where the candidate FT motor drive's Mean Time to Failure (*MTTF* in hours) is compared with the expected *MTTF* of the baseline (standard) topology without fault-tolerant features, $MTTF_{std}$, by taking the ratio of these two values. This metric provides a first-pass quantified indicator for evaluating the level of expected reliability benefits achieved by replacing a baseline topology with a more fault-tolerant alternative. The higher the value of $FTFOM_1$, the greater the benefits of the topology's FT features for improving the motor drive's system reliability compared to the selected baseline (typically a two-level VSI).

The second FoM metric in this sub-class is $FTFOM_2$ that quantifies the improvement of the motor drive system reliability achieved by a candidate topology over that of the baseline topology ratioed to the reliability of the group of modular drive units that comprise the candidate topology (i.e., the level of reliability improvement achieved by adopting a modular topology with repairable drive unit modules). $FTFOM_2$ is defined as

$$FTFOM_2 = \Delta MTTF \,/\, MTMF \quad \text{[unitless]} \tag{6.5.3}$$

where the improvement in the candidate topology's MTTF over that of the baseline topology, *ΔMTTF*, is expressed as

$$\Delta MTTF = MTTF - MTTF_{std} \quad \text{[hrs]} \tag{6.5.4}$$

and the module group mean time to failure (*MTMF*) is defined as the expected time to the first failure of the total population of n_m identical FT drive modules used to implement the candidate topology. That is, if the mean time to failure of a single module is $MTTF_m$, then the value of the *MTMF* would be $MTTF_m$ / n_m assuming that all of the modules are operating under the same baseline conditions. Summarizing, this metric can be interpreted as the reliability improvement achieved by a candidate topology normalized by the mean time to the first failure among the group of n_m modular drive units. A higher value of $FTFOM_2$ is desirable because it indicates that a candidate FT topology is achieving a larger increase in its system MTTF for the same value of module group mean time to failure (MTMF).

6.5.1.2. Single Point Failure & Repairability Characterization Metrics

The two FT-FoM metrics in the second sub-class, $FTFOM_3$ and $FTFOM_4$, are useful for assessing the impact of single point failures (i.e., failure modes that bypass the FT modular drive components) and the system repair rate (i.e., the frequency of repairing faulted modules) on the overall drive system reliability.

The first of these two FoM metrics, $FTFOM_3$, is defined as

$$FTFOM_3 = MTTF \,/\, MTTSPF \quad \text{[unitless]} \tag{6.5.5}$$

where Mean Time to Single Point Failures (*MTTSPF*) represents the expected time to failure for non-redundant components in the drive system (e.g., bearings in a standard motor). A $FTFOM_3$

value that is close to one indicates that a candidate FT drive topology is predominantly determined by the single point failure rate. This means that increasing the number of redundant modules or improving the repair rate will have a negligible effect on increasing the drive system MTTF value. As a result, the value of $FTFOM_3$ is valuable for helping the user to decide whether reliability improvements efforts should be focused on reducing single point failures or improving the FT module reliability and/or repair rate.

The second of these FT-FoM metrics, $FTFOM_4$, provides a measure of the sensitivity of a candidate FT drive topology's *MTTF* value to the drive system's repair rate. It is defined as

$$FTFOM_4 = MTTF_{HR} / MTTF_{NR} \quad \text{[unitless]} \tag{6.5.6}$$

where $MTTF_{HR}$ is the candidate topology's MTTF with a specified high repair rate, and $MTTF_{NR}$ is the topology's MTTF value without any repairs. A FT candidate system with a higher value of $FTFOM_4$ indicates that it is benefiting more from a selected repair rate compared to another topology with a lower $FTFOM_4$ value evaluated at the same repair rate.

6.5.1.3. Reliability/Performance Tradeoff Metrics

The third and final sub-class of FoM metrics provides a means of quantifying the reliability improvement achieved by a candidate FT drive topology in comparison to a second metric that represents a performance penalty (e.g., mass) of the candidate topology. Each of these reliability/performance FoM metrics takes the following form

$$FTFOM = \frac{\Delta MTTF}{P} \tag{6.5.7}$$

where P is any quantifiable performance penalty metric that applies to the candidate topology. Three examples of this sub-class of FT FoMs that are applicable to aerospace propulsion applications are defined in this section using the following three performance penalty metrics of

candidate FT drive topologies: FT drive system mass, module steady-state power overrating, and topology maximum steady-state kVA output power capability.

Minimizing the added system mass (Δkg) associated with the incorporation of FT features is arguably the most important performance penalty in aerospace applications. The first of the reliability/performance FT-FoM metrics, $FTFOM_5$, directly captures this tradeoff by forming the ratio of the MTTF improvement achieved by the candidate topology to the mass penalty Δkg (i.e., increase in FT topology mass above baseline system mass):

$$FTFOM_5 = \Delta MTTF / \Delta kg \qquad \text{[hrs/kg]} \tag{6.5.8}$$

Unfortunately, determining the mass penalty Δkg in (6.5.8) is often difficult during concept studies and not easily determined using analytical formulas. In this situation, the use of power overrating factors can be used as a simplified stand-in for the mass penalty. Such overrating factors also have a correlation with the cost of the fault-tolerant drive system which is another important overall drive system metric that may be more important than mass in some applications.

Throughout this study, it is assumed that a FT drive system requires module power overrating compared to a baseline drive without fault tolerance in order to maintain output performance equivalent to that of the original healthy drive system until the system enters its final failed state. It can be expected that this power overrating will be accompanied by increased mass, volume, and cost due to the impact of the increased combined power rating of the components used to build the FT drive system. A basic overrating factor F is defined in (6.1.1) to capture the impact of this overrating of both the machine and power electronics in a simplified manner. This leads to the second FT-FoM in this sub-class, $FTFOM_6$, that is defined as the ratio of the candidate FT topology's MTTF improvement to its overrating factor, expressed as

$$FTFOM6 = \Delta MTTF / F \quad \text{[hr]} \tag{6.5.9}$$

A candidate FT topology with a high value of $FTFOM_6$ indicates that it can provide a larger improvement in the drive system mean time to failure with a smaller amount of module steady-state power overrating than other topologies.

A modified version of this FT-FOM metric can be defined using a different version of the overrating factor that focuses on the total cumulative steady-state kVA rating of the power electronics inverters in a candidate FT topology compared to the kVA rating of the single module inverter in the baseline (standard) topology. This alternative kVA overrating factor, KVAOF, is defined as

$$KVAOF = \frac{\text{Summed total kVA ratings of all inverter modules}}{\text{kVA rating of inverter in baseline design}} \quad \text{[unitless]} \tag{6.5.10}$$

Where all of the kVA ratings are based on steady-state operation. This KVAOF overrating factor reflects the same overrating characteristics captured by the overrating factor *F* but does so with an additional level of detail by focusing on the total cumulative kVA ratings of the power electronics modules included in a candidate FT topology rather than simply using the number of modules. This leads to a different version of the overrating FoM metric in (6.5.9) that is expressed as

$$FTFOM_7 = \frac{\Delta MTTF}{KVAOF} \quad \text{[hr]} \tag{6.5.11}$$

Further, this this kVA factor can also be modified based on expected increased inductance from the machine and its associated power factor. Generally, FT machines with a power factor of 0.7 are expected to have a characteristic current of 1 per-unit. An important metric for the machine but certainly to the detriment of drive kVA sizing.

Both versions of this overrating FT-FoM, $FTFOM_6$ and $FTFOM_7$, can prove to be useful alternatives to the mass-based FT-FoM, $FTFOM_5$, in cases where the mass scaling relationships associated with modular topologies are poorly understood with large error bands, or cases where drive system cost is more important than mass.

It is recognized that power converter modules can be designed in some cases to deliver overload power values higher than their rated values for limited periods of time. In some applications, it may be possible to take advantage of these overload power capabilities during fault conditions. As a result, the steady-state power ratings of these modules can be reduced, thereby reducing the mass and penalty associated with the modular drive configuration. In fact, the value of KVAOF can be reduced to 1 if the modules all have sufficient short-term power overload capability so that no increase in the module steady-state kVA ratings is needed to handle the fault cases. This benefit will automatically be reflected in the value of $FTFOM_7$ since lower values of KVAOF result in higher values of this metric.

This discussion could lead to the over-simplified conclusion that designing FT drive topologies that take advantage of the overload power operation of drive modules during faults will always be superior to other candidate topologies that are designed using the more conservative approach based entirely on module steady-state power ratings. The tradeoffs between these two approaches are more complicated in reality because operating the modules in their overload mode increases their electrical and thermal stresses which, in turn, reduces the configuration's $\Delta MTTF$ value that appears in the numerator of these FT-FoM definitions. As a result, the increased level of machine drive stress associated with overload operation must be reflected in the *MTTF* calculation, a topic that is discussed in Section 6.5.4.

TABLE 6.5-1 SUMMARY OF PROPOSED FT FOMS

Metric Group	*FT-FOM*	*Calculation*	*Measure*
System Reliability Improvement	1	$MTTF\ /\ MTTF_{std}$	Measure of FT topology reliability normalized by MTTF of a baseline topology (often 2-level VSI)
	2	$\Delta MTTF\ /\ MTMF$	Measure of topology reliability improvement normalized by MTTF of the module group (MTMF)
SPF & Repairability Characterization	3	$MTTF\ /\ MTTSPF$	Metric indicating the dominance level of the single point failure rate in determining FT topology reliability
	4	$MTTF_{HR}\ /\ MTTF_{NR}$	Measure of the influence level of the repair rate on the reliability of a FT drive topology
Performance Tradeoff Metrics	5	$\Delta MTTF\ /\ \Delta kg$	Measure of FT drive topology reliability improvement gained per increment in topology mass
	6	$\Delta MTTF\ /\ F$	Measure of FT drive topology reliability improvement in relation to the level of required module overrating
	7	$\Delta MTTF\ /\ KVAOF$	Variant of $FTFOM_6$ that uses the combined steady-state kVA overrating of the modules for the normalization

6.5.1.4. Proposed Fault Tolerant Figure of Merit Summary

A summary of the proposed FT-FoM metrics introduced in this section is provided in TABLE 6.5-1. Each metric provides a different insight into specific attributes of a candidate FT drive system topology from both system reliability and performance perspectives. Used in combination, these metrics make it possible to develop a more complete comparative evaluation of alternative FT drive topologies and the tradeoffs between them. As a result, they give users valuable tools to help them determine which FT topologies are best suited for their application, or to evaluate where engineering effort should be directed to improve system reliability with the lowest negative impact on key performance metrics. Finally, the TABLE 6.5-1 metrics can be modified and customized to meet the specific needs of the user's application. Examples of applying these FT-FoM metrics to various test cases are provided in Section 6.2.5.

6.5.2. Determining Mean Time to Failure (MTTF) Using Markov Chains

The performance metric that appears in the definitions of all of the FT-FoM metrics provided in Section 6.5.1 is the Mean Time to Failure (*MTTF*) of the candidate fault-tolerant motor drive system. For these FT-FoM metrics to be useful, it is critical to develop *MTTF* calculation methodologies that allow users to quickly make comparisons and draw conclusions about alternative FT motor drive topologies. This this presents an evaluation methodology using Markov Chains and component failure rates, although other evaluation methods such as those described in [153], [216] can be used depending on the level of detail desired by the user. This section summarizes a methodology for evaluating the *MTTF* value for a candidate FT motor drive topology using Markov Chains.

Continuous-time Markov Chains break a system into multiple unique states dependent on the operating mode of the system (e.g., healthy, failed, faulted, aged, etc.). An individual state that is a member of an *n*-state system will have transitions entering and leaving the studied state as shown in Fig. 6.5-2 and can be described by the following differential equation

$$\frac{dM_i}{dt} = \sum_{k=1,k\neq i}^{n} (\lambda_{m,ki} \cdot M_k - \lambda_{m,ik} \cdot M_i) \tag{6.5.12}$$

where M_i represents the probability of being in state-M_i at time t and $\lambda_{m,ik}$ representing the probability of a transition occurring from state-M_i to state-M_k. For reliability evaluation and calculation of *MTTF*, these transition probabilities are derived from failure rates of the underlying system components at the source state (e.g., transition $\lambda_{m,ik}$ represents the failure rate associated with operation in state-M_i shown in Fig. 6.5-2, causing a transition into a different fault or failure state k).

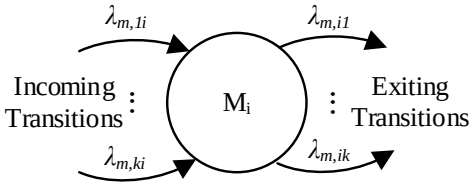

Figure 6.5-2 Single Markov chain state with incoming and exiting transitions shown.

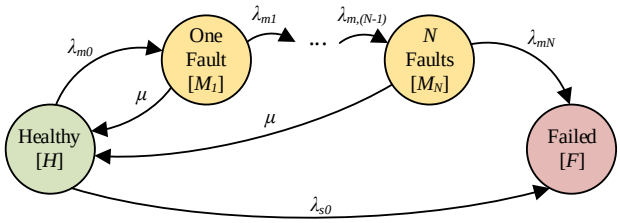

Figure 6.5-3 Generic FT-system with simplified transition notation showing with healthy, faulted, and failed states shown.

These states can be assembled into a complete system diagram such as the generic FT system example in Fig. 6.5-3 using a simplified notation following the FT categorization of states. At a minimum, FT systems are separated into three groups of states: healthy (state-*H*), faulted (state-*M*), and failed (state-*F*). Similar designations can be adopted for transition probabilities. Transitions from healthy-to-faulted, faulted-to-faulted, and faulted-to-failed states are referred as module failure rates ($\lambda_{m,k}$), from healthy-to-failed states as single point failure (SPF) rates ($\lambda_{s,k}$), and return transitions from faulted-to-healthy states as repair rates (μ). The failed state in Fig. 6.5-3 is shown to be absorbing (no transitions from failed to healthy) to reflect applications where operation in a failed state leads to a catastrophic outcome

Each state shown in Fig. 6.5-3 has a defining state equation similar to (15), which can be assembled into the $n\times n$ system

$$\begin{bmatrix} \dot{H} \\ \dot{M}_1 \\ \dot{M}_2 \\ \vdots \\ \dot{M}_{N-1} \\ \dot{M}_N \\ \dot{F} \end{bmatrix} = \begin{bmatrix} -\lambda_{m0}-\lambda_{s0} & \mu & \cdots & \mu & 0 \\ \lambda_{m0} & -\lambda_{m1}-\mu & \cdots & 0 & 0 \\ 0 & \lambda_{m1} & \cdots & 0 & 0 \\ \vdots & \vdots & \ddots & \vdots & 0 \\ 0 & 0 & \cdots & 0 & 0 \\ 0 & 0 & \cdots & -\lambda_{mN}-\mu & 0 \\ \lambda_{s0} & 0 & \cdots & \lambda_{mN} & 0 \end{bmatrix} \begin{bmatrix} H \\ M_1 \\ M_2 \\ \vdots \\ M_{N-1} \\ M_N \\ F \end{bmatrix} \tag{6.5.13}$$

which is in the general form and corresponding solution

$$\begin{aligned} \dot{x} &= Ax \\ x &= e^{At}x_0 \end{aligned} \tag{6.5.14}$$

with state probability vector x, transition probability matrix A, and x_0 represents the initial state of the system. Since the system is assumed healthy at the beginning of its life, the initial state is represented as $x_0 = [1, 0, \ldots, 0]^T$. State probabilities can be determined by calculating the matrix exponential in (6.5.14) that is valuable for calculating the system *MTTF* (different than (6.2.2)) according to

$$MTTF = \int_0^\infty (1-F)dt = \int_0^\infty (H + \sum_{i=1}^N M_i)dt \tag{6.5.15}$$

The process of determining the matrix exponential in (6.5.14) to find the state probabilities and then evaluating (6.5.14) to determine the *MTTF* is cumbersome for large and complex systems. Alternatively, *MTTF* can more easily be determined by taking advantage of Laplace transform properties. The Laplace transform of (6.5.14) is

$$X(s) = (sI - A)^{-1}x_0 \tag{6.5.16}$$

where I is the identity matrix. The *MTTF* of a system can be determined using the Final Value Theorem.

$$\begin{aligned} MTTF &= \lim_{s\to 0}\left[s \cdot \mathcal{L}\left\{ \int_0^t \left(H + \sum_{i=1}^N M_i \right) dt \right\} \right] \\ &= \lim_{s\to 0}\left[s \cdot \frac{1}{s} \cdot \left(H(s) + \sum_{i=1}^N M_i(s) \right) \right] \\ &= H(0) + \sum_{i=1}^N M_i(0) \end{aligned} \tag{6.5.17}$$

Two critical observations can be made about (6.5.17). First, (6.5.17) clearly quantifies the non-failed state contributions to the overall reliability, or *MTTF*, of a FT system. This ability to segregate the added reliability hours per FT state can be beneficial to the user for determining whether the expected gain in reliability justifies the cost and complexity of adding another FT state.

A second critical observation from (6.5.17) is that the determination of *MTTF* is independent of the failed state probability *F* allowing for the direct calculation of *MTTF* from the transition matrix and initial conditions. This is to be expected since a key assumption of the system diagram in Fig. 6.5-3 is that the failed state is absorbing (i.e., no exiting transitions). This means that the final row and column of the *A* transition matrix can be eliminated leading to a reduced matrix A' with dimensions $(n\text{-}1)\times(n\text{-}1)$. Similarly, the initial conditions vector can be reduced to x_0' with the failed state row removed. The *MTTF* is directly determined from the matrix inverse of A' and modified initial conditions matrix x_0' by combining (6.5.16) and (6.5.17)

$$\begin{aligned} X'(0) &= -\left[A'\right]^{-1} x_0' \\ MTTF &= \sum_{i=1}^{n-1} X'[i](0) \end{aligned} \tag{6.5.18}$$

The result in (6.5.18) can be easily implemented in most coding environments allowing for simplified calculation of *MTTF* for any FT-system Markov Chain which is a key step in the evaluation of the proposed FT-FoMs presented in Section 6.5.1. A similar derived outcome is provide in [219], though above is unique in its Laplace transform approach.

6.5.2.1. Three-state analytical MTTF example

In some instances, it is desirable to produce analytical MTTF formulas for a given FT-system to better understand the relationship between the underlying failure transitions and component failure rates. This process is illustrated using the elementary FT-system state diagram in Fig. 6.2-

2 consisting of a single faulted state. These states are represented by a set of three differential equations.

$$\begin{aligned} \dot{H} &= \mu \cdot M_1 - (\lambda_{m0} + \lambda_{s0}) \cdot H \\ \dot{M}_1 &= \lambda_{m0} \cdot H - (\mu + \lambda_{m1}) \cdot M_1 \\ \dot{F} &= \lambda_{s0} \cdot H + \lambda_{m1} \cdot M_1 \end{aligned} \tag{6.5.19}$$

As mentioned above, the failed state probability *F* is not used in the *MTTF* derivation in (6.5.17) and will be ignored moving forward since the failed state is absorbing, thus reducing the relevant number of equations to two. The corresponding Laplace-transformed versions of the first two equations in (6.5.19) are

$$\begin{aligned} H(s) \cdot s - 1 &= \mu \cdot M_1(s) - (\lambda_{m0} + \lambda_{s0}) \cdot H(s) \\ M_1(s) \cdot s &= \lambda_{m0} \cdot H(s) - (\mu + \lambda_{m1}) \cdot M_1(s) \end{aligned} \tag{6.5.20}$$

which can be solved for both *H(s)* and $M_1(s)$

$$\begin{aligned} H(s) &= \frac{(s + \mu + \lambda_{m1})}{(s + \mu + \lambda_{m1}) \cdot (s + \lambda_{m0} + \lambda_{s0}) - \lambda_{m0} \cdot \mu} \\ M_1(s) &= \frac{\lambda_{m0}}{(s + \mu + \lambda_{m1}) \cdot (s + \lambda_{m0} + \lambda_{s0}) - \lambda_{m0} \cdot \mu} \end{aligned} \tag{6.5.21}$$

As the final step, the FT-system *MTTF* is calculated by applying (6.5.17):

$$\begin{aligned} MTTF &= H(0) + M_1(0) \\ &= \frac{\lambda_{m0} + \lambda_{m1} + \mu}{\lambda_{m0} \cdot \lambda_{m1} + \lambda_{s0} \cdot \mu + \lambda_{s0} \cdot \lambda_{m1}} \end{aligned} \tag{6.5.22}$$

matching the previously presented equation (6.2.4).

The derivation of analytical formulas for *MTTF* increase rapidly in complexity as the number of states and transitions grows. Powerful software tools like MAPLE can be used to assist with the extraction of analytical expressions for *MTTF* in these more complicated cases. Critical to the

calculation of *MTTF* is the underlying component failure data and the subsequent determination of the failure rates for all the fault and failure state transitions. These items are discussed in upcoming sections.

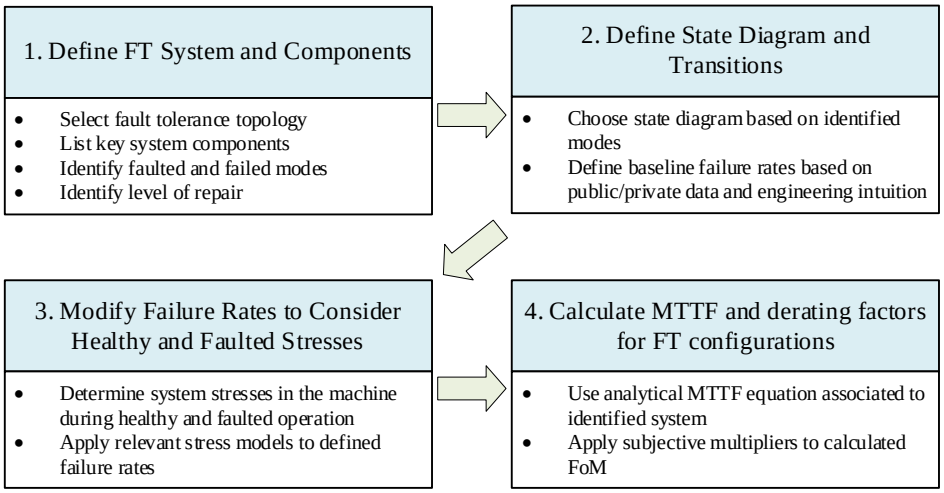

Figure 6.5-4 Recommended procedure for the evaluation of FT-FoMs for candidate FT-systems.

6.5.3. Procedure for Use of FT-FoMs

A recommended four-step procedure for evaluating the FT-FoMs defined in Section 6.2.1 is summarized in Fig. 6.5-4 and described in this section. The purpose of this procedure is to assist users with the task of developing Markov Chain models for candidate FT-systems, including the determination of faulted states and transition values. The developed state model can then be used to estimate the *MTTF* of the FT-system which is critical to evaluating the FT-FoMs.

6.5.3.1. Step 1: Define FT System and Components

The first step in the Fig. 6.5-4 procedure is the definition of the FT-system and its components. More specifically, this process involves identifying all relevant components in the FT-system (e.g., switches, capacitors, machine windings, etc.), the associated fault modes and their interactions, the

impact of repairing any faults, and the ultimate system failure mode. In addition, the user must define the desired system operating capabilities during each of the fault and failure modes.

6.5.3.2. Step 2: Define State Diagram and Transitions

The next step in the procedure is to organize the fault and failure modes identified in Step 1 into healthy, faulted, and failed states based on their effects leading to development of a state diagram. In FT-systems, simplifications are typically made when modeling a single module that any component failure inside the module results in the same fault state which, typically, is inoperability of the module. If there are *n* identical modules in the system with the same fault state, the fault modes for these *n* modules can be grouped together into a single equivalent fault state with a combined module failure rate that is *n* times that of a single module.

Transitions between states is initiated by component failures and other failure events (e.g, damage from foreign objects), each of which is quantified by its associated failure rate. In many cases, the fault states are associated with several different component failures and other failure events. When this is the case, the overall fault transition probability λ is determined by forming the sum of the failure rates. Typical values of component failure rate can be secured from either user internal sources, component data sheets, or from the published literature. Table 6.4-1 highlights sample data for the modular machine study. A FT-system state diagram will almost always also have two additional important transition paths for single point failures (λ_{s0}) and repair transitions (μ). The effects of both of these variables is discussed in the modular machine study in Section 6.4.

6.5.3.3. Step 3: Modify Failure Rates to Consider Operating Stresses

The Step 2 failure transition values can be modified to reflect expected operating stresses during both healthy and faulted operation. In many cases it may be challenging to make significant

modifications if this procedure is being used early in a FT topology screening process and specific design details of the studied FT topologies are unknown. However, parametric studies exploring the impact of post-fault stress on the FT-system reliability are still possible and valuable in some cases.

Some basic pre- and post-fault stress details can be determined by understanding the FT topology itself and how the system reconfigures itself after a failure. In this procedure, the operating stress factors will be selected based on the concept of pi-factors suggested in MIL-HDBK-217F [156] where a baseline component failure rate λ_{BL} is modified by multisource stress factors π_i, leading to an overall stressed failure rate of λ_{STR}

$$\lambda_{STR} = \prod_{i=1} (\pi_i) \cdot \lambda_{BL} \tag{6.5.23}$$

In general, it is recommended that users apply physical principles underlying component life-calculation formulas or by looking at datasheets of module components. Using this approach, the pi-factors can be extracted by ratioing life-estimation results

$$\pi_i = \frac{\lambda_{STR,i}}{\lambda_{BL}} = \frac{L_{BL}}{L_{STR,i}} \tag{6.5.24}$$

Where L_{BL} represents the baseline life under healthy operating conditions and $L_{STR,i}$ refers to stressed-state life operating under stressed condition i. Formulas for component lifetimes and pi-factors for typical electric machine components together can be found in the above modular machine study and in the literature review chapter of this thesis.

6.5.3.4. Step 4: Calculate MTTF and Derating Factors for FT Configurations

A fully assembled Markov chain state diagram of the studied FT-system with numerically determined failure transitions should be assembled before initiating this step, with equations in a form matching those in Section 6.5.1.

These techniques for calculating the value of MTTF set the stage for evaluating the FT-FoMs $FTFOM_1$ to $FTFOM_4$ described in Section 6.5.1 and summarized in TABLE 6.5-1. $FTFOM_6$ and $FTFOM_7$ require determination of the overrating factors F and $KWAOF$ defined by (6.1.1) and (6.5.10), respectively. The remaining FT-FoM, $FTFOM_5$, requires calculation of the added mass required for implementing the studied FT system topology compared to the baseline topology without fault tolerance features:

$$\Delta kg = m_{FT} - m_{BL} \tag{6.5.25}$$

where Δkg is the difference in masses, m_{BL} is the mass of the baseline system, and m_{FT} is the mass of the FT system topology that is being investigated. The determination of (6.5.25) is likely impractical at an early design stage when the objective is to compare multiple FT topology concepts. However, it may be possible to estimate the mass of a candidate FT topology using available reference designs with comparable power and voltage ratings. The reference motor design mass m_{ref} must first be divided into the power electronics and machine mass contributions as shown in

$$m_{ref} = m_{em} + m_{pe} \tag{6.5.26}$$

where m_{em} is the machine mass and m_{pe} is the power electronics mass. Mass scaling factors for the FT system can be estimated from derating factors or component part counts leading to

$$\Delta kg = MMF \cdot m_{em} + DMF \cdot m_{pe} - m_{ref} \tag{6.5.27}$$

where *MMF* is the machine-mass scaling factor and *DMF* is the power electronics drive-mass scaling factor. The estimation of these FT mass scaling factors can take a wide variety of approaches. For the example FT topologies used as examples in Section V, the value *MMF* is proportional to the overrating factor *F* (6.1.1) and *DMF* is proportional to the ratio of the power electronics drive component counts in the candidate FT topology and the baseline configuration, shown as

$$\begin{aligned} MMF &= k_{MMF} \cdot F \\ DMF &= k_{DMF} \cdot n_{pe,FT} \,/\, n_{pe,ref} \end{aligned} \tag{6.5.28}$$

where the power electronics component count ratio is $n_{pe,FT} / n_{pe,ref}$, and the k_{MMF} and k_{DMF} are user-selected tuning factors for the machine and power electronics equations, respectively. Despite the obvious limitations of this approach, it provides a suggested starting point for the user to estimate the candidate FT topology mass penalty Δkg that is needed to evaluate $FTFOM_5$.

6.5.4. FT-FoM Case Study

This section demonstrates the evaluation of the proposed FT-FoMs presented in the preceding sections and the types of insights that can be gained from this exercise. Four topologies are considered that include the five-phase motor drive shown in Fig. 6.5-5(a) and a direct redundant topology shown in Fig. 6.5-5(b). In addition, a two-module MMD and a four-module MMD are included which were described during the quadcopter machine reliability evaluation above. A fifth variant topology is added that consists of a modified four-module system that moves two of the significant single-point-failure (SPF) components (resolver and cooling system) into the module paths by making them redundant, leaving only bearings in the SPF failure path. In addition, the failure rates of all of the SPF components identified in Table 6.4-1 are reduced by a factor of 17 for all five topologies, reflecting aspirational improvements of their reliability that result in more

meaningful comparisons of the topologies. Application of the FT FoM evaluation steps presented in Fig. 6.5-4 are briefly addressed in the following discussion.

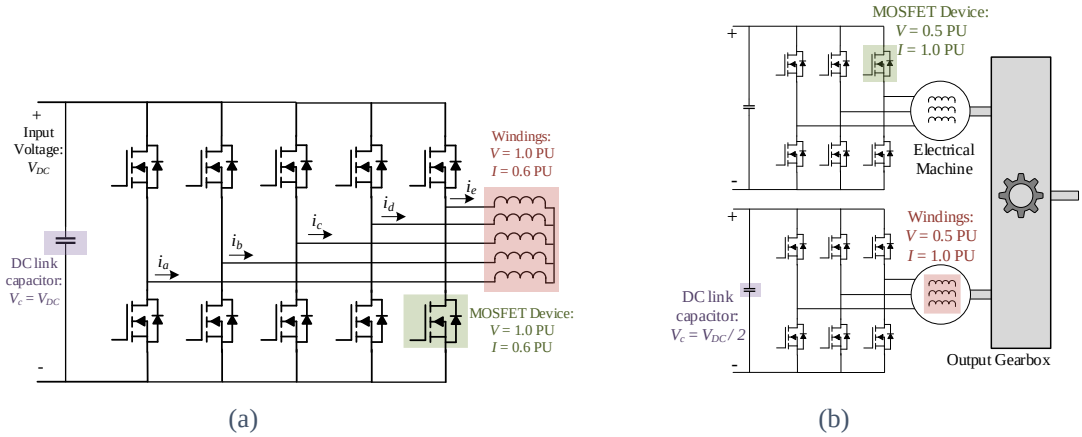

Figure 6.5-5 Case study topologies not yet presented: (a) five phase FT topology with component ratings under healthy conditions; and (b) direct motor drive redundant topology with component ratings under healthy conditions.

6.5.4.1. Definition of FT Topologies & Components

As noted above, four basic FT topologies are compared in this study: 1) five-phase machine drive with two allowable switch failures; 2) direct redundant motor drive; 3) two-module MMD; and 4) four-module MMD. A two-level VSI has been selected for the baseline topology. The basic VSI topology consists of MOSFET devices with anti-parallel diodes (x6), a single dc-link capacitor (x1), and a three-phase machine winding set (x1). Other components include machine bearings pair (x1), coolant system (x1), current sensors (x3), gate drivers (x6), controller (x1), and rotor angular position resolver (x1). Other components (rotor structure, magnets, etc.) are assumed to have much lower failure modes compared to the preceding identified components and are ignored in this evaluation.

The five-phase VSI enables drive reconfiguration by adding phase legs to the baseline concept that provide phase redundancy for open-circuit faults as shown in Fig. 6.5-5(a). In the event of a

switch or winding open-circuit fault, the faulted phase leg is isolated by opening the corresponding complementary switch. The remaining healthy phases are then able to continue operating, perhaps with some phase angle changes in their excitation, to retain a large fraction of the healthy drive's original output power capability. In this study, the five-phase VSI assumes that two open-circuit phase-leg faults can be tolerated before a failure.

The second FT topology is the simplest, applying redundancy directly to the baseline three-phase motor drive system (i.e., direct redundant) by adopting a dual motor drive redundant topology. These two redundant motor drives are coupled together mechanically using a gearbox as shown in Fig. 6.5-5(b). In the event of a motor drive failure, the failed unit is decoupled from the gearbox, and operation continues using the remaining healthy motor drive.

It is also assumed that each of the two drives in the two-module topology is excited using a DC link voltage that is 50% of the value used for the baseline topology, lowering the voltage rating of all of the inverter switches while their current rating is unchanged. If one of the two modules fails, the remaining healthy module must deliver approx. twice the current it supplies during normal healthy operation in order to return the topology to its full power capability. This increases the electrical and thermal stress on the healthy power switches that must be reflected in the stress factors for the inverter switches.

The final two FT topologies each takes the form of a modular motor drive (MMD) where redundancy is implemented at both the power electronics and machine windings level. This is accomplished by dividing the single stator assembly into multiple three-phase winding sets, each supplied by its own independent power electronics and control as described in the quadcopter machine reliability study. For the first of these two topologies, there are two modules that each delivers half of the rated power during healthy operation, similar to the direct redundant topology.

Each module is assumed to operate with $V_{DC}/2$ and the same rated current as the baseline VSI topology ($V_{DC}/4$ for the four-module case). It is important to note that the two-module MMD configuration is only capable of continuing operation following a single module fault. In comparison, the four-module MMD configuration is capable of continued operation following two module faults.

As noted in the introduction of this subsection, a fifth topology is included in the study that is almost identical to the four-module topology described above except that the total single-point failure rate is significantly reduced by adding modular redundancy for the resolver and the cooling system, thereby removing them from the SPF path. In addition, the values of the failure rates for the SPF components in Table 6.4-1 have been reduced substantially by a factor of 17 for all of the considered topologies in order to prevent the single-point failure rate from dominating the FT FoM

TABLE 6.5-2 STUDIED FT TOPOLOGIES AND FAULT COVERAGE CAPABILITY

Topology	**PE Failure Protection** (x – yes, o – no)			**Machine Failure Protection** (x – yes, o – no)			**Non-Power Electronics or Machine Failure Protections & Vulnerabilities**	
	Switch Short Ckt.	Switch Open Ckt.	Cap.	Term. Ph. Open	Term. Ph. Short	Internal Short	Redundant Comp.	Single Pt. Failures
Baseline (two-level VSI)	O	O	O	O	O	O	-	Controller, resolver, current sensors, bearings, cooling system
Five-Phase VSI	O	X	O	X	O	O	-	Controller, resolver, current sensors, bearings, cooling system
Direct Redundancy	X	X	X	X	X	X	Controller, resolver, current sensors, bearings	Gearbox, cooling system
2-Module Independent MMD	X	X	X	X	X	X	Controller, current sensors	Resolver, bearings, cooling system
4-Module Independent MMD	X	X	X	X	X	X	Controller, current sensors	Resolver, bearings cooling system
4-Module Independent MMD with reduced SPF	X	X	X	X	X	X	Controller, current sensors, resolver, cooling system	Bearings

values and thereby interfering with the objective of highlighting the key fault tolerance differences among the 5 topologies.

A summary of the studied FT topologies and fault coverage capability for each of the five studied topologies is provided in in Table 6.5-2.

6.5.4.2. Developing Markov Chain Models

A detailed discussion of the development of the Markov chain models is provided in Sections 6.2 through 6.4. Summarizing, fault-states are added to the state-space diagram based on their failure mode effects. Transitions between states corresponds to relevant failure rates that initiate changes between states. Technique for assembling transfer matrices and developing analytical equations for calculating MTTF are outlined in Section 6.5.2.

6.5.4.3. Baseline Failure Rates and Modifications for Impact of Operating Stresses

Baseline failure rates for evaluating the MTTF values of the shared FT topologies are summarized in Table 6.4-1. Readers are reminded that the failure rates for all of the single-point failure components are reduced by a factor of 17 for all five topologies when calculating the FoM values. For the direct redundant configuration, the failure rate of the gearbox, one of the major single point failure sources in this topology, is assumed to be equal to the bearing failure rate.

The same failure rates are applied to each topology in its healthy state in order to provide meaningful comparisons of the reliability characteristics for these topologies. However, the topologies operate with varying levels of post-fault stress that will be represented by π stress factors defined previously by (6.5.24). The calculated stress factors for this analysis are summarized in Table 6.5-3 with corresponding justifications addressed briefly in the following paragraphs.

TABLE 6.5-3 DEVELOPED STRESS FACTORS FOR CASE STUDY

Topology	Component	Post-Fault Stressor (π-factor)	π-Factor Quantity	Notes
Five-Phase Design	Winding (M_1 state)	Temp. ($\pi_{cls,T,1}$)	3.0	Stresses related to first faulted state
	Device (M_1 state)	Temp. ($\pi_{sw,T,1}$)	2.5	
	Winding (M_2 state)	Temp. ($\pi_{cls,T,2}$)	6.7	Stresses related to second faulted state
	Device (M_2 state)	Temp. ($\pi_{sw,T,2}$)	5.1	
Direct Redundant	Winding	Temp. ($\pi_{cls,T}$)	16.0	
	Winding	Voltage ($\pi_{cls,V}$)	32.0	
	Capacitor	Voltage ($\pi_{cap,V}$)	41.3	
	Device	Temp. ($\pi_{sw,T}$)	10.4	
	Device	Voltage ($\pi_{sw,V}$)	403.0	
2-Module MMD	Winding	Temp. ($\pi_{cls,T}$)	16.0	
	Winding	Voltage ($\pi_{cls,V}$)	32.0	
	Capacitor	Voltage ($\pi_{cap,V}$)	41.3	
	Device	Temp. ($\pi_{sw,T}$)	10.4	
	Device	Voltage ($\pi_{sw,V}$)	403.0	
	Bearing	UMP (π_{brg})	8.0	
4-Module MMD	Winding (M_1 state)	Temp. ($\pi_{cls,T,1}$)	3.4	Stresses related to first faulted state
	Winding (M_1 state)	Voltage ($\pi_{cls,V,1}$)	3.2	
	Capacitor (M_1 state)	Voltage ($\pi_{cap,V,1}$)	3.5	
	Device (M_1 state)	Temp. ($\pi_{sw,T,1}$)	2.8	
	Device (M_1 state)	Voltage ($\pi_{sw,V,1}$)	7.4	
	Bearing (M_1 state)	UMP ($\pi_{brg,1}$)	2.4	
	Winding (M_2 state)	Temp. ($\pi_{cls,T,1}$)	16.0	Stresses related to second faulted state
	Winding (M_2 state)	Voltage ($\pi_{cls,V,2}$)	32.0	
	Capacitor (M_2 state)	Voltage ($\pi_{cap,V,2}$)	41.3	
	Device (M_2 state)	Temp. ($\pi_{sw,T,2}$)	10.4	
	Device (M_2 state)	Voltage ($\pi_{sw,V,2}$)	403.0	
	Bearing (M_2 state)	UMP ($\pi_{brg,2}$)	8.0	

Post-fault stresses are heightened in all topologies because they are assumed to deliver full power output after a fault for this case study. The post-fault healthy module phase current must increase in proportion to the machine overrating factor F defined (6.1.1), and the corresponding winding losses scale as F^2. For purposes of this analysis, it is assumed that the machine and power electronics thermal system experience post-fault temperature rises proportional to F^2.

Similar simplifications are made to consider the impact of unbalanced magnetic pull (UMP) on the rotor after the loss of a module (i.e., increased dynamic load on the bearing) which worsens

as the number of faulted modules increases. For this analysis, it is assumed that the increase in bearing dynamic load ratio (*C/P*) is proportional to the machine overrating factor *F*. In some instances, the loss of a subsequent phases or modules could reduce or completely cancel the unbalanced pull on the rotor (e.g., opposite modules). However, the possibility of unbalanced force cancellation will be ignored during this case study.

The direct redundant and modular configurations are defined to be connected in series resulting in higher module voltages after a fault. Machine winding voltage stress factors are estimated using the insulation life-time relationships. Capacitor and device voltage stresses are assumed to use relationships presented in component datasheets. Voltage ratings of healthy device and winding insulation are assumed to be overrated to 200% of the component nominal operating voltages to allow for more reasonable voltage stress ratio values.

6.5.4.4. Repair rate

For all of the MTTF and FT FoM calculations, it is assumed that machine failures will be repaired within 24 operating hours on average, corresponding to a repair rate of μ =1/24 = 0.0417 hrs^{-1}. As noted earlier, it is assumed that the system retains its ability to deliver its rated steady-state power until the system failure event occurs. The alternative of allowing for partial degradation of the system steady-state power delivery following a module fault is not considered here in order to avoid the additional complications it would introduce.

A single dc input supply value is assumed for all of the candidate FT topologies. For topologies with multiple dc inputs, it is assumed these inputs are connected in series. In the event of a module fault, it is assumed the faulted module is bypassed by a short circuit across its dc input terminals, resulting in the total supply voltage being applied to the remaining series-connected healthy modules.

6.5.4.5. Calculation of MTTF and Derating Factors for FT Configurations

Module component failure rates defined in TABLE 6.4-1 are multiplied by the corresponding π stress factors presented in Table 6.5-3 to establish their post-fault failure rates. Next, the MTTF values are evaluated for the five topologies. $FTFOM_1$, $FTFOM_2$, and $FTFOM_3$ can be directly determined from these *MTTF* values and previously calculated transitions. $FTFOM_4$ is evaluated by making the drive system *MTTF* calculation using repair transition rates of $\mu = 0.99$ hrs^{-1} (highly frequent repairs, corresponding to repairs every 1.01 hours of operation, representing a limiting case) and $\mu = 0.0$ hrs^{-1} (no repairs).

Derating factors *F* and *KVAOF* have been calculated for each topology using the provided formulas and the established component ratings. These derating factors are used to calculate $FTFOM_6$ and $FTFOM_7$. A summary of performance derating factors is provided in Table 6.5-4. Note that the *KVAOF* metrics reflect the 50% voltage derating for topologies capable of full output torque after one fault for the direct-redundant and two-module topology, and after two faults for the four-module topologies, as discussed above.

TABLE 6.5-4 SUMMARY OF DERATING FACTORS AND MASS MULTIPLIER FACTORS FOR FTFOMS 5, 6, 7.

Topology	Derating Factors		Mass Multipliers		Notes
	F	***KVAOF***	***MMF***	***DMF***	
Five-Phase	1.25	1	1.25	1.59	Added devices: 4-devices, 4-gate drives, 2-current sensors
Direct-Redundant	2	2	4	2	Added devices: 6-devices, 6-gate drives, 3 current sensors, 1-controller, 1-capacitor Subjective multiplier of 2 applied to MMF to reflect gearbox mass, multiple housings, cooling loops, etc.
Two MMD	2	2	2	2	Added devices: 6-devices, 6-gate drives, 3-current sensors, 1-controller, 1-capacitor
Four MMD	1.33	2	1.33	4	Added devices: 18-devices, 18-gate drives, 9-current sensors, 3- controllers, 3-capacitors

$FTFOM_7$ requires the estimation of mass differences between the studied FT topology and baseline configuration using (6.5.25)-(6.5.28). The machine described in Chapter 5 is used as a reference with an estimated power electronics mass m_{pe} = 6 kg and machine mass m_{em} = 14 kg. Resulting topology-specific mass multiplying factors *MMF* and *DMF* are included in Table 6.5-4.

6.5.4.6. Evaluation and Interpretation of FT-FoM Values for Fault-Tolerant Topologies

Case study FT-FoM metric values have been calculated using the failure rates, stress factors, derating factors, and mass multiplier values described in the preceding subsection. For this discussion, only four of the seven metrics (FT-FoMs 1, 3, 4, and 5) are plotted in Fig. 6.5-6. A complete set of calculated FT-FoMs are summarized in Table 6.5-5.

The bar charts for these four FT-FoM values exhibit some notable differences between the topologies that are helpful for highlighting their individual strengths and limitations. Some of the differences between the topologies that become visible in these FT-FoM bar charts will be discussed here.

1. The five-phase topology exhibits the worst FoM metrics, particularly for $FTFOM_1$, due to its insufficient fault coverage to realize significant MTTF benefit for the motor drive system.
2. The direct redundant topology achieves a significant MTTF improvement as observed in $FTFOM_1$ due to its improved fault mode coverage compared to the five-phase toplogy, which can be further improved with higher repair rates since it is the least saturated among the five topologies by the SPF rate as indicated in $FTFOM_3$. However, it is disadvantaged by a mass penalty compared to the three modular machine topologies that is reflected in is lower value of $FTFOM_5$.

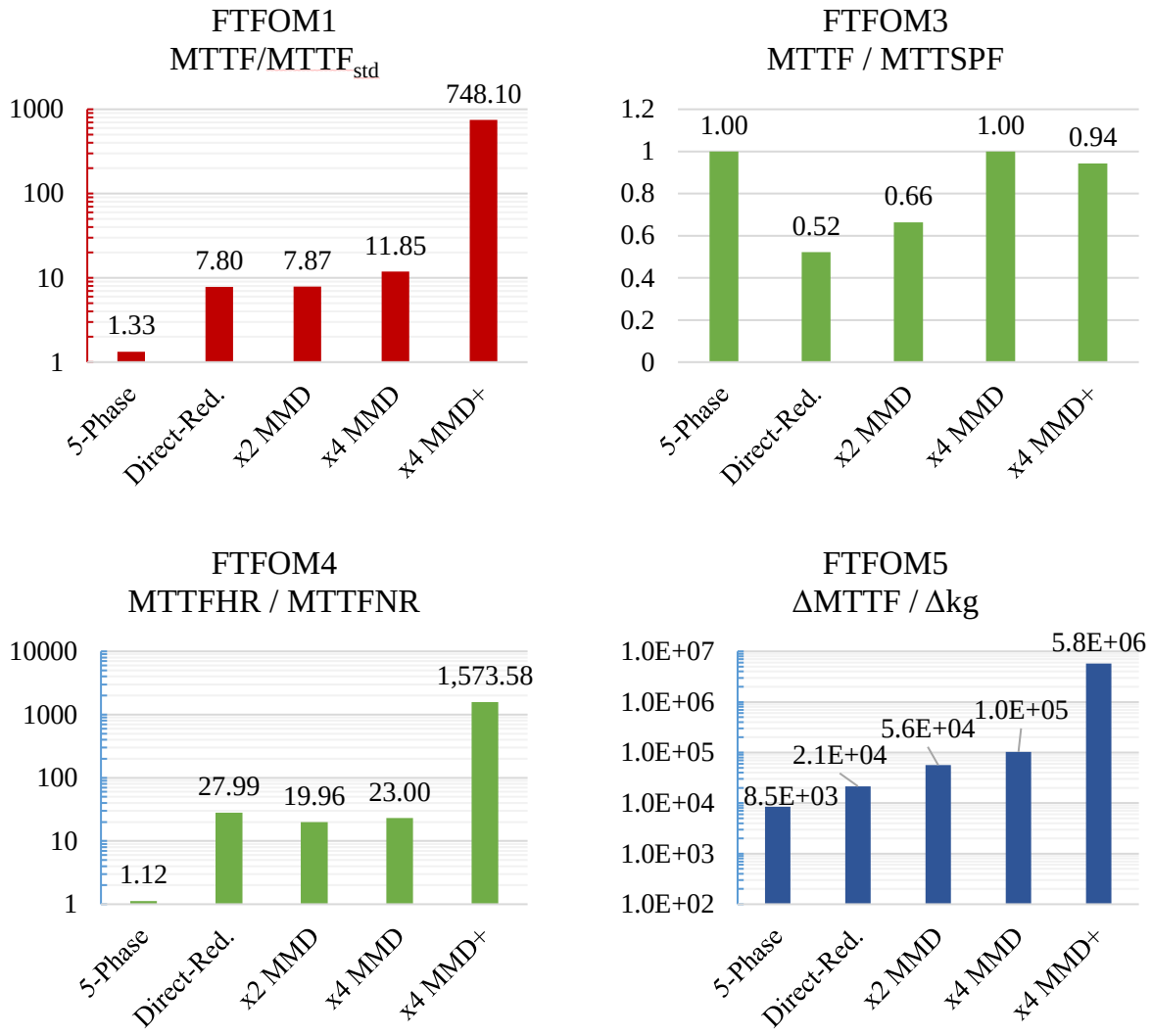

Figure 6.5-6 FT FoM case study results for five-phase (5-Phase), direct redundancy through a gearbox (Direct-Red), two-module MMD (x2 MMD), four-module MMD (x4 MMD), and four-module MMD with reduced single-point failures (x4 MMD+).

TABLE 6.5-5 SUMMARY OF CASE STUDY FOM RESULTS

FTFOM		5-Phase	Direct-Red.	x2 MMD	x4 MMD	x4 MMD+
1	MTTF/MTTF$_{std}$	1.33	7.80	7.87	11.85	748.10
2	ΔMTTF / MTMF	0.13	6.45	5.67	7.29	541.50
3	MTTF / MTTSPF	1.00	0.52	0.66	1.00	0.94
4	MTTF$_{HR}$ / MTTF$_{NR}$	1.12	27.99	19.96	23.00	1573.58
5	ΔMTTF / Δkg	8.5E+03	2.1E+04	5.6E+04	1.0E+05	5.8E+06
6	ΔMTTF / F	4.3E+04	5.6E+05	5.6E+05	1.3E+06	9.2E+07
7	ΔMTTF / KVAOF	5.4E+04	5.6E+05	5.6E+05	8.9E+05	6.1E+07

3. Comparing the 2- and 4-module MMD topologies without the enhanced SPF rate, the 4-module MMD topology achieves significantly higher values of both $FTFOM_1$ and $FTFOM_5$, highlighting its advantages in terms of higher drive system *MTTF* and reduced mass penalty. This suggests the desirability of increasing then number of modules in the MMD topology to values higher than 2.
4. The fact that the value of $FTFOM_3$ for the 4-module topology without the enhanced SPF rate is 1.0 indicates that the single-point failure rate is limiting its ability to achieve still higher values of drive system *MTTF*. This is confirmed by the dramatic increase in the $FTFOM_1$, $FTFOM_4$, and $FTFOM_5$ values that results from reducing the SPF rate for the 4-module topology.

Taken together, the results of this *FT-FoM* case study reinforce previous observations in Section 6.4 about the most promising approach to overcoming the daunting motor drive reliability gap in aerospace applications that was highlighted in Fig. 6.1-1. More specifically, these *FT-FoM* values support the conclusion that the path to achieving the highest possible drive system reliability consists of maximizing the repair rate (i.e., fast response to failures), and suppressing all single point failures using the most-effective available techniques including health monitoring, redundancy, etc. The results also suggest that increasing the module count in modular drives to a value higher than two is desirable for reducing the over-rating factors and associated mass penalty.

6.6. Chapter Summary

The developed machine and power electronics models presented in Chapter 5 have been used as inputs to a reliability analysis of a modular machine drive for a quadrotor application. Machine and power electronics failure rates have been collected from the literature and modified to account

for the stress levels in the system. A Markov chain model has been developed to estimate the machine drive's Mean Time to Failure (MTTF). The predicted MTTF of a FT modular motor drives system is shown to increase significantly when a high repair rate is assumed, which is a reasonable assumption for future quadrotor motor drives used in commercial applications.

Major additional reliability enhancement is achieved by reducing or eliminating identifiable single-point failure sources that afflict the modular motor drive. As a limiting case and aspirational objective, MTTF improvements approaching 1000:1 are predicted for the considered quadcopter modular motor drive if all single-point failures are eliminated. This result is consistent with the observation that a modular machine drive configuration can achieve major improvements in the drive's predicted reliability because the power electronics and winding components are removed from the single-point failure sources. While complete elimination of single-point failure sources will be extremely difficult to achieve, the Markov chain model is valuable for identifying the most promising opportunities for achieving significant reliability improvements.

The second half of this chapter is dedicated to the development and demonstration of newly created Fault Tolerance Figures of Merit (FT FoMs). This new tool provides new quantitative metrics for comparing different FT topologies by highlighting the level of predicted system reliability improvement and the degree to which this improvement is offset by penalties in other drive system performance metrics such as drive system mass or the required component power ratings. The seven FT FoMs that are defined fall into three classes: (1) relative system reliability improvement compared to the reliability of the baseline topology or single module; (2) dependence of reliability improvement on key variables such as repair rate and single point failure rate; and (3) relative reliability improvement measured against mass and cost penalties. Since the calculation

of MTTF is essential to these metrics, analytical derivations of MTTF have been developed that enable faster evaluation. Step-by-step instruction are presented for evaluating the FT FoMs.

A case study that applies the FT FoMs to five FT motor drive topologies is presented to explore the reliability differences between these topologies and to investigate the usefulness of the FT FoMs for making these comparisons. Among the five candidates, the FT modular motor drive topology with four modules and a lowered single point failure rate achieved significantly higher predicted reliability levels than the other four topologies. This comparison achieved its objectives by confirming the appealing fault tolerance potential of modular motor drives with more than two modules, as well as highlighting the critical importance of maximizing the repair rate while minimizing the single point failure rate to achieve the largest reliability improvement.

Chapter 7

Enhanced Isolation Features, Scaling Relationship, and Low-Power Demonstrator Analysis

Isolation between three-phase machine modules is critical for Fault-Tolerance Modular Motor Drives (FT MMD) which divides a FT stator into multiple redundant three-phase winding sets, each with their own dedicated and independent power electronics. To maintain operation after a failure it is necessary these modules are electrically, thermally, and magnetically isolated in order to minimize the possibility of faults propagating between winding sets. The realization of thermal and magnetic isolation is further complicated in designs that utilize double layer (DL) windings that have inter-module coils sharing stator slots.

Chapter 4 and 5 outline techniques for realizing DL magnetic and thermal isolation via the introduction of flux barriers in the stator back iron and the removal in interphase tooth tips, and the use of in-slot cooling structures using highly thermally conductive ceramic cooling channels. These isolation methods are applied to a 70kW IMMD that is presented in Chapter 4. This machine achieves a Module Isolation Ratio (*MIR*) of 2.7%, on par with conventionally isolated single layer (SL) designs, and high inductance to limit fault currents. Additionally, the developed in-slot cooling channels and insulation scheme is shown to limit interactions between phases after fault events. In total the developed machine meets the active power density requirement of 13.3 kW/kg necessary for a quadcopter application.

In this chapter the power-scalability of the developed magnetic and thermal isolation features are assessed for both megawatt-scale and low-power (<10kW) machine designs. A four-module 2MW-rated fractional slot concentrated winding (FSCW) machine is presented which aims to meet the direct-drive aerospace propulsion requirements defined by ARPA-E in [16]. The power-density

sizing equations presented in Chapter 2 are applied providing initial machine dimensions, which are further optimized in electromagnetic finite element analysis (FEA). A final electromagnetic machine design is presented along with FEA results. Magnetic and thermal isolation is assessed using FEA. Overall, the developed study highlights the applicability of the developed isolation techniques at higher power levels, reaching a power density of 23.5 kW/kg and MIR of 2.1%. However, the study shows the limitations of proposed bobbin and potted-channel cooling method for larger machine geometries using conventional encapsulation materials

The second half of this chapter focuses on the design of a 7kW rated two-module demonstrator utilizing the developed isolation features. This design applies practical considerations for the machine design (flux barrier and in-slot cooling design) which is later built and tested (see Chapter 8 for details). These considerations also discuss the tradeoffs associated with the cooling system beyond the design of the coolant channel itself. Specifically, FT and system tradeoffs related to the in-slot cooling interconnections. Overall, this demonstrator is predicted to have *MIR* isolation rating of 1.7%. Last, the presented in-slot cooling channel using alumina tubes is shown to be highly effective cooling the machine winding, with operating capability of 20 A_{rms}/mm^2 continuous.

7.1. 2MW Modular Motor Drives with Enhanced Isolation

The scalability of the developed electrical and thermal isolation features is studied for conceptual megawatt power machine for aerospace propulsion. Machine requirements and characteristics are defined followed by magnet and thermal FEA results, including evaluations of magnetic isolation capability. For brevity specific design and performance steps will be neglected in favor of focus on results due to commonality with the steps presented in Chapter 5. Differing

from the Chapter 5 design, post-fault capability or derating is not considered to focus on general scaling trends. Finally, result discussions are stator-focused due to the nature of the developed isolation technique.

7.1.1. Megawatt Propulsion Requirements & Sizing

Requirements for the 2MW machine study are guided by the ongoing ARPA-E ASCEND research program [16]. High level specifications based on ASCEND program target and selected system design requirements are provided in Table 7.1-1. For comparison, these are contrasted against the 1MW rated machine from the NASA ULI program discussed in Chapter 2. To achieve FT capability, the developed MMD is assumed to have four-modules like the quadrotor machine described in Chapter 5. Requirements related to the machine-propulsor integration are neglected.

TABLE 7.1-1 SELECTED 2MW MACHINE SPECIFICATIONS & NASA ULI PROGRAM COMPARISONS

Spec.	Isolated 2MW Concept	NASA ULI Machine	Units
Max. Power	2,000	1,000	kW
Speed	5,000	20,000	RPM
Torque	3819	477.5	N-m
DC Bus Volt. / Module	1,100	667	V
Min. Assembled Power Density	20	-	kW/kg
Active Power Density Target	30	22.7	kW/kg
Module Num.	4	6	-
Stator Cooling Method	Cooling Bobbin and Stator Jacket	Flooded Stator and Cooling Jacket	-
Rotor Topology	Radial Flux SPM	Radial Flux SPM	-

The power density targets defined in Table 7.1-1 are more aggressive than the NASA ULI program. Achieving this level of power density is further complicated by the direct-drive speed requirement, four times lower than the NASA ULI program. Besides speed, machine materials (CoFe laminations, etc.) and rotor topology are held constant. Other commonalities include machine target metrics like shear stress and tip speed and magnetic loading. Flexibility in machine

pole-count is allowed in order to utilize a slot-pole combination that fits the four-module topology, the selected magnetic isolation approach, and similar operating fundamental frequency. Ultimately the 48-slot, 40 pole (SPP = 2/5) topology is selected meeting all of these criteria.

Details related to the magnetic design are shared in the following subsection with system level results related to the defined specifications given here. Key machine metrics after the machine sizing and 3D FEA study is summarized in Table 7.1-2. Notably, the torque average torque given in Table 7.1-2 is slightly lower than the spec in Table 7.1-1 taking into account machine end effects. Relatedly, the presented active power density is lower than the spec in Table 7.1-1 due to lower output torque related to end-effects and higher machine saturation—items not captured in the generalized sizing equations in Chapter 2.

TABLE 7.1-2 COMPARISON OF FINAL 2MW CONCEPT AGAINST NASA ULI MACHINE

Machine Metric	Isolated 2MW Concept	NASA ULI Machine	Units
Current Rating Per Module	794	445.1	A_{pk}
Slot/Pole	48/40	18/12	-
Fundamental Freq.	1,666.7	2,000	Hz
Avg. Torque	3710.1	477.5	N-m
Tip Speed	197.3	200	m/s
Rotor Diameter	753.6	190	mm
Stack Length	86	155	mm
Current Density	21.0	35.6	A_{rms}/mm^2
Shear Stress	48.4	54.3	kPa
Magnet Loading	0.7	0.7	T
Electric Loading	138.2	155	kA/m
Physical Airgap (total with sleeving)	1.0 (3.5)	1.5 (4.7)	mm
Active Power Density	23.5	22.6	kW/kg
Turns per coil	5	7	-
Slot Fill Factor	0.46	0.26	-

None the less, the developed isolated 2MW design still reaches active power density levels comparable to the NASA ULI machine. This is not surprising since similar key metrics like tip-speed and shear stress are held constant. Differences in current density and slot fill factor reflect

the decisions related to the differing in-slot cooling methods. Overall, the developed 2MW machine it is a suitable representation of a megawatt-rated machine for aerospace propulsion and is used to evaluate the developed isolation features. A rendering of the developed design and its slot layout is provided in Fig. 7.1-1.

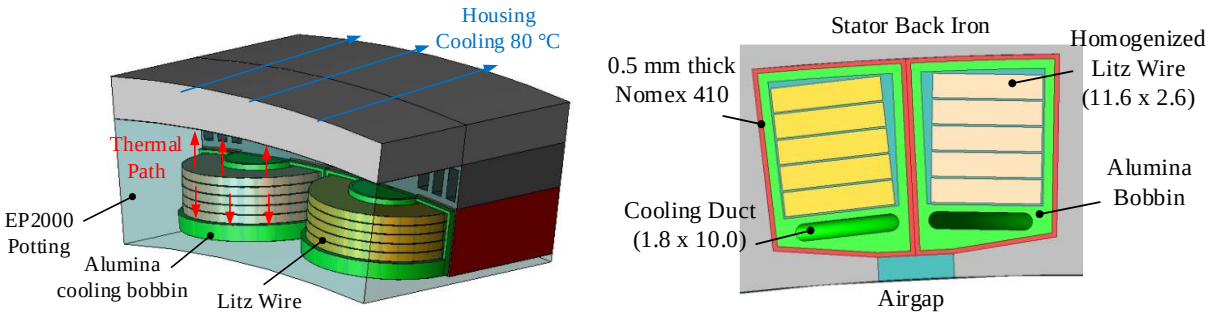

Figure 7.1-1 Developed 2MW stator concept with both back-iron isolation features and in-slot cooling bobbin (left), and slot layout with intra-phase tooth tips shown (right).

7.1.2. Electromagnetic FEA Design Summary

Machine electromagnetic features and machine design approach match what is described in Chapter 5 including the use of cobalt-iron laminations (VAC48), high temperature samarium-cobalt magnets (Recoma35E) in a Halbach magnet array, and thermally conductive potting material (EP2000). Rotor magnets are assumed to sufficiently segmented resulting in small levels of losses relative to other components (e.g., stator and rotor core losses). Similarly, the carbon fiber retaining sleeve is assumed to have minimal loss. Last, for further simplification AC losses related to high frequency fields are ignored due to the use of rectangular type-8 litz (with dimension 11.6 x 2.6 mm) wire with fine strands.

A transient electromagnetic analysis is completed using JMAG Designer to evaluate the full load characteristics of the machine. Final 2MW machine dimensions and associated full-load flux

density FEA results are provided in Fig. 7.1-2. Machine 3D electromagnetic performance results and machine parameters are summarized in Table 7.1-3 and Table 7.1-4 respectively.

TABLE 7.1-3 ELECTROMAGNETIC PERFORMANCE OF A 2MW ISOLATED PMSM

Spec.	Value	Units
Torque	3710	N-m
Speed	5000	rpm
Shaft Power	1942.7	kW
Torque Ripple	5.2	%
Winding Loss	27.7	kW
Core Loss	11.2 (S), 1.2 (R)	kW
Total Active Mass	82.6	kg
Power Density	23.5	kW/kg

TABLE 7.1-4 CALCULATED 2MW RATED MACHINE MODULE PARAMETERS

Machine Module Metric	Quantity
Rated Module Phase Current [A_{pk}]	794
Rated Module Phase Voltage [V_{pk}]	742.5
Module flux linkage with 200 °C Magnets [Wb]	0.0414
Module Phase Inductance [µH]	51.8
Characteristic Current [A_{pk}]	658.2
Module DC Phase Resistance [mΩ]	7.325

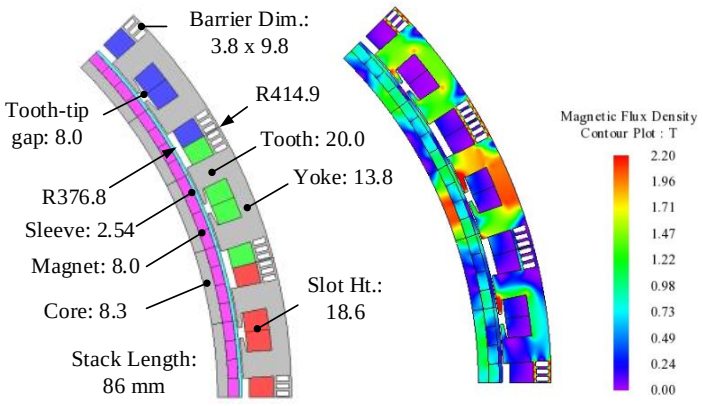

Figure 7.1-2 Machine electromagnetic dimensions and full-load flux density contours for single three-phase winding in a four-module 48-slot 40-pole design.

7.1.2.1. Evaluation of Tooth Tips Design & Electromagnetic Isolation

Interphase tooth tips are removed in the Fig. 7.1-2 design to assess their associated inductance benefits. Without the tooth tips the module inductance drops to 45.8 μH or a 11.6% reduction in machine inductance compared to the inductance value provided Table 7.1-4. It is clear this inductance contribution could increase by closing the 8 mm gap between tooth tips in Fig. 7.1-2. This notable change in machine inductance highlights the importance of the leakage inductance associated with these tooth-tips and the potential design hazards of completely removing all tooth tips to reduced current unbalance caused by mutual leakage inductance between adjacent phases. Further, increased self-inductance via this tooth-tip leakage will improve *MIR* metrics. In this design the inclusion of these tooth tip features is critical for realizing high inductance and low characteristic current.

The previously used Module Isolation Ratio (*MIR*) can be used to assess the magnetic isolation of the developed 2MW design. This ratio is determined by calculating the ratio self- and mutual-flux linkages between adjacent machine phases. A *MIR* metric of 2.1% is calculated for the presented 2MW design indicating good magnetic isolation between modules. This compares to the original quadcopter design in Chapter 5 which has an *MIR* factor of 2.7%. As such, the developed 2MW design confirms the effectiveness of the developed magnetic isolation approach at high power levels.

7.1.3. Thermal FEA Summary

The steady-state thermal performance of the bobbin cooling system described in Figure 7.1-1 is evaluated using JMAG Designer's 3D FEA thermal package. This evaluation uses materials and associated properties matching those provided in Table 5.1-3. These include polyester amide-imide strand insulation, Nomex 410 slot liner (thickened to 0.5 mm to reflect higher operating voltages),

ceramic cooling bobbin made from thermally conductive 3D printed alumina, and Lord EP2000 potting material which encapsulates the winding. Homogenized litz wire thermal conductivities are estimated using [186]. Last, cooling surfaces on the machine outer housing and bobbin cooling channel surfaces (shown in Fig. 7.1-1) are cooled by 80 °C fluid. Contact resistances between components are neglected in this conceptual study.

Loss densities for each of the stator components are provided in Table 7.1-5, along with full-load loss densities associated with the 70kW design from Chapter 5. Utilizing the same heat transfer coefficients from the Chapter 5 (1000 W/m^2-K for coolant channel surfaces and 5000 W/m^2-K for housing channel surfaces) results in a calculated steady state maximum winding temperature of 277.7 °C—well beyond the target maximum of 180 °C. The previously stated thermal assumptions are reconsidered to determine the circumstances where the proposed cooling would work.

TABLE 7.1-5 COMPONENT THERMAL LOSS DENSITIES USED IN 2MW THERMAL STUDY

Component	2MW Design	70kW Design	Ratio
Stator Core Loss Density [W/m^3]	2.10e6	1.52e6	1.38
Winding Loss Density [W/m^3]	1.33e7	1.11e7	1.20

First, the EP2000 potting is replaced with an ideal potting material with thermal conductivity of 10 W/m-K (nearly 5x larger), which is also applied to the turn homogenization. This potting assumption is aspirational as it extends beyond typical stand-alone encapsulant material capabilities [104]. Next, heat transfer coefficients are adjusted until the coil temperature is below the strand insulation limit of 180 °C. These correspond to a convection coefficient of 10,000 W/m^2-K for the housing cooled surface and 2,000 W/m^2-K for the cooling duct channels (a 2x increase from the 70 kW machine). Temperature contours of the 2MW machine under rated loads with

enhanced materials is shown in Fig. 7.1-3 with the top-most turn located in the center of the stack showing a peak temperature of 171.2 °C.

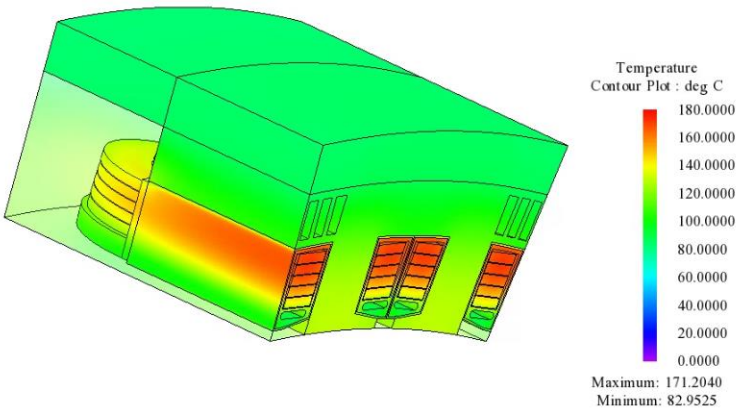

Figure 7.1-3 Temperature contours for 2MW machine under full-load loss contours. Enhanced potting and cooling applied in order to meet 180 °C target.

7.1.3.1. Limitations of Proposed In-Slot Cooling Method

Clearly the need for enhanced potting materials and cooled surfaces for the Fig. 7.1-3 analysis exposes the limitations of the proposed in-slot cooling method. Several observations can be made to understand why this cooling scheme is less capable for megawatt scale cooling compared to the 70 kW design:

1. Higher loss densities in the winding (Table 7.1-5) increasing cooling requirements.
2. A thicker slot liner insulation is used for the 2MW design to reflect higher operating voltages (x5 times thicker compared to 70 kW design) effectively eliminating the cooling path through the stator back-iron.
3. Larger overall machine dimensions and associated thermal paths to cooled surfaces. The potted channel cooling distance (from end windings to housing) is 2.1x larger than the 70kW design. Further, the slot height is also 2.1x larger increasing the thermal path from the topmost turn to the cooling duct in the bottom of the slot. Last, the machine

stack length is 2.6x longer, reducing the effectiveness of end-winding oriented cooling like the potted channel approach.

The above reasons summarize the scaling limitations of the proposed cooling bobbin approach, beyond enhanced potting material availability. Certainly, its effectiveness could be better utilized for different megawatt machine geometries with high tip speeds (larger diameters and shorter stack lengths), shallower stator slots, or perhaps modified housing geometries to reduce the potted channel length. In general, more intimate cooling techniques that cool turns individual, like the direct cooling approaches investigated for the NASA ULI machine should be considered.

7.1.3.2. Megawatt Scale Thermal Isolation Using In-slot Cooling

The developed model with enhanced potting material is used in a thermal isolation study, where one coil is assigned healthy and the other faulted. The faulted coil loss is increased relative to healthy coil and maximum coil temperatures are recorded. Results of the study are shown in Figure 7.1-4 highlighting this proposed in-slot cooling with advanced material still achieves good thermal isolation between modules. Overall, only a 10°C temperature rise is observed for a 2x increase in loss in the faulted coil and corresponding 95°C rise.

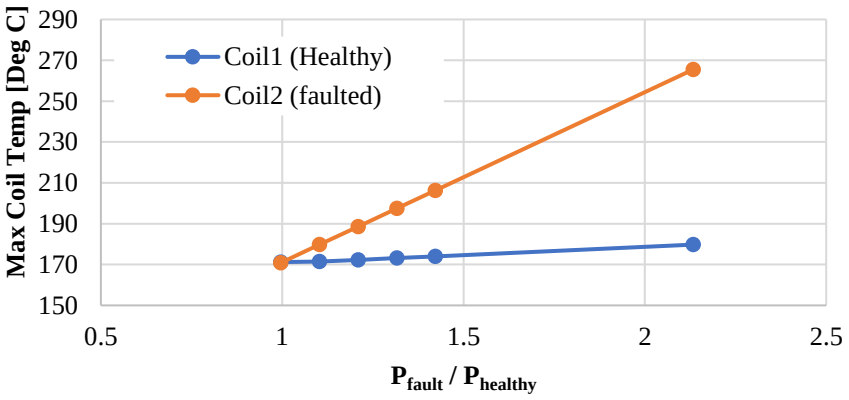

Figure 7.1-4 2MW thermal isolation study coil maximum temperatures for varying faulted coil loss quantities.

7.1.4. 2MW Design Conclusions

Presented in this section is a 2MW rated design with high-power density oriented towards a direct drive propulsion application. This machine possesses the magnetic and thermal isolation features that were previously presented in Chapter 5 for a 70kW rated design, which are assessed for the 2MW power level. The electromagnetic design for the 2MW design is summarized and is shown to have an *MIR* of 2.1% indicating good isolation between modules—confirming the scalability of the proposed magnetic isolation approach. Last, it is identified the use of intra-phase tooth tips can increase the machine phase inductance by > 10%.

The losses calculated in the electromagnetic study are applied to a steady state thermal analysis. The proposed cooling method is shown to be ineffective using similar material properties and cooling conditions as the 70kW reference design. This is attributed to increased loss densities to realize higher power density and general machine geometry increases related to scaling from 70kW to 2MW. The use of high thermal conductivity potting materials along with increase convection coefficients can assist with thermal feasibility, though the availability of such materials is questionable. The model using idealized potting is used in a thermal isolation model, confirming the effectiveness of in-slot cooling methods isolating phases from one another.

7.2. Design & Evaluation of Low-Power Modular Motor Drives with Enhanced Isolation Features

The previous section presented a high-power FSCW SPM utilizing isolation features similar to the Chapter 5 quadcopter design. This scaling study is now repeated for machines at lower power levels (<10 kW). This analysis is presented in the context of the development of a low-power FT PMSM demonstrator machine. Instead of a power density focus, this machine design is motivated

for fabrication at low cost and speed which is reflected in the design decisions. The fabrication and test of this machine is presented in Chapter 8.

This chapter focuses on the overall performance, design tradeoffs, and isolation evaluation associated with the implemented design. This includes the presentation of the design specifications, and electromagnetic and thermal FEA analyses using JMAG Designer.

7.2.1. Machine Specifications & Overview

The lower power demonstrator design seeks to incorporate the 70 kW quadcopter machine FT features into a smaller 7 kW rated package with reduced complexity. The objective of this machine is to demonstrate the developed magnetic and thermal isolation features, using readily available materials and existing sample designs through the WEMPEC lab. An IEC100 frame-size design reference is selected as a starting point, which is illustrated in Fig. 7.2-1. Note reference machine dimensions are illustrative of the general scaling and not a representation of the final design.

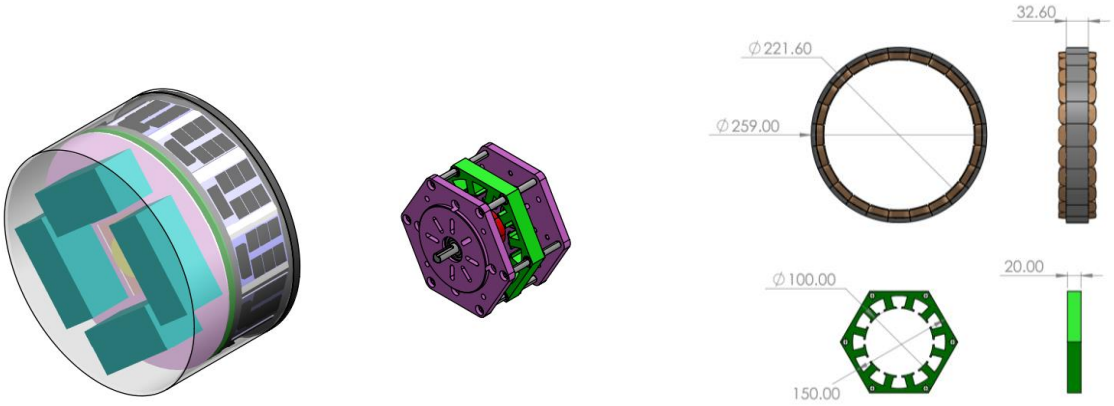

Figure 7.2- 1 To-scale comparisons of the developed quadrotor machine and identified sample design: (a) housing integration; and (b) stator dimensions in millimeters. Note the final demonstrator dimensions vary from those shared above.

High level machine specifications are defined based on the selected reference design geometry and available dyne equipment in the WEMPEC lab. Notably the availability of high-speed dynes

up to 8,000 is limited so this design assumes the use of a self-dyne test which utilizes the modularity of the machine, circulating power between machine modules as shown in Fig. 7.2-2. This test configuration is discussed more in Chapter 8. Assuming a self-dyne test, the machine speed rating is set for 8,000 rpm at peak power of 7 kW. Due to the shrinking size of the machine in Fig. 7.2-1, only two three-phase winding sets are considered for geometry reasons, leading to the decision to use a 12-slot 14-pole machine design which is compatible with presented isolation features.

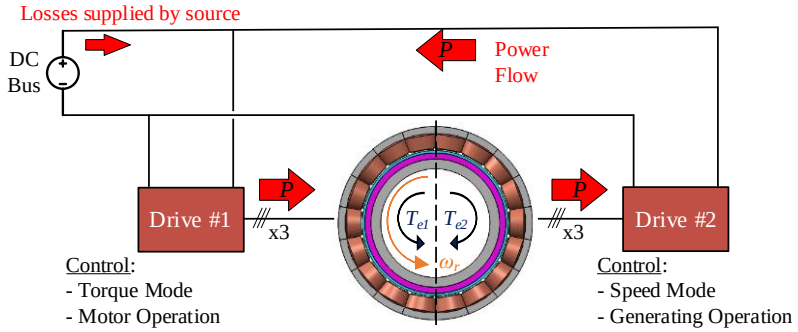

Figure 7.2-2 Self-dyne alternative test configurations with the test machine uncoupled from the dyne with power circulating within the machine.

TABLE 7.2-1 DEMONSTRATOR METRICS DEFINED BY MACHINE TEST PARAMETERS

Spec. [units]	Value	Notes
Slot/Pole	12/14	Similar topology to quadrotor machine design
Torque Rating [N-m]	8.3	Approximately 10% of quadrotor rating
Number of Modules	2	Three-phase modules
Peak Shaft Power Coupled [kW]	2.6	Directly measurable using dyne setup
Peak Speed Coupled [rev/min]	3000	Fundamental = 350 Hz
Peak Power Self-Dyne [kW]	6.9	3.5 kW per module to be measured using voltage and current measurements
Peak Speed Self-Dyne [rev/min]	8000	Fundamental = 933.3 Hz
DC Bus Limit [VDC]	350	Target parameters set in advance for both power electronics and machine.
Rated Current [A]	15.3	

Further, the developed machine is to be designed to operate in both healthy and faulted-module states. Faulted states include three-phase terminal open- and short-circuit faults, and internal short circuits to demonstrate both thermal and magnetic isolation. Overall machine specifications are summarized in Table 7.2-1.

The shared target ratings are modified after taking into consideration 3D effects and manufacturing requirements, later reducing the power rating of the machine to 5.6 kW at 8,000 rpm. This rated power reduction is further discussed in the subsections below.

7.2.1.1. Electromagnetic Material Selection

Electromagnetic components (laminations, magnet wire, and magnets) are selected based on availability and cost point. Both lamination material and magnet wire are available in the WEMPEC lab. Copper magnet wire with a polyester amide-imide (NEMA MW 35-C, 200 °C rating) coating is selected for the stator turns. Strand sizes between 16AWG and 20AWG were considered though multiple strands-in-hand of 20AWG ultimately selected for ease of manufacturability. Next, a range of lamination steels are available through the WEMPEC lab. Specifically, a 28Ga C5-coated M19 non-grain-oriented steel is selected with thickness 0.014 inches or 0.356 mm.

The selection of magnet materials is complicated by the need for both low-cost and availability. As such the use of a Halbach magnet array, custom magnets, or high-performance magnet materials are infeasible. Standard NdFeB rectangular magnet geometries from K&J Magnetics were considered in combination with varying rotor topologies leading to the selection of the K&J B842SH magnet—a high temperature NdFeB magnet (grade N42SH) with dimension ½” x ¼” x 1/8” thickness. The lamination stack length is increased to 1” (25.4 mm) to accommodate the length of the magnet (the ¼” dimension) requiring four magnets stacked axially per magnet slot.

Last, a Nomex 410 slot liner with 0.070” thickness is selected to provide insulation between coil strands and the stator core. Table 7.2-2 gives a summary of the materials related to the electromagnetic design.

TABLE 7.2-2 ELECTROMAGNETIC AND THERMAL MATERIALS USED IN ANALYSIS OF A LOW POWER DEMONSTRATOR.

Machine Component	Mfg.	MFG PN	Relevant Characteristics
Magnet Wire	Essex Brownell	GP/MR-200	• NEMA MW 35-C, polyester amide-imide (200°C) • 20 AWG (copper diameter 0.813 mm, insulated diameter 0.892 mm)
Lam. Steel Stack	-	-	• 29Ga C5 M19 NGO Steel, 0.356 mm total thickness • C5 film thickness ~6μm • Assumed stacking factor: 96% • Saturation flux density: ~1.8 T
Magnets	K&J Magnetics	B842SH	• NdFeB (grade N42SH), rated 150 °C, • Dim. 0.5” x 0.25” x 0.125” • B_r = 1.31 T, H_c = ~1100 kA/m • Reduce model B_r by 4% to reflect magnet stacking factor
Slot Liner	Nomex	410	• 0.007” thickness (0.139 W/m-K thermal conductivity) • 180°C temperature rating.
Alumina Tubing	McMaster Carr	8746K312	• Tube OD and ID: 1/8” and 0.063” respectively • dielectric strength 220 V/mil • thermal conductivity 28.0 W/m-K • resistivity > 10^{14} Ω-cm
Winding Encapsulant	Epic Resins	S7527	• Thermal conductivity 0.77 W/m-K, • dielectric strength 450 V/mil • dielectric constant 3.8

7.2.1.2. Dimensional Constraints

Machine stator outer dimensions and hexagonal shape are fixed by the selected WEMPEC reference design, which are shared in Fig. 7.2-3. Holes are placed in the stator back iron to accommodate 8mm diameter stator support shafts that are used to connect the stator to the machine endbells as illustrated in Fig. 7.2-1. Remaining holes in the stator back-iron represent the selected flux barrier geometry separating phases.

An initial rotor diameter of 100 mm is chosen (see Fig. 7.2-1), though this is later reduced to 87 mm to allow for more reasonable magnet wire sizes and lower winding loss as illustrated in Fig. 7.2-3. The rotor bore dimensions is set to accommodate a 30 mm shaft and key. Other notable dimensional constraints include the inclusion of small holes (x6) in the rotor back iron to be used for the attachment of an axial clamping plate to help axially-support the lamination and magnet stacks. Last, it should be noted this machine has a relatively large airgap of 1.5 mm for its size as shown in Fig. 7.2-3. This was selected to minimize assembly risks associated with this being a student-made machine and the related component tolerance risks.

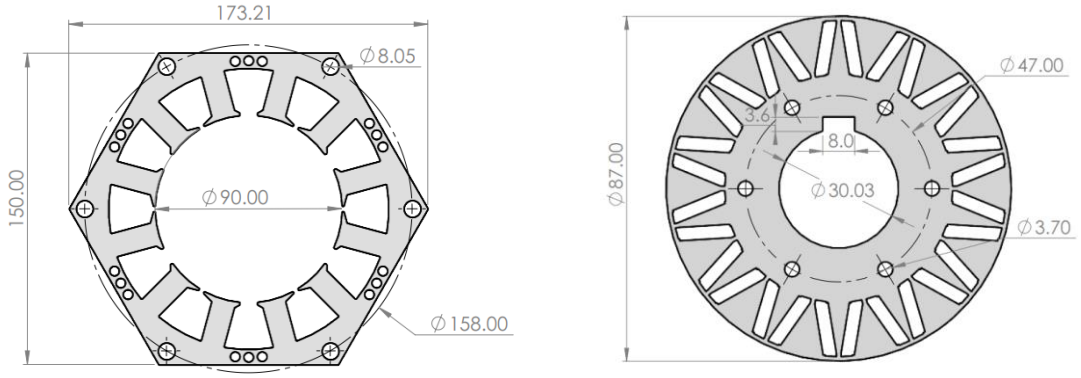

Figure 7.2-3 Dimensional constraints in mm for low-power demonstrator: stator (left) and rotor (right).

7.2.1.3. Selection of V-shape IPM rotor

Alternative rotor topologies including inset SPM, spoke interior permanent magnet (IPM), and v-shape IPM were considered for their ability to best accommodate the planned 14 rotor poles and the limited rectangular magnet sizes available at the desired grade and temperature. The inset-SPM topology is appealing due to commonality with previously shared designs, though is limited by the available magnet grades and dimension, 1.5 mm physical airgap, and further penalized by the supporting magnetic bridges.

The spoke IPM and v-shape IPM are desirable for their flux focusing features allowing for higher airgap flux densities. This is focusing effect is illustrated in linear representation of a v-shape IPM in Fig. 7.2-4 showing two-rotor poles over pole pitch τ_p along with magnetization directions and typical v-shape IPM dimensions.

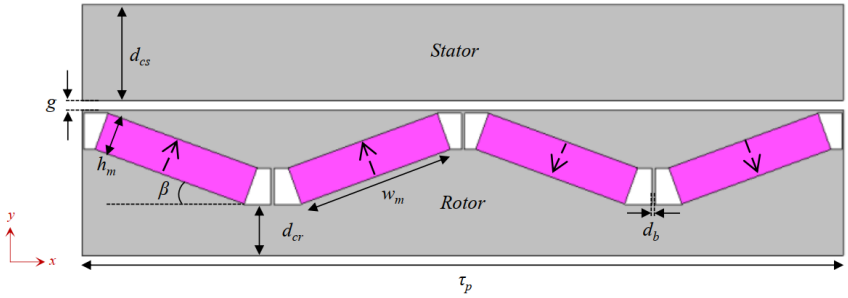

Figure 7.2-4 Linearized representation of v-shape interior permanent magnet (IPM) rotor with typical dimensions and magnetization directions shown.

The flux focusing effect (when the IPM airgap flux B_g exceeds that of an SPM with same thickness h_m and magnet material) is realized by manipulating angle of the v-magnet allowing the magnet width w_m to increase so the total length of the v-shape magnets ($2 \cdot w_m$) is greater than of a half a pole pitch leading to the flux focusing requirement:

$$\frac{B_{g,ipm}}{B_{g,spm}} = \frac{4 \cdot w_m}{\tau_p} > 1 \tag{7.2.1}$$

The above ratio excludes impacts of bridges and posts supporting the magnet and core saturation, which blunts the flux focusing effect. Further, the spoke IPM can be considered an extreme version of v-shape IPM with the β-angle (defined in Fig. 7.2-4) equal to 90° with magnet width w_m only constrained by the rotor radii and pole count of the spoke IPM. Ultimately, the v-shape IPM is selected due to available magnet geometries and simplified bridge design. This leads to an angle of 44.4° between pole-facing magnets leading to a flux focusing ratio of 1.3 and no-

load airgap flux density of B_{g1} = 0.78 T (80 °C magnet) and B_{g1} = 0.84 T (20 °C magnet), which is comparable to the previously discussed 70kW and 2MW designs using thick high-grade magnets in Halbach magnet arrays.

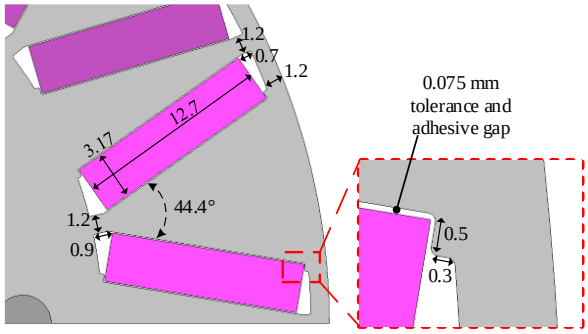

Figure 7.2-5 Final IPM magnet dimensions and associated manufacturing features.

The selected v-shape geometry in Fig. 7.2-5 is highlighted along with the selected post and bridge thicknesses. These bridge and post thickness are confirmed using structural FEA and indicate significant safety margins on the rotor steel (>10x) at 8,000 rpm. Note a 0.075 mm gap between the magnets and laminations is shown reflecting the lamination and purchased magnets tolerancing, and for spacing for the magnet adhesive bonding material. Also shown in Fig. 7.2-5 is a small shoulder that is used to locate the position of the rotor magnet. The impact of this gap and shoulder is discussed in a later subsection.

7.2.1.4. In-Slot Cooling Implementation

The previously studied in-slot cooling techniques involved using a 3D printed bobbin made out of highly thermally conductive alumina. Companies like Ceramco offer custom 3D printed alumina and ceramic components. Unfortunately, lead-times associated to these parts is extensive (>10 weeks at the time of this writing) along with significant geometric constraints related to fabrication. As a result, alternative simplified in-slot cooling methods were investigated.

In-slot cooling using alumina rectangular tubes was considered, though the ready availability of custom and standard rectangular tubing is limited. Ultimately, it was decided to use standard alumina tubing available through CoorsTek or McMaster Carr. An alumina tube with a 1/8” outer diameter tube with a 0.063” inner diameter is selected. A thick wall thickness (0.031”) is chosen to improve robustness during assembly and testing. Relevant material properties for the selected alumina tube are provided in Table 7.2-2.

These alumina tubes are cut to a length of 95 mm and assembled into a six-tube stack. This stack is inserted between all machine coils as shown in Fig. 7.2-6. Slot space is budgeted between coils to account for these tubes in the machine design and analysis. Coolant flows in parallel between the six tubes. In totality, this in-slot method is the only active cooling implemented for this machine. External connections between the stacks and associated tradeoffs are discussed in a later section.

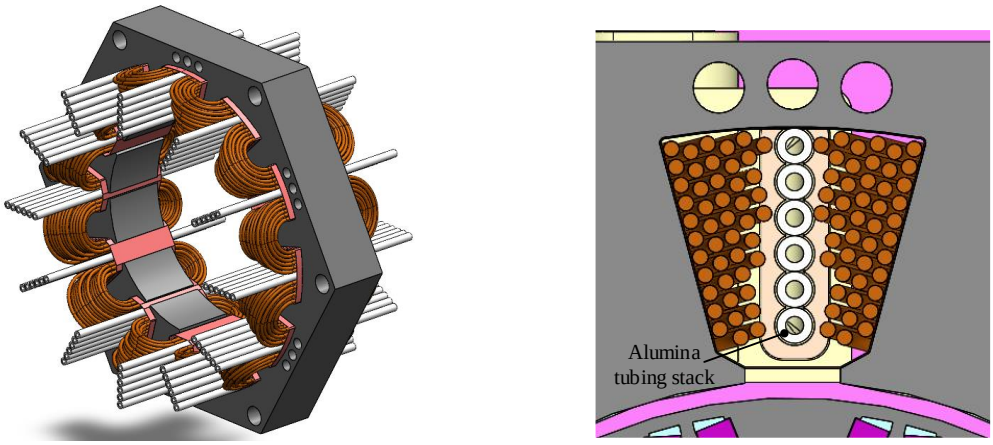

Figure 7.2-6 Integration of alumina tubing into stator (left), and slot cross section (right).

Critical to the in-slot cooling is the choice of winding potting materials. The lead time and cost of previously presented EP2000 (thermal conductivity of 1.9 W/m-K) disqualified it from consideration. To save cost, potting samples were requested from several distributors. As a result, Epic Resins S7527 2-part urethane potting (thermal conductivity of 0.77 W/m-K) is used in this

machine analysis and build. Material properties for both the S7527 potting and the alumina tubing are provided in Table 7.2-2.

Last, a propylene glycol mixture (Koolance 705) is selected for the machine coolant due to is good fluid electrical conductivity (approximately two orders of magnitude lower than typical tap water) which is necessary due to coolant proximity to energized coils. This fluid is also compatible with available pump ERM-3K3UA. Supplier given properties of Koolance 705 are compared against water in Table 7.2-3.

TABLE 7.2-3 PROPYLENE GLYCOL THERMAL PROPERTIES COMPARED TO WATER AT 20°C

Property (symbol)	Water	Koolance 705 (propylene glycol)	Units
Dyn. Viscosity (μ)	1.0016	4.300	mPa-s
Kin. Viscosity (ν)	1.0034	3.956	mm^2/s
Density (ρ)	998.2	1087	kg/m^3
Specific Heat (c_p)	4180	3600	J/kg-K
Thermal Cond. (k)	0.58	0.38	W/m-K
Elec. Conductivity	200-800 (tap)	3	µS/cm

7.2.2. Electromagnetic Analysis

The described geometric constraints above define key stator and rotor dimensions related to machine diameters and magnet placement. Remaining geometric optimization is oriented towards finalizing stator tooth width, tooth tips (both inter- and intra-phase), and back iron thickness for maximum torque and inductance, and minimal torque ripple for a fixed 15.3A q-axis input current and 350V dc bus limit shown in Table 7.2-1. This optimization utilized an idealized model of the machine (e.g., no gap between magnets and rotor core in 7.2-5, negligible end-effects, etc.) and idealized flux barriers (majority removal of back-iron material).

This optimization was completed using built-in JMAG optimization tools resulting in the dimensions described in Fig. 7.2-7(a). Notably a stub tooth is added between non-alike coils to

keep torque ripple to a minimum. Last, the Fig. 7.2-7(b) drawing reflects updated stator back-iron flux barriers set at a diameter of 4.5 mm (60% of the overall back-iron thickness) to maintain the structural integrity of the stator. Ideally more back-iron material would be removed to improve isolation and torque performance.

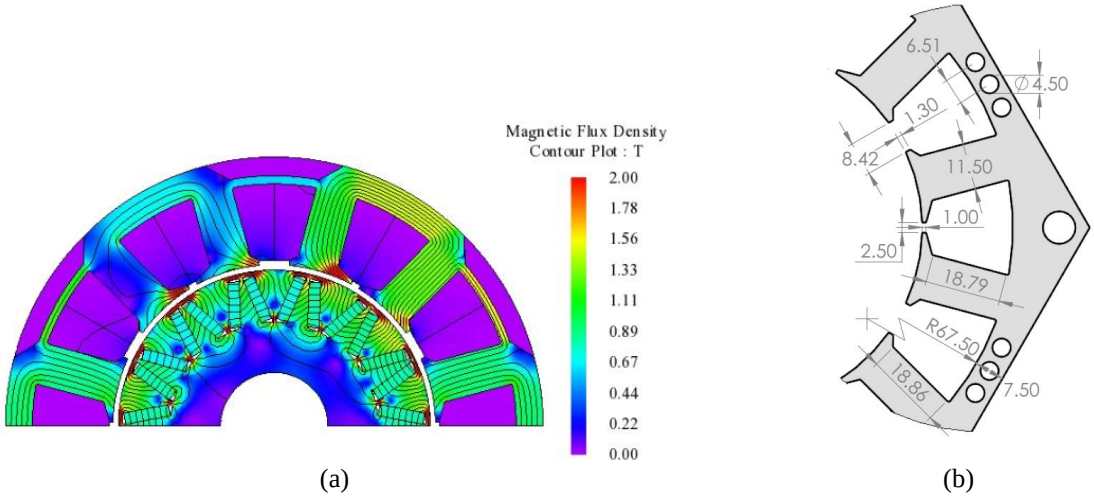

(a) (b)

Figure 7.2-7 Final 2D stator optimization: (a) 2D tooth tip optimization result and full load flux density contours with simplified geometry and idealized stator back iron flux barriers; and (b) final machine dimensions with manufacturing and assembly considerations included.

Initial 2D evaluations show torque performance degrade to 7.6 N-m from the target 8.3 N-m with fixed current and an 80 °C magnet temperature. This analysis also finalized the machine turn count to 47-turns per coil. Further torque performance degradations are observed when additional non-ideal effects are captured in the analysis. These torque reductions are determined acceptable since this machine is a demonstration of the developed isolation features—not of torque performance. In other instances, further design iterations would be required to recover this lost performance. These non-idealities are summarized below in combination with the expected machine performance.

7.2.2.1. Modified Performance Considering Impact of End Effects & Manufacturing Considerations

Initial idealized machine optimization was performed using 2D FEA for ease of evaluation. However, performance from the idealized 2D optimization degrades once 3D end effects and manufacturing constraints are considered. This subsection summarizes the final machine performance including machine end-effects and updated lamination geometry reflecting the as-built design. These lamination changes include the magnet gaps and shoulders described in Fig. 7.2-5 and the updated flux barrier and outer machine hexagonal geometry in 7.2-7(b). The combined effect of all of these changes is summarized here, though each component individually chips away at the machine torque performance.

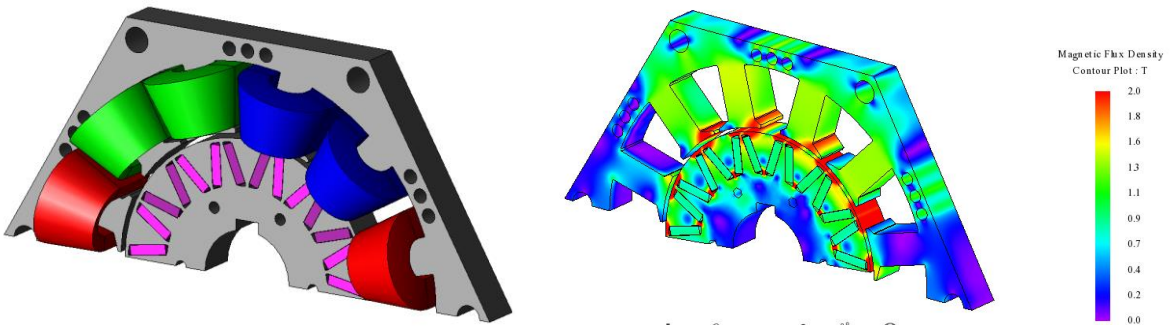

Figure 7.2-8 Updated 3D FEA of the demonstrator machine with non-ideal geometry considerations and corresponding full load flux density (20 °C magnet).

The developed 3D machine model and corresponding full load flux density contours are provided in Fig. 7.2-8. It should be noted that the magnitude of the flux density in the Fig. 7.2-8 model is comparable to the Fig. 7.2-7 result as expected. Even still, the combined effect of these non-idealities lowers the expected machine output torque to 7.2 N-m (20 °C magnet) or 6.7 N-m (80 °C magnet).

The developed 3D model is used to calculate other machine loss components similar to the procedure described in Chapter 5. Machine core loss contours at 8,000 rpm (933 Hz fundamental)

and full-current (15.3A) are shown in Fig. 7.2-9(a). Peak stator core losses are observed in the tooth tips, which is consistent with observed stator saturation in Fig. 7.2-8. Peak rotor core loss is identified in the rotor post closest to the airgap. In total, a full load core loss of 140.2W and 18.9W is expected for the stator and rotor, respectively.

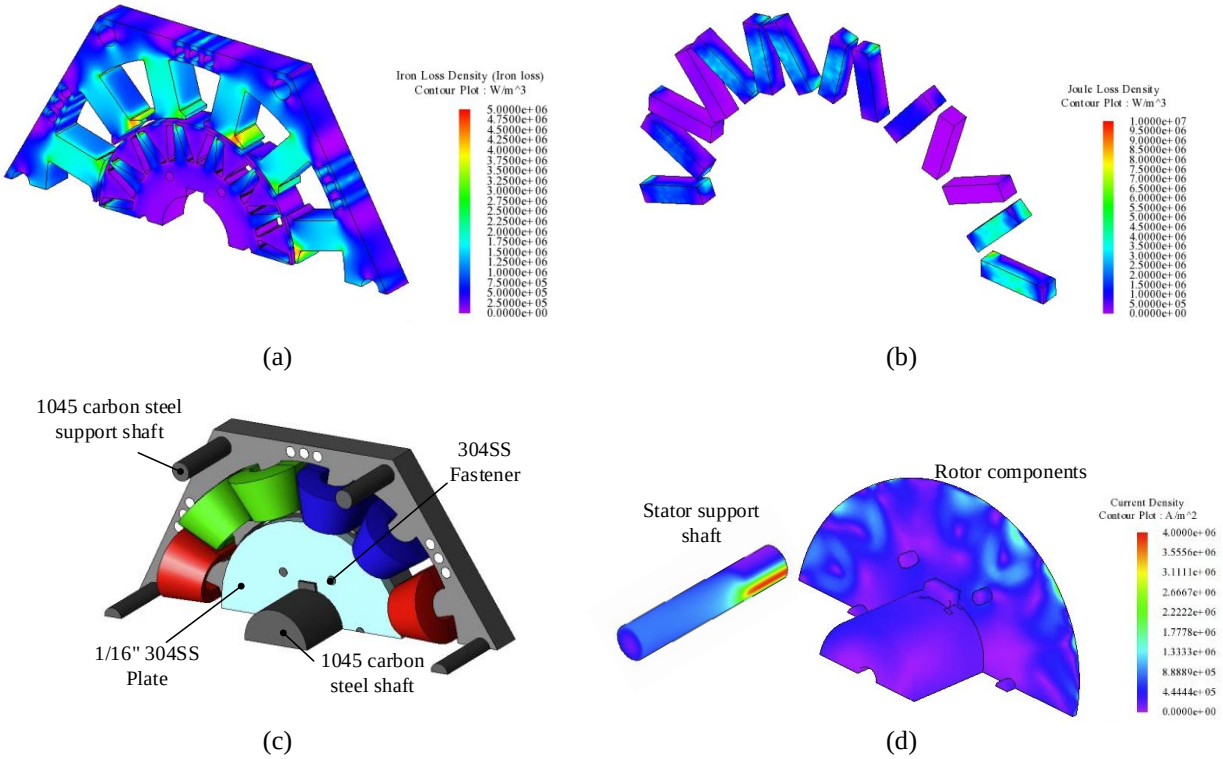

Figure 7.2-9 Full-load and speed (933 Hz fundamental) loss studies: (a) core loss; (b) ¼" magnet segment loss; (c) model capturing structural components surrounding the machine; and (d) structural current densities.

A single ¼" magnet segment is modeled to assess magnet joule losses. Full load loss joule loss density contours are shown in Fig. 7.2-9(b). Each magnet segment is estimated to have an average loss of 0.095W, leading to a total full load magnet loss of 10.6W (112 magnet segments total).

A similar full-load joule loss study is performed to evaluate eddy current losses in structural components near magnetic components. Considered structural components are highlighted in Fig. 7.2-9(c) and induced current density (corresponding to loss locations) in Fig. 7.2-9(d). Overall,

these loss contributions are quite low at 5.7W, with most of this loss coming from the 1/16” thick stainless-steel plate supporting the magnet and lamination stacks.

The largest contributor to machine loss comes from the windings—specifically from the dc resistance. Each coil consists of 47 turns of two-in-hand (two parallel strands) 20AWG copper strands. Initial machine calculations assumed an end-winding geometry resembling what is described in Fig. 7.2-8 where the end-windings arc around the tooth in a perfect circle leading to a coil resistance calculation of 0.0974 Ω/coil at 20 °C.

In reality, the machine end windings were much flatter against the stator tooth following the contours of the stator geometry. This is reflected in the as-wound resistance of 0.0900 Ω/coil at 20 °C or 0.1251 Ω/coil at 120 °C. The associated dc loss related to the as-wound condition is 126.4 W (20 °C) or 175.7 W (120 °C). The as-wound 150 °C loss metric will be used for the machine efficiency calculation. Last, the developed rated dc current density is 10.4 A_{rms}/mm^2. This corresponds to a copper fill factor of 37.2% considering only the wound area and 25.4% considering the entire slot area including coolant channel and slot liner space.

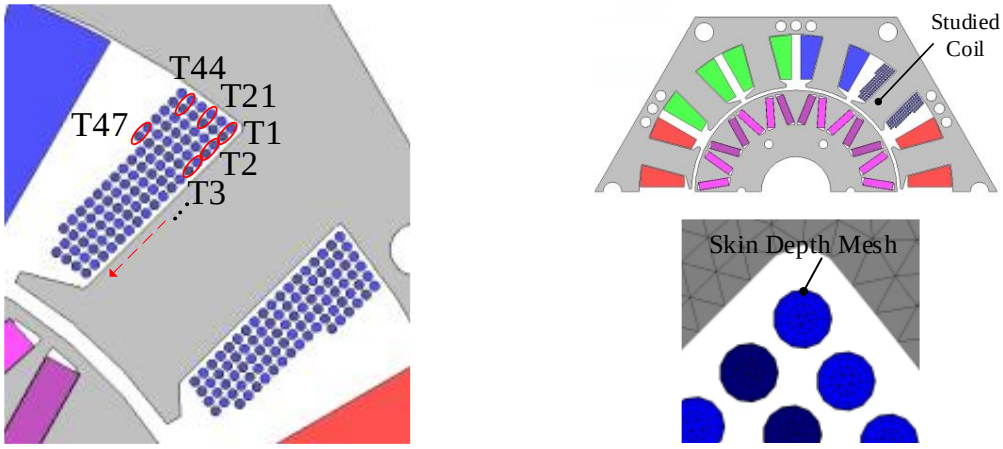

Figure 7.2-10 AC loss model with each strand modeled individually: turn layout and winding pattern (left); overall model (top right); and strand FEA meshing (bottom right).

Next, ac losses are evaluated for the machine winding considering the high fundamental operating frequency of 933Hz and for the use of non-transposed magnet wire. To evaluate the impact of high frequency losses, a single machine slot is modeled with each turn set as a conductor with resistivity of 2.34e-8 Ω-m (120 °C). The overall 2D machine model, slot, and mesh are shown in Fig. 7.2-10. For this design frequency, the skin depth is 2.5 mm which is considerably larger than the selected strand size of 0.813 mm.

Four FEA test cases are completed to assess ac losses. Case 1 is a baseline case with full load current in the machine winding at low speed (100 rpm, 11.7 hz) to confirm expected dc loss performance. Case 2 is a no-load case at full speed at 8,000 rpm (933.3 Hz). Case 3 is a 50% load (7.5A) case at full-speed, and Case 4 is a 100% load (15.3A) at full-speed.

For each case the in-slot losses (both dc and ac combined) are calculated using FEA. The end-winding loss is calculated separately using the dc end winding resistance (0.071 Ω/coil total at 120 °C). These are combined into a total power loss value containing ac losses P_{ac} allowing for the determination of ac loss factors (*ACLF*):

$$ACLF = \frac{P_{total}}{P_{dc}} \tag{7.2.2}$$

Current density contours at peak phase current for each of the defined cases are provided in Fig. 7.2-11 along peak current density, loss summary, and *ACLF*s. As expected, the FEA calculated current density and losses match the expected dc levels previously discussed for case 1. For the high-speed no-load condition (case 2), minimal winding losses related to the radial rotor fields are observed. What minimal current density is observed is limited to the strands nearest the airgap on the side of the slot with the stub tooth.

The effect of proximity losses becomes more apparent with increased current loading as observed in cases 3 and 4. For 50% current load the ACLF increases to 1.14. As current increases to 100% rating, the dc losses dominate causing the ACLF to decrease to 1.11 corresponding to a total winding loss of 195.0W.

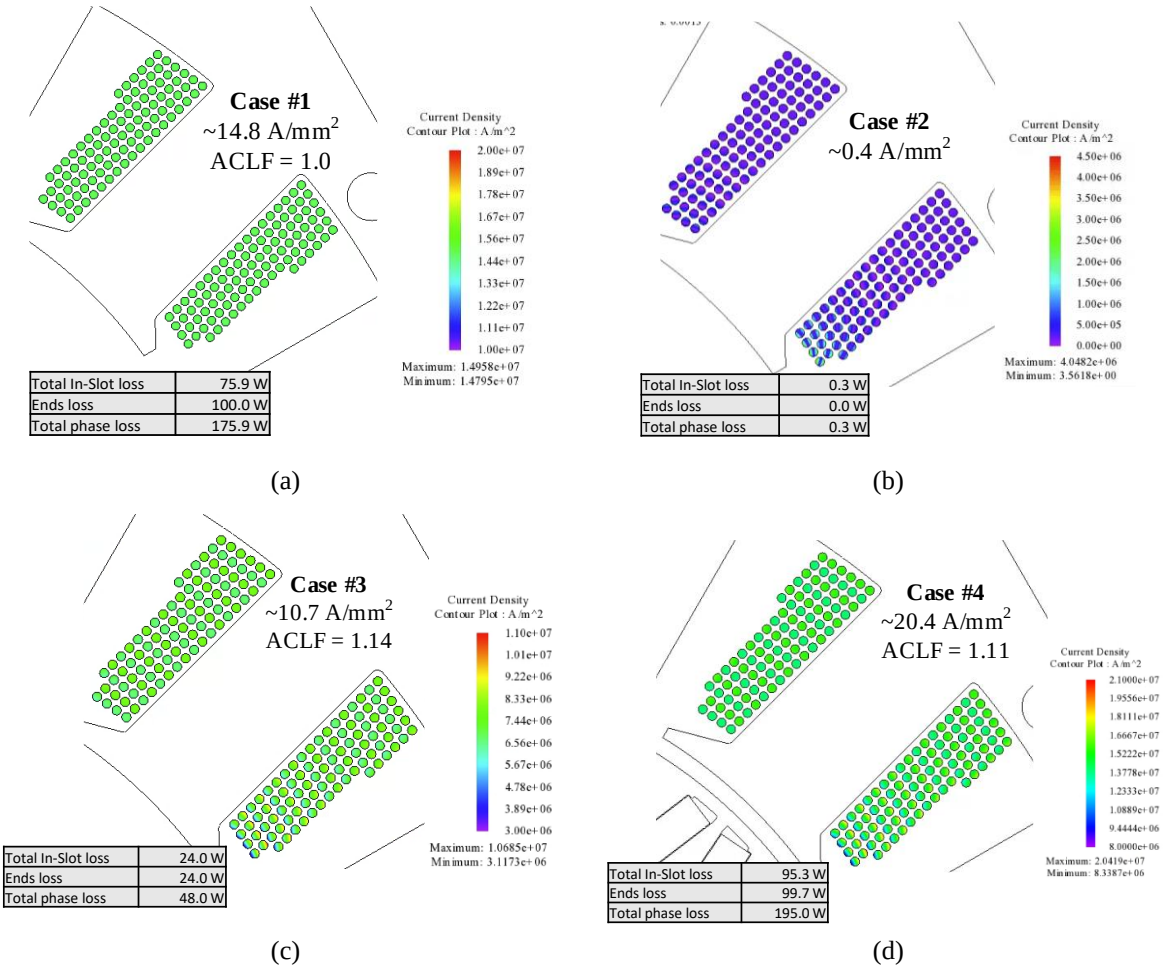

Figure 7.2-11 Current density at varying loads and loss: (a) 100 rpm, 15.3A phase current; (b) 8000 rpm, 0A phase current; (c) 8000 rpm, 7.5A phase current; (d) 8000 rpm, 15.3A phase current.

Total machine performance is summarized in Table 7.2-4 including the results above. Total machine efficiency is 93.9% at the maximum operating point. Rated power factor is 0.662 at the peak operating point. This poor power factor is a reflection of the degraded output torque discussed

above. As mentioned, the purpose of this machine is not to maximize performance but rather demonstrate the developed FT features. Machine efficiency improves up to 95% for the lower temperature operating points in Table 7.2-4.

Performance numbers related to the full-torque 3,000 rpm operating point are provided since this will be the highest-power coupled operating point. Further, room temperature operating point data (for both magnets and windings) is provided, which is useful for evaluating the Chapter 8 test results. For simplicity, ac losses are assumed equal for both temperatures even though the results would change with lower winding resistivity and stronger fields from the rotor magnets.

TABLE 7.2-4 SUMMARY OF MACHINE PERFORMANCE AT VARYING OPERATING POINTS

Metric	3,000 rpm (20 °C)	8,000 rpm (20 °C)	3,000 rpm (T_{rated})	8,000 rpm (T_{rated})	Notes
Speed [rev/min]	3000	8000	3000	8000	Coupled (low speed) and uncoupled (high speed)
Avg. Torque [N-m]	7.2		6.7		Rated 80°C magnets
Power [kW]	2.3	6.0	2.1	5.6	End effects considered
Module Line-Line Voltage [$V_{ll,pk}$]	144.3	370.5	130.1	339.8	Module Terminal Values Number of turns per coil = 47
Module Current [A_{pk}]	15.3				10.4 A_{rms}/mm^2
Winding Loss [W]	126.4		175.7		Rated 120 °C winding temp.
AC Winding Loss [W]	3.3	19.3	3.3	19.3	Assume approximately equal losses at 20 °C
Stator Core Loss [W]	29.5	140.2	29.5	140.2	Higher performance core materials available
Rotor Core Loss [W]	4.0	18.9	4.0	18.9	
3D Magnet Loss [W]	0.5	3.3	0.5	3.3	¼” magnet segments
Structure Loss [W]	-	5.7	-	5.7	1/16” 304SS plate dominate
Efficiency [%]	93.4%	95.0%	90.8%	93.9%	
Power Factor	0.644	0.643	0.671	0.662	

7.2.2.2. Machine Module Equivalent Circuit Parameters

Module equivalent circuit parameters related to the presented machine are summarized below for both room temperature windings and magnets, and for rated operating temperatures (120 °C windings, 80 °C magnets). Characteristic current values are determined by applying negative d-axis currents to the 3D model until zero d-axis flux linkage is reached. Note the low characteristic current relative to rated current. This is expected due to the low power factors in Table 7.2-4.

While low power factor (and therefore characteristic current) is generally undesirable due to the increased kVA requirements for the power electronics, it is beneficial from a FT perspective to have high inductance to limit fault currents. This is especially true for PMSMs which are vulnerable to demagnetization related to fault transients and high characteristic currents. To evaluate demagnetization risks, a negative d-axis current is applied to the model. Following the demagnetization evaluation method outlined in Chapter 5, negligible demagnetization is observed for 3x rated current (45.9A) on the negative d-axis with an 80 °C magnet.

TABLE 7.2-5 CALCULATED DEMONSTRATOR EQUIVALENT CIRCUIT MACHINE PARAMETERS

Machine Module Metric	Quantity (20 °C)	Quantity (T_{rated})
Rated Module Phase Current [A_{pk}]	15.3	15.3
Rated Module Phase Voltage [V_{pk}]	213.9	196.2
Module flux linkage Magnets [Wb]	0.0231	0.0216
Module q-axis Inductance [mH]	1.69	1.72
Module d-axis Inductance [mH]	1.88	1.91
Characteristic Current [A_{pk}]	11.5	10.6
Module DC Phase Resistance [mΩ]	180.0	250.2

7.2.2.3. Evaluation of Magnetic Isolation & Tooth Tip Inductance Contribution

Interphase tooth tips are removed in the Fig. 7.2-8 model to assess the associated inductance benefits. Without the tooth tips, the module d- and q-axis inductances drop respectively by 0.24 mH (12.6%) and 0.25 mH (14.5%) compared to the rated temperature inductances given Table

7.2-5. This change in inductance is in similar proportion to the previously presented 2MW design further highlighting its capability to influence overall machine inductance.

This inductance contribution could increase with further manipulation of the interphase tooth tips. However, this is likely unnecessary given the calculated low power factor, and perhaps these tooth-tips could be modified to improve the overall machine power factor. In any case, the developed tooth-tip is shown to be an additional design handle for machine designers.

Magnetic isolation of the demonstrator design is assessed using the Module Isolation Ratio (*MIR*). Once again, this ratio is determined by calculating the ratio of mutual- and self- flux linkages between adjacent machine phases. A *MIR* metric of 1.7% is calculated indicating exceptional isolation between modules—significantly lower than the previous studied machines.

7.2.3. Thermal Evaluation

The loss calculations from the previous section are used in a stator steady-state thermal FEA model to assess the cooling capability of the proposed in-slot method. The developed two-coil stator cooling model, assumptions, and material properties is shown Fig. 7.2-12. For simplicity, contact resistance between components are neglected. Anisotropic stator properties for the stator lamination stack are estimated using [220]. A thermal conductivity of 23 W/m-K is used for in the lamination plane and 1.63 W/m-K is used for the perpendicular axis. A homogenized coil is shown with winding and perpendicular direction thermal conductivities estimated using [186], the copper fill factors, insulation dimensions defined above, and the potting thermal conductivity (0.77 W/m-K). This leads to a coil direction thermal conductivity of 141.8 W/m-K and 1.50 W/m-K for the perpendicular direction.

A 3D printed 4mm thick endplate made from Onyx (Markforged) material is included to better represent the final machine assembly. Anisotropic material properties for Onyx are given in [221] which are based on the direction of the print extrusion. For model simplicity, an isotropic material with the lower-bound thermal conductivity of 0.3 W/m-K is assumed. Other material properties are summarized in Table 7.2-2.

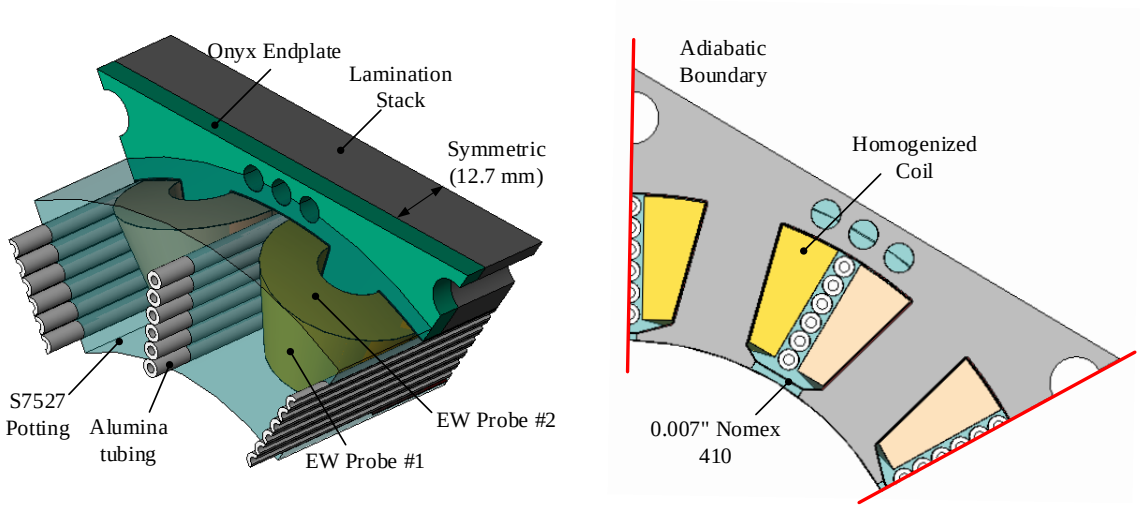

Figure 7.2-12 Steady stator model used in the thermal analysis for the developed demonstrator machine.

7.2.3.1. Cooled Surfaces Heat Transfer Coefficients

Cooled surfaces in the Fig. 7.2-12 include inner surfaces of the alumina tubes and ambient air convection on the stator and endplate exposed surfaces. Both 20°C air and Koolance 705 inlet fluid is assumed (see Table 7.2-3 for fluid properties). For simplicity, a heat transfer coefficient of 5 W/m^2-K is assumed for surfaces exposed to ambient air. Interior duct flow correlations are used estimate reasonable heat transfer coefficients for tube inner surfaces. The reader is referred to Chapter 5 for further discussions about these internal flow calculations.

This evaluation is expanded to consider the hydraulic connections between in-slot cooling channels and the related tradeoffs from a connection complexity and FT-implication standpoint.

In total, this stator possesses twelve cooling ducts (corresponding to 12 coils and slots) which can be connected in series, parallel or some combination. Possible coolant connection schemes are shown in Fig. 7.2-13(a) which are compatible with the two-module machine.

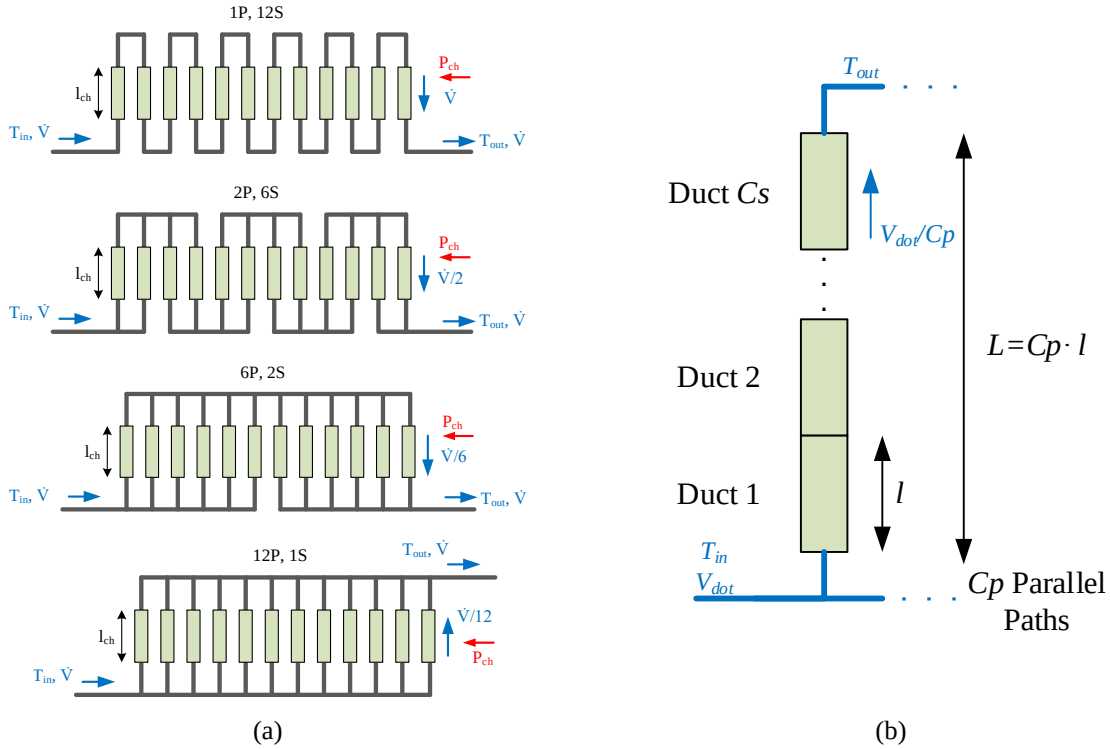

Figure 7.2-13 Series and parallel in-slot cooling connection diagrams (a); and straight-line duct model for correlations analysis (b) with variables duct length *l*, number of series and parallel connected ducts C_s and C_p respectively.

The selected connection scheme must take into consideration both machine and thermal system tradeoffs. A series connected system has system power density advantages with less hardware and fittings compared to a parallel system (e.g., manifolding, balancing valves, hoses, etc.). The obvious disadvantage to a series connected system is high operating pressures and related constricted flow affecting the pump decision. It may be necessary to increase cooling duct dimensions to accommodate higher flows, though this is at the expense of valuable slot area that

would otherwise be occupied by copper. Further, the series connected system is penalized due to fluid temperature rise ΔT related to loss Q and mass flow $\dot{m}$

$$\Delta T = \frac{Q}{\dot{m} \cdot c_p} \tag{7.2.3}$$

Without sufficient flow, down stream components will have higher inlet fluid temperatures from upstream heating, degrading thermal performance of coils nearest the outlet. Mitigation can be realized by increasing the mass flow rate, exacerbating the identified pressure-flow problem. The all-series connected system also has disadvantages from a FT thermal isolation perspective. Heat related to a fault event in an upstream coil will affect inlet fluid temperatures of healthy coils downstream.

As stated, a parallel system allows for lower operating pressures and potentially smaller ducts creating opportunities for greater amounts of slot copper and reduced winding losses. The obvious implication is the increased number of components related to the paralleled systems which will affect cost and number of failure points. Further, a parallel system has greater thermal isolation benefits due to decoupled inlet fluid temperatures. The isolation problem is shifted to the heat exchanger and its ability to reject additional heat related to the winding failure and post-fault overload operation to maintain torque. The heat exchanger and pump must be oversized to manage these increased loads. Last, a parallel system does have redundancy benefits where a channel can clog without failing the entire cooling loop.

Clearly both series and paralleled cooling connections have distinct tradeoffs with likely optimum solution using a combination of parallel and series fluid paths. The selection of the series parallel connection must consider the modularity of the stator to maintain better thermal isolation

between modules. Compatible two-module series and parallel flow paths for the 12-slot design are given in Fig. 7.2-13(a)

In an ideal FT system, redundancy could be applied the thermal management system improving thermal isolation between modules at the expense of higher component counts. Ultimately the selection of connection scheme must be made in-combination with pump sizing. In general, a series connected system must have a pump with high-pressure, low-flow characteristics. Conversely a more parallel system must have a pump system with low-pressure, high-flow characteristics. Pressure flow calculations using correlations for each of the 7.2-13(a) connections are made assuming a single line diagram in 7.2-13(b). The calculated pressure will be underestimated as it excludes bends between tube connections and pressure-losses related to cooling-loop components. For this demonstrator test, a Koolance ERM-3K3U reservoir-pump is used with maximum speed-setting pump curve given in Fig. 7.2-14 against the calculated pressure flow characteristics of the identified duct configurations.

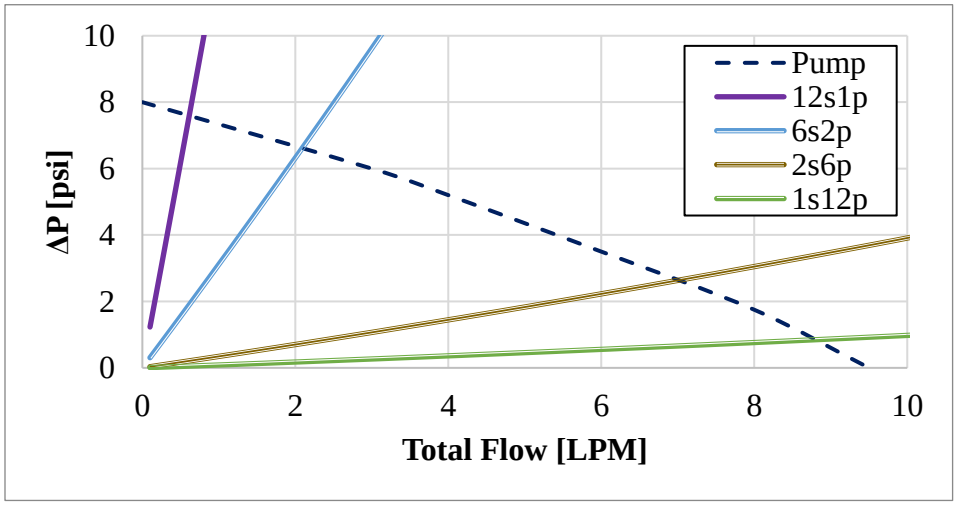

Figure 7.2- 14 Straight line pressure-flow characteristics of the identified duct connections and selected pump maximum-speed pump curve.

All of the flow points shown in Fig. 7.2-14 are for laminar flow. Expected flow operating points occur at the intersection of the pump curve in Fig. 7.2-14, further highlighting the tradeoffs between series and parallel connections. A 2-series 6-parallel connection is selected allowing two-series ducts-per-coil, reducing thermal interactions between phases. The expected operating point for this configuration is 7 LPM. For this analysis the expected flow rate is reduced to 3.5 LPM (a 2x safety factor reduction) to reflect the non-idealities not captured in the analysis and the later reduced pump operating speed during the test. As a result, a heat transfer coefficient of 1,800 W/m^2-K is used for tube surfaces based on correlation calculations.

7.2.3.2. Steady State Thermal Analysis

Seven steady thermal operating point are considered to evaluate the developed cooling system. Cases 1 & 2 refer to 50% and 100% current-load levels with room-temperature windings at low speed (minimal core loss). These points will be useful for evaluating the machine thermal performance in Chapter 8. Cases 3 and 4 are for the full-current 3,000 rpm operating speed and room-temperature winding losses from Table 7.2-4. Case 5 captures the 8,000 rpm full-load operating point in Table 7.2-4 at rated temperature. Case 6 corresponds to an overload test condition discussed in Chapter 8. Last, the limits of the developed cooling system are evaluated in case 7 with current density pushed up to 20 A_{rms}/mm^2 and maximum stator core loss. All losses are assumed evenly distributed in the shown geometry.

These cases are summarized in Table 7.2-6 along with corresponding steady state FEA results. These include maximum coil temperatures, maximum core temperatures, and end winding surface probe temperatures defined in Fig 7.2-12. Temperature contours related to cases 5 and 7 are given in Fig. 7.2-15.

Overall, the simulated cooling scheme meets the material thermal limits defined in Table 7.2-2 (< 155 °C) for all cases. Even under the highest loss-load scenario of 609W (case 7) the peak calculated winding temperature is 92.1 °C (or a 72.1°C temperature rise)—nearly a 63°C margin on material limits highlighting the effectiveness of the developed in-slot cooling method. Certainly, greater increases in current density are feasible due to the extensive thermal margin. Next, the results suggest the winding losses presented in Table 7.2-4 as overly conservative and can be updated with an iterative loss and thermal analysis.

TABLE 7.2-6 STEADY STATE FEA STUDY RESULTS (20 °C FLUID)

Case	Case Description	Total Coil Loss [W]	Total Core Loss [W]	Max. Coil Temp. [°C]	Max. Core Temp [°C]	EW #1 Probe Temp [°C]	EW #2 Probe Temp [°C]
1	50% current, low speed	31.2	0	24.1	23.6	22.3	23.9
2	100% current, low speed	126	0	36.2	34.0	29.7	35.3
3	3,000 rpm, 100% current, low temp coil	129.3	29.5	39.1	37.2	30.8	38.0
4	3,000 rpm, 100% current, high temp coil	179	29.5	45.4	42.7	34.6	43.9
5	8,000 rpm, 100% current, high temp coil	195	140.2	58.2	58.0	39.4	55.2
6	Low-speed 37% overload	238.1	0	50.6	46.3	38.2	48.7
7	20 A_{rms} /mm^2 overload and full core loss	468.8	140.2	92.1	85.8	60.1	87.7

The FEA temperature contours in Fig. 7.2-15 highlight the maximum winding temperature located the upper corner of the stator slot at the portion of the coil furthest from the cooling ducts. Further, the maximum stator core temperature tracks well with the maximum coil temperature as indicated in the temperature FEA contours and Table 7.2-6. Thermal imaging of the stator core will be a useful technique for evaluating the peak winding temperature to complement

thermocouples mounted on the end windings. As observed in the FEA contours and in the Table 7.2-6 summary, thermal gradients exist in the end winding which may cause variation in the measured temperature.

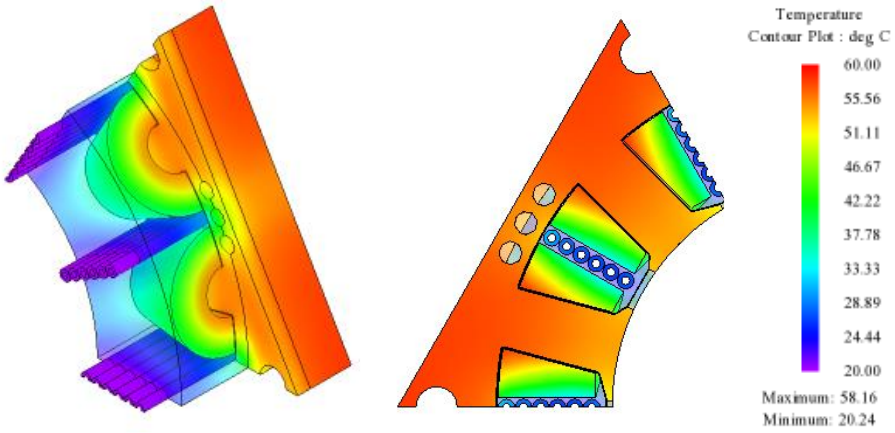

(a)

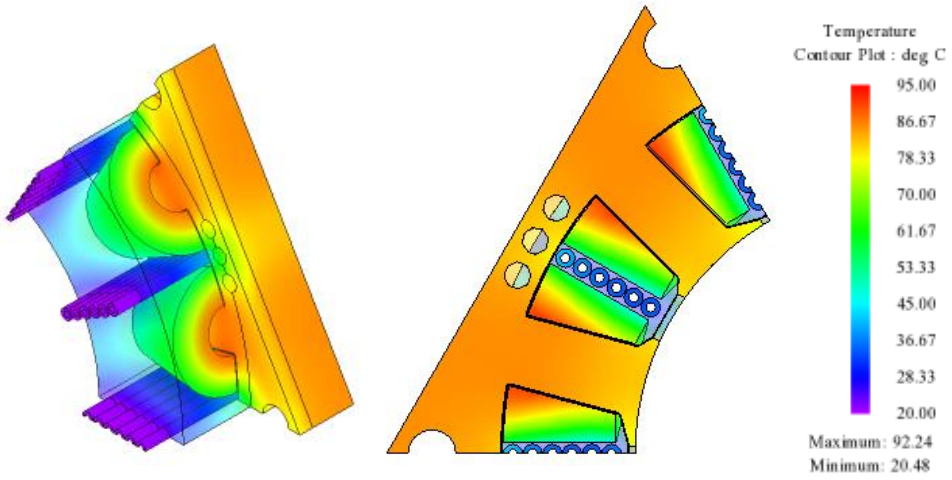

(b)

Figure 7.2-15 Steady state FEA flux density contours: (a) case 5 peak loss condition; and (b) case 7 peak overload condition.

7.2.3.3. Thermal Isolation Evaluation

Thermal isolation is assessed by assigning healthy and faulted coils to the two-coil thermal FEA model. Losses in the faulted coil are increased relative to the healthy coil, and the corresponding

maximum temperature rise is recorded. Steady state thermal FEA results are given in Fig. 7.2-16 summarizing the isolation study. For a 3x increase in loss, the faulted coil temperature increases 42.2 °C compared to only an 8.7 °C rise in the healthy coil indicating reasonable thermal isolation between phase coils confirm the low-power scalability of the proposed thermal isolation feature.

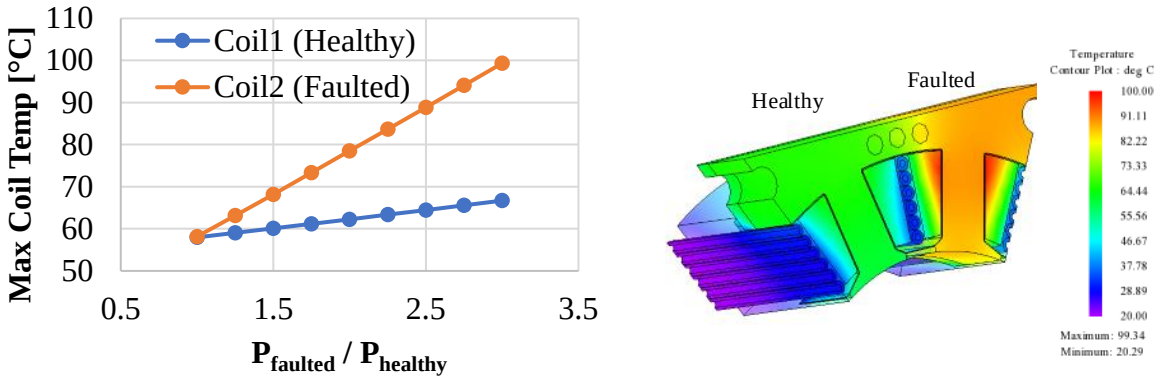

Figure 7.2-16 Thermal isolation summary of the demonstrator machine (left) showing healthy and faulted maximum coil temperatures against relative faulted coil loss increase and steady state temperature contour showing healthy and faulted coil temperatures at 3x loss condition.

7.3. Chapter Summary

This chapter presents scaling studies related to the studied enhanced magnetic isolation features and in-slot cooling methodology. Flux-barriers, modified stator tooth tips, and in-slot cooling is studied for magnetic and thermal isolation scaling capabilities up to 2MW and down to 7kW power levels. The selected approach for isolation scaling is to develop representative machines with these features at the power levels of interest and calculating relevant isolation metrics.

The 2MW design is guided by electrified propulsion criteria provided by ARPA-E (5000 rpm direct drive, 12 kW/kg total power density for both machines and drives). Other design sizing

criteria are inspired by the NASA ULI 1MW machine described in Chapter 2 which inform an initial sizing analysis of a 48-slot 40-pole design that utilizes the developed isolation features. After FEA optimization, the machine shows a reasonable active power density of 23.5 kW/kg, on par with the presented NASA ULI design.

A magnetic isolation study of the 2MW design indicates a MIR isolation rating of 2.7% demonstrating the proposed magnetic isolation features scale to higher power levels. The same study shows the inductance boosting capability of the innermost-tooth tip on the overall inductance. Removing these tooth tips from the design result in an 11.6% reduction in machine inductance.

The 2MW machine is then evaluated for its thermal performance using the same ceramic bobbin and potted channel cooling approach introduced in Chapter 5. The cooling capability of the bobbin approach shows limited ability to effectively cool the 2MW winding, requiring highly thermally conductive potting materials in order to realize reasonable temperatures. This difficulty can be traced to general loss density increases due to the high-power density requirements and the general geometric scaling expected for megawatt scale designs. In general, the cooling bobbin technique does not scale well at megawatt power levels without enhanced materials or significant co-optimization between the electromagnetic and thermal designs to reduce thermal resistances to coolant. Last, thermal isolation between coils is confirmed, although the steady state performance is poor.

The second half of this chapter introduces a 7kW demonstrator utilizing the previously described isolation features. Differing from the previous studied machines, this design is to be fabricated and tested to experimentally confirm the FT isolation features. Requirements for the machine are outlined, reflecting the need for readily available materials and ease of manufacture.

As such 12-slot 14-pole design with v-shape IPM rotor topology is selected that is compatible with two three-phase modules.

Electromagnetic performance of the machine is presented. The analysis shows degradation in machine torque performance and power factor related manufacturing considerations (tolerancing, etc) and 3D effects which are significant for the developed short stack length machine. A complete 3D FEA loss analysis is presented. At rated load and temperatures, the machine is expected to achieve a 93.9% efficiency.

The developed electromagnetic models are assessed for magnetic isolation and a *MIR* score of 1.7% is calculated confirming the scalability of isolation features to lower power level. Further, the contribution of the inner-most tooth tips is assessed, indicating a 12.6% contribution to the total inductance—in similar proportion to the mentioned 2MW machine.

The calculated losses are applied to a steady-state thermal model in FEA. Differing from the other designs, this machine utilizes in-slot cooling via alumina tubes positioned in the center of the slot. For rated conditions this machine shows exceptional cooling with a calculated 38 °C maximum temperature rise. The thermal limits of this machine are assessed, and simulations indicate $20A_{rms}/mm^2$ continuous current density is feasible with maximum coil temperature below 100 °C. The developed model is then used in a thermal isolation study. The proposed cooling channels show good thermal isolation between machine phases confirming the low power scalability of the thermal isolation technique.

Chapter 8

Fabrication and Test of Two-Module FT Demonstrator with Enhanced Isolation Features

Chapter 7 presents the design and analysis of a low-power fault tolerant (FT) permanent magnet synchronous machine (PMSM) with a double layer (DL) fractional slot concentrated winding (FSCW) consisting of two independent three-phase modules. Isolation between modules is achieved by the implementation of specialized isolation features in the stator that mitigate both thermal and electromagnetic interactions between modules. These features include the introduction of flux barriers between phases in the stator back iron and the removal of interphase tooth tips. Intra-phase tooth tips remain which are utilized to increase the machine inductance, reducing the characteristic current of the machine. Thermal isolation between phases is achieved via direct cooling of the winding using thermally conductive alumina tubes placed between the coil sides in each slot carrying a circulating low electrical conductivity fluid. The analysis in Chapter 7 highlights the effectiveness of this approach to isolate DL windings.

The low-power machine has been fabricated and tested to evaluate the developed model and proposed isolation approach. This chapter presents a comprehensive summary of machine fabrication and testing work for this machine including both healthy and faulted module operation. In general, both healthy and faulted test data aligns extremely well with simulated results in Chapter 7. Faulted module tests include terminal open and short circuit testing. Additionally, turn-to-turn faults are built into one of the machine phases, allowing for the external application of turn-to-turn short circuits. To avoid permanent damage to the machine, turn-to-turn fault testing is limited to only 1000 rpm and fault currents less than 32A (~2x rated current). Overall, the developed thermal isolation strategy is shown to effectively isolate phases during these fault events.

Faulted testing concludes with demonstration of a machine terminal short circuit to suppress turn-to-turn fault currents. Last, electromagnetic isolation has been evaluated statically by exciting the modules at high frequency with a stationary rotor, confirming the low mutual coupling between the two modules.

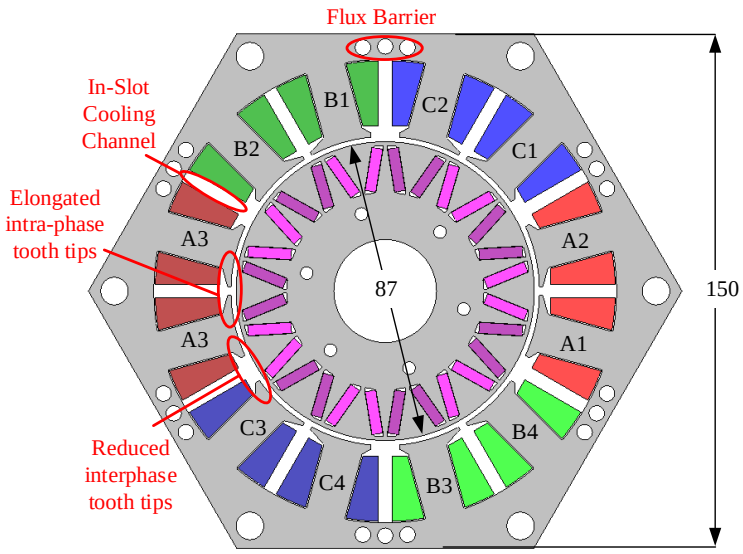

Figure 8.1-1 Demonstrator isolation features, phase arrangement, and stator and rotor outer diameter dimensions in mm.

8.1. Demonstrator Machine Description and Test Objectives

The demonstrator machine that was designed and built is a double layer (DL) 12-slot 14-pole fractional slot concentrated wound (FSCW) stator with a V-shape interior permanent magnet (IPM) rotor topology. The stator is modularized into two three-phase winding sets allowing for the loss of a module without loss of torque operation. Machine phases are isolated from one another using a combination of stator flux barriers and modified stator tooth tips. The winding is directly cooled by flowing a low-electrical-conductivity coolant through tubes placed between coils. Doing so provides physical separation between coils and isolates coils from thermal interactions between

phases—both desirable features for FT machines. Machine outer dimensions and feature summary are given in Fig. 8.1-1. The overall core stack length of the machine is 25.4 mm. Greater details related to machine magnetic and thermal performance can be found in Chapter 7.

Machine ratings and calculated circuit parameters are summarized in Table 8.1-1. Only room temperature resistances and magnet flux linkages are provided due to observed low operating temperatures during the test. Further, shared performance characteristics are limited to 3,000 rpm reflecting the maximum operating speed in this test. The machine is rated for 8,000 rpm though a compatible dyne was not available for the test. A self-dyne technique was attempted to reach full-power but was ultimately limited to lower speeds due to unbalanced magnet pull (UMP) related to self-dyne operation causing significant vibration.

TABLE 8.1-1 CALCULATED MACHINE RATINGS AND EQUIVALENT CIRCUIT PARAMETERS AT LOW TEMPERATURE

Machine Module Metric	Quantity
Speed [rpm]	3,000
Torque [N-m]	7.2
Shaft Power [kW]	2.3
Rated Module Phase Current [A_{pk}]	15.3
Rated Module Phase Voltage [V_{pk}]	213.9
Module flux linkage Magnets [Wb]	0.0232
Module q-axis Inductance [mH]	1.69
Module d-axis Inductance [mH]	1.88
Characteristic Current [A_{pk}]	11.5
Module DC Phase Resistance [mΩ]	180.0

The demonstrator machine is fully tested up to 3,000 rpm (speed limit of the test dyne) under both healthy and faulted conditions. The implemented machine test sequence is given in Table 8.1-2 reflecting risk-minimization strategy performing low risk testing first to achieve the most out of the test machine in the event of a major failure. For ease of presentation test results are presented out of the actual test sequence with relevant chapter sections provided in Table 8.1-2.

TABLE 8.1-2 TEST SEQUENCE AND ASSOCIATED MODULE CONFIGURATION AND CHAPTER SECTION

Test Seq. #	Test (measurement)	Config.	Section
1	Static Testing (inductance, resistance)	1	8.4
2	No-load (back emf)	1	8.4
3	Light load testing (torque)	1	8.5
4	Full-load testing (torque, temperature)	1	8.5
5	Initial OC and SC terminal testing (fault performance, drag torque estimation)	1	8.6
6	Full-Load Testing (reconfigured)	2	8.5
7	OC and SC terminal fault testing (reconfigured)	2	8.6
8	Turn-to-turn fault testing (current amplitude)	2	8.6
9	Static Isolation Testing (mutual coupling)	2	8.4
10	OC and SC terminal fault response testing (transient response and post-fault operation)	2	8.6
11	Aggressive turn-to-turn fault testing and SC fault response (thermal response, transient response, fault amplitudes)	2	8.6
12	Overload test and thermal heat run (torque, temperature)	2	8.5

Also given in Table 8.1-2 is a configuration number related to the module coil arrangements during the associated test (M_1 representing module-1 and M_2 representing to module-2). Configuration-1 refers to coil combinations: M_1[A1, A2, C1, C2, B1, B2] and M_2[A3, A4, C3, C4, B3, B4] (see Fig. 8.1-1 for coil placement). Configuration-2 refers to coil combinations: M_1[A1, A2, C3, C4, B1, B2] and M_2[A3, A4, C1, C2, B3, B4]. In other words, configuration 1 represents a split or halved stator arrangement, and configuration 2 represents an interleaved phase arrangement.

Before discussing test results, details related to the machine fabrication and test setup are provided.

8.2. Machine Fabrication

Details related to the fabrication of the demonstrator machine are summarized in this section. Machine fabrication details are presented based on assembly step and subassembly. These are

ordered: stator assembly, cooling assembly, rotor assembly and general assembly. Specialized steps related to the insertion of turn-to-turn short circuits is also discussed.

8.2.1. Stator Assembly

Components consisting of the stator assembly include bonded lamination stacks, slot liner material, 3D printed onyx endplate material, 20 AWG magnet wire, and end winding thermocouples. Rotor lamination stack bonding is discussed here due to the concurrence of stator and rotor core fabrication.

Stator and rotor laminations are laser cut from 0.356 mm thick M19 steel. A total of 72 laminations are stacked and bonded per core using 3M Scotchcast 265. Based on the machine final stack length, a machine stacking factor of 0.97 is estimated. Fig. 8.2-1(a) shows stator and rotor cores after bonding. 3D printed onyx endplates (4 mm thick) are attached axially to the machine to avoid winding on sharp stator core edges. A 0.007” Nomex 410 is formed and taped in place inside the stator slot as shown in Fig. 8.2-1(b).

Each stator tooth is wound with 47 turns of 20 AWG wire (x2 in parallel). A 37.2% fill factor is calculated for the winding window (25.4% fill factor for entire slot area). Wedges are placed between coils to prevent coil relaxation into the coolant channel space. A .015” thick NKN555 laminate strip is placed between the coil and tooth tips to hold coils in place and to further insulate coils from exposed tooth tip iron. Final machine winding is shown in Fig. 8.2-1(c). Note the substantially smaller end windings in Fig. 8.2-1(c) than what is modeled in Chapter 5. Last, type-K thermocouples from TC Direct (201-301) are taped to machine end windings as shown in Fig. 8.2-1(d).

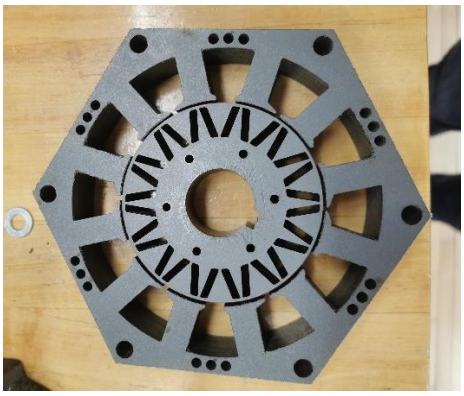

(a)

(b)

(c)

(d)

Figure 8.2-1 Stator fabrication steps: (a) lamination bonding; (b) endplate and slot liner installation; (c) completed wound stator with spacer wedges; and (d) thermocouple installation.

8.2.2. Cooling Assembly

Stock alumina tubing with inner and outer diameters of 0.063” and 0.125” is purchased and cut to 95 mm length. The wound stator in Fig. 8.2-1 is inserted into a specially designed potting fixture, spacing wedges are removed from the coils, and the cut alumina tubes are inserted and held in place by the potting fixture as shown in Fig. 8.2-2(a). Epic Resins S7527 potting material is mixed and poured into the potting fixture, placed under vacuum to remove air bubbles, and cured at room temperature. Final potting result is shown in Fig. 8.2-2(b).

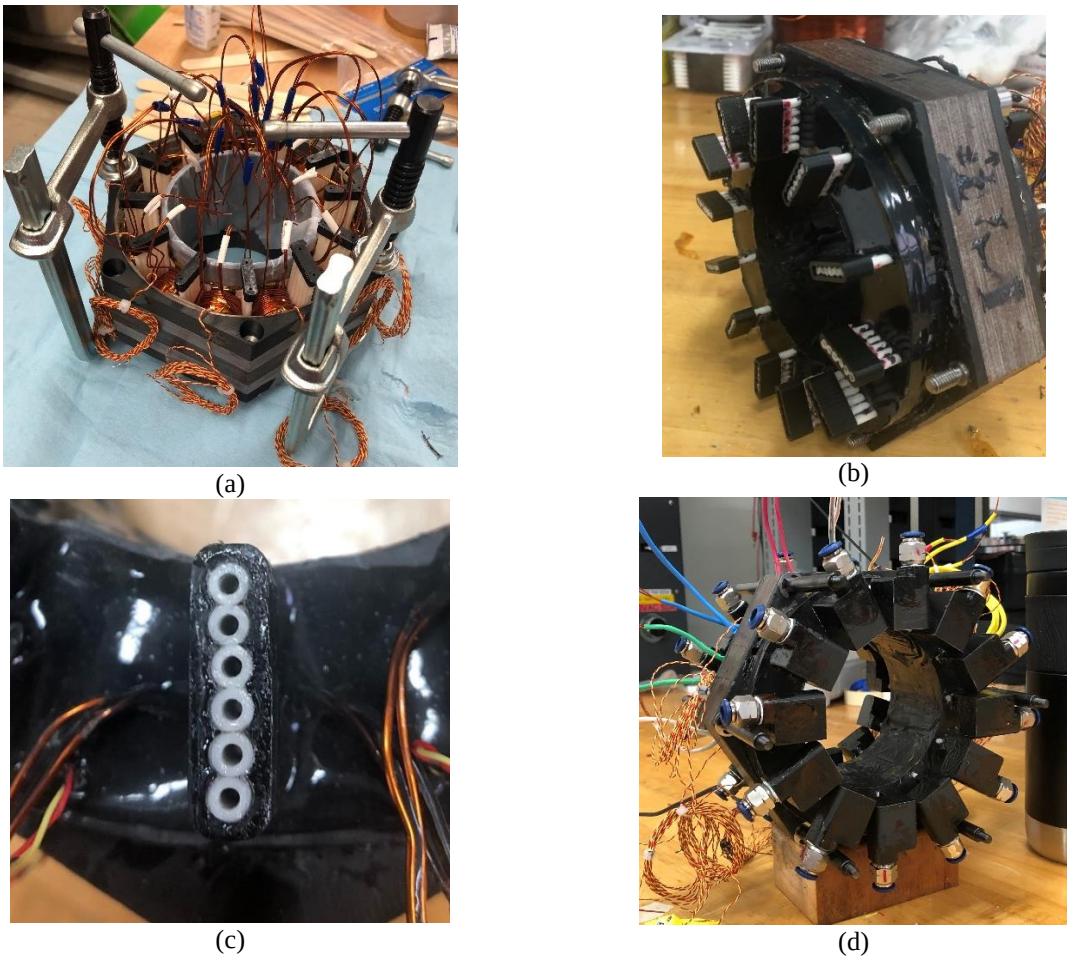

(a) (b) (c) (d)

Figure 8.2-2 Cooling assembly fabrication steps: (a) alumina tubing insertion into the stator and potting assembly fixturing; (b) post cure potting result; (c) endpiece 1 (EP1) attached to end of alumina tubes; and (d) final stator assembly with cooling endpiece 2 (EP2) and quick disconnects installed.

Two 3D printed PLA endpieces are used to connect and seal tube endings. The first endpiece (EP1) is placed around tube endings as shown in Fig. 8.2-2(b) and (c). Gaps between the tubes and EP1 are filled with gap filling Loctite 416, with the sealed result shown in Fig. 8.2-2(c). The second endpiece (EP2) seals against the outer rectangular surface of EP1 using the same Loctite 416. This EP2 has a tapped 1/8” NPT hole and a quick disconnect fitting (with universal threads and a gasket seal) is attached. EP2 is designed to direct fluid radially outward toward the mentioned quick disconnect fitting in Fig. 8.2-2(d). Each cooling channel is plugged and pressurized with air up to

10 psi to identify leaks. Identified leaks are marked and additional Loctite 416 is applied until all observable leaks are removed.

Notably, several of the EP2 prints had porous walls causing air to escape during the pressure test. Loctite 416 is painted onto the surface of the endpiece to patch porous sections as evident by the glossy appearance of several EP2 components in Fig. 8.2-2(d).

The combined stator and cooling assembly is shown in Fig. 8.2-2(d) before general machine assembly. Note the stator support shafts from Misumi located at the corners of the stator hexagon are inserted in Fig. 8.2-2(d).

8.2.3. Rotor Assembly

The bonded rotor core lamination stack is described and shown above in Fig. 8.2-1(a). Next, NdFeB rotor magnets (B842SH) from K&J Magnetics are bonded inside the rotor core magnet slots using Loctite 332 structural adhesive. Each magnet has a length of 6.35 mm so four magnets per slot are required for the 25.4 mm stack length, leading to a total of 112 magnets inserted in all slots. Special tooling, fixturing, and processes were developed to assist with the magnet insertion to ensure all magnets were inserted properly and in the correct orientation. Rotor pole orientations were later confirmed using a gaussmeter. The rotor core assembly with all magnets installed is shown in Fig. 8.2-3(a).

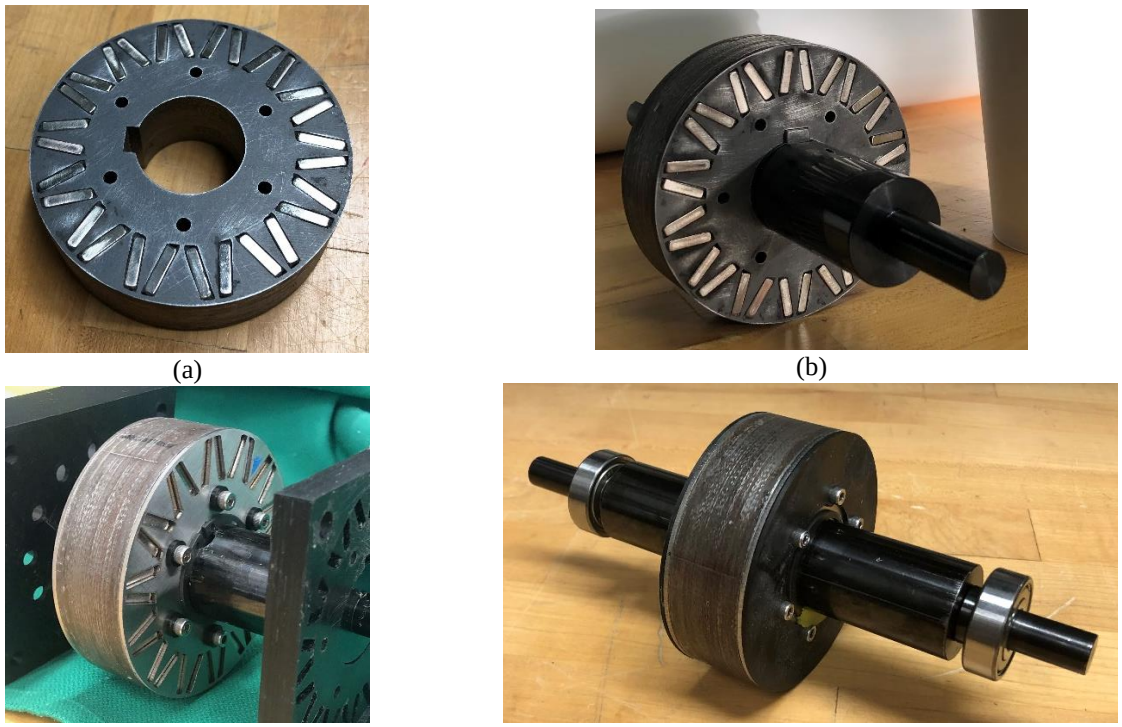

(a) (b)

(c) (d)

Figure 8.2-3 Rotor fabrication: (a) post magnet installation; (b) after key and shaft installation; (c) modified axial support endplate for rotor laminations; and (d) final rotor assembly before general assembly.

After, the rotor shaft (custom Misumi stepped shaft) and key is pressed into the rotor core as shown in Fig. 8.2-3(b). A 1/16th stainless steel 316 plate is designed with magnet cutouts to axially support the lamination stack and is installed (Fig. 8.2-3(c)). This is a modified version of the plate design presented in Chapter 7 since magnet and rotor core surfaces are not axially flush (i.e., some magnets extend outside the rotor core). This endplate is fastened to the rotor core using 316 stainless steel fasteners and locknuts. Retaining rings on the shaft hold the core-plate assembly in place.

Last, bearing spacers and bearing (B6201ZZ) were installed onto the shaft. A fiberglass reinforced Onyx cover is placed over the rotor endplate to cover the rotor endplate and exposed magnets as shown in Fig. 8.2-3(d). The total rotor assembly (without bearings) is balanced at 3,000 rpm.

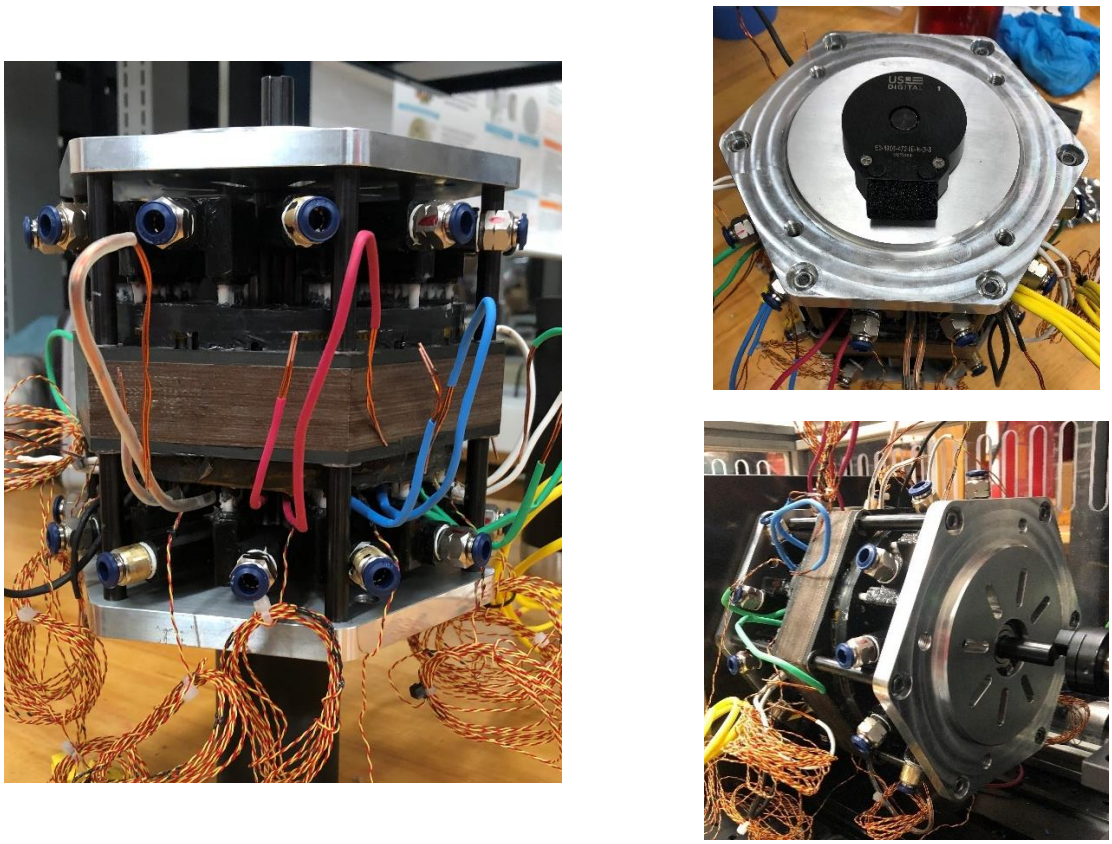

Figure 8.2-4 Final machine assembly.

8.2.4. General Assembly

Overall general assembly steps are provided without providing precise detail (e.g., fastener and retaining ring installation steps). This general assembly consists of insertion of stator supporting shafts into the stator core (shown in Fig. 8.2-2(d)), non-drive end (NDE) endbell installation onto the stator supporting shafts, rotor assembly insertion into the stator assembly bore, drive end (DE) endbell installation, and the encoder installation onto the NDE shaft extension and endbell. Both endbells are made from Al6061 and the selected encoder is a US Digital E3-1800-472-IE-H-D-3. Photos of the final machine assembly are given in Fig. 8.2-4.

Overall, the built machine has an axial length of 169.5 mm from outer surfaces of both endbells. Between endbell inner surfaces the axial length is 138 mm. The core stack length is 25.4 mm and

overall axial length with end windings is a ~46mm (a bit more if potting material is included). This leads to only 33% of the available endbell space being utilized by active components. The remaining 66% is predominantly used for coolant channel accommodations. Certainly, this can be reduced with greater design effort, though this at least highlights one of the major challenges associated with the proposed in-slot cooling method.

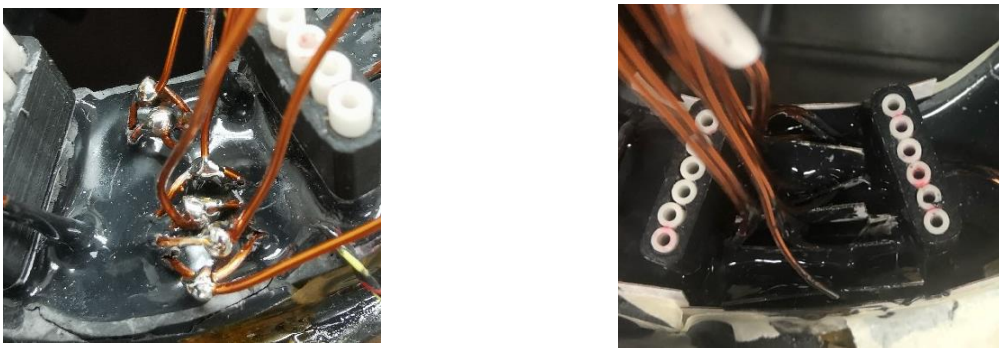

(a) (b)

Figure 8.2-5 Faulted turns 27, 36, and 47 (6 strands total) in phase A3: (a) exposed turns after solder step and (b) re-insulation solder joints and strands.

8.2.5. Faulted Turn Implementation

A critical step not highlighted in the winding section is the inclusion of jumper wires into one of the machine phases (coil A4 in Fig. 8.1-1 above) allowing for the external application of turn-to-turn faults. Specifically strands from turns 27, 36, and 44 (of 47) are wound outside the coil. These turns were selected due to their ease of removal during the winding process, though allow for a range of faulted turn combinations. Sufficient length is extended so the looped turns extend above the potting step shared in Fig. 8.2-5(a). The exposed strands are stripped and soldered to 20AWG magnet wire strands as Fig. 8.2-5(a). After, the solder joints and exposed strands are separated using NKN555 slot liner and potted using leftover S7527 potting material in Fig. 8.2-5(b).

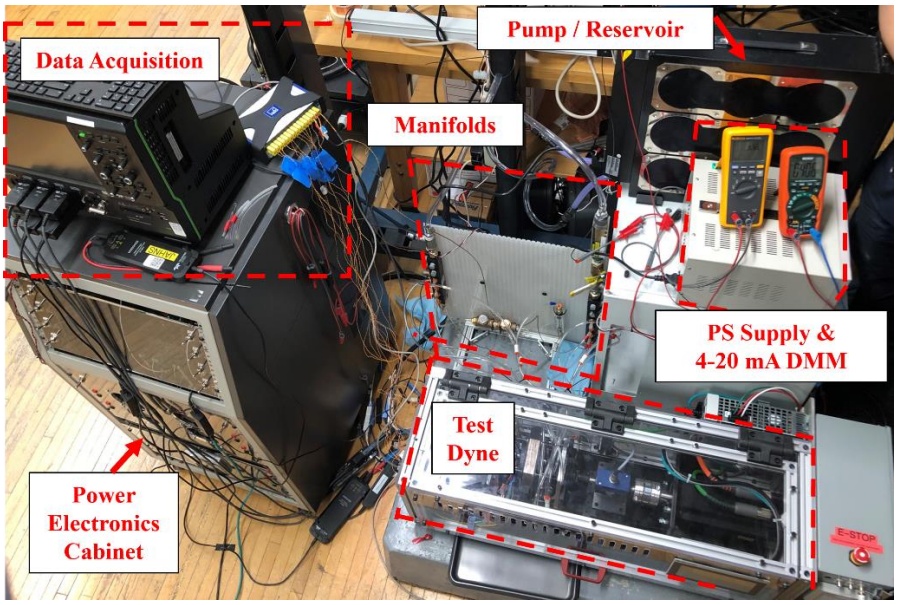

Figure 8.3-1 Experimental test space layout and components.

8.3. Test Setup

Components and systems related to the test space are shown in Fig. 8.3-1. Not shown is a 600Vdc 40A Magna power supply and resistive load bank for the dynamometer (necessary for dyne generator operation).

8.3.1. Test Dynamometer

The dyne drive lineup is shown in Fig. 8.3-2. Going from right-to-left in Fig. 8.3-2, the dynamometer consists of an Allen Bradley MPL-A540K load machine and a Ultra3000 motor drive. Using this setup, the dyne is capable of 4.1 kW at 3,000 rpm. The load machine is connected to the torque transducer with a bellows style flex coupling. The torque transducer is an HBM T21WN/20NM with voltage output with scaling of 0.5 V/N-m. The torque transducer is connected to the test machine using hub-style flexible coupling with a slotted disk hub.

Neutral and phase connections are made to stripped magnet wire leads using WAGO 221-stye clamp terminal blocks. While convenient, this style of terminal blocks did have notable contact

resistance and heating during the test. For some connections one of the two-parallel strands would disconnect, forcing rating current into a single strand (~30 A/mm^2 current density). Module leads, and faulted turns are brought out the back of the dyne towards the power electronics cabinet.

Cooling duct connection and tubing is brought out on a separate side of the machine dyne to the coolant manifolds. Cooling loop connections are discussed in a lower section.

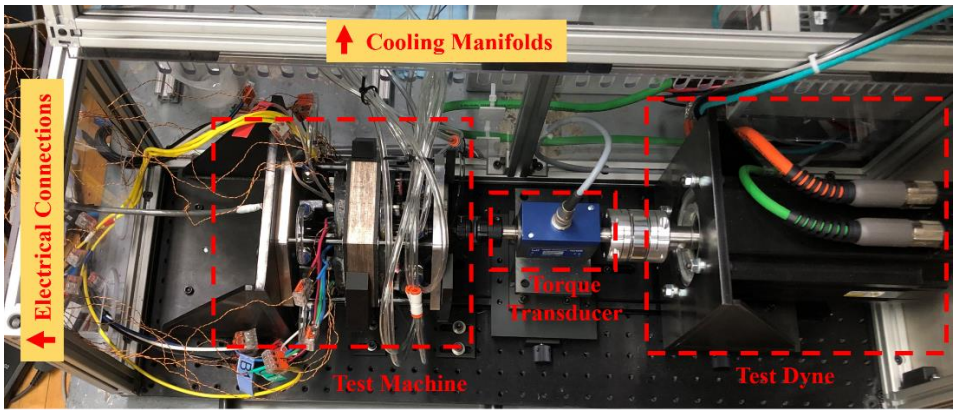

Figure 8.3-2 Test dynamometer setup.

8.3.2. Modular Power Electronics & Machine Control

The power electronics cabinet in Fig. 8.3-1 contains modular power electronics to drive the two-different windings sets of the demonstrator machine. A detailed review of the power electronics design and the overall control is beyond the scope of this thesis, and the reader is referred to UW-Madison student Hao Zeng's PhD thesis titled "Distributed Control and Self-Sensing of Permanent-Magnet Modular Motor Drives (MMDs) for Electric Aircraft Propulsion" which discusses this power electronics design among other control related topics surrounding FT modular motor drives. Instead, a brief description of the power electronics is given.

The overall architecture of the power electronics and control is summarized in Fig. 8.3-3. Each machine-module has its own dedicated custom power-electronics consisting of SiC switching devices in stacked half-bridge configuration. Each machine and power electronics module has its

own dedicated controller, receiving independent commands from the host computer. These controllers only communicate in the event of a fault and the appropriate remedial action is followed. This faut response and controller interaction is captured and discussed later in this chapter.

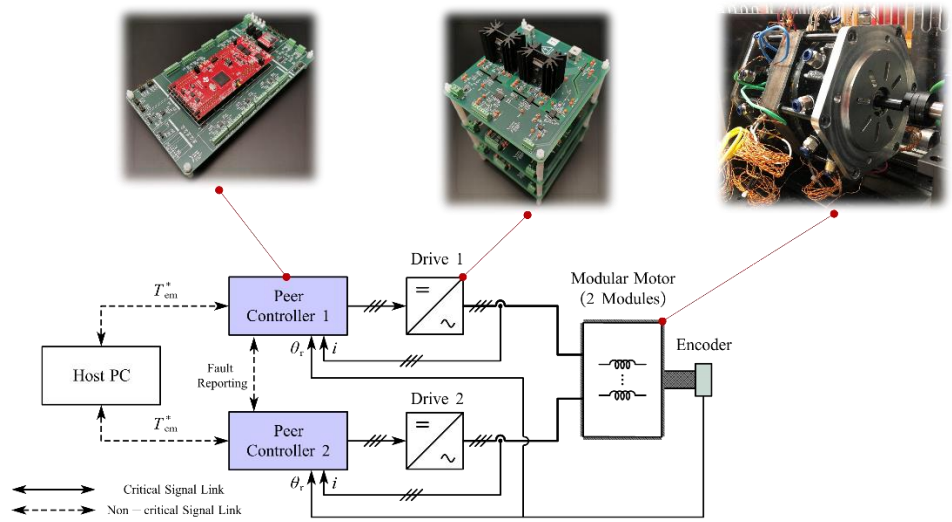

Figure 8.3-3 Control, power electronics, and machine architecture (image credit: Hao Zeng, 2023).

8.3.3. Data Acquisition

Primary data collection is made using a Teledyne Lecroy MDA810A oscilloscope that receive voltage measurement signals from HVD3102 voltage and CP031 current probes measuring machine phase voltages and currents. Additional torque transducer voltage output signals are measured using the scope. In some instances, torque measurements are recorded manually from the dyne interface (reading the same torque transducer feedback).

Temperature data from the twelve end winding thermocouples and three cooling loop thermocouples is collected using HBM QuantumX MX1609KB with data observed through the MX Assistance software. This software does not allow for exported temperature measurement data, so only screenshots of various test points are available. For thermal heat run tests, a FLIR thermal image camera is used to assess the stator core and potting temperature.

Additional test measurements are recorded manually in a test notebook during the test. These include dc supply display voltages and currents, multimeter measured 4-20 mA signals from the cooling pressure sensors shown in Fig. 8.3-1, and flow measurements from rotameters in the cooling loop. Finally, test noise is recorded using an iPhone 8 and processed using an FFT application to illustrate vibration related noise and the associated frequencies.

8.3.4. Cooling Loop

Machine fluid connections are made at the quick disconnect fittings on either side of the machine using 5/32” ID tubing. A 6-parallel 2-series fluid connection scheme is used (discussed in Chapter 7) resulting in all inlet and outlet connections on the DE side of the machine, and tube jumpers on the NDE side as shown in Fig. 8.3-4(a). Inlet and outlet hoses are routed to supply and return manifolds away from the dyne setup as shown in Fig. 8.3-1. It should be noted some variation in hose length is determined acceptable due to the difficulty of connecting hoses under the machine while mounted.

The manifold layout and components are given in Fig. 8.3-4(b). Each manifold has 12 connection ports allowing a 12-parallel test configuration if required, though remaining 6 ports per manifold are plugged for the presented experiment. Each manifold has a threaded thermocouple (McMaster Carr 1245N12) to measure bulk supply and return fluid temperature. One leg of the supply manifold connects to a pipe-assembly with an additional thermocouple and inline volumetric flow meter (McMaster Carr 8051K39, 2.2 to 22 gph scale). A factor of 0.9567 is used to correct flow readings for the higher specific gravity of the selected coolant.

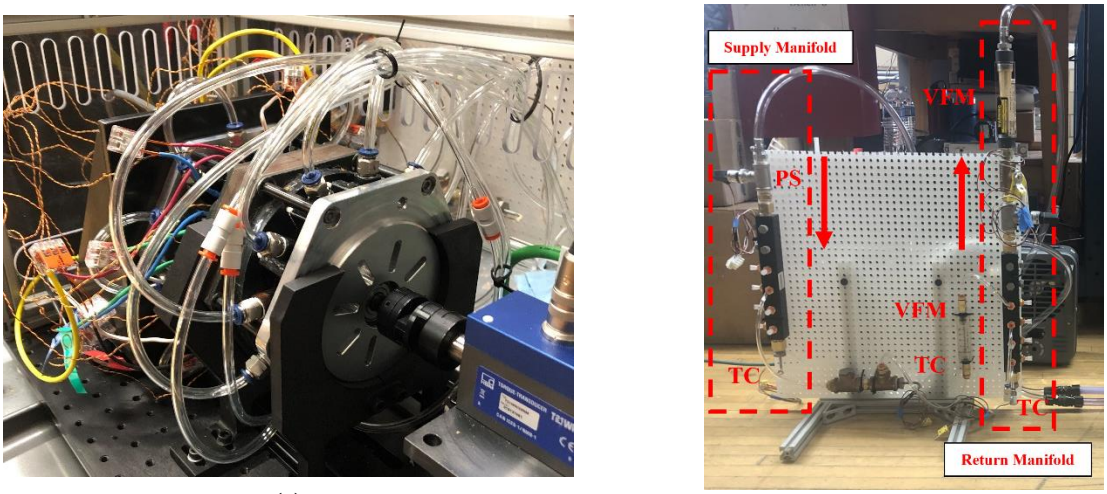

(a) (b)

Figure 8.3-4 Cooling loop: (a) machine cooling connections, and (b) manifold components (PS – pressure sensor, VFM – volumetric flow meter, and TC – thermocouple).

Upstream from the inlet manifold (and downstream from the return manifold) are pressure sensors (McMaster Carr 319K51, pressure range 0-15 psi) allowing for assessing the pressure drop of the manifold/motor system. These output a 4-20 mA signal which is read on the digital multimeters as shown in Fig. 8.2-1. A second volumetric flow meter (McMaster Carr 8051K42) is added to the return manifold to measure the bulk flow. The overall system is driven by a Koolance ERM-3K3U pump-reservoir with Koolance 705 (propylene glycol) fluid.

After filling the machine will fluid, the measurements are made for various pump speed settings (1-10 with 10 being maximum speed). Measurements were stopped at a pump speed of 6 due to excessive bubbling coming from the pump supply at higher speeds. Table 8.3-1 and Table 8.3-2 provides recorded pressure/flow measurements for pump setting 6. These pressure-flow characteristics are consistent throughout all of the presented experiments.

Several observations can be made from Table 8.3-1. First, the estimated bulk flow of this system is less than the 3.5 LPM assumed in Chapter's 7 thermal analysis (approx. 22.9% lower). Next, there is a notable difference between the estimated branch flow (from the bulk calculation) and the

flow measured from a single branch. Some difference may be attributable to the wide error bands of the sensors (+/- 5%) and human error in reading the rotameter, though the level of measurement difference indicates some level of unbalanced flow in the system. Another likely source is the asymmetry associated with the branch that has the flowmeter. In any case, these measurements suggest the observed thermal performance will be worse than simulated due to lower flows, and some unbalanced heating will likely be observed related to the uneven branch flows.

TABLE 8.3-1 TEST VOLUMETRIC FLOW MEASUREMENTS

Pump Setting	Bulk Volumetric Flow			Branch Volumetric Flow		
	Measured GPM	S.G. Corrected LPM	Est. Branch Flow [LPM]	Measured GPH	S.G Corrected LPM	ΔBranch flow [LPM]
6	0.8	2.90	0.483	12	0.756	0.273

TABLE 8.3-2 TEST MANIFOLD PRESSURE MEASUREMENTS

Pump Setting	Pressure Measurement				
	Supply (mA)	Supply (psi)	Return (mA)	Return (psi)	Pressure Difference (psi)
6	8.02	3.8	5.64	1.5375	2.2

8.4. Machine Parameters Validation

Machine parameters are estimated using a series of static and rotating measurements to validate the machine parameters provided in Table 8.1-1. These parameters include machine phase resistances, inductances, magnet flux linkage, characteristic current, and module isolation ratio *MIR*.

8.4.1. Phase Resistance Measurement

Machine coil resistances are measured using a six-digit digital multimeter after the fabrication of the machine. These coil resistances are summarized in Table 8.4-1.

TABLE 8.4-1 MEASURED COIL RESISTANCES IN OHMS AFTER WINDING.

Coil	Resistance (low)	Resistance (high)	Resistance (avg)	Resistance Dev.
1	0.090057	0.090207	0.090132	0.1%
2	0.089053	0.090103	0.089578	-0.5%
3	0.090135	0.090205	0.090170	0.2%
4	0.088930	0.089530	0.089230	-0.9%
5	0.090206	0.090317	0.090262	0.3%
6	0.090473	0.090571	0.090522	0.6%
7	0.089243	0.089381	0.089312	-0.8%
8	0.089980	0.090068	0.090024	0.0%
9	0.088864	0.088889	0.088877	-1.3%
10	0.090910	0.091350	0.091130	1.3%
11	0.090827	0.090965	0.090896	1.0%
12	0.089549	0.090225	0.089887	-0.1%
		Overall Avg.	**0.090002**	-

The phase resistance given in Table 8.1-1 reflect the measured coil resistances in Table 8.4-1. All measured machine resistances are well balanced within 3% of the overall average. Initial analytical calculations overestimated the coil resistance by approximately 7.5% due to differences in end winding geometry. The as-built machine has much smaller end windings compared to what was modeled in Chapter 7.

8.4.1.1. Faulted Turns Resistances

Additional resistances related to the faulted turns in Table 8.2-5 are measured using the same six-digit digital multimeter. These measured turn resistances relative to the phase lead (turn 1) are given in in Table 8.4-2.

TABLE 8.4-2 MEASURED FAULTED TURN RESISTANCES IN OHMS

Measurement Location	Avg. Resistance (Ω)
Turn 1 - Turn 27	0.057151
Turn 1 - Turn 36	0.074178
Turn 1 - Turn 44	0.089770

8.4.2. Inductance Measurement

Machine inductances are measured using RLC meter 4263B (500 mV 1kHz) at various rotor positions while the machine is coupled to the dyne. The rotor position is moved manually and locked in place for each inductance measurements. Rotor position is recorded using the dyne encoder. Inductance measurements for A1-neutral connection are given in Fig. 8.4-1 for approximately 1/6th of a mechanical rotation.

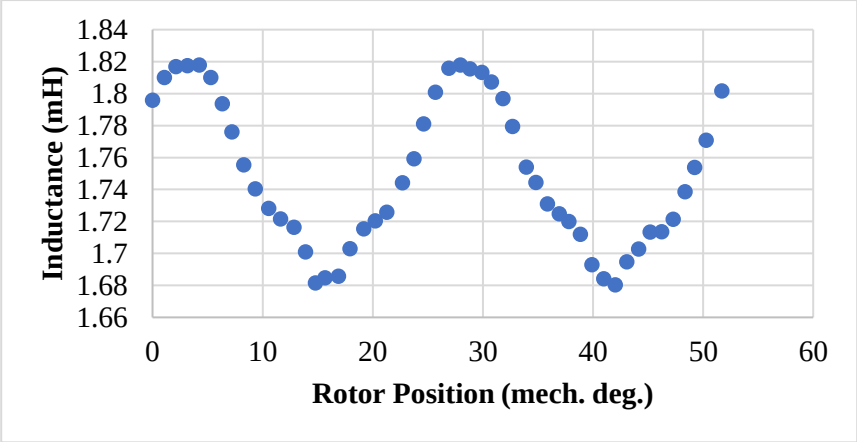

Figure 8.4- 1 Measured phase inductance for rotor position.

The shown inductances are sinusoidal in shape with peak values corresponding to the d-axis inductance (1.817 mH) and minimum values corresponding to q-axis inductance (1.685). In general, both inductance measurements agree very well with the calculated 1.88 mH and 1.69 mH d- and q-axis inductances respectively.

8.4.3. Magnet Flux Linkage Measurement

Magnet flux linkage can be determined from no-load phase voltage measurements capturing the back-emf of the machine. The magnet flux linkage is calculated from the fundamental component of the back-emf E_{i1} and electrical frequency:

$$\lambda_{pm1} = E_{i1} / \omega_e \tag{8.4.1}$$

No-load back-emf voltage measurements are made for machine speeds up to 3,000 rpm. Fig. 8.4-2 shows the three-phase back-emf voltages (from phase to neutral) from module 1 at 3,000 rpm. At 3,000 rpm the plateau of the back-emf voltage is approximately 48V. The frequency components of the measured back-emf voltage at 3,000 rpm are calculated with results provided in Figure 8.4-3. These are contrasted against JMAG design back-emf FFT results also given in Figure 8.4-3.

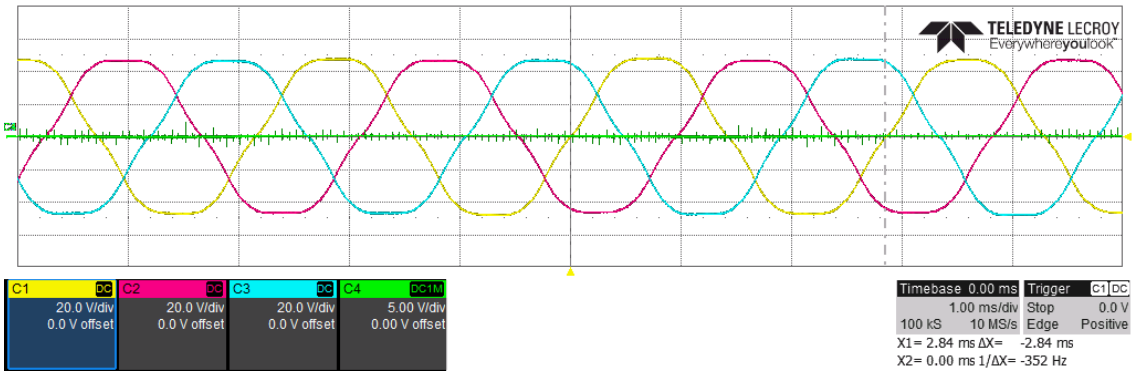

Figure 8.4-2 Module 1 back-emf line-neutral voltages at 3,000 rpm.

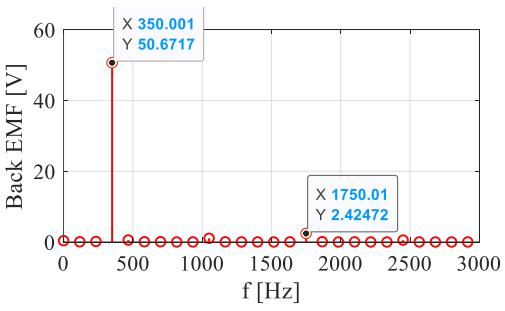

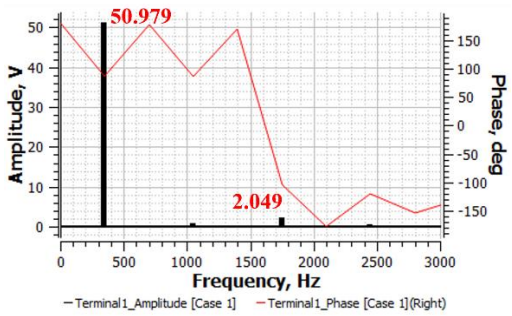

Figure 8.4-3 Back-emf measurement FFTs (left) and JMAG designer calculated FFT (right) at 3,000 rpm.

Using the fundamental component of the voltage measurement in Fig. 8.4-3, a magnet flux linkage of 0.0230 Wb is calculated which is within 1% of the JMAG calculated 0.0232 Wb. A notable difference between the two calculations is the amplitude of the fifth harmonic which is about 0.4V higher than simulation.

8.4.4. Characteristic Current Measurement

The machine characteristics current is calculated by applying three-phase shorts to both modules and ramping machine speed. This measurement is made with interleaved machine phases (configuration 2 described above). Module-1 phase currents at 3,000 rpm under the three phase currents is shown in Fig. 8.4-4(a) showing peak currents of 11.4A. This compares to the 11.5A calculation from JMAG. Measured peak short circuit current different operating speeds is given in Fig. 8.4-4(b) showing a current amplitude plateau of 11.4A

The terminal short circuit test allows for the evaluation of machine braking torque T_{brk}. This is calculated analytically using machine parameters [121]:

$$T_{brk} = -\frac{3P}{4} r_s \lambda_{pm}^2 \omega_e \frac{r_s^2 + \omega_e^2 L_q^2}{\left(R^2 + \omega_e^2 L_q L_d\right)^2} \tag{8.4.2}$$

Measured braking torque is compared to an analytical calculation using (8.4.2) and the machine parameters defined in Table 8.1-1 and shown in Fig. 8.4-5. In general, both curves have the same general shape with peak torques occurring near 140 rev/min. However, a small difference in peak drag torque is observed. The measured result is approximately 0.3 N-m lower than the analytical and can be attributed to non-linearities in the machine parameters.

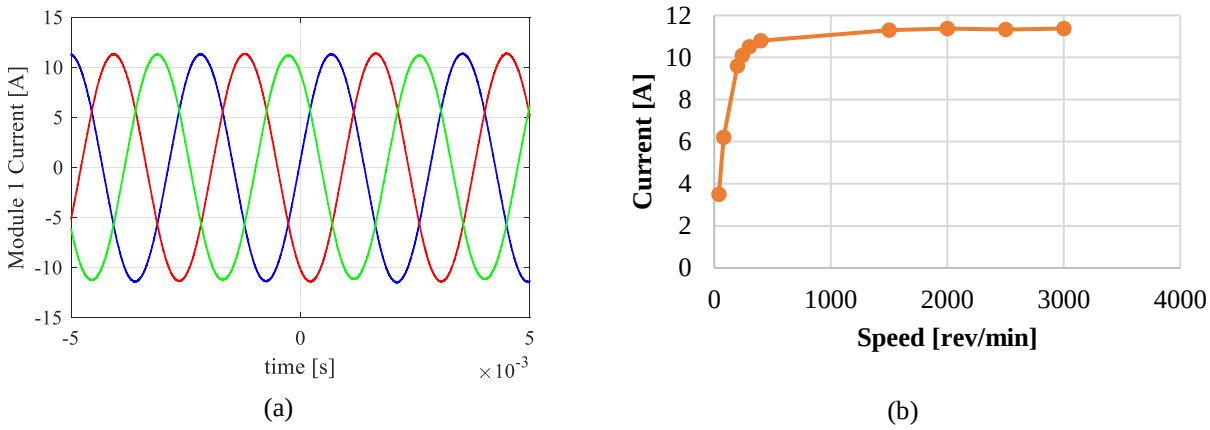

(a) (b)

Figure 8.4- 4 Measured machine currents after a fault: (a) 3000 rpm module 1 currents; and (b) observed peak current amplitude over tested speed range.

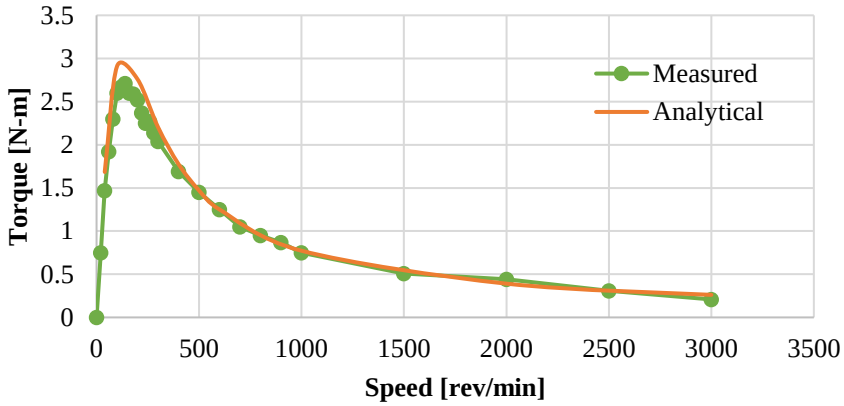

Figure 8.4-5 Measured and analytical braking torques for three-phase short circuits applied to modules 1 and 2.

8.4.5. Module Isolation

Finally, the machine's magnetic isolation capability is tested by exciting one module with high frequency current i_{abc1} and measuring the other modules voltage v_{abc2} at zero speed. Since the machine is not spinning (no back emf) and no current is flowing in the machine windings, then the measured voltage on phase v_{a2} equals

$$v_{a2} = M_{lkg} \cdot \frac{d}{dt}\left(i_{b1} + i_{c1}\right) \tag{8.4.3}$$

for adjacent coils current i_{b1} and i_{c1} (for an interleaved configuration) and mutual leakage coupling M_{lkg}. Assuming balanced current I_{s1} on Module 1 and steady state operation allowing derivative terms to be replaced with $j \cdot \omega_e$, leads to a mutual leakage calculation

$$M_{lkg} = \frac{V_{a2}}{\omega_e \cdot I_{s1}} \tag{8.4.4}$$

This is implemented experimentally by providing module 1 with 10 A_{pk} of current at 1 kHz and measuring a single phase of Module 2. A scope capture of the measured excitation currents and voltage is shown in Fig. 8.4-6. Significant voltage ripple from Module 1 switching current affects the voltage measurement though a fundamental component is apparent. A frequency analysis of the voltage waveform is completed to extract the 1 kHz component with result share in Fig. 8.4-7. A 3.63V peak amplitude is observed at 1 kW with other predominant harmonics observed near 20 kHz (drive switching frequency).

Applying (8.4.4) yields an approximated mutual leakage inductance of 57.8 μH. The ratio of this leakage against the average phase inductance in 8.4-1 (1.75 mH) results in a module isolation ratio of 3.3%--approximately double than the estimate in Chapter 7. The source of the error stems from the method of simulated *MIR* calculation and differences in saturation state. The presented *MIR* calculations in this thesis disable magnets, result in the stator being in a different magnetization state during the calculation. This decision was made to give comparisons between topologies uncoupled from saturation effects. If saturation is considered, then the experimental and simulated *MIR* metrics agree. Further, this highlights the potential negative affects saturation

can have on leakage mutual coupling. Although this metric is degraded, a 3.3% *MIR* is still a reasonable level of isolation for a FT modular machine.

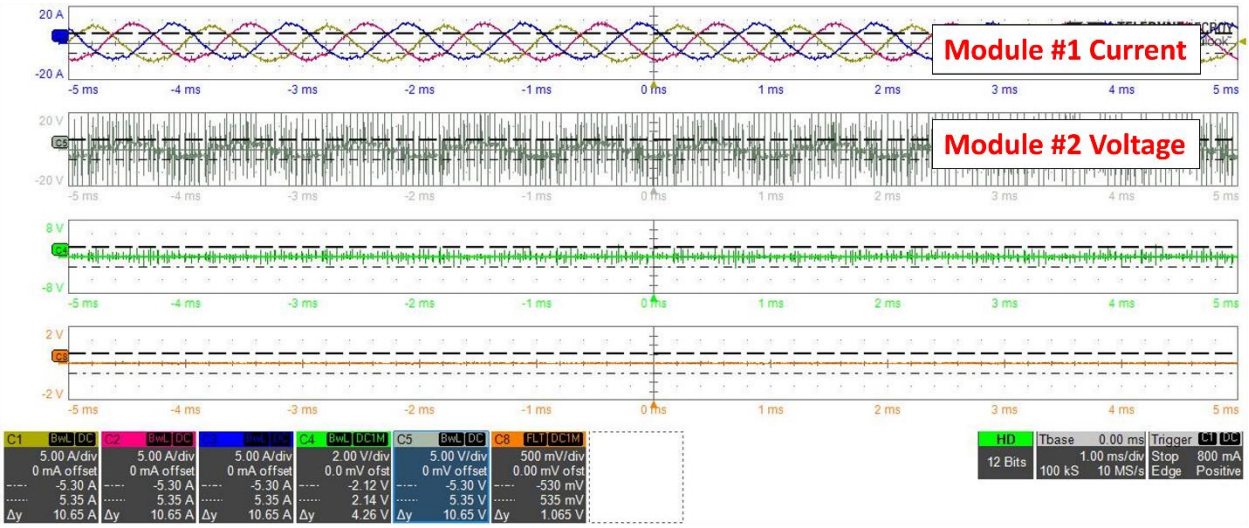

Figure 8.4-6 Scope measurement of module 2 open circuit voltage with module 1 exited with 15.3A of current at 1kHz.

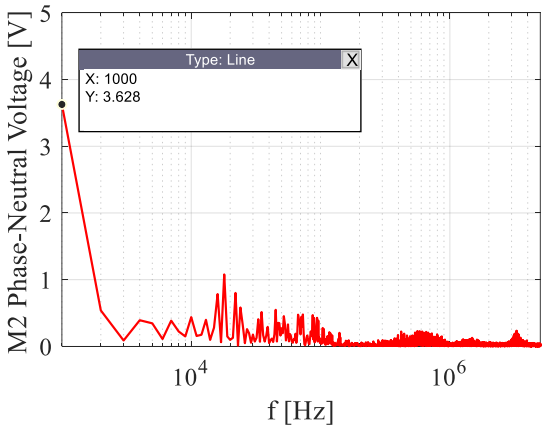

Figure 8.4-7 Magnetic isolation test voltage FFT of module 2 phase voltage

8.5. Healthy Testing

The machine is operated under healthy (non-faulted) conditions to validate torque and thermal performance. This section reviews test results from speeds 1000 rpm, 2000 rpm, and 3000 rpm

capturing torque output for 50% and 100% current rating points. An additional two overload points at 1.37x and 1.50x current rating to fully test the developed in-slot cooling methods.

8.5.1. Torque Validation

Machine phase currents, single phase line-to-neutral voltages, and torque transducer voltage outputs are provided for the 1000 rpm, 2000 rpm, and 3000 rpm operating points in Fig. 8.5-1, Fig. 8.5-2, and Fig. 8.5-3 for 50% and 100% current. Overloaded operating points can be found in 8.5-4.

8.5.1.1. 1000 rev/min Test

1000 rpm 50% (7.6A) and 100% (15.3A) test operating point data is given in Fig. 8.5-1 (for winding configuration #2). This test was completed with a 75V dc bus. Note some current unbalance is observed on module #2 currents (and none on module #1) related to the mentioned contact resistance problem with the selected phase terminal blocks. For the purposes of torque evaluation this is determined acceptable.

An average torque of 3.571 N-m is observed for the 50% load case, which aligns well with the expected 3.6 N-m (0.8% error). The ~0.3N-m level of torque ripple also reasonably matches the modeled torque ripple around ~0.4 N-m. Based on the measured torques and speeds, the shaft output power is 374.0W.

An average torque of 7.079 N-m is observed for the 100% load case, which also aligns decently well with the expected 7.2 N-m (1.7% error). The level of torque ripple doubles to nearly ~0.6 N-m. This torque ripple also aligns with FEA calculations near ~0.5 N-m. Based on the measured torques and speeds, the shaft output power is 741.3W.

A dc bus current of 5.82A (436.5W power in) and 12.64A (948.0W power in) is observed for the 50% and 100% test, respectively. This corresponds to measured system efficiencies of 85.7% and 78.4% and loss levels of 62.4W and 204.8W. At this speed the machine dc resistance losses should dominate the overall loss which correspond to 31.2W and 126.4W (room temperature resistance).

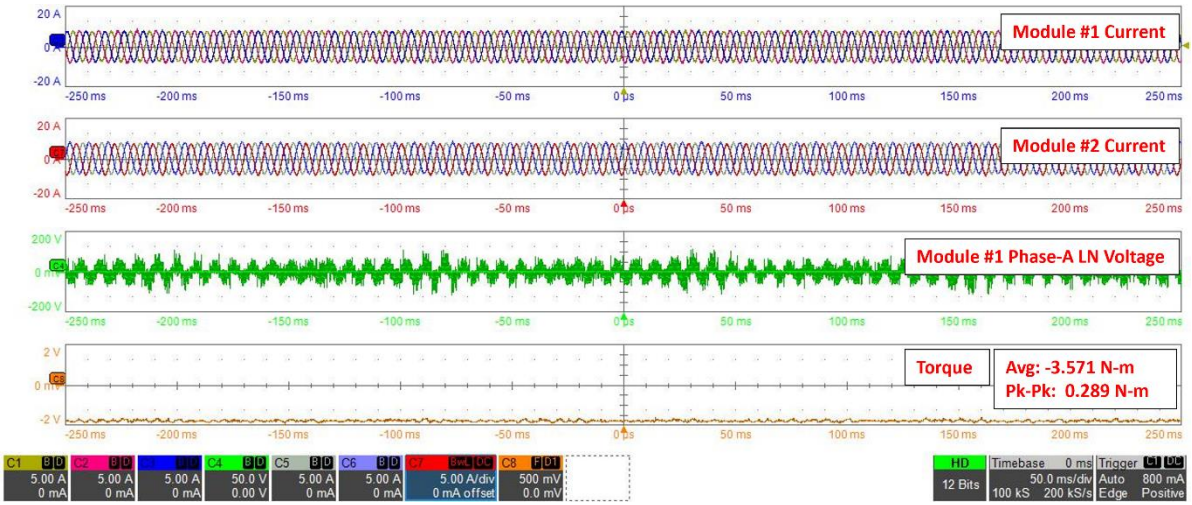

(a)

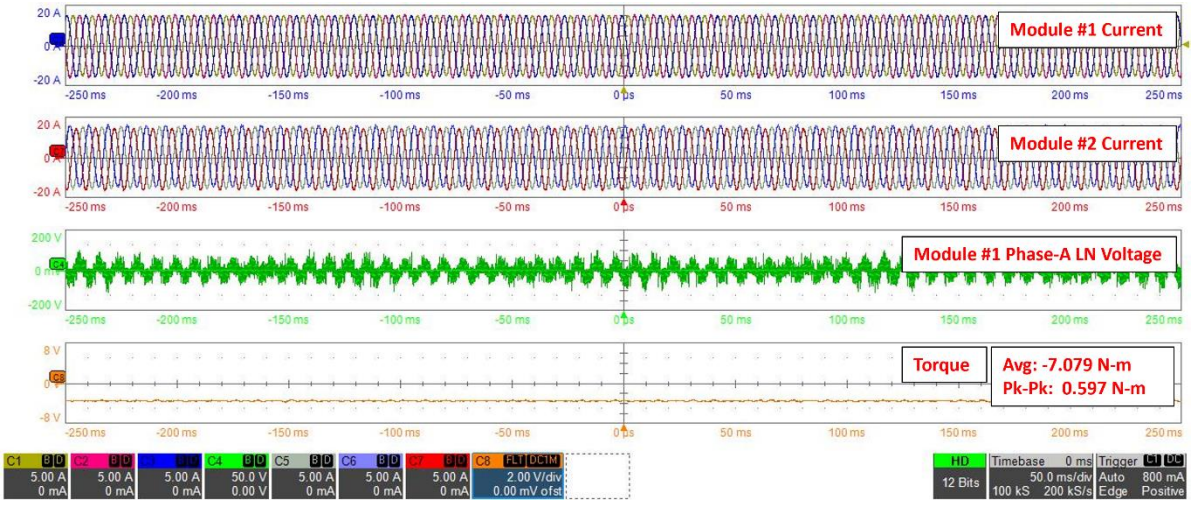

(b)

Figure 8.5-1 1000 rpm operating points: (a) 50% current; and (b) 100% current.

8.5.1.2. 2000 rev/min Test Speed

2000 rpm 50% (7.6A) and 100% (15.3A) test operating point data is given in Fig. 8.5-2 (for winding configuration #1). This test was completed with a 150.2V dc bus. Note the previously mentioned contact-resistance resistance-related unbalanced current is resolved for this test.

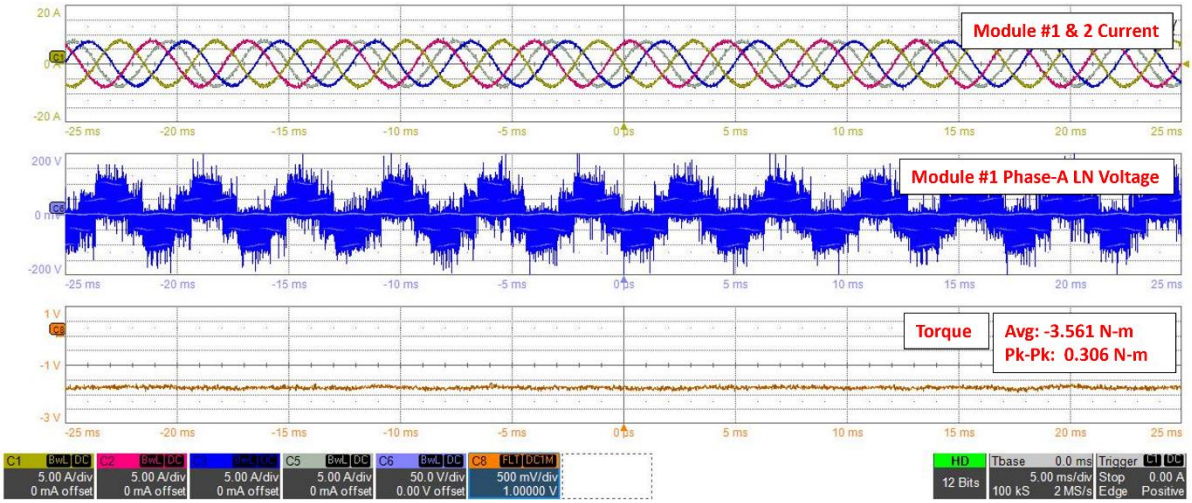

(a)

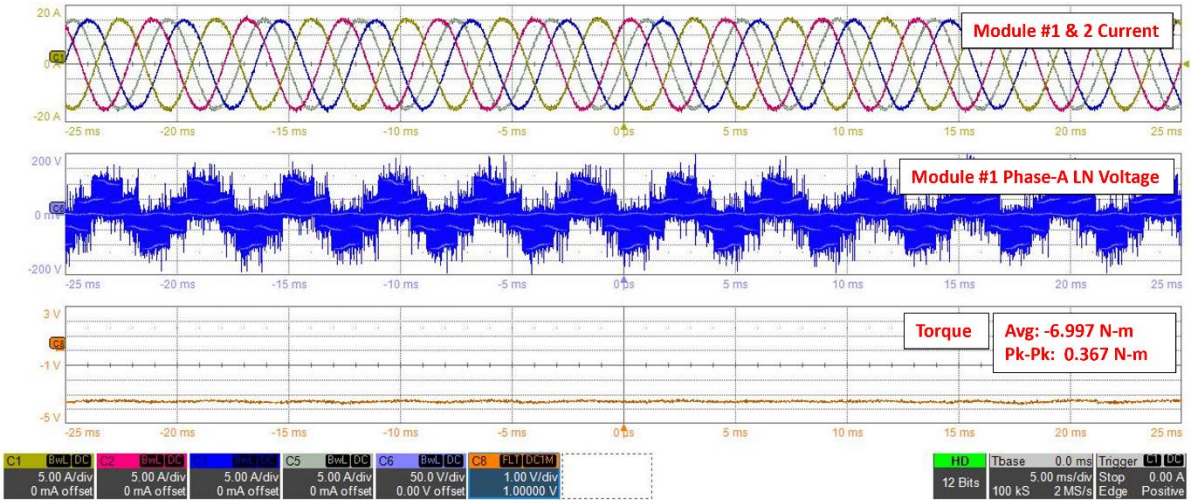

(b)

Figure 8.5-2 2000 rpm operating points: 50% current; and (b) 100% current.

An average torque of 3.561 N-m is observed for the 50% load case, which aligns well with the expected 3.6 N-m (1.1% error). Once again, the measured torque ripple reasonable matches FEA around 0.3 N-m. Based on the measured torques and speeds, the shaft output power is 745.8W.

An average torque of 6.997 N-m is observed for the 100% load case, which is below the expected 7.2 N-m (2.8% error). The level of observed torque ripple only marginally increases to ~0.4 N-m. This torque ripple also aligns with FEA calculations near ~0.5 N-m. Based on the measured torques and speeds, the shaft output power is 1465.4W.

A dc bus current of 5.48A (823.1W power in) and 11.34A (1702.3W power in) is observed for the 50% and 100% test, respectively. This corresponds to measured system efficiencies of 90.6% and 86.1% and loss levels of 77.3W and 236.9W spread between the drive and the machine. At this speed, the dc resistance losses still have a significant role, though other loss components related to frequency and dc bus voltage are apparent.

8.5.1.3. 3000 rev/min Test Speed

3000 rpm 50% (7.6A) and 100% (15.3A) test operating point data is given in Fig. 8.5-3 (for winding configuration #1). This test was completed with a 175.1V dc bus.

An average torque of 3.540 N-m is observed for the 50% load case, which aligns well with the expected 3.6 N-m (1.7% error). Once again, the measured torque ripple reasonable matches FEA around 0.4 N-m. Based on the measured torques and speeds, the shaft output power is 1112.1W.

An average torque of 6.984 N-m is observed for the 100% load case, which is below the expected 7.2 N-m (3.0% error). The level of observed torque ripple only marginally increases to ~0.5 N-m aligning with FEA calculations near ~0.5 N-m. Based on the measured torques and speeds, the shaft output power is 2194.1W.

A dc bus current of 6.87A (1202.9W power in) and 14.04A (2458.4W power in) is observed for the 50% and 100% test, respectively. This corresponds to measured system efficiencies of 92.5% and 89.2% and loss levels of 90.8W and 264.3W divided between the drive and the machine.

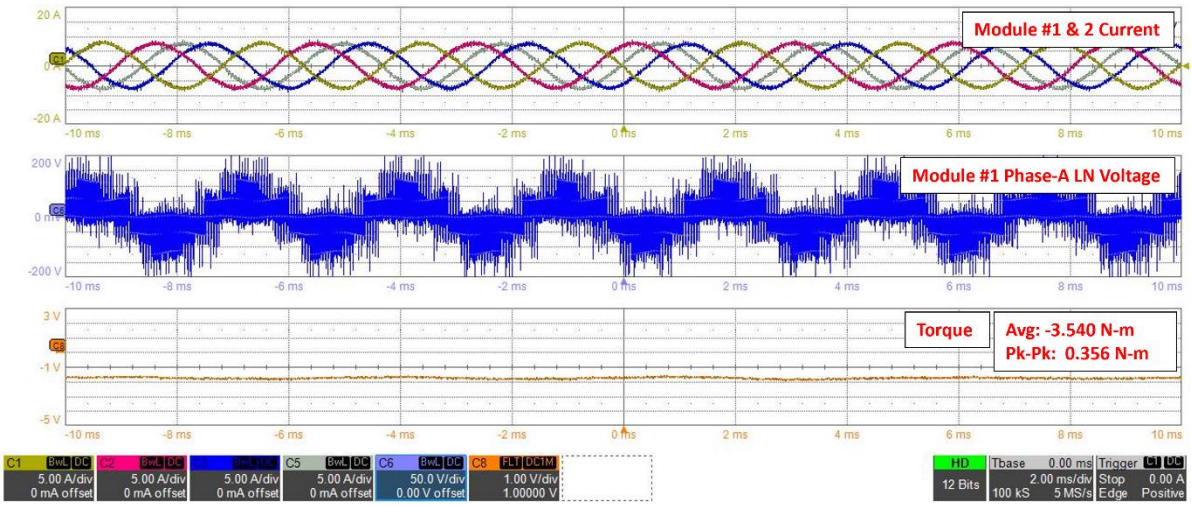

(a)

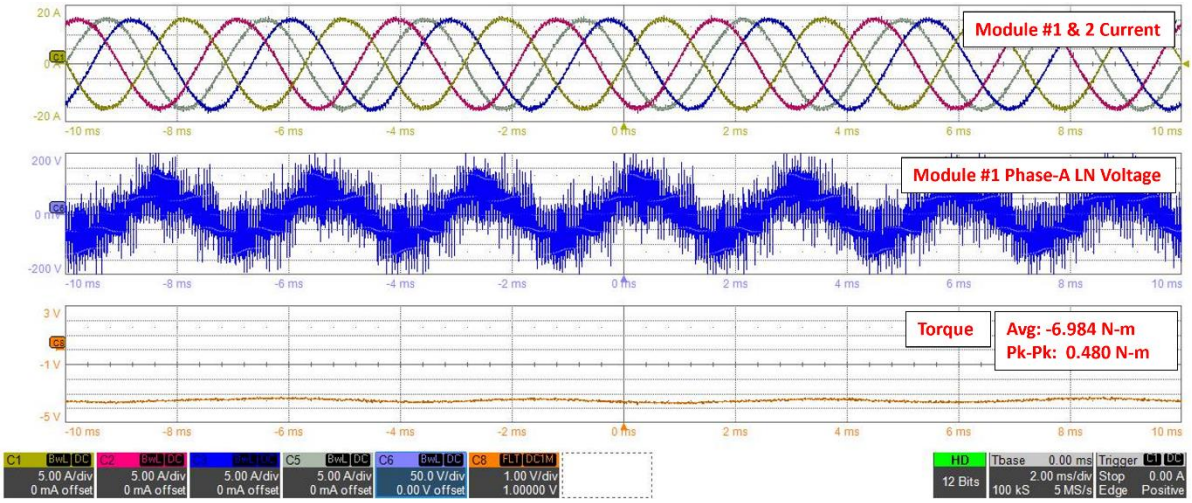

(b)

Figure 8.5-3 3000 rpm operating points: 50% current; and (b) 100% current.

8.5.1.4. Overload Testing at 1000 rev/min

An additional two overload points at 1.37x and 1.50x current ratings at 1000 rpm speed are completed (for winding configuration #2) to further test the thermal performance of the machine. Recorded torque, current, and voltage waveforms are given in 8.5-4. Note the contact resistance related unbalance on module 2 as discussed above. The dc bus voltage during this test is measured at 110.3V.

An average torque of 9.351 N-m is observed for the 1.37x overload case (21A command), which is somewhat lower than FEA calculated 9.6 N-m (2.6% error). Further, a much higher torque ripple is observed around 0.650 N-m when approximately 0.4 N-m is expected (with torque ripple improving with machine saturation). This additional ripple may be related to the observed unbalance on module 2 (related to contact resistance on the phase connectors). Based on the measured torque and speed, the corresponding shaft power is 979.2W.

An average torque of 9.949 N-m is observed for the 1.5x overload case (23A command), which is also lower than FEA calculated 10.3 N-m (3.4% error). Further, a much higher torque ripple is observed around 0.687 N-m when approximately 0.4 N-m is expected. As indicated, this torque ripple may be related to the observed unbalance or perhaps other issues in the machine related to other potentially damaging tests in the machine (it was completed after the aggressive turn-to-turn fault testing as indicated in Table 8.1-1). Further, at this operating point an apparent resonance was observed on the machine leads causing them to flap. This experiment was cut short after a couple minutes due to a lead short to ground. In any case, the observed average torques reasonably align with the simulated results. Based on the measured torque and speed, the corresponding shaft power is 1041.9W.

A dc bus current of 12.34A (1361.1W power in) and 13.72A (1513.3W power in) is observed for the 50% and 100% test, respectively. This corresponds to measured system efficiencies of 71.9% and 68.8% and loss levels of 381.8W and 534.1W divided between the drive and the machine. While these efficiencies are poor, these losses predominately belong to the machine windings approximating 238.1W for 1.37x overload and 285.7W for 1.50x overload (assuming room temperature windings).

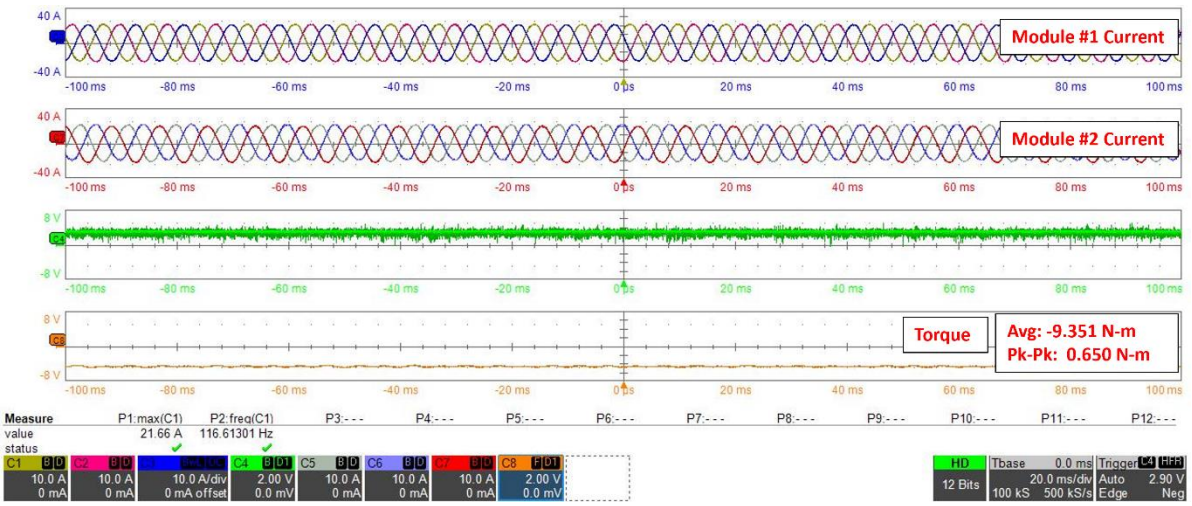

(a)

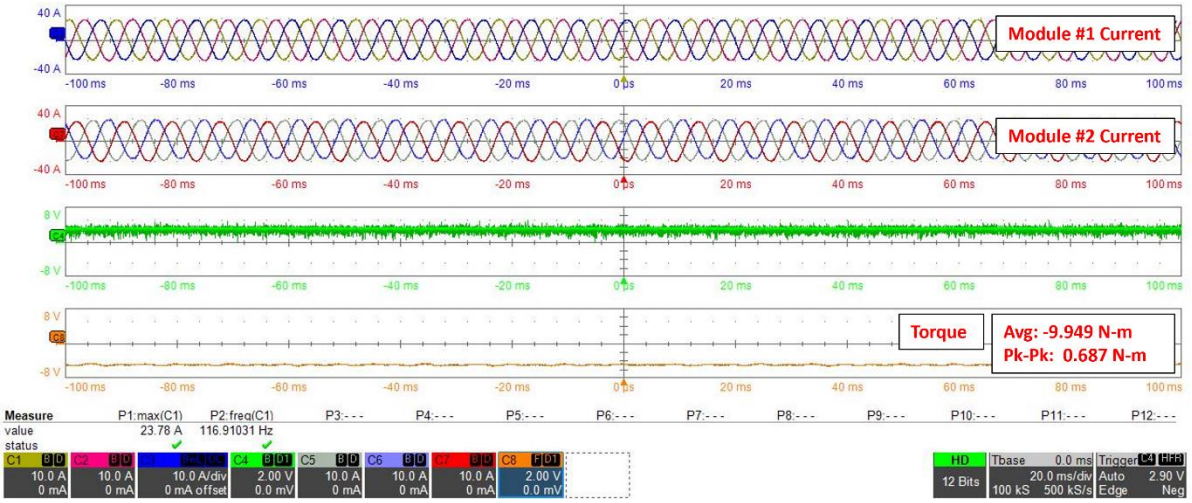

(b)

Figure 8.5-4 Overload testing at 1000 rpm: (a) 21A command (1.37x overload); and (b) 23A command (1.5x overload).

8.5.2. Thermal Testing

The machine thermal performance is evaluated at each healthy operating point with a limited set of results shared here. Each thermal test is run for 6 to 8 minutes (approximately when temperature data begins to plateau) to evaluate thermal trends with transient temperature data recorded. The presented set of results correspond to the cases given in Chapter 7 (Table 7.2-6): 1000 rpm 50% current (case 1), 1000 rpm 100% current (case 2), 3000 rpm 100% current (case 3),

and 1000 rpm, 137% current (case 6). Results related to the 150% overload current case are shared, though this experiment was unable to reach the time threshold mentioned.

8.5.2.1. Case 1: 1000 rev/min, 50% current

Machine end winding, supply and return manifold fluid temperatures are measured while the demonstrator machine is operating at 1000 rpm and 50% rated current. A transient waveform of the observed temperatures is given in Fig. 8.5-5 for a period of seven minutes after the application of the load.

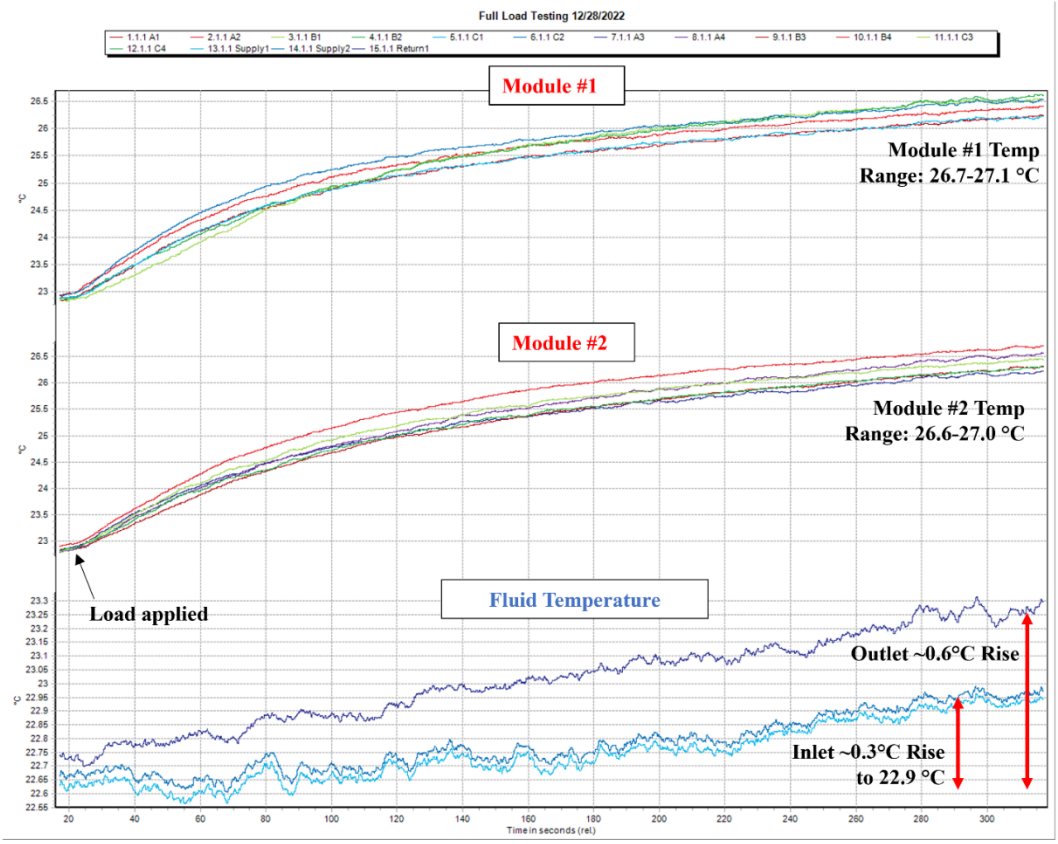

Figure 8.5-5 Transient end winding and cooling loop temperature measurement for case 1 load.

In general. all machine thermocouple reading transients are similar and generally agree with one another. The peak temperature rise in the winding is 4.2 °C at the end of the recording. This value is expected to slightly increase as the machine reaches final steady state, but strongly tracks

with the expected end winding temperature rises presented in idealized model in Chapter 7 (Table 7.2-6) which estimates a rise of 2.3 to 3.9 °C.

To validate the stated transient assumption, the temperatures from the Fig. 8.5-5 have been fitted with a first-order exponential curve to estimate the thermal time constant with result shared in Fig. 8.5-6. From this plot the time constant is estimated to be approximately 120 seconds with a final temperature of 27.1 °C. The experimental results shared in this section are measured after six minutes (3x the thermal constant) which should give a valid indication of the final steady state result.

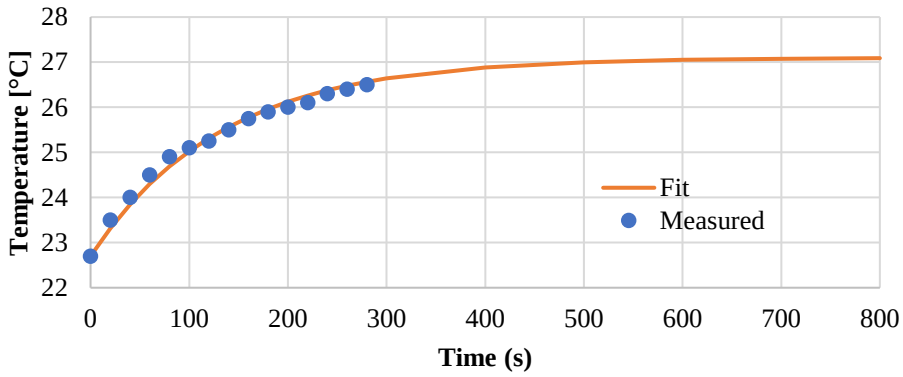

Figure 8.5-6 Plotted case 1 thermocouple measurements against fitted curved with thermal time constant of 120 seconds.

8.5.2.2. Case 2: 1000 rev/min, 100% current

Machine end winding, supply and return manifold fluid temperatures are measured while the demonstrator machine is operating at 1000 rpm and 100% rated current. A transient waveform of the observed temperatures is given in Fig. 8.5-7 for a period of six minutes after the application of the load. At the end of the recording a maximum end winding temperature rise of 17.2 °C is observed compared to the inlet fluid temperature. Similar to case 1, this tracks well the steady-

state FEA result of 9.7 to 15.3 °C temperature rise within the end winding, and a 16.2 °C rise at the winding hot spot.

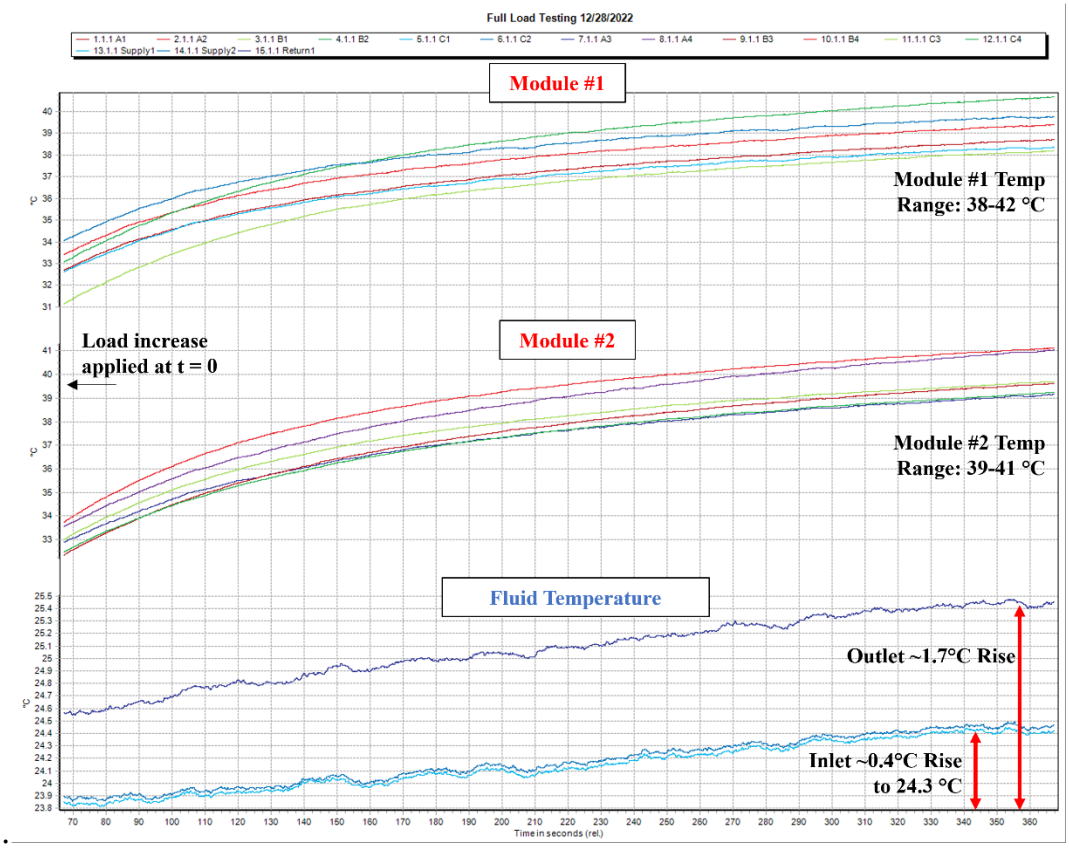

Figure 8.5-7 Transient end winding and cooling loop temperature measurement for case 2 load.

8.5.2.3. Case 3: 3000 rev/min, 100% current

Machine end winding, supply and return manifold fluid temperatures are measured while the demonstrator machine is operating at 3000 rpm and 100% rated current. A transient waveform of the observed temperatures is given in Fig. 8.5-8 for a period of seven minutes after the application of the load. At the end of the recording a maximum end winding temperature rise of 18.7 °C is observed compared to the inlet fluid temperature. This also tracks well the steady-state FEA result of 10.8 to 18.0 °C temperature rise within the end winding. A thermal image of the stator is taken after the test showing a maximum stator temperature of 44.4 °C (or a 20.1 °C rise from fluid temperature) which is close to the modeled 17.2 °C.

It is worth noting that there is some difference between thermocouple groupings in Fig. 8.5-7 and Fig. 8.5-8. This difference is likely attributable to the unbalanced flows into each of the channels (discussed in the cooling setup section above).

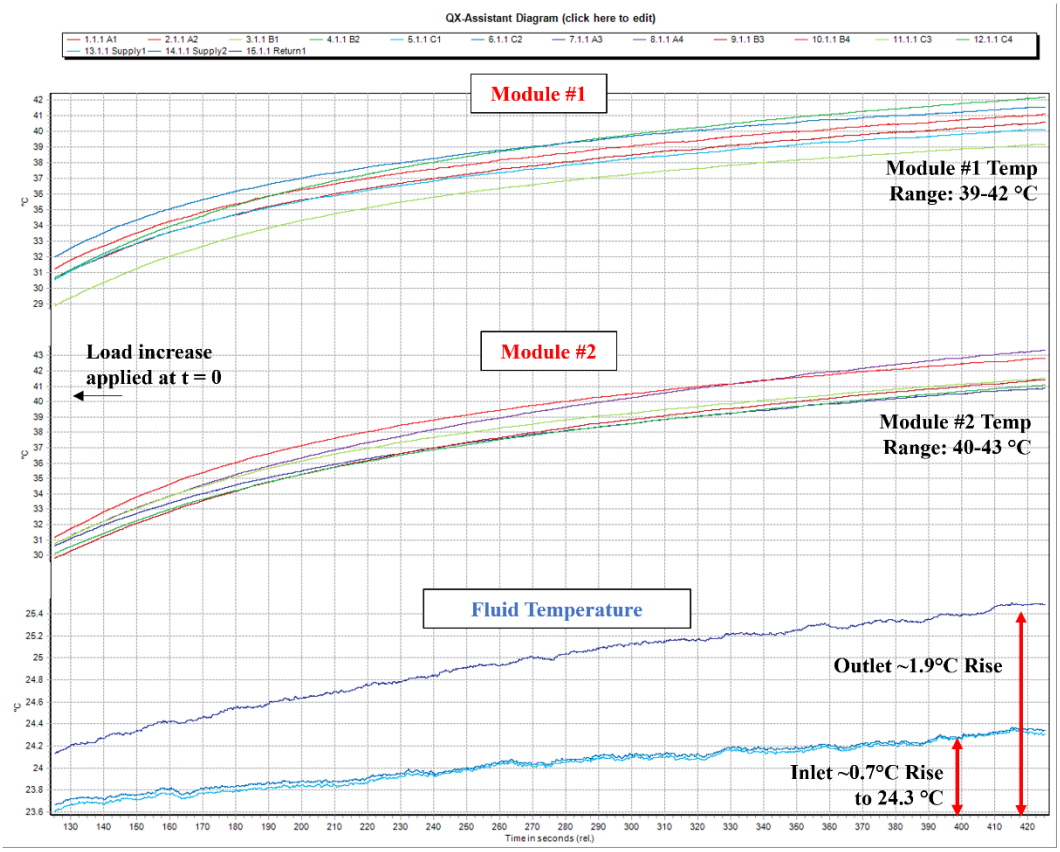

Figure 8.5-8 Transient end winding and cooling loop temperature measurement for case 3 load.

Figure 8.5-9 Thermal image of demonstrator stator after case 3 test.

8.5.2.4. Case 6: 1000 rev/min, 37% overload

Machine end winding, supply and return manifold fluid temperatures are measured while the demonstrator machine is operating at 1000 rpm and 137% rated current. A transient waveform of the observed temperatures is given in Fig. 8.5-10 for a period of eight minutes after the application of the load. At the end of the recording a maximum end winding temperature rise of 31.2°C is observed compared to the inlet fluid temperature. This measurement tracks on the higher end of the steady-state FEA result of 18.2 to 28.7°C temperature rise within the end winding, and even closer to maximum FEA coil temperature of 30.6 °C.

The previously observed difference in phase coil temperatures worsens in this case due to the increased heat loads. Once again this difference is related in unbalanced fluid flow in phase ducts (approximately 6 °C between coils).

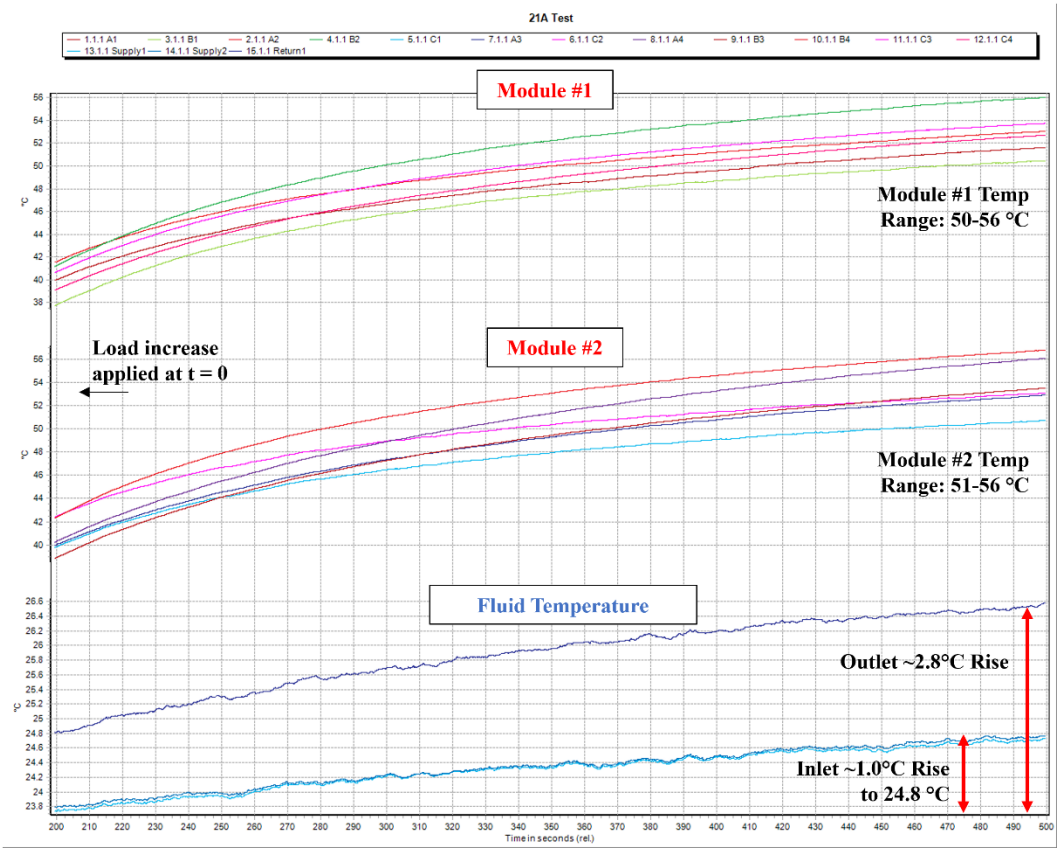

Figure 8.5-10 Transient end winding and cooling loop temperature measurement for case 6 load.

8.5.3. Overload testing: 1000 rev/min & 150% current

Machine end winding, supply and return manifold fluid temperatures are measured while the demonstrator machine is operating at 1000 rpm and 150% rated current. Transient measurements are shown in Fig. 8.5-11. The machine only operated in this state for approximately four minutes before a fault unrelated to the thermal system occurred, ending the experiment at that time. Right before the fault the machine reached peak end winding temperatures of 65 °C. The Fig. 8.5-12 thermal image of the stator immediately after the experiment shows the potting material just above the end windings at 62.9 °C validating the measurement. Peak stator core temperature after the test is 52.8 °C.

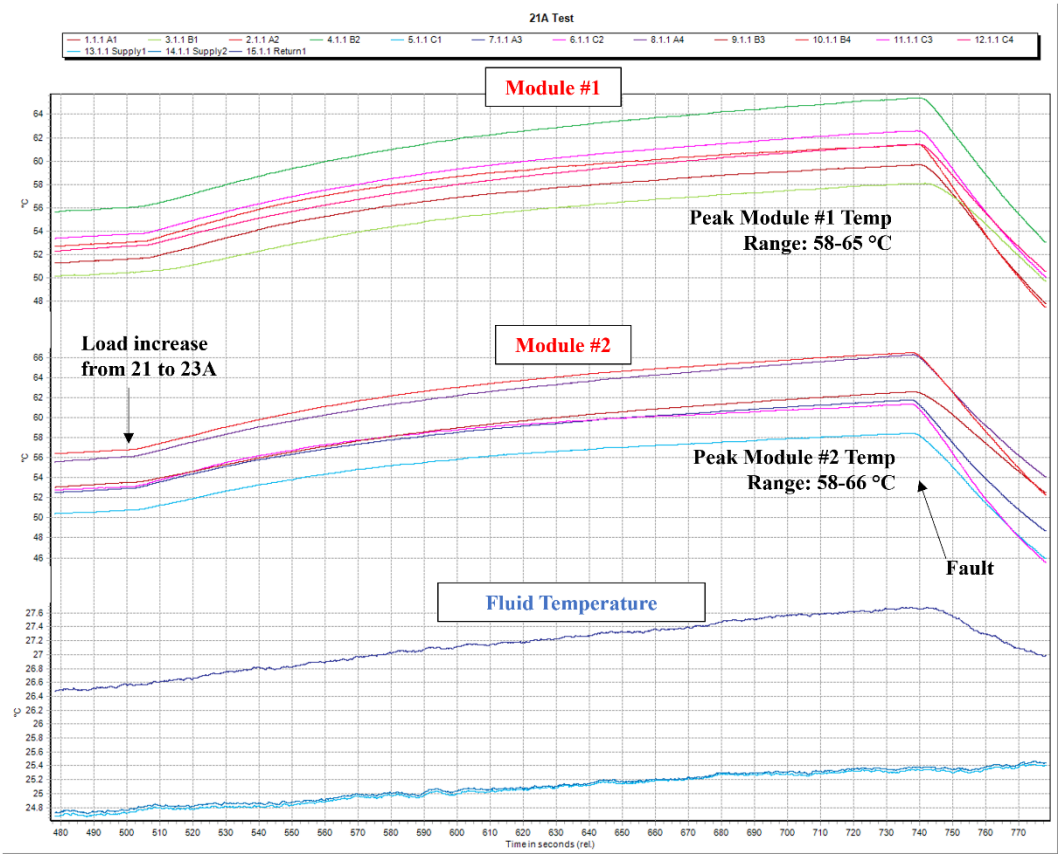

Figure 8.5-11 Transient thermal results for 150% overload condition.

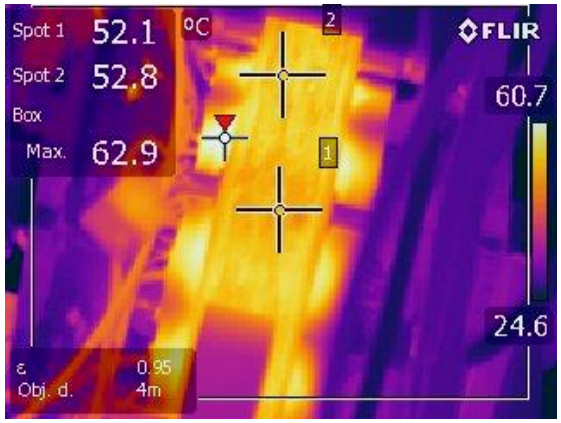

Figure 8.5-12 Stator thermal image after 150% overcurrent test.

8.6. Faulted Testing

This demonstrator possesses modular motor-drive features representing a class of FT used in applications requiring high reliability, where motor-drive expected to continue operation after a stator or power electronics failure. This section summarizes tests completed on the machine under stator failure modes related to terminal open circuit, terminal short circuit, and internal-short circuits between turns. The tests shared in this section are up to 1000 rpm and use configuration 2 module arrangement.

8.6.1. Terminal Open Circuit Operation

Perhaps the most benign of the range of faults stated is the terminal open circuit fault. A demonstration of an open-circuit fault and associated response is shown in Fig. 8.6-1. At $t<0$, both modules are operating in a healthy state at 50% current load. A fault occurs (channel 4 signal dipping to zero) where module 2 is open circuited. Module 1 immediately responds by increasing its current by a factor of 2 to make up for the lost module without any interruption in shaft torque or noticeable difference in torque ripple. The test results in Fig. 8.6.-1 demonstrate the developed modular motor drive system is capable of FT operation during open circuit transients.

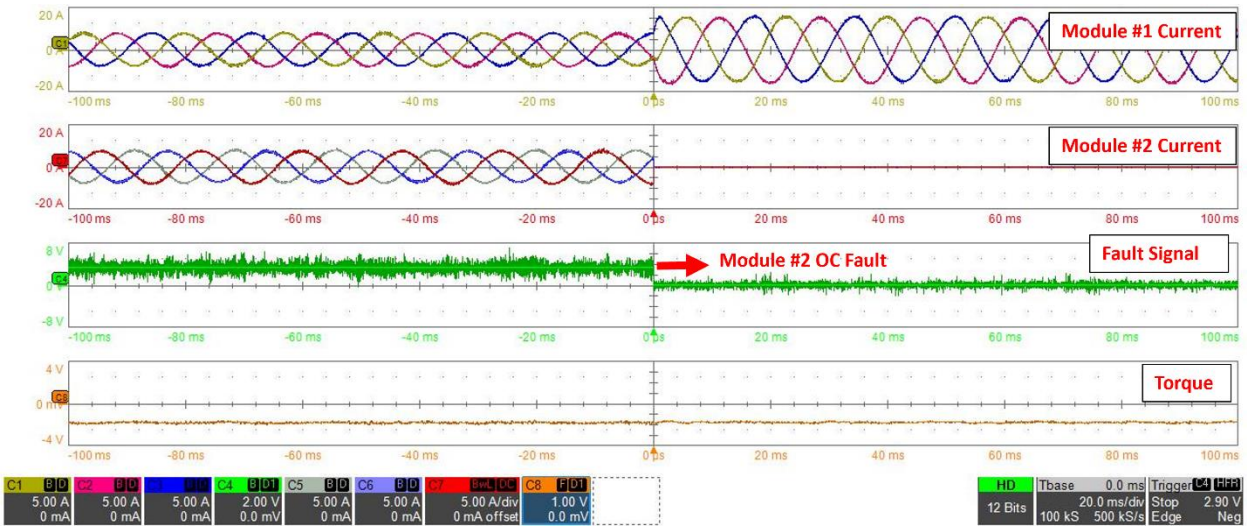

Figure 8.6-1 Open circuit fault demonstration at 500 rpm showing healthy operation, fault event and post fault response.

8.6.1.1. Module Thermal Isolation

Thermal isolation between phases is a critical aspect of FT machine design. The developed design uses in-slot cooling channels to thermally buffer interactions between modules in the event of a failure. This is demonstrated under a full-current open circuit test where module 2 is open circuit and module 1 delivers rated current—matching the post fault condition in Fig. 8.6-1.

Thermocouple transients are shown for this condition in Fig. 8.6-2. The healthy module temperatures rise to expected levels observed under 100% current conditions (nearing 40°C) while the open circuit coils remain at lower temperatures near the coolant temperature (and in fact are still being cooling from a previous test). The observed sustained difference in temperature agrees with the thermal isolation simulation results in Chapter 7.

A similar thermal response is expected for a terminal short-circuit faults on module 2. Primary difference being the module 2 temperatures will rise to temperatures related to the characteristic

current I^2R losses. For this reason, thermal isolation discussions related to terminal faults is limited to the presented open circuit demonstration.

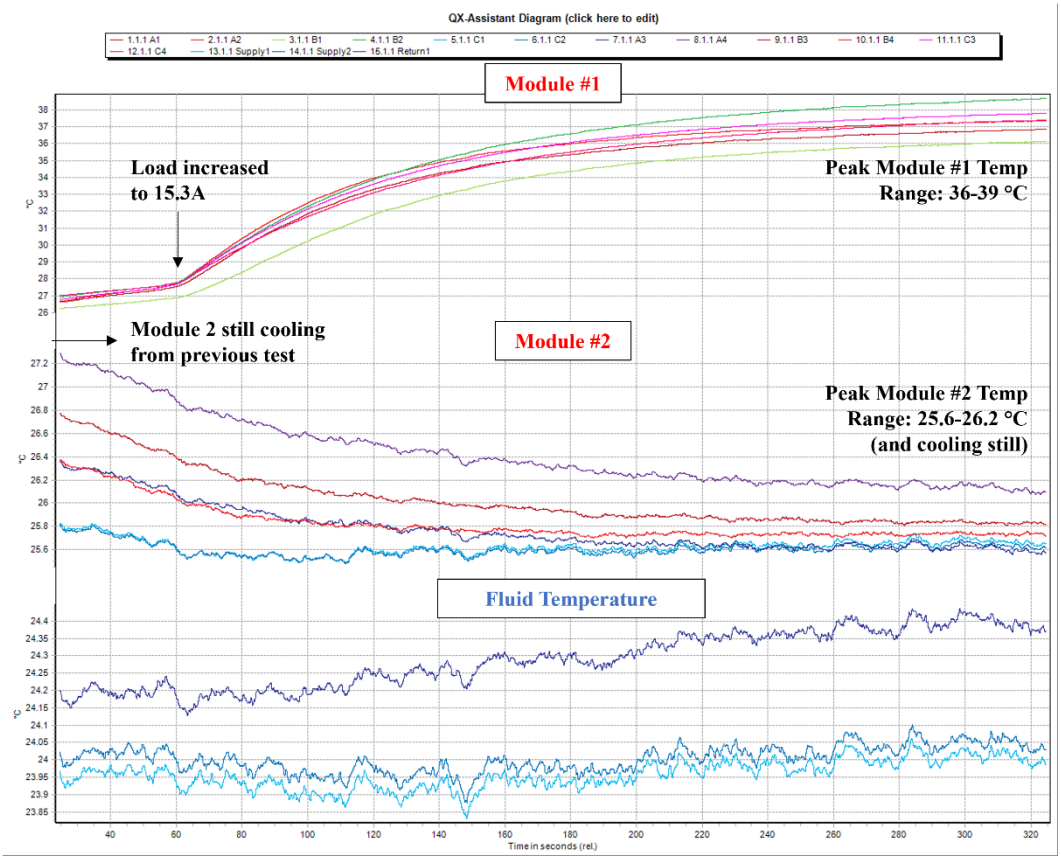

Figure 8.6-2 Thermal isolation demonstration under full-load module 2 open circuit fault.

8.6.2. Terminal Short Circuit Operation

A more serious failure mode for PMSMs is high current transients from a terminal three-phase short circuit and post-fault characteristic current that can potentially demagnetize rotor magnets. The required steps for mitigating these risks were taken for this machine design: high inductance to minimize fault currents, and magnet material selection with strong coercivity at high temperatures to withstand peak transient currents 3x rated current.

The short-circuit characteristics of the built machine is presented above confirming characteristic current calculations. This demonstration follows a similar methodology to the open-

circuit case shared in Fig. 8.6-1, both modules operate under healthy conditions until a t=0 where the terminal short circuit is applied. The healthy module responds by increasing its current to compensate for the lost torque. The results of the test are shown in Fig. 8.6-3. After the application of a three-phase short, a peak transient current of 15.3 is observed. Additionally, the overall output torque of the machine is reduced after the fault due to braking torque from the shorted module. Complete machine (both modules shorted) braking characteristics are measured in Fig. 8.4-5. Further, module #1 healthy currents are balanced and unaffected by adjacent faulted coils. The test results in Fig. 8.6.-3 demonstrate the developed modular motor drive system is capable of FT operation during short circuit transients.

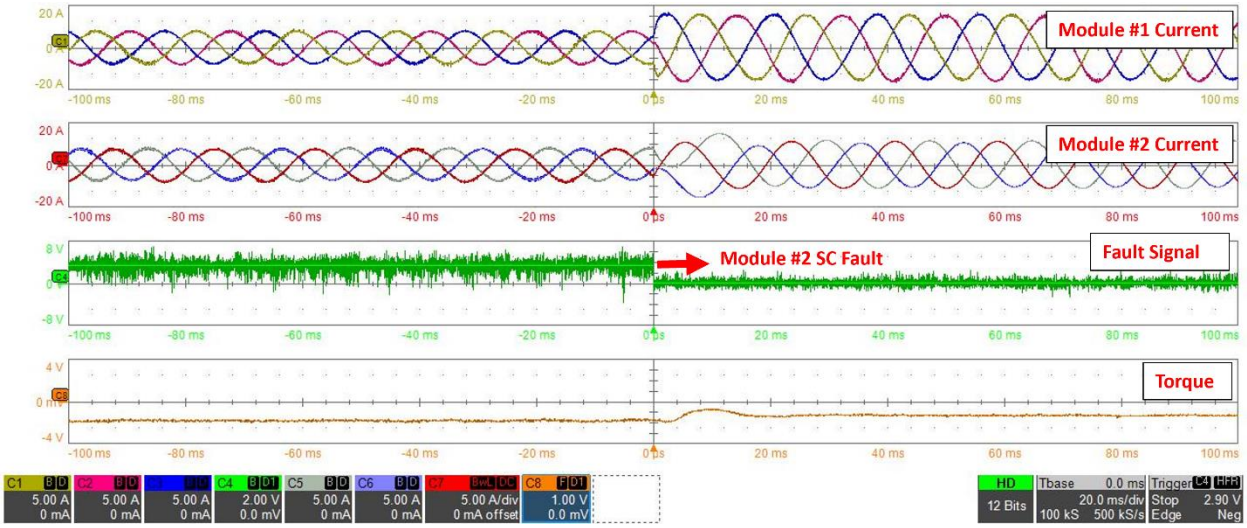

Figure 8.6-3 Short circuit fault demonstration at 500 rpm showing healthy operation, fault event and post fault response.

8.6.3. Internal Short Circuit Operation

Internal short-circuit faults are the final fault mode considered for this FT demonstration. For PMSM machines these faults can be devasting due to significant current being driven through shorted turns by the rotor permanent magnets. To study these faults, three-turns are brought out of a single phase in module 2 allowing for the external application of faults. Initial testing is passive

(no drives) where the amplitude of fault current for varying fault resistance is measured 1000 rpm. Results are compared against simulation and extrapolated to higher speeds. After, an active turn-to-turn fault demonstration is completed using the developed modular drives.

8.6.3.1. Passive Turn-to-Turn Fault Testing Parameters

Details related to the extraction of stator turns is described in 8.2.5 with relevant details reiterated here. Turns 27, 36, and 44 are tapped from the end winding of phase A4. Measured turn resistances are given in Section 8.4.1. The studied turn-to-turn fault combinations are provided in Table 8.6-1. Power resistors are used to simulate expected fault resistance with values given in Table 8.6-2 (measured at the resistor leads). Each of the faulted turn combinations in Table 8.6-1 is tested with the resistors defined in Table 8.6-2. A final test will be conducted as a dead-short with turns directly connected.

TABLE 8.6-1 FAULTED TURN COMBINATIONS

Studied Faulted Turn Combinations
Turn 27 – Turn 44
Turn 27 – Turn 36
Turn 44 – Turn 47

TABLE 8.6-2 FAULT RESISTANCES USED IN TURN-TO-TURN FAULT STUDY (20°C)

External Fault Resistor Label	Resistance Measurement (Ω)
RF5	5.12447
RFp22	0.22845
RF0	direct short

The turn-to-turn fault resistor is connected to the studied faulted turns before spinning the machine. For each resistance, speed is ramped up to 1000 rpm or until fault current exceeds 32A (approximately 2x the rated current) to avoid damaging the machine. Peak amplitudes of fault current are recorded.

8.6.3.2. Passive Turn-to-Turn Faults (0 – 1000 rev/min)

The observed peak currents for the above faulted turn scenarios are plotted in Fig. 8.6-4 for each of the different resistance and fault combinations stated above.

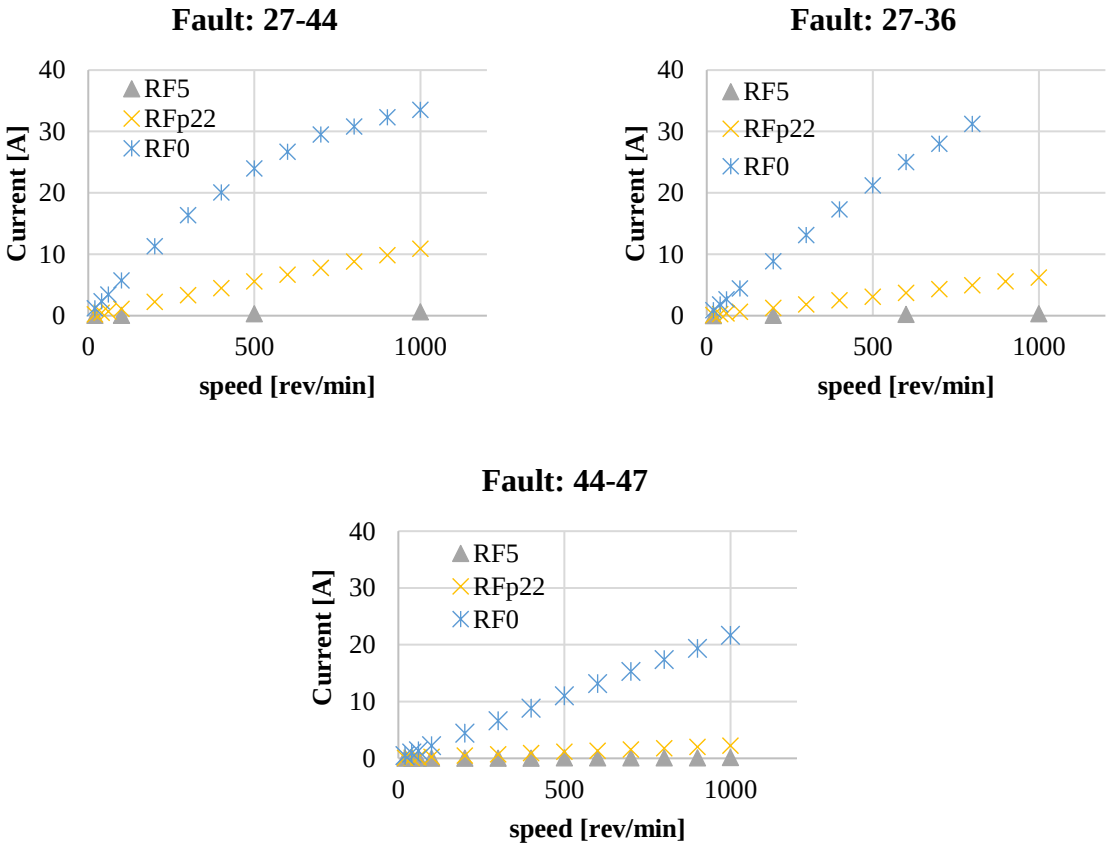

Figure. 8.6-4 Peak short-circuit currents for varying fault resistances.

The results in Fig. 8.6-4 show how quickly fault currents develop with speed in the event of an internal short circuit and it is clear to see how these can faults can quickly become destructive. In the case of the turn 27-36 fault scenario, testing was halted at 800 rpm due to the rapidly increasing currents exceeding the defined current thresholds.

Other observations include higher fault currents at lower speeds for turns 27-44 faults, though the observed current begins to plateau at higher speeds for a direct short. Conversely, the turns 44-47 case had the lowest observed currents. At higher speeds, it is expected the 44-47 fault currents

will dominate. Next, although not clear from Fig. 8.6-4, there is observable current through the 5Ω fault resistor in all cases, reaching as much as 0.625A at 1000 rpm for the 27-44 fault scenario.

For all tests, audible noise and vibration were observed for higher amplitude fault currents further highlighting some of the possible techniques for fault detection.

8.6.3.3. Turn-to-turn Fault Thermal Isolation

The passive turn-to-turn fault testing allows for additional evaluation of the proposed thermal isolation scheme. This is illustrated for the turn 27-44 direct short fault test at 1000 rpm corresponding to peak fault current 33.5A. Thermocouple measurements of the fault transient are shown in Fig. 8.6-5. The faulted coil temperature rises dramatically in 2 minutes while only minor increases in temperature are observed in adjacent coils (~0.3 °C).

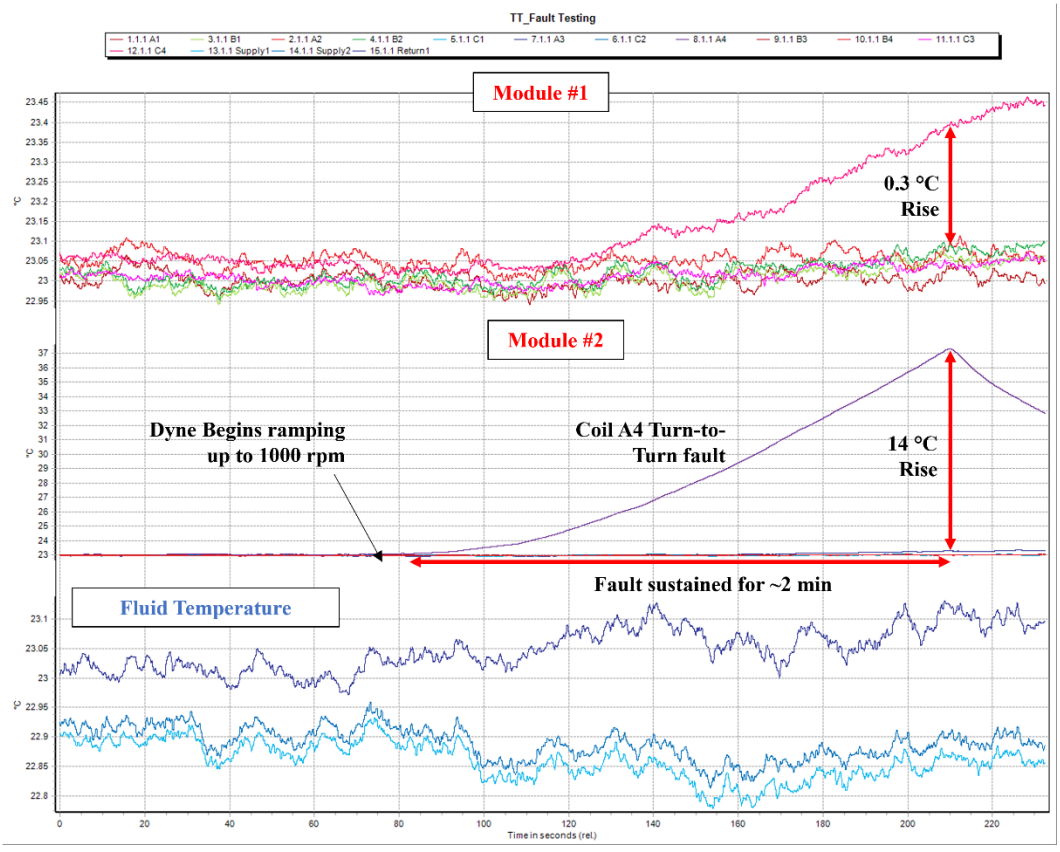

Figure 8.6-5 Thermal transient during turn-to-turn fault between turns 27 and 44 inside A4.

This experiment demonstrates the specific role in-slot cooling has in fault tolerant machines for higher levels of fault current (e.g., single turn faults at high speed): in-slot cooling provides sufficient thermal isolation on a transient basis to blunt the impact of elevated fault related losses, giving time for the implemented fault detection scheme to identify the problem and react.

8.6.3.4. Internal short circuit operation response

The response to an internal short circuit is demonstrated for a direct short between turns 44-47 at 500 rpm in Fig. 8.6-6. Before t =0, the machine is operating in an undetected fault state with a sustained internal short inside Module 2 phase A. At t=0 the fault is detected and a three-phase terminal short is applied to the windings, suppressing the faulted turn current. Healthy module 1 responds by increasing its phase current to compensate for the lost module 2 torque contributions.

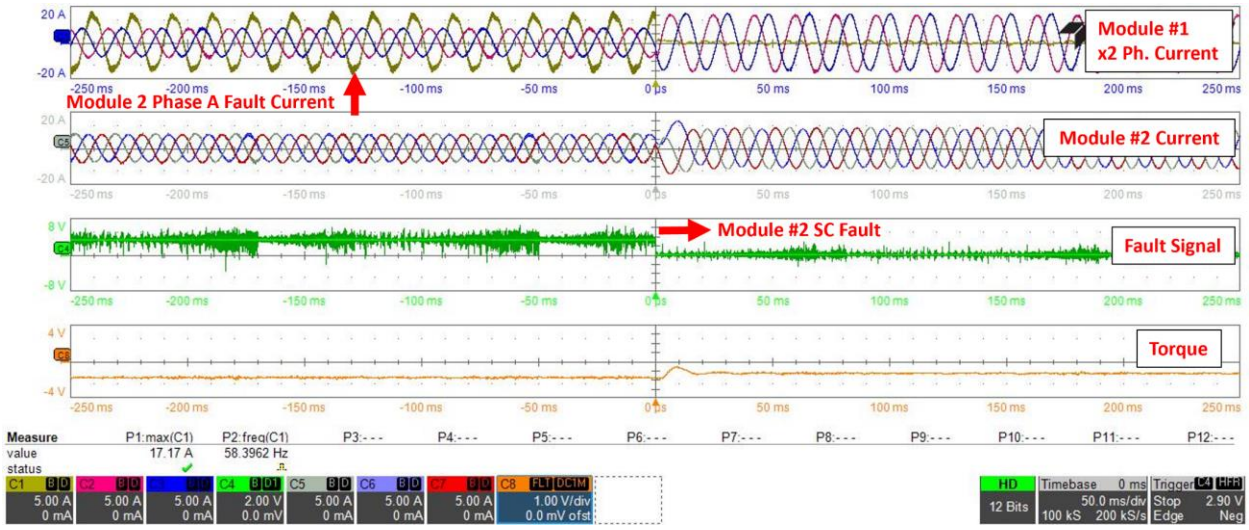

Figure 8.6-6 Internal Short circuit fault demonstration at 500 rpm showing internal short circuit current, fault response trigger and post fault response.

8.7. Chapter Summary

This chapter has presented the experimental results from testing a low-power fault-tolerant demonstrator machine that incorporates the electromagnetic isolation and in-slot cooling features which lie at the heart of this research program. These features include the introduction of flux barriers in the stator back-iron, an asymmetric tooth tip implementation minimizing leakage flux between phases and maximizing self-leakage inductance, and a direct cooled in-slot winding approach using alumina tubes. Details related to the fabrication and test configuration have been presented. A brief overview of the machine parameters (discussed in greater detail in Chapter 7) and the aforementioned features is provided together with the developed test plan.

The experimental test program has succeeded in accomplishing the following objectives arising from the analytical results presented in Chapter 7: (1) validate machine equivalent circuit parameters; (2) validate electromagnetic isolation; (3) validate torque output; (4) validate thermal performance at defined operating points; (5) demonstrate fault tolerance capability for terminal and internal short circuit fault modes; (6) demonstrate thermal isolation; and (7) validate the self-dyne concept for modular machines. Key observations are summarized in the following paragraphs.

Machine resistance, magnet flux linkage, inductance, and characteristic current are all confirmed to be within 3% of simulation via static measurements and rotating testing. Electromagnetic isolation is confirmed by locking the rotor and applying high frequency current in one module and measuring the open-circuit voltage in the other module. Doing so results in a Module Isolation Ratio *MIR* value of 3.3% which is higher than simulated due to saturation but still a very strong indicator of high electromagnetic isolation. Machine torque operation is confirmed via dyne testing up to 3,000 rpm. For rated operating points (< 15.3A per module), the

observed torque is within 3% of simulated. For overloaded operating point 3, the observed torque is within 5% of simulated.

Thermal performance has been tested by operating the machine at load for extended periods of time. The presented results track well with the idealized model in Chapter 7, although the observed temperature is slightly higher. This can partly be attributed to lower operating coolant flow rates than initially considered and for the simplifying assumptions made in the Chapter 7 model. Overall, the observed test temperatures are well below maximum temperature ratings of the utilized components.

The machine fault tolerance capability has been validated via a series of fault demonstrations. These include the sudden application of terminal faults (open- and short-circuit) during healthy testing and observations of the resulting post-fault response. This demonstration has been extended to turn-to-turn faults that are intentionally applied, and the machine response was observed.

Part of this fault tolerance demonstration included examining coil temperatures during fault events and determining whether there are significant thermal interactions between healthy and faulted coils. The presented results show these interactions are minimal, confirming that the proposed thermal isolation approach is a promising approach for realizing both effective coil cooling and good thermal isolation.

Chapter 9

Research Summary, Contributions, and Future Work

This research program has focused on investigating the development of fault-tolerant (FT) modular electrical machines and drives and quantifying their associated reliability benefits. This chapter provides a summary of major observations and conclusions drawn from this thesis, presents the major research contributions of this work, and proposes recommended future work.

9.1. Research Program Review

A literature review has been presented in Chapter 2 that summarizes the current state-of-the-art of FT PMSM machines and drives, and machine-drive reliability evaluation methods. This review is presented in the context of emerging electrically-propelled aircraft that require machines with power densities and reliability well beyond existing technology levels. This is especially true for emerging electrified Vertical Takeoff and Landing (VTOL) vehicles, where experts have identified electrical machines and drives as reliability-limiting components. A review of published examples of these machines is presented, highlighting key trends in this design space. In general, Permanent Magnet Synchronous Machines (PMSMs) using a Surface Permanent Magnet (SPM) rotor topology with Fractional-Slot Concentrated Windings (FSCW) are popular choices to reach the necessary power density levels. The surveyed aerospace propulsion machines are oriented towards meeting the aggressive power density requirements associated with electrified aircraft propulsion without addressing the significant reliability challenges associated with electrified flight.

Key shared features of the surveyed power dense machines are identified, including high levels of magnetic loading, machine speed, shear stress, and tip speeds. The technologies used to push

the limits of these machine characteristics are identified. Additional power density benefits are realized by integrating the power electronics into the machine housing in an Integrated Motor Drive (IMD) configuration. In addition, valuable reliability benefits can be achieved by dividing the stator and power electronics into redundant modules to form an Integrated Modular Motor Drive (IMMD) configuration.

PM synchronous machines is the leading machine topology for realizing the power densities required for flight, although they also create challenging engineering tradeoffs. For example, the adoption of PM machines poses significant challenges for achieving fault tolerance due to the constant presence of the rotor magnet flux in spinning rotors, generating back-emf voltages that can induce substantial fault currents when an inverter switch or winding failure occurs. FT machine drive features can be implemented to mitigate these risks. Published FT machine drive architectures and their implementations are presented and reviewed. In general, FT PM machines require high inductance to minimize currents after a winding failure, redundant power channels (i.e., multiple redundant phases), and electromagnetic isolation between redundant power channels to prevent the propagation of faults.

A common FT machine implementation divides the machine into multiple three-phase modules, each excited by its own voltage-source inverter (VSI). Electrical, electromagnetic, and thermal isolation between machine modules is identified as critical for preventing the propagation of faults between these modules. Electromagnetic isolation of modular machines can be implemented in several ways. This is often accomplished by using a single-layer (SL) winding, where machine coils are physically separated by stator teeth. Alternative approaches using spacer teeth have been proposed to give greater design flexibility by placing spacer teeth between modules instead of between each coil.

A review of reliability evaluation techniques is also provided. Markov Chains are commonly used to estimate the reliability of FT motor drives systems, allowing for the quantification of the FT implementation system reliability benefits. Overall, this literature review sets the stage for a more thorough investigation of FT PMSMs and the related reliability and performance (e.g., power density) tradeoffs.

In Chapter 3, the key design characteristics of power dense electrical machines (shear stress, current density, etc.) are used to develop a sizing methodology and equation set. The developed machine sizing tool is used to explore the power dense machine design space for given sets of machine specifications, identifying candidate power dense SPM designs and the related winding loss tradeoff. These power density principles are confirmed in the discussion in the context of a 1 MW rated machine and a lower power (200 kW) demonstrator version of the machine. In principle, these machines are also fault tolerant due to their IMMD structure, with the stator windings divided into six independent 3-phase winding sets or modules. However, controlled fault testing on the lower power demonstrator shows the machine has significant electromagnetic coupling between machine phases resulting in current unbalance following a module fault. The key source of this unbalance is related to mutual flux leakage between module phases—primarily through tooth tip leakage. Furthermore, the choice of an 18-slot, 12-pole (SPP = ½) topology exacerbates the challenge due to inherently high coupling between machine phases. Metrics like the Module Isolation Ratio (MIR) are proposed as a useful indicator of electromagnetic isolation between modules that is useful for comparing FT machine topologies in later chapters.

In Chapter 4, tradeoffs between electromagnetic isolation and power density are explored in the context of a quadcopter application for power and speed ratings of 70 kW and 8,000 rev/min, respectively, requiring power dense high performance machine designs. A comparative evaluation

of alternative PMSM topologies with electromagnetic isolation features is presented to compare the power densities achieved by modular machine topologies with that of a conventional power-dense double-layer (DL) winding configuration. The study results show that the introduction of conventional FT isolation features (SL windings, spacer teeth) degrades the machine power density and losses compared to that of a baseline machine design without the FT features, exposing one of the major challenges associated with the development of high-performance FT modular motor drives. Alternative isolation approaches are considered and results are presented that highlight promising electromagnetic isolation concepts that require minimal performance sacrifice.

Based on these tradeoff study results, a promising approach that introduces stator yoke cavities and modified tooth tips is proposed for a four-module 24-slot, 28-pole FSCW machine. Simulations of the proposed machine configuration demonstrate effective electromagnetic isolation of the machine modules under demanding operating conditions, including a short-circuit event in an adjacent module that is particularly challenging for FT machines. Analytical results also highlight the superiority of this proposed FT modular motor drive for minimizing any sacrifices of power density or efficiency compared to other reported FT modular motor drive topologies.

Alternative slot-pole combinations are considered for compatibility with the newly developed isolation technique and modified tooth tip structure. In general, machine windings possessing anti-periodic adjacent windings of the same phase (i.e., producing a localized winding flux path) are the most promising topologies to utilize the developed approach. Generalized observations about electromagnetic isolation are summarized, and simplified guidelines for assessing the required level of isolation are presented based on electromagnetic isolation metrics and the expected fault current.

A more detailed evaluation of the quadrotor machine with enhanced electromagnetic isolation is presented in Chapter 5, which is subsequently used as a reference machine in the Chapter 6 reliability evaluation section. The results of a multi-physics design and analysis process are presented. Machine features include the modular electromagnetic isolation features noted above, a rotor with a surface-mounted Halbach magnet array, and integrated modular power electronics. Calculated machine performance and loss characteristics are reviewed, indicating a predicted full-load machine efficiency of 96.0% with an active-mass machine power density of 14.0 kW/kg.

A consequence of the high power density metrics is significant winding loss, and a special 3D-printed in-slot cooling configuration has been developed that enables direct winding cooling on the underside of the coils to achieve better slot fill. Thermal analysis of the proposed machine topology is also presented that confirms the effectiveness of the in-slot direct cooling approach and its beneficial role in thermally isolating the machine modules. Predicted machine performance under faulted module conditions is also presented which shows that the proposed machine retains its ability to deliver rated torque and power after the loss of one of the machine modules. Specific attention is devoted to turn-to-turn faults since they represent one of the most serious and dangerous failure modes in PM machines, and models are developed to assess post-fault performance.

The developed quadrotor machine's reliability is evaluated in Chapter 6 using Markov chain analysis. Machine and power electronics failure rates have been collected from the literature and modified to account for the stress levels in the system. In contrast to other Markov chain-based reliability studies in this area published to date that focus narrowly on single components or expand their scopes too broadly, this model is distinguished by focusing squarely on the FT machine and drive configuration. More specifically, the new Markov chain model has been developed to

estimate the machine drive's Mean Time to Failure (MTTF), providing the user with a convenient way to explore the impact of changing the number of machine drive modules, the failure and repair rates, and single-point failure paths. Further refinements of the model allow for direct calculation of MTTF from the machine state diagram and selected failure rates, further simplifying the reliability calculation.

Exercising this new model clearly shows that the predicted machine drive MTTF increases significantly in a modular FT system when a high repair rate is assumed, which is a reasonable assumption for commercial aircraft applications. The model has also proven valuable for highlighting a key finding that major additional reliability enhancement is achieved by reducing or eliminating single-point failures from the machine drive system. As a limiting case, MTTF improvements approaching 1000:1 are predicted if all single-point failures are removed. This result is consistent with the observation that a modular machine drive configuration removes power electronics and winding components from the single-point failure sources, resulting in improved reliability. The analysis is further generalized to consider a variable number of modules and post-fault stress levels. Finally, the developed MTTF calculation techniques are used to define several FT figures of merit (FoM) metrics that quantify the value of added reliability provided by modularity as ratios with several of the key cost-metrics (e.g., mass), providing a promising method for comparing different types of FT motor drive configurations.

Returning to the developed in-slot cooling and magnetic isolation features introduced in Chapters 4 and 5, Chapter 7 presents a scaling study of these isolation and cooling features up to 2 MW and down to 7 kW. The 2 MW design is oriented towards megawatt scale propulsion, following the specifications provided by ARPA-E and guided by the NASA ULI megawatt machine development effort. A representative design of a megawatt machine is developed

following the Chapter 2 sizing methodology, and its rated load performance presented. The machine electromagnetic isolation features are shown to scale well up to 2 MW with a low MIR ratio of 2.7%. However, the observed scaling of the bobbin-cooling approach presented in Chapter 5 does not scale well to higher power levels due to the geometric scaling of the machine, increasing the distance between the coil hot spot and the cooling duct. This is further exacerbated by the higher heat densities associated with the extreme power density requirement. However, it is shown that the feasibility of this cooling approach is restored if the thermal conductivity of the stator winding potting compound can be raised to values >10 W/m-K. Finally, the contribution of the inner tooth-tips to the inductance of the proposed machine topology is evaluated and shown to increase the machine phase inductance by >10%.

The scaling study is repeated in the opposite power rating direction for a two-module 7 kW rated FT machine design. Instead of the high performance materials used in the preceding studies, this machine is intended to be fabricated at relatively low cost, and for ease and speed of assembly. In addition, the cooling design is simplified, with the design utilizing highly thermally conductive alumina tubes instead of a 3D printed cooling bobbin. A conventional potting material is used to reduce cost. Finally, a V-shaped interior permanent magnet (IPM) rotor is designed in order to achieve similar levels of magnet airgap flux density compared to the previously presented machines. As a final constraint, the machine overall dimensions were limited to an IEC100 frame. The electromagnetic and thermal analysis of the machine is presented, resulting in a predicted value of the *MIR* ratio of 1.7%. From a thermal standpoint, the simulated design achieves a predicted cooling capability above $20A_{rms}/mm^2$ and good thermal isolation between modules. Further considerations related to the thermal management system are provided discussing the nuances of in-slot cooling and thermal isolation.

Chapter 8 presents experimental results of the developed lower power demonstrator up to 3,000 rpm and rated torque. Details related to the machine fabrication and test setup are provided. The collected test results exhibit good agreement between modeled and measured machine parameters (<3% difference). Similarly, torque performance under rated conditions also agrees with the developed models within 3%. Torque measurements for operating conditions at 150% overload current are also reasonable, achieving agreement within 5% of modeled values. Similarly, the thermal test results track well with the model presented in Chapter 7, although slight temperature differences are observed that can be likely attributed to reduced and unbalanced flow in the experimental system compared to what was modeled. High module electromagnetic isolation is also validated via static testing of the inductance characteristics. The measured *MIR* factor for the machine is 3.3% which is higher than modeled indicating higher magnetic leakage between modules that was not captured in the FEA simulation. Nevertheless, the low measured MIR value of 3.3% is still very good and validates the electromagnetic isolation concept.

The fabricated machine has been tested under several fault conditions to confirm its fault tolerance capabilities. Terminal open circuit and short circuit faults were applied to the machine at speed, and the desired post-fault operating capability has been confirmed with minimal torque degradation. Thermal isolation has been evaluated during the open-circuit fault test, confirming the presence of significant temperature differences between the two sets of module coils (healthy vs faulted). More aggressive turn-to-turn faults were applied by using jumper leads to short selected turns in the coil's end winding region. Initial passive testing (i.e., spinning without drives) was carried out to measure the magnitude of the interturn fault currents. The test was then repeated under active excitation conditions (i.e., drives on), demonstrating the turn-to-turn current response and the post-fault capability. The turn-to-turn testing also provided another opportunity to evaluate

the thermal isolation effectiveness, confirming that the proposed in-slot cooling technique is capable of thermally isolating the adjacent coil from the effects of the faulted turns.

9.2. Contributions

This research is focused on an investigation of FT IMD configurations for their use in high-reliability applications including aerospace aircraft propulsion. There are two new contributions resulting from this research program that are discussed in this section.

9.2.1. Development of Fault-Tolerant PMSMs with Integrated Power Electronics Capable of Achieving Improved Reliability

This research program has thoroughly investigated FT modular machine drives for their use in future high-reliability and high-performance applications including aerospace drives. This investigation included a comparison of alternative published FT machine drive topologies that has rarely been addressed in the published literature. This led to the development of a new fault-tolerant PM machine configuration and its associated integrated power electronics that offers important performance advantages over any previous FT PM machine and drive reported in the literature to date. More specifically, the new fault-tolerant modular PM machine adopts a concentrated-winding fractional winding (FSCW) configuration with enhanced electromagnetic and thermal isolation between adjacent three-phase stator winding modules that significantly reduces opportunities for serious faults in one of the modules from propagating into any of the other healthy stator modules. The chosen approach has been carefully selected and designed to minimize any mass, volume, and efficiency penalties associated with introduction of the fault-tolerant architecture. Closed-form analysis, simulation, and experimental tests have been carried out to verify the effectiveness of this new FT PM integrated motor drive for meeting its demanding

performance objectives, including analytical and experimental demonstrations of the critical fault tolerance features that lie at the heart of the contribution. Key research elements and initiatives that together comprise this contribution include:

9.2.1.1. Identification and comparison of FT machine approaches and the associated performance and cost tradeoffs

- Comparative evaluation of the conventional FT isolation approaches to FSCW machines (SL winding, and spacer tooth approaches), considering different slot-per-pole-per-phase combinations and phase numbers.
- Development of Figures of Merit (FoM) that facilitate improved comparisons across FT machine designs. These FoMs are defined to quantify the ratio of the associated reliability improvement of a fault-tolerant topology to its associated cost (e.g., mass).
- Development and experimental validation of modular machine models for Modular SPM machines that capture the impact of poor electromagnetic isolation between three-phase modules. Further, these models are capable of quantifying the impact of module implementation (e.g., interleaved, etc.) in the electric machine, demonstrating that they can have a significant impact on the level of electromagnetic coupling between modules.
- Development of sizing equations and design methodology which can be used to size modular SPM machines for high power density.
- Design guidelines are developed to assist with the design of FT modular machine designs using fractional slot concentrated windings.
- The evaluation of power-rating scalability of modular systems and the impact of FT capability at higher (2MW) and lower power levels (70kW).
- Experimental confirmation of key performance and isolation characteristics of a 7 kW two-module modular machine during healthy and faulted operation.

9.2.1.2. Development of alternative isolation approaches for modular PMSM machines

- Investigations of alternative techniques for physical, thermal, and magnetic isolation approaches that extend beyond conventional single-layer winding or spacer tooth approaches.
- Development of electromagnetic isolation metrics and rules-of-thumb for assessing and quantifying the need for isolation between modules
- Development and demonstration of an enhanced electromagnetic isolation approach for double-layer windings using stator cavities and partially removed stator tooth tips. Evaluation of this technique using FEA and analytical models demonstrates minimal coupling between modules. Electromagnetic isolation is confirmed experimentally.
- Identification of FSCW slot-pole topologies that are compatible with the proposed enhanced electromagnetic isolation technique.
- Development of models to evaluate the impact of in-slot cooling and insulation design on thermal and physical isolation between modules. Thermal isolation concepts validated experimentally.
- Investigation of two in-slot cooling approaches, one using a cooling bobbin, and the other using thermally conductive ceramic tubes positioned along the center of the slot between adjacent coils.
- Experimental testing of demonstrator machine using the developed isolation features confirming their effectiveness. Electromagnetic and thermal isolation have been validated under several fault conditions.

9.2.1.3. The development of a modular surface permanent magnet machine and VSI for a quadrotor application

- Detailed design and multi-physics analysis of a three-phase 24-slot, 28-pole machine with four-modules, allowing for potential failures in two-modules.
- Design of modular power electronics to evaluate expected drive stresses during healthy and faulted operation. In addition, the development of an integration strategy of power electronics into the machine housing and end bells.
- Development of a cooling scheme for both power electronics and machine windings enabling high power density.
- Evaluation of the developed machine under healthy and faulted conditions, considering thermal, electrical, and mechanical stresses in the machine.
- A turn-to-turn fault study of the proposed four-module machine structure has been completed using FEA to evaluate the transient and steady-state performance of a faulted system.

9.2.2. Development of a New Reliability Estimation Technique for Modular FT Machine Drives based on Markov Chain Analysis

The second major contribution of this research program is development of a new analytical approach for estimating the reliability of fault-tolerant modular machine drives. One of its most important benefits is that it provides a valuable tool for developing a roadmap for the future development of these FT modular motor drives that can meet the incredibly demanding reliability requirements of applications such as commercial aviation equipment. As noted in Chapter 1, the failure rates of conventional industrial-grade motor drives are between 5 and 6 orders of magnitude lower than the failure rate levels required for flight-critical equipment in large commercial aircraft.

This reliability deficit is so large that it makes it difficult for engineers to confidently determine how to achieve such a massive improvement in the achievable motor drive failure rates. The new analytical tool uses Markov chain techniques to estimate the failure rates of modular motor drives in a highly flexible manner that makes it easy to explore the impact of many key variables including the number of machine and drive modules, module failure rates, module repair rates, and the impact of single-point failure paths. The convenience and flexibility of using this reliability estimation model makes it a valuable tool for engineers to quickly evaluate the impact of changes in the modular drive architecture and key module failure/repair rates. As a result, it opens the door to parametric and comparative studies to investigate alternative designs in order to identify the most promising approaches to make major advances in the reliability characteristics of future fault-tolerant modular motor drives. Key research elements and initiatives that together comprise this contribution include:

9.2.2.1. Use of the new reliability estimation tool to investigate the failure rates of promising fault-tolerant modular motor drive configurations.

- Completion of a Markov chain reliability analysis of a four-module 24-slot, 28-pole machine considering continued operation after two faulted modules.
- Incorporation and application of the developed quadrotor machine and power electronics stresses into the component failure rates.
- Expansion of tool for use in evaluation of figures of merit for FT machines to enable better comparisons between FT motor-drive topologies.
- Development of convenient analytical formulas for mean time to failure (MTTF) calculations, simplifying the reliability calculation process.
- Derivation of a direct MTTF calculation from failure-transition matrix using properties of Laplace transforms

9.2.2.2. Parametric and sensitivity studies using the new reliability estimation tool to evaluate the impact of key design variables on the failure rates of alternative FT MMD configurations

- Evaluation of the impact of the number of faults, the number of modules, and the level of healthy and faulted stress in the machine on the overall system reliability.
- Completion of sensitivity study comparing failure rates of machine windings and power electronics to single point failures in the bearings and heat exchanger. Guidelines for improving modular system reliability are provided.

9.3. Key Research Conclusions

Complementing the list of major technical contributions and supporting research activities presented in the preceding section, key results from each research component of this research program are summarized:

9.3.1. Identification and Comparison of FT Machine Approaches and the Associated Tradeoffs

This thesis presents an extensive evaluation of various types of FT modular machines considering a range of factors including mass, electromagnetic and thermal isolation, and reliability impact. The implementation of fault tolerance is accompanied by significant tradeoffs involving the aforementioned drive performance features and metrics. Electromagnetic and thermal FEA combined with experimental testing have been used to perform these evaluations. Key results include:

- **Traditional modular isolation approaches have appreciable power density and performance tradeoffs that limit their viability in weight-sensitive applications like the studied quadcopter application.**

  A tradeoff study comparing conventional FT approaches has been completed comparing their power density, loss, and torque ripple characteristics to those of a conventional machine without special fault tolerance feature which achieves high levels of power density necessary for the application. Typical single-layer (SL) winding implementations are heavily penalized by large end windings and high rotor core loss attributable to their elevated spatial harmonics. In addition, these enlarged end windings add mass and losses that are highly undesirable in applications requiring the highest possible power density. Short stack lengths (and large diameters) are needed in some of these applications, further penalizing machine designs with extended end windings attributable to their SL windings. Similar observations regarding mass and volume penalties apply to the fault-tolerant dual-stator isolation approach. Other approaches that are based on the addition of spacer teeth or split tooth flux barriers suffer from the extra mass and volume required for these features that is otherwise occupied by copper, hurting their viability for high power density. This work highlights the need for new technical approaches that can achieve excellent module isolation characteristics with reduced mass, volume, and loss penalties.

- **Implementation of modular fault tolerance requires proactive consideration of all aspects of fault tolerance as demonstrated by analytical and experimental machine testing during this research program**

The fault testing and expanded simulation of the aerospace demonstrator machine in Chapter 3 illustrates the importance of a comprehensive approach for FT machine design. Although the machine possesses multiple three-phase winding sets, its poor electromagnetic isolation and elevated characteristic current value highlight its limitations as a fault tolerant modular machine. This research developed a comprehensive approach to modular fault tolerant machine design that was demonstrated during the design and analysis of the quadcopter IMMD in Chapter 4. Specifically, this machine was designed with the maximization of module isolation and the minimization of mass and loss penalties as key design objectives from the beginning.

- **Use of flux barriers and modified tooth tips to achieve high module electromagnetic isolation scales well over a wide range of power rating. However, the in-slot cooling technique developed during this research exhibits higher thermal benefits in low power machine designs.**

  The developed module isolation features have been evaluated for machines at three power rating levels covering the range from <10 kW to > 1 MW. Both isolation features have been shown to be effective for providing effective inter-modular isolation characteristics at all three of these power levels. More specifically, the effectiveness of the electromagnetic isolation approach works well at all power levels. However, geometric scaling laws gradually degrade the heat removal characteristics of the presented in-slot cooling technique as the power rating increases because of the longer paths from coil hot spots to the in-slot cooling channels associated with larger machines.

Further development beyond the scope of this research program is needed to adapt the presented in-slot cooling technique to the larger high-power machines.

9.3.2. Development of alternative electromagnetic and thermal isolation approaches for modular PMSMs

Thermal and electromagnetic isolation between modules in MMDs has been a core theme in this research program since it has such a large impact on the feasibility of a modular FT PMSM. This research program has proposed a new method for realizing isolation which demonstrate similar levels of effectiveness compared to conventional approaches but with lower machine mass and loss penalties. Key results include:

- **Traditional approaches of providing modular isolation penalize mass and performance that can be addressed by alternative forms of isolation including flux barriers and in-slot cooling**

  Traditional electromagnetic and thermal isolation approaches are accompanied by notable mass and loss tradeoffs, limiting their potential use in demanding applications such as aerospace machines. This research has developed a new approach for achieving electromagnetic isolation by using a double layer winding with modified electromagnetic features to eliminate mutual leakage coupling between adjacent phases. The implementation of these features can only be applied to machines using fractional-slot concentrated windings (FSCW) that incorporate an anti-periodic winding pattern resulting in a localized magnetic flux path that exhibits minimum electromagnetic coupling with the adjacent phase windings. A methodology has been developed during

this research program to identify these eligible machine winding configurations using winding functions.

For thermal isolation, an in-slot cooling technique has been developed that provides an effective method for thermally isolating coils that share the same slot. Although this in-slot cooling technique is not conventional, the literature review revealed that the broader class of in-slot cooling isolation techniques is drawing increasing attention as a promising means to achieve higher power density values in machines that need to push the power density frontier.

- **The amount of mutual coupling between modules is predominately determined by the choice of slot-pole combination, and tools and metrics for evaluating slot-pole combinations have been proposed.**

The flux barrier and modified tooth tip design approach is only applicable to a narrow set of FSCW slot-pole combinations that naturally exhibit negligible synchronous flux linkage with other phases. In general, slot-pole combinations exhibit non-zero synchronous mutual flux in addition to mutual leakage flux between modules as observed in the testing and simulation results presented in Chapter 4 for the slot-per-phase-per-pole (SPP) value of ½. Electromagnetic isolation metrics utilizing winding functions have been proposed that highlight the significance of this mutual coupling. In addition, this research highlights the importance of considering the winding function approach on the individual phase module basis in order to avoid misleading results. For example, full-winding synchronous flux cancellation may disappear when considering coil phase windings on an individual basis as observed for the single-layer 12-slot, 10-pole electromagnetic isolation study.

- **Electromagnetic isolation criteria are proposed to determine when isolation features are required.**

  This work highlights the underlying mechanisms that induce unbalanced currents which are influenced by unbalanced leakage flux between phases, unbalanced module inductances internal to a module, and machine speed. This work proposes useful criteria for assessing the level of electromagnetic isolation required for an application based on the size of the expected faults and the unbalanced mutual coupling between modules.

- **The tested in-slot cooling method demonstrates the effectiveness of in-slot cooling and thermal isolation**

  Both simulation and experimental results demonstrate the effectiveness of the proposed in-slot cooling method using alumina tubing. The developed cooling technique is estimated to have cooling capability above 20 A_{rms}/mm^2 which is appealing for high power density machines. Importantly, this in-slot cooling technique is effective for providing thermal isolation that minimizes the temperature changes in healthy windings during fault events in adjacent coil windings that share the same slot. For the most serious fault conditions, the coolant channel serves as a transient thermal buffer between the two coils, giving the implemented fault detection scheme sufficient time to respond to faults before the healthy phase winding has time to overheat.

9.3.3. Development of reliability estimation tool to investigate the failure rates of promising fault-tolerant motor drive configurations

This work presents a Markov chain analysis tool that is useful for quantitatively evaluating the reliability improvement of alternative FT motor drive configurations by calculating their predicted

failure rates for comparison with that of a baseline configuration. The tool has been applied to the evaluation of a 24-slot, 28-pole modular motor drive proposed for a quadcopter application. Key results include:

- **A 24-slot, 28-pole modular motor drive with four modules has been studied to assess potential pathways to improve the reliability of the integrated modular motor drive system.**

  The design of a representative 70 kW 24-slot, 28-pole modular motor drive has been presented for a quadcopter aircraft. A Markov chain reliability model of the machine is presented that uses the developed machine model as a reference for modifying component failure rates based on operating stresses. The developed tool has also been used to calculate the predicted mean time to failure (MTTF) for various repair rates. The results highlight the importance of frequent repairs (i.e., fast responses to module faults) for achieving increased MTTF values. The achievable improvement in the MTTF is shown to be highly dependent on the single point failure rate.

- **The number of acceptable module failures is studied and MTTF impact is assessed using the developed Markov chain tools**

  The four-module quadcopter IMMD is theoretically capable of operating with as many as three modules failed. The developed Markov chain analysis tool was modified to accommodate this scenario, and it shows increasing the number of allowed faults before drive system failure only has benefits for low repair rate scenarios. Diminishing MTTF improvements are observed for each incremental increase in the number of allowed module failures before system failure. This is important because raising the number of allowed module failures requires increased levels of power overrating for the

individual modules in order to retain acceptable drive system performance following multiple module failures, penalizing drive system mass and cost. The upper bound on the MTTF is still set by the single point failure rate.

- **Scenarios that remove single point failure components have been studied, and the potency of single point failure removal has been demonstrated.**

  The four-module quadcopter reliability model was modified to evaluate the impact of removing single-point failure components via redundancy or by fault detection methods. The results highlight the potential of achieving a massive improvement in the drive system MTTF when all single-point failures are removed; drive system MTTF values rise by factors exceeding 1000:1 when high repair rates are assumed. Such impressive MTTF improvement highlights the critical important of minimizing single-point failure rates to dramatically boost the reliability characteristics of existing motor drives to reach their required values for flight-critical aerospace applications. This exercise also highlights the critical role of modularity for removing the drive power electronics and machine windings from the single-point failure path.

9.3.4. Generalization of Reliability Model and the Identification of Key Variables to Improve Overall Motor-Drive Reliability

The research has resulted in the development of a generalized reliability analysis technique for motor drives that allows broader conclusions to be drawn than those described in the focused 24-slot, 28-pole case study. General fault tolerance relationships have been identified, leading to the development of figures of merit that are valuable for comparing alternative implementations of fault tolerant modular motor drives. Key conclusions from this work include:

- **The benefit of increased number of modules for low repair rates and with varying levels of post-fault stress have been evaluated**

  The four-module IMMD reliability tool has been generalized to consider the impact of multiple modules as well as the impact of increased levels of post-fault stress on components. For one portion of this study, the module repair rate has been reduced to zero to look exclusively at the impact of modularity by itself. The derived analytical formulas for drive system MTTF make it easy to spot trends that, in this case, include degrading drive system reliability as the number of modules increases due to the negative impact of increasing numbers of drive components. This degradation is amplified if elevated post-fault stress is introduced (a likely outcome in most fault tolerant systems). The maximum MTTF increase above that of the standard VSI baseline configuration (i.e., no modularity) is 1.5x for the case of two modules with negligible post-fault stress. This results highlights the limited value of modularity by itself without repairs. Higher numbers of modules are effective for raising the drive system MTTF only if significant repair rates can be assumed.

- **Several fault tolerance figures of merit (FT-FoM) have been proposed with definitions that quantify the achievable reliability improvements offset by the costs of introducing modularity, and they have been applied to alternative FT MMD topologies to highlight key differences between these FT topologies.**

  A set of fault tolerance figures of merit (FT-FoMs) have been proposed that make it easier to develop comparisons of FT topologies by quantifying their reliability benefits (change in MTTF by introducing the proposed FT feature) offset by their cost/penalties associated with mass, number of modules, etc. Methods for calculating the MTTF

values from the component failure rates are discussed. These FT-FoM metrics provide engineers with useful tool for developing insights into the strengths and liminations of alternative FT MMD configurations. They also highlight the fact that the highest-scoring FT MMD topology for any of the FT-FoM metrics is dependent on the values of the component failure rates and repair rates that are used to evaluate them.

- **Development of analytical mean time to failure formulas make it possible to investigate the sensitivity of their values to key formula inputs including the module repair rate, single-point failure rate, and the repair rate.**

  A method using Laplace transforms is introduced and implemented for deriving the analytical MTTF formulas. These formulas are useful for exploring sensitivity of the calculated MTTF values to the underlying component failure rates. If the module failure rate is high and comparable to the single point failure rate, then the effect of increasing the number of modules and the repair rate are more significant. Conversely, systems with high single-point failure rates relative to the module failure rate exhibit limited benefits from modularity.

9.4. Future Work

Based on the completed research program, the following tasks are proposed for future work expanding on the presented research:

1. Improve the fidelity of the developed Markov chain reliability estimation tools

This work presents a Markov chain tool that is effective for identifying key trends that are very helpful for improving the modular motor drive reliability. However, the developed implementation is a simplified version of reality that leaves opportunities for developing enhanced versions of the

tool, enabling investigations of MMD fault tolerance and reliability that would be more useful and accurate for real-world applications. Opportunities include: 1) incorporation of the mission profile into the model that includes the impact of fault timing, profile-related stresses, etc.; 2) development of more accurate component failure rates based on physics of failure methods that include improved models for stressed component failure rates; 3) more realistic implementations of the repair rate that reflect real-world constraints on when repairs can be made (e.g., between flights); development of time-varying failure rates that include the impact of aging and wear.

2. Investigation of modular current source inverter (CSI) implementation in FT MMDs including power-dense inductor designs

The current source inverter (CSI) offers intriguing opportunities for improving the short-circuit fault response of PMSMs compared to baseline voltage source inverters, making it a promising candidate for FT MMD applications. However, its usefulness for aerospace applications ultimately depends on its ability to match/exceed the power density, mass, reliability, and cost characteristics of VSIs. Key issues including the availability of power switches with reverse-voltage-blocking capability and power-dense inductors have a major impact on the future prospects of CSIs in FT MMD applications. An investigation of the CSI's key performance metrics and reliability improvement potential in a fault tolerant modular motor drive configuration would provide valuable insights into its potential advantage and limitations. This work could include an investigation of opportunities for applying the concepts guiding the design of power-dense machines to CSI inductors (direct cooling, larger diameters, etc.) to reduce their mass and losses. In addition, a modular drive configuration could open opportunities for sharing the inductor's magnetic structure among multiple modules to reduce its total mass without introducing single-point failures.

3. Improved in-slot cooling for high power applications

The scaling study presented in this work highlights the challenges of in-slot cooling at higher power levels due to increased overall dimensions and longer thermal paths. This suggests alternative in-slot cooling structures are required to better cool megawatt-scale machine windings. Future work might include enhanced co-optimization using thermal and electromagnetic FEA tools to identify feasible scenarios where in-slot cooling is feasible. Alternatively, future research may consider distributed cooling channels throughout the slot to reduce thermal resistances.

Alternatively, in-slot cooling would be improved if alternative winding encapsulants with higher thermal conductivity become available. Future work could investigate the effectiveness of adding alternative filler materials such as alumina powder to the base potting compound to achieve these improved thermal characteristics.

4. Unbalanced Magnetic Pull in fault tolerant modular motor drives

Unbalanced magnetic pull (UMP) resulting from post-fault unbalanced excitation of modular machines was a background topic during this research program that received limited attention. However, it played a role in limiting the maximum operating speed of the low-power concept demonstrator machine presented in Chapter 8 due to the resulting excessive vibration. This observed vibration creates risk for damaging the bearings and mechanical components, as well as potentially causing physical rubbing inside the machine winding that would accelerate coil faults. Future work could be oriented towards characterizing and mitigating the unbalanced magnetic pull in modular motor drives during faulted operation via some combination of improved machine structural design, alternative machine topologies, or adaptive control algorithms. In addition, physics of failure modeling techniques could be applied to calculate stress factors that can be used

in future reliability models to better characterize the impact of post-fault mechanical stresses on modular machine windings and other components.

5. **Fault tolerance investigations of megawatt-class cryogenically-cooled machines with high rotor fields and similar low inductance machine topologies.**

Presently there are two leading parallel approaches to achieving high levels of power density for megawatt-class machines. The first is the use of PMSMs, which is the primary focus of this research. The second parallel track investigates the use of cryogenically-cooled wound-field rotors (WFSM) to enable high airgap flux densities approaching 2.0 T in some cases. While an advantage of the WFSM is the ability to disable rotor fields during a fault event, it is unclear whether that type of response is feasible on the required timescales before a winding failure becomes catastrophic, considering the magnitude of fields and the likely air core (low-inductance, high airgap flux exposure) implementation. Similar types of investigations can be applied to PMSM topologies using air-gap windings such as the machine developed at the University of Illinois Urbana-Champaign by Prof. Kiruba Haran and his students [17]. Future research into these topologies would yield valuable insights into the feasibility of these approaches for use in future aircraft and well as potential enhancements.

Chapter 10

Bibliography

[1] J. A. Weimer, “The role of electric machines and drives in the more electric aircraft,” in *IEMDC 2003 - IEEE International Electric Machines and Drives Conference*, 2003, vol. 1, pp. 11–15. doi: 10.1109/IEMDC.2003.1211236.

[2] B. Sarlioglu and C. T. Morris, “More Electric Aircraft: Review, Challenges, and Opportunities for Commercial Transport Aircraft,” *IEEE Trans. Transp. Electrif.*, vol. 1, no. 1, pp. 54–64, 2015, doi: 10.1109/TTE.2015.2426499.

[3] W. Cao, B. C. Mecrow, G. J. Atkinson, J. W. Bennett, and D. J. Atkinson, “Overview of electric motor technologies used for more electric aircraft (MEA),” *IEEE Trans. Ind. Electron.*, vol. 59, no. 9, pp. 3523–3531, 2012, doi: 10.1109/TIE.2011.2165453.

[4] S. W. Ashcraft, A. S. Padron, K. A. Pascioni, G. W. Stout Jr., and D. L. Huff, “Review of Propulsion Technologies for N+3 Subsonic Vehicle Concepts,” 2011. [Online]. Available: https://ntrs.nasa.gov/archive/nasa/casi.ntrs.nasa.gov/20110022435.pdf

[5] National Academies of Sciences Engineering and Medicine, *Commercial Aircraft Propulsion and Energy Systems Research: Reducing Global Carbon Emissions*. Washington, D.C.: National Academies Press, 2016. doi: 10.17226/23490.

[6] P. Wheeler, T. S. Sirimanna, S. Bozhko, and K. S. Haran, “Electric/Hybrid-Electric Aircraft Propulsion Systems,” *Proc. IEEE*, vol. 109, no. 6, pp. 1115–1127, Jun. 2021, doi: 10.1109/JPROC.2021.3073291.

[7] C. L. Bowman, T. V. Marien, and J. L. Felder, “Turbo- and Hybrid-Electrified Aircraft Propulsion for Commercial Transport,” in *2018 AIAA/IEEE Electric Aircraft Technologies Symposium*, 2018, pp. 1–8. doi: 10.2514/6.2018-4984.

[8] C. Perullo *et al.*, “Sizing and Performance Analysis of a Turbo-Hybrid-Electric Regional Jet for the NASA ULI Program,” Aug. 2019. doi: 10.2514/6.2019-4490.

[9] H. D. Kim, A. T. Perry, and P. J. Ansell, “A Review of Distributed Electric Propulsion Concepts for Air Vehicle Technology,” in *2018 AIAA/IEEE Electric Aircraft Technologies Symposium*, Jul. 2018, pp. 1–21. doi: 10.2514/6.2018-4998.

[10] W. Johnson and C. Silva, “NASA concept vehicles and the engineering of advanced air mobility aircraft,” *Aeronaut. J.*, vol. 126, no. 1295, pp. 59–91, Jan. 2022, doi: 10.1017/aer.2021.92.

[11] Eviation, “Alice Commuter.” https://www.eviation.co/ (accessed Aug. 24, 2019).

[12] W. Johnson, C. Silva, and E. Solis, “Concept vehicles for VTOL air taxi operations,” 2018.

[13] C. Silva, W. R. Johnson, E. Solis, M. D. Patterson, and K. R. Antcliff, “VTOL Urban Air Mobility Concept Vehicles for Technology Development,” in *2018 Aviation Technology, Integration, and Operations Conference*, Jun. 2018, pp. 1–16. doi: 10.2514/6.2018-3847.

[14] Lilium, “Making Urban Air Mobility a Reality.” https://lilium.com/the-jet (accessed Aug. 21, 2021).

[15] “Joby Aviation,” 2021. https://www.jobyaviation.com/

[16] ARPA-E, “Aviation Class Synergistically Cooled Electric Motors with Integrated Drives (ASCEND) Funding Opportunity Announcement (FOA) No. DE-FOA-0002238,” 2019. [Online]. Available: https://arpa-e-foa.energy.gov/Default.aspx?foaId=22888746-6728-479a-8b27-f53f97f587a9

[17] A. Yoon, X. Yi, J. Martin, Y. Chen, and K. Haran, “A high-speed, high-frequency, air-core PM machine for aircraft application,” 2016. doi: 10.1109/PECI.2016.7459221.

[18] A. K. Yoon, D. Lohan, F. Arastu, J. Xiao, and K. Haran, “Direct Drive Electric Motor for STARC-ABL Tail-Cone Propulsor,” in *AIAA Propulsion and Energy 2019 Forum*, Aug. 2019, no. August, pp. 1–10. doi: 10.2514/6.2019-4516.

[19] C.-G. Cantemir, A. Munteanu, and R. Jansen, “10 MW Ring Motor,” 2016.

[20] T. Tallerico, J. J. Scheidler, D. Lee, and K. S. Haran, “Electromagnetic Redesign of NASA’s High Efficiency Megawatt Motor,” in *AIAA Propulsion and Energy 2020 Forum*, Aug. 2020, pp. 1–15. doi: 10.2514/6.2020-3600.

[21] C. Anghel, “Hybrid Electric Propulsion Technologies 1MW High Efficiency Generator.” 2015.

[22] J. Swanke, D. Bobba, T. Jahns, and B. Sarlioglu, “Design of High-Speed Permanent Magnet Machine for Aerospace Propulsion,” Aug. 2019. doi: 10.2514/6.2019-4483.

[23] P. de Bock, “Aviation-Class Synergistically Cooled Electric Motors With Integrated Drives (ASCEND),” 2022. [Online]. Available: https://arpa-e.energy.gov/sites/default/files/2022-08/2. ARPA-E ASCEND- Reaching Cruise Altitude - deBock.pdf

[24] T. M. Jahns and H. Dai, “The Past , Present , and Future of Power Electronics Integration Technology in Motor Drives,” *CPSS Trans. Power Electron. Appl.*, vol. 2, no. 3, pp. 197–216, 2017.

[25] U.S. Department of Transportation Federal Aviation Administration, “System Design and Analysis,” *FAA Advisory Circular AC, No. 25. 1309-1A*. 1988.

[26] P. R. Darmstadt *et al.*, “Hazards Analysis and Failure Modes and Effects Criticality Analysis (FMECA) of Four Concept Vehicle Propulsion Systems,” 2019. [Online]. Available: http://www.sti.nasa.gov

[27] W. Johnson and C. Silva, “Observations from exploration of VTOL urban air mobility designs,” October, 2019.

[28] A. G. Jack, B. C. Mecrow, and J. A. Haylock, “A comparative study of permanent magnet and switched reluctance motors for high-performance fault-tolerant applications,” *IEEE Trans. Ind. Appl.*, vol. 32, no. 4, pp. 889–895, 1996, doi: 10.1109/28.511646.

[29] B. C. Mecrow *et al.*, “Design and testing of a 4 phase fault tolerant permanent magnet machine for an engine fuel pump,” in *IEEE International Electric Machines and Drives*

Conference, 2003. IEMDC'03., 2003, vol. 2, no. 4, pp. 1301–1307. doi: 10.1109/IEMDC.2003.1210407.

[30] P. H. Mellor, J. Yon, J. L. Baker, D. North, and J. D. Booker, "Electromagnetic and thermal coupling within a fault-tolerant aircraft propulsion motor," in *2017 IEEE International Electric Machines and Drives Conference (IEMDC)*, May 2017, pp. 1–7. doi: 10.1109/IEMDC.2017.8002214.

[31] N. J. Baker, D. J. B. Smith, M. C. Kulan, and S. Turvey, "Design and Performance of a Segmented Stator Permanent Magnet Alternator for Aerospace," *IEEE Trans. Energy Convers.*, vol. 33, no. 1, pp. 40–48, Mar. 2018, doi: 10.1109/TEC.2017.2739201.

[32] R. N. Argile, B. C. Mecrow, D. J. Atkinson, A. G. Jack, and P. Sangha, "Reliability analysis of fault tolerant drive topologies," in *4th IET International Conference on Power Electronics, Machines and Drives (PEMD 2008)*, 2008, no. 525, pp. 11–15. doi: 10.1049/cp:20080474.

[33] B. A. Welchko, T. A. Lipo, T. M. Jahns, and S. E. Schulz, "Fault Tolerant Three-Phase AC Motor Drive Topologies: A Comparison of Features, Cost, and Limitations," *IEEE Trans. Power Electron.*, vol. 19, no. 4, pp. 1108–1116, Jul. 2004, doi: 10.1109/TPEL.2004.830074.

[34] R. L. de Araujo Ribeiro, C. B. Jacobina, E. R. C. da Silva, and A. M. N. Lima, "Fault-Tolerant Voltage-Fed PWM Inverter AC Motor Drive Systems," *IEEE Trans. Ind. Electron.*, vol. 51, no. 2, pp. 439–446, Apr. 2004, doi: 10.1109/TIE.2004.825284.

[35] N. Bianchi, S. Bolognani, and M. D. Pre, "Impact of Stator Winding of a Five-Phase Permanent-Magnet Motor on Postfault Operations," *IEEE Trans. Ind. Electron.*, vol. 55, no. 5, pp. 1978–1987, May 2008, doi: 10.1109/TIE.2008.920645.

[36] C. B. Jacobina, R. S. Miranda, and A. M. N. Lima, "Reconfigurable Fault Tolerant Dual-Winding AC Motor Drive System," in *IEEE 36th Conference on Power Electronics Specialists, 2005.*, 2005, vol. 2005, no. III, pp. 1574–1579. doi: 10.1109/PESC.2005.1581840.

[37] N. K. Nguyen, F. Meinguet, E. Semail, and X. Kestelyn, "Fault-Tolerant Operation of an Open-End Winding Five-Phase PMSM Drive With Short-Circuit Inverter Fault," *IEEE Trans. Ind. Electron.*, vol. 63, no. 1, pp. 595–605, Jan. 2016, doi: 10.1109/TIE.2014.2386299.

[38] X. Jiang, W. Huang, R. Cao, Z. Hao, and W. Jiang, "Electric Drive System of Dual-Winding Fault-Tolerant Permanent-Magnet Motor for Aerospace Applications," *IEEE Trans. Ind. Electron.*, vol. 62, no. 12, pp. 7322–7330, Dec. 2015, doi: 10.1109/TIE.2015.2454483.

[39] Y. Wang, T. A. Lipo, and D. Pan, "Robust operation of double-output AC machine drive," in *8th International Conference on Power Electronics - ECCE Asia*, May 2011, pp. 140–144. doi: 10.1109/ICPE.2011.5944562.

[40] X. Huang *et al.*, "Fault-Tolerant Brushless DC Motor Drive For Electro-Hydrostatic Actuation System In Aerospace Application," in *Conference Record of the 2006 IEEE Industry Applications Conference Forty-First IAS Annual Meeting*, Oct. 2006, vol. 1, no. c, pp. 473–480. doi: 10.1109/IAS.2006.256562.

[41] M. Aten, G. Towers, C. Whitley, P. Wheeler, J. Clare, and K. Bradley, "Reliability comparison of matrix and other converter topologies," *IEEE Trans. Aerosp. Electron. Syst.*, vol. 42, no. 3, pp. 867–875, Jul. 2006, doi: 10.1109/TAES.2006.248190.

[42] H. Dai, "Investigation of Current Source Inverter using Wide Bandgap Devices for Integrated Motor Drive Applications," University of Wisconsin-Madison, 2021.

[43] G. El Murr, A. Griffo, J. Wang, Z. Q. Zhu, and B. Mecrow, "Reliability assessment of fault tolerant permanent magnet AC drives," in *IECON 2015 - 41st Annual Conference of the IEEE Industrial Electronics Society*, Nov. 2015, pp. 002777–002782. doi: 10.1109/IECON.2015.7392522.

[44] A. P. Thurlbeck and Y. Cao, "A Mission Profile-Based Reliability Modeling Framework for Fault-Tolerant Electric Propulsion," *IEEE Trans. Ind. Appl.*, vol. 58, no. 2, pp. 2312–2323, Mar. 2022, doi: 10.1109/TIA.2022.3144620.

[45] International Air Transport Association, "IATA Forecasts Passenger Demand to Double Over 20 Years," *IATA Press Release No.: 59*, 2016. http://www.iata.org/pressroom/pr/Pages/2016-10-18-02.aspx (accessed May 03, 2018).

[46] G. J. Atkinson, J. W. Bennett, B. C. Mecrow, D. J. Atkinson, A. G. Jack, and V. Pickert, "Fault tolerant drives for aerospace applications," *2010 6th Int. Conf. Integr. Power Electron. Syst. CIPS 2010*, pp. 1–7, 2011, [Online]. Available: https://ieeexplore.ieee.org/document/5730645

[47] C. Gerada and K. J. Bradley, "Integrated PM Machine Design for an Aircraft EMA," *IEEE Trans. Ind. Electron.*, vol. 55, no. 9, pp. 3300–3306, Sep. 2008, doi: 10.1109/TIE.2008.927970.

[48] M. Villani, M. Tursini, G. Fabri, and L. Castellini, "High Reliability Permanent Magnet Brushless Motor Drive for Aircraft Application," *IEEE Trans. Ind. Electron.*, vol. 59, no. 5, pp. 2073–2081, May 2012, doi: 10.1109/TIE.2011.2160514.

[49] J. W. Bennett, B. C. Mecrow, A. G. Jack, and D. J. Atkinson, "A Prototype Electrical Actuator for Aircraft Flaps," *IEEE Trans. Ind. Appl.*, vol. 46, no. 3, pp. 915–921, 2010, doi: 10.1109/TIA.2010.2046278.

[50] Xiaoyan Huang, A. Goodman, C. Gerada, Youtong Fang, and Qinfen Lu, "Design of a Five-Phase Brushless DC Motor for a Safety Critical Aerospace Application," *IEEE Trans. Ind. Electron.*, vol. 59, no. 9, pp. 3532–3541, Sep. 2012, doi: 10.1109/TIE.2011.2172170.

[51] J. W. Bennett, B. C. Mecrow, D. J. Atkinson, and G. J. Atkinson, "Safety-critical design of electromechanical actuation systems in commercial aircraft," *IET Electr. Power Appl.*, vol. 5, no. 1, p. 37, 2011, doi: 10.1049/iet-epa.2009.0304.

[52] V. Madonna, P. Giangrande, L. Lusuardi, A. Cavallini, C. Gerada, and M. Galea, "Thermal Overload and Insulation Aging of Short Duty Cycle, Aerospace Motors," *IEEE Trans. Ind. Electron.*, vol. 67, no. 4, pp. 2618–2629, Apr. 2020, doi: 10.1109/TIE.2019.2914630.

[53] E. D. Ganev, "Electric Drives for Electric Green Taxiing Systems: Examining and Evaluating the Electric Drive System," *IEEE Electrification Magazine*, vol. 5, no. 4, pp. 10–24, Dec. 2017. doi: 10.1109/MELE.2017.2757618.

[54] Z. Xu, C. Tighe, M. Galea, T. Hamiti, C. Gerada, and S. J. Pickering, “Thermal design of a permanent magnetic motor for direct drive wheel actuator,” in *2014 International Conference on Electrical Machines (ICEM)*, Sep. 2014, pp. 2186–2192. doi: 10.1109/ICELMACH.2014.6960487.

[55] A. La Rocca *et al.*, “Thermal management of a high speed permanent magnet machine for an aeroengine,” in *2016 XXII International Conference on Electrical Machines (ICEM)*, Sep. 2016, pp. 2732–2737. doi: 10.1109/ICELMACH.2016.7732908.

[56] A. M. EL-Refaie, M. R. Shah, and K.-K. Huh, “High-Power-Density Fault-Tolerant PM Generator for Safety-Critical Applications,” *IEEE Trans. Ind. Appl.*, vol. 50, no. 3, pp. 1717–1728, May 2014, doi: 10.1109/TIA.2013.2282852.

[57] J. J. Wolmarans, H. Polinder, J. A. Ferreira, and D. Clarenbach, “Selecting an optimum number of system phases for an integrated, fault tolerant permanent magnet machine and drive,” 2009.

[58] G. M. Gilson, T. Raminosoa, S. J. Pickering, C. Gerada, and D. B. Hann, “A combined electromagnetic and thermal optimisation of an aerospace electric motor,” in *The XIX International Conference on Electrical Machines - ICEM 2010*, Sep. 2010, pp. 1–7. doi: 10.1109/ICELMACH.2010.5607893.

[59] Glenn Research Center, “Hybrid Electric Propulsion Airplane Concepts.” https://www1.grc.nasa.gov/aeronautics/hep/airplane-concepts/

[60] J. J. Berton and W. J. Haller, “A Noise and Emissions Assessment of the N3-X Transport,” in *52nd Aerospace Sciences Meeting*, Jan. 2014, no. January. doi: 10.2514/6.2014-0594.

[61] J. L. Felder, “NASA Electric Propulsion System Studies,” *NASA, GRC-E-DAA-TN28410*, 2015. https://ntrs.nasa.gov/

[62] A. Dubois, M. van der Geest, J. Ben Bevirt, S. Clarke, R. J. Christie, and N. K. Borer, “Design of an electric propulsion system for SCEPTOR,” in *16th AIAA Aviation Technology, Integration, and Operations Conference*, 2016, pp. 1–29.

[63] Airbus, “E-Fan X Demonstrator.” https://www.airbus.com/innovation/zero-emission/electric-flight/e-fan-x.html

[64] B. Kirk, “Airbus E-Fan X: The Bold Hybrid-Electric Airliner That Fizzled Into Vaporware,” *autoevolution*, 2022.

[65] Airbus, “EcoPulse: A new approach to distributed propulsion for aircraft.” https://www.airbus.com/en/innovation/zero-emission/electric-flight/ecopulse

[66] “Magnix.” https://www.magnix.aero/

[67] Beta, “ALIA-250c.” https://www.beta.team/aircraft/

[68] P. R. Darmstadt *et al.*, “Reliability and Safety Assessment of Urban Air Mobility Concept Vehicles,” 2021. [Online]. Available: https://ntrs.nasa.gov/citations/20210017188

[69] R. Krishnan and A. S. Bharadwaj, “A comparative study of various motor drive systems for aircraft applications,” in *Conference Record of the 1991 IEEE Industry Applications Society*

Annual Meeting, 1991, pp. 252–258. doi: 10.1109/IAS.1991.178163.

[70] I. Cotton, R. Gardner, D. Schweickart, D. Grosean, and C. Severns, "Design considerations for higher electrical power system voltages in aerospace vehicles," in *2016 IEEE International Power Modulator and High Voltage Conference (IPMHVC)*, Jul. 2016, pp. 57–61. doi: 10.1109/IPMHVC.2016.8012771.

[71] M. Liben and D. C. Ludois, "Analytical Design and Experimental Testing of a Self-Cooled, Toroidally Wound Ring Motor With Integrated Propeller for Electric Rotorcraft," *IEEE Trans. Ind. Appl.*, vol. 57, no. 3, pp. 2342–2353, May 2021, doi: 10.1109/TIA.2021.3058197.

[72] D. Lee *et al.*, "Detailed Design and Prototyping of a High Power Density Slotless PMSM," *IEEE Trans. Ind. Appl.*, pp. 1–8, 2022, doi: 10.1109/TIA.2022.3230379.

[73] "Successful test by UIUC, NASA, and Collins gets us one step closer to electric aircraft," 2021. https://ece.illinois.edu/newsroom/news/40942

[74] X. Yi and K. S. Haran, "Thermal Integration of a High-Frequency High-Specific-Power Motor within Electrically Variable Engine," in *AIAA Propulsion and Energy 2019 Forum*, Aug. 2019, no. August, pp. 1–10. doi: 10.2514/6.2019-4405.

[75] R. Jansen *et al.*, "High Efficiency Megawatt Motor Conceptual Design," Jul. 2018. doi: 10.2514/6.2018-4699.

[76] R. Jansen *et al.*, "High Efficiency Megawatt Motor Preliminary Design," Aug. 2019. doi: 10.2514/6.2019-4513.

[77] J. J. Scheidler, T. Tallerico, W. A. Miller, and W. Torres, "Progress Toward the Critical Design of the Superconducting Rotor for NASA's 1.4~MW High-Efficiency Electric Machine," in *AIAA Propulsion and Energy 2019 Forum*, Aug. 2019, no. August, pp. 1–13. doi: 10.2514/6.2019-4496.

[78] A. Woodworth *et al.*, "Thermal Analysis of Potted Litz Wire for High Power Density Aerospace Electric Machines," in *AIAA Propulsion and Energy 2019 Forum*, Aug. 2019, no. August, pp. 1–13. doi: 10.2514/6.2019-4509.

[79] J. Banke, "NASA, GE Complete Historic Hybrid-Electric Propulsion Tests," 2022. https://www.nasa.gov/feature/glenn/2022/nasa-ge-complete-historic-hybrid-electric-propulsion-tests

[80] F. Wu and A. M. EL-Refaie, "Additively Manufactured Hollow Conductors with Integrated Cooling for High Specific Power Electrical Machines," in *2020 International Conference on Electrical Machines (ICEM)*, Aug. 2020, pp. 1497–1503. doi: 10.1109/ICEM49940.2020.9270871.

[81] F. Wu and A. M. EL-Refaie, "Investigation of an Addtively-Manufactured Modular Permanent Magnet Machine for High Specific Power Design," in *2019 IEEE Energy Conversion Congress and Exposition (ECCE)*, Sep. 2019, pp. 777–784. doi: 10.1109/ECCE.2019.8912763.

[82] D. Golovanov, Z. Xu, D. Gerada, A. Page, and T. Sawata, "Designing an Advanced

Electrical Motor for Propulsion of Electric Aircraft," in *AIAA Propulsion and Energy 2019 Forum*, Aug. 2019, no. August, pp. 1–12. doi: 10.2514/6.2019-4482.

[83] M.-S. Donea and D. Gerling, "Optimal electrical drive configuration to use in a Do 128-6 aircraft taking into account the electromagnetic, mechanical and aerodynamic designs," in *IECON 2015 - 41st Annual Conference of the IEEE Industrial Electronics Society*, Nov. 2015, pp. 004544–004549. doi: 10.1109/IECON.2015.7392808.

[84] M. S. Donea and D. Gerling, "Design and calculation of a 300 kW high-speed PM motor for aircraft application," in *2016 International Symposium on Power Electronics, Electrical Drives, Automation and Motion, SPEEDAM 2016*, 2016, no. 3, pp. 1–6. doi: 10.1109/SPEEDAM.2016.7525839.

[85] L. Xu *et al.*, "Design and Experimental Evaluation of a High Specific Power Permanent Magnet Synchronous Machine," in *2019 IEEE International Electric Machines & Drives Conference (IEMDC)*, May 2019, pp. 1296–1302. doi: 10.1109/IEMDC.2019.8785246.

[86] Safran, "ENGINeUS Smart Electric Motors." https://www.safran-group.com/products-services/engineustm

[87] H3X, "Integrated Motor Drives for Electric Aircraft," 2022. https://www.h3x.tech/

[88] A. El-refaie and M. Osama, "High Specific Power Electrical Machines : A System Perspective," *CES Trans. Electr. Mach. Syst.*, vol. 3, no. 1, pp. 88–93, 2019.

[89] D. Hall, J. Chin, A. Anderson, A. Smith, R. Edwards, and K. P. Duffy, "Development of a Maxwell X-57 High Lift Motor Reference Design," in *AIAA Propulsion and Energy 2019 Forum*, Aug. 2019, no. August, pp. 1–24. doi: 10.2514/6.2019-4481.

[90] X. Zhang and K. S. Haran, "High-specific-power electric machines for electrified transportation applications-technology options," in *2016 IEEE Energy Conversion Congress and Exposition (ECCE)*, Sep. 2016, pp. 1–8. doi: 10.1109/ECCE.2016.7855164.

[91] R. R. Moghaddam, "High speed operation of electrical machines, a review on technology, benefits and challenges," in *2014 IEEE Energy Conversion Congress and Exposition (ECCE)*, Sep. 2014, no. mm, pp. 5539–5546. doi: 10.1109/ECCE.2014.6954160.

[92] A. M. El-Refaie, "Role of advanced materials in electrical machines," in *2017 20th International Conference on Electrical Machines and Systems (ICEMS)*, Aug. 2017, pp. 1–6. doi: 10.1109/ICEMS.2017.8055927.

[93] T. J. Woolmer and M. D. McCulloch, "Analysis of the Yokeless And Segmented Armature Machine," in *2007 IEEE International Electric Machines & Drives Conference*, May 2007, vol. 1, pp. 704–708. doi: 10.1109/IEMDC.2007.382753.

[94] Wei Zhang, Mingyao Lin, Da Xu, Xinghe Fu, and Li Hao, "Novel Fault-Tolerant Design of Axial Field Flux-Switching Permanent Magnet Machine," *IEEE Trans. Appl. Supercond.*, vol. 24, no. 3, pp. 1–4, Jun. 2014, doi: 10.1109/TASC.2014.2304841.

[95] F. Yu, M. Cheng, and K. T. Chau, "Controllability and Performance of a Nine-Phase FSPM Motor Under Severe Five Open-Phase Fault Conditions," *IEEE Trans. Energy Convers.*, vol. 31, no. 1, pp. 323–332, Mar. 2016, doi: 10.1109/TEC.2015.2486521.

[96] A. S. Thomas, Z. Q. Zhu, R. L. Owen, G. W. Jewell, and D. Howe, "Multiphase Flux-Switching Permanent-Magnet Brushless Machine for Aerospace Application," *IEEE Trans. Ind. Appl.*, vol. 45, no. 6, pp. 1971–1981, 2009, doi: 10.1109/TIA.2009.2031901.

[97] A. M. EL-Refaie, "Fractional-Slot Concentrated-Windings Synchronous Permanent Magnet Machines: Opportunities and Challenges," *IEEE Trans. Ind. Electron.*, vol. 57, no. 1, pp. 107–121, Jan. 2010, doi: 10.1109/TIE.2009.2030211.

[98] M. van der Geest, H. Polinder, J. A. Ferreira, and M. Christmann, "Power Density Limits and Design Trends of High-Speed Permanent Magnet Synchronous Machines," *IEEE Trans. Transp. Electrif.*, vol. 1, no. 3, pp. 266–276, Oct. 2015, doi: 10.1109/TTE.2015.2475751.

[99] A. Krings, M. Cossale, A. Tenconi, J. Soulard, A. Cavagnino, and A. Boglietti, "Characteristics comparison and selection guide for magnetic materials used in electrical machines," in *2015 IEEE International Electric Machines & Drives Conference (IEMDC)*, May 2015, vol. 23, no. 6, pp. 1152–1157. doi: 10.1109/IEMDC.2015.7409206.

[100] H.-C. Lahne, O. Moros, and D. Gerling, "Design considerations when developing a 50000 rpm high-speed high-power machine," in *2015 17th European Conference on Power Electronics and Applications (EPE'15 ECCE-Europe)*, Sep. 2015, no. September 2015, pp. 1–10. doi: 10.1109/EPE.2015.7311716.

[101] M. Ziegler, M. Schneider, M. Hubert, and J. Franke, "Potentials of the Rotary Cutting Process for Electrical Steel Strip," in *2018 8th International Electric Drives Production Conference (EDPC)*, Dec. 2018, pp. 1–6. doi: 10.1109/EDPC.2018.8658297.

[102] M. Henke *et al.*, "Challenges and Opportunities of Very Light High-Performance Electric Drives for Aviation," *Energies*, vol. 11, no. 2, 2018, doi: 10.3390/en11020344.

[103] J. D. Widmer, C. M. Spargo, G. J. Atkinson, and B. C. Mecrow, "Solar Plane Propulsion Motors With Precompressed Aluminum Stator Windings," *IEEE Trans. Energy Convers.*, vol. 29, no. 3, pp. 681–688, Sep. 2014, doi: 10.1109/TEC.2014.2313642.

[104] M. C. Kulan, S. Sahin, and N. J. Baker, "An Overview of Modern Thermo-Conductive Materials for Heat Extraction in Electrical Machines," *IEEE Access*, vol. 8, pp. 212114–212129, 2020, doi: 10.1109/ACCESS.2020.3040045.

[105] W. Yin *et al.*, "Highly thermally conductive insulation for high power density electric machines," in *AIAA Propulsion and Energy 2019 Forum*, Aug. 2019, no. August. doi: 10.2514/6.2019-4510.

[106] A. Acquaviva, S. Skoog, and T. Thiringer, "Manufacturing of tooth coil winding PM machines with in-slot oil cooling," in *2020 International Conference on Electrical Machines (ICEM)*, Aug. 2020, pp. 2314–2320. doi: 10.1109/ICEM49940.2020.9270747.

[107] M. U. Naseer, A. Kallaste, B. Asad, T. Vaimann, and A. Rassõlkin, "A Review on Additive Manufacturing Possibilities for Electrical Machines," *Energies*, vol. 14, no. 7, p. 1940, Mar. 2021, doi: 10.3390/en14071940.

[108] A. Kallaste, T. Vaimann, and A. Rassalkin, "Additive Design Possibilities of Electrical Machines," in *2018 IEEE 59th International Scientific Conference on Power and Electrical Engineering of Riga Technical University (RTUCON)*, Nov. 2018, pp. 1–5. doi:

10.1109/RTUCON.2018.8659828.

[109] D. C. Deisenroth and M. Ohadi, “Thermal Management of High-Power Density Electric Motors for Electrification of Aviation and Beyond,” *Energies*, vol. 12, no. 19, p. 3594, Sep. 2019, doi: 10.3390/en12193594.

[110] W. Sixel, M. Liu, G. Nellis, and B. Sarlioglu, “Ceramic 3D Printed Direct Winding Heat Exchangers for Improving Electric Machine Thermal Management,” in *2019 IEEE Energy Conversion Congress and Exposition (ECCE)*, Sep. 2019, pp. 769–776. doi: 10.1109/ECCE.2019.8913234.

[111] N. Simpson, C. Tighe, and P. Mellor, “Design of High Performance Shaped Profile Windings for Additive Manufacture,” in *2019 IEEE Energy Conversion Congress and Exposition (ECCE)*, Sep. 2019, pp. 761–768. doi: 10.1109/ECCE.2019.8912923.

[112] R. Abebe *et al.*, “Integrated motor drives: state of the art and future trends,” *IET Electr. Power Appl.*, vol. 10, no. 8, pp. 757–771, Sep. 2016, doi: 10.1049/iet-epa.2015.0506.

[113] A. M. El-Refaie, “Integrated electrical machines and drives: An overview,” in *2015 IEEE International Electric Machines & Drives Conference (IEMDC)*, May 2015, pp. 350–356. doi: 10.1109/IEMDC.2015.7409083.

[114] A. Tenconi, F. Profumo, S. E. Bauer, and M. D. Hennen, “Temperatures Evaluation in an Integrated Motor Drive for Traction Applications,” *IEEE Trans. Ind. Electron.*, vol. 55, no. 10, pp. 3619–3626, Oct. 2008, doi: 10.1109/TIE.2008.2003099.

[115] J. J. Wolmarans, M. B. Gerber, H. Polinder, S. W. H. de Haan, J. A. Ferreira, and D. Clarenbach, “A 50kW integrated fault tolerant permanent magnet machine and motor drive,” in *2008 IEEE Power Electronics Specialists Conference*, Jun. 2008, pp. 345–351. doi: 10.1109/PESC.2008.4591953.

[116] A. Ebrahimian, W. A. Khan, S. Iman Hosseini S, and N. Weise, “Electrothermal Design of a GaN-Based Axially Stator Iron-Mounted Fully Integrated Modular Motor Drive,” in *2022 IEEE Transportation Electrification Conference & Expo (ITEC)*, Jun. 2022, pp. 733–739. doi: 10.1109/ITEC53557.2022.9813979.

[117] D. Han, S. Li, W. Lee, and B. Sarlioglu, “Adoption of wide bandgap technology in hybrid/electric vehicles-opportunities and challenges,” in *2017 IEEE Transportation Electrification Conference and Expo (ITEC)*, Jun. 2017, vol. 3, pp. 561–566. doi: 10.1109/ITEC.2017.7993332.

[118] L. Papini, T. Raminosoa, D. Gerada, and C. Gerada, “A High-Speed Permanent-Magnet Machine for Fault-Tolerant Drivetrains,” *IEEE Trans. Ind. Electron.*, vol. 61, no. 6, pp. 3071–3080, Jun. 2014, doi: 10.1109/TIE.2013.2282604.

[119] Y. Bai, S. Wang, A. Zhang, X. Wang, and J. Mao, “A Novel Concept of Permanent Magnet Synchronous Generators With Automatic Turn-to-Turn Short-Circuit Fault-Tolerance Capability,” *IEEE Trans. Energy Convers.*, vol. 34, no. 1, pp. 98–108, Mar. 2019, doi: 10.1109/TEC.2018.2860128.

[120] B. Vaseghi, N. Takorabet, J. P. Caron, B. Nahid-Mobarakeh, F. Meibody-Tabar, and G. Humbert, “Study of Different Architectures of Fault-Tolerant Actuator Using a Two-

Channel PM Motor," *IEEE Trans. Ind. Appl.*, vol. 47, no. 1, pp. 47–54, Jan. 2011, doi: 10.1109/TIA.2010.2090930.

[121] N. Bianchi, M. D. Pre, and S. Bolognani, "Design of a Fault-Tolerant IPM Motor for Electric Power Steering," *IEEE Trans. Veh. Technol.*, vol. 55, no. 4, pp. 1102–1111, Jul. 2006, doi: 10.1109/TVT.2006.877716.

[122] A. G. Sarigiannidis, M. E. Beniakar, P. E. Kakosimos, A. G. Kladas, L. Papini, and C. Gerada, "Fault Tolerant Design of Fractional Slot Winding Permanent Magnet Aerospace Actuator," *IEEE Trans. Transp. Electrif.*, vol. 2, no. 3, pp. 380–390, Sep. 2016, doi: 10.1109/TTE.2016.2574947.

[123] T. Hopper and C. Stuckmann, "Building electric motors for space, with redundancy and high reliability," in *14th European Space Mechanisms & Tribology Symposium --ESMATS 2011*, 2011, no. September, pp. 28–30.

[124] A. J. Mitcham, G. Antonopoulos, and J. J. A. Cullen, "Favourable slot and pole number combinations for fault-tolerant PM machines," *IEE Proc. - Electr. Power Appl.*, vol. 151, no. 5, p. 520, 2004, doi: 10.1049/ip-epa:20040584.

[125] N. Bianchi, M. D. Pre, G. Grezzani, and S. Bolognani, "Design considerations on fractional-slot fault-tolerant synchronous motors," in *IEEE International Conference on Electric Machines and Drives, 2005.*, 2005, pp. 902–909. doi: 10.1109/IEMDC.2005.195829.

[126] S. Nall and P. H. Mellor, "Compact direct-drive permanent magnet motor for a UAV rotorcraft with improved faulted behaviour through operation as four separate three-phase machines," in *IET Conference Publications*, 2008, no. 538 CP, pp. 245–249. doi: 10.1049/cp:20080520.

[127] G.-J. Li, Z.-Q. Zhu, M. P. Foster, D. A. Stone, and H.-L. Zhan, "Modular Permanent-Magnet Machines With Alternate Teeth Having Tooth Tips," *IEEE Trans. Ind. Electron.*, vol. 62, no. 10, pp. 6120–6130, Oct. 2015, doi: 10.1109/TIE.2015.2427112.

[128] Q. Chen, G. Liu, W. Gong, and W. Zhao, "A New Fault-Tolerant Permanent-Magnet Machine for Electric Vehicle Applications," *IEEE Trans. Magn.*, vol. 47, no. 10, pp. 4183–4186, Oct. 2011, doi: 10.1109/TMAG.2011.2146238.

[129] P. Zheng, Y. Sui, J. Zhao, C. Tong, T. A. Lipo, and A. Wang, "Investigation of a Novel Five-Phase Modular Permanent-Magnet In-Wheel Motor," *IEEE Trans. Magn.*, vol. 47, no. 10, pp. 4084–4087, Oct. 2011, doi: 10.1109/TMAG.2011.2150207.

[130] F. Magnussen and C. Sadarangani, "Winding factors and Joule losses of permanent magnet machines with concentrated windings," in *IEEE International Electric Machines and Drives Conference, 2003. IEMDC'03.*, 2006, vol. 1, pp. 333–339. doi: 10.1109/IEMDC.2003.1211284.

[131] D. Wang and Y. Chen, "Fault-Tolerant Control of Coil Inter-Turn Short-Circuit in Five-Phase Permanent Magnet Synchronous Motor," *Energies*, vol. 13, no. 21, p. 5669, Oct. 2020, doi: 10.3390/en13215669.

[132] G. Heins, D. M. Ionel, and M. Thiele, "Winding Factors and Magnetic Fields in Permanent-Magnet Brushless Machines With Concentrated Windings and Modular Stator Cores,"

IEEE Trans. Ind. Appl., vol. 51, no. 4, pp. 2924–2932, Jul. 2015, doi: 10.1109/TIA.2015.2394444.

[133] Jiabin Wang, K. Atallah, Z. Q. Zhu, and D. Howe, "Modular Three-Phase Permanent-Magnet Brushless Machines for In-Wheel Applications," *IEEE Trans. Veh. Technol.*, vol. 57, no. 5, pp. 2714–2720, Sep. 2008, doi: 10.1109/TVT.2007.914476.

[134] J. Wang, Z. P. Xia, and D. Howe, "Three-Phase Modular Permanent Magnet Brushless Machine for Torque Boosting on a Downsized ICE Vehicle," *IEEE Trans. Veh. Technol.*, vol. 54, no. 3, pp. 809–816, May 2005, doi: 10.1109/TVT.2005.847224.

[135] T. M. Jahns, "Improved Reliability in Solid-State AC Drives by Means of Multiple Independent Phase Drive Units," *IEEE Trans. Ind. Appl.*, vol. IA-16, no. 3, pp. 321–331, May 1980, doi: 10.1109/TIA.1980.4503793.

[136] E. Jung, H. Yoo, S.-K. Sul, H.-S. Choi, and Y.-Y. Choi, "A Nine-Phase Permanent-Magnet Motor Drive System for an Ultrahigh-Speed Elevator," *IEEE Trans. Ind. Appl.*, vol. 48, no. 3, pp. 987–995, May 2012, doi: 10.1109/TIA.2012.2190472.

[137] P. Arumugam, T. Hamiti, and C. Gerada, "Modeling of Different Winding Configurations for Fault-Tolerant Permanent Magnet Machines to Restrain Interturn Short-Circuit Current," *IEEE Trans. Energy Convers.*, vol. 27, no. 2, pp. 351–361, Jun. 2012, doi: 10.1109/TEC.2012.2188138.

[138] B. Wang, J. Wang, B. Sen, A. Griffo, Z. Sun, and E. Chong, "A Fault-Tolerant Machine Drive Based on Permanent Magnet-Assisted Synchronous Reluctance Machine," *IEEE Trans. Ind. Appl.*, vol. 54, no. 2, pp. 1349–1359, Mar. 2018, doi: 10.1109/TIA.2017.2781201.

[139] M. Barcaro, N. Bianchi, and F. Magnussen, "Analysis and Tests of a Dual Three-Phase 12-Slot 10-Pole Permanent-Magnet Motor," *IEEE Trans. Ind. Appl.*, vol. 46, no. 6, pp. 2355–2362, Nov. 2010, doi: 10.1109/TIA.2010.2070784.

[140] D. Jiang and F. Wang, "Current-ripple prediction for three-phase PWM converters," *IEEE Trans. Ind. Appl.*, vol. 50, no. 1, pp. 531–538, 2014, doi: 10.1109/TIA.2013.2270224.

[141] W. Lee, S. G. Min, and B. Sarlioglu, "Modular 2n-phase Inverter (M2I) Topology with Novel Phase Current Injection Scheme for Fault-tolerant Multiphase Electric Machine Drives," in *2019 IEEE Energy Conversion Congress and Exposition (ECCE)*, Sep. 2019, pp. 345–352. doi: 10.1109/ECCE.2019.8913054.

[142] V. Madonna, G. Migliazza, P. Giangrande, E. Lorenzani, G. Buticchi, and M. Galea, "The Rebirth of the Current Source Inverter: Advantages for Aerospace Motor Design," *IEEE Ind. Electron. Mag.*, vol. 13, no. 4, pp. 65–76, Dec. 2019, doi: 10.1109/MIE.2019.2936319.

[143] Y. Zhang, "Investigation of Approaches for Improving the Performance and Fault Tolerance of Permanent Magnet Synchronous Machine Drives Using Current-Source Inverters by," University of Wisconsin-Madison, 2016. [Online]. Available: http://ieeexplore.ieee.org/document/7409178/

[144] S. Lee, F. Chen, T. M. Jahns, and B. Sarlioglu, "Review on Switching Device Fault, Protection, and Fault-Tolerant Topologies of Current Source Inverter," in *2021 IEEE 13th*

International Symposium on Diagnostics for Electrical Machines, Power Electronics and Drives (SDEMPED), Aug. 2021, pp. 489–495. doi: 10.1109/SDEMPED51010.2021.9605513.

[145] P. Eduardo and C. Palavicino, "Analysis , Modeling , and Detection of Inter-Turn Short Circuits in Interior Permanent Magnet Synchronous Machines by," University of Wisconsin-Madison, 2021.

[146] H. Wang, K. Ma, and F. Blaabjerg, "Design for reliability of power electronic systems," in *IECON 2012 - 38th Annual Conference on IEEE Industrial Electronics Society*, Oct. 2012, pp. 33–44. doi: 10.1109/IECON.2012.6388833.

[147] A. Binder, T. Schneider, and M. Klohr, "Fixation of buried and surface-mounted magnets in high-speed permanent-magnet synchronous machines," *IEEE Trans. Ind. Appl.*, vol. 42, no. 4, pp. 1031–1037, Jul. 2006, doi: 10.1109/TIA.2006.876072.

[148] F. A. L. Souza, P. C. T. Pereira, H. de Paula, B. J. C. Filho, and A. V. Rocha, "Motor drive systems reliability: Impact of the environment conditions on the electronic component failure rates," in *2014 IEEE Industry Application Society Annual Meeting*, Oct. 2014, no. iii, pp. 1–8. doi: 10.1109/IAS.2014.6978463.

[149] S. Yang, D. Xiang, A. Bryant, P. Mawby, L. Ran, and P. Tavner, "Condition Monitoring for Device Reliability in Power Electronic Converters: A Review," *IEEE Trans. Power Electron.*, vol. 25, no. 11, pp. 2734–2752, Nov. 2010, doi: 10.1109/TPEL.2010.2049377.

[150] P. Sun, W. Sima, X. Jiang, D. Zhang, J. He, and L. Ye, "Review of accumulative failure of winding insulation subjected to repetitive impulse voltages," *High Volt.*, vol. 4, no. 1, pp. 1–11, Mar. 2019, doi: 10.1049/hve.2018.5051.

[151] ABB, "Effects of AC drives on motor insulation," 1998. [Online]. Available: https://library.e.abb.com/public/fec1a7b62d273351c12571b60056a0fd/voltstress.pdf

[152] S. Choi *et al.*, "Fault Diagnosis Techniques for Permanent Magnet AC Machine and Drives—A Review of Current State of the Art," *IEEE Trans. Transp. Electrif.*, vol. 4, no. 2, pp. 444–463, Jun. 2018, doi: 10.1109/TTE.2018.2819627.

[153] R. P. Heydorn and P. D. T. O'Connor, *Practical Reliability Engineering*, no. 4. 2011.

[154] J. Pukite and P. Pukite, *Modeling for Reliability Analysis*. IEEE Press, 1998.

[155] J. C. Shaw, P. Norman, S. Galloway, and G. Burt, "A Method for the Evaluation of the Effectiveness of Turboelectric Distributed Propulsion Power System Architectures," *SAE Int. J. Aerosp.*, vol. 7, no. 1, pp. 2014-01–2120, Sep. 2014, doi: 10.4271/2014-01-2120.

[156] "MIL-HDBK-217F - Military Handbook: Reliability Prediction of Electronic Equipment." 1991.

[157] "Handbook of Reliability Prediction Procedures for Mechanical Equipment (NSWC-11/LE10)." 2011.

[158] W. Li and M. Cheng, "Investigation of influence of winding structure on reliability of permanent magnet machines," *CES Trans. Electr. Mach. Syst.*, vol. 4, no. 2, pp. 87–95, Jun.

2020, doi: 10.30941/CESTEMS.2020.00013.

[159] G. J. Anders, J. Endrenyi, G. L. Ford, and G. C. Stone, "A probabilistic model for evaluating the remaining life of evaluating the remaining life of electrical insulation in rotating machines," *IEEE Trans. Energy Convers.*, vol. 5, no. 4, pp. 761–767, 1990, doi: 10.1109/60.63150.

[160] T. Geyer and S. Schroder, "Reliability Considerations and Fault-Handling Strategies for Multi-MW Modular Drive Systems," *IEEE Trans. Ind. Appl.*, vol. 46, no. 6, pp. 2442–2451, Nov. 2010, doi: 10.1109/TIA.2010.2070477.

[161] Y. Fujimoto and T. Sekiguchi, "Fault-tolerant configuration of distributed discrete controllers," *IEEE Trans. Ind. Electron.*, vol. 50, no. 1, pp. 86–93, Feb. 2003, doi: 10.1109/TIE.2002.804977.

[162] M. Molaei, H. Oraee, and M. Fotuhi-Firuzabad, "Markov Model of Drive-Motor Systems for Reliability Calculation," in *2006 IEEE International Symposium on Industrial Electronics*, Jul. 2006, pp. 2286–2291. doi: 10.1109/ISIE.2006.295929.

[163] I. Bolvashenkov, J. Kammermann, and H.-G. Herzog, "Reliability assessment of a fault tolerant propulsion system for an electrical helicopter," in *2017 Twelfth International Conference on Ecological Vehicles and Renewable Energies (EVER)*, Apr. 2017, pp. 1–6. doi: 10.1109/EVER.2017.7935864.

[164] I. Bolvashenkov, J. Kammermann, T. Lahlou, and H.-G. Herzog, "Comparison and choice of a fault tolerant inverter topology for the traction drive of an electrical helicopter," in *2016 International Conference on Electrical Systems for Aircraft, Railway, Ship Propulsion and Road Vehicles & International Transportation Electrification Conference (ESARS-ITEC)*, Nov. 2016, no. 1, pp. 1–6. doi: 10.1109/ESARS-ITEC.2016.7841328.

[165] I. Bolvashenkov and H.-G. Herzog, "Approach to predictive evaluation of the reliability of electric drive train based on a stochastic model," in *2015 International Conference on Clean Electrical Power (ICCEP)*, Jun. 2015, pp. 486–492. doi: 10.1109/ICCEP.2015.7177561.

[166] I. Bolvashenkov, J. Kammermann, S. Willerich, and H. G. Herzog, "Comparative study of reliability and fault tolerance of multi-phase permanent magnet synchronous motors for safety-critical drive trains," 2016. doi: 10.24084.

[167] T. Tallerico, T. Krantz, M. Valco, and J. Salem, "Urban Air Mobility Electric Motor Winding Insulation Reliability: Challenges in the Design and Qualification of High Reliability Electric Motors and NASA's Research Plan," 2022. [Online]. Available: https://ntrs.nasa.gov/citations/20220004926

[168] D. Hirschmann, D. Tissen, S. Schroder, and R. W. De Doncker, "Reliability Prediction for Inverters in Hybrid Electrical Vehicles," *IEEE Trans. Power Electron.*, vol. 22, no. 6, pp. 2511–2517, Nov. 2007, doi: 10.1109/TPEL.2007.909236.

[169] B. Hu *et al.*, "Failure and Reliability Analysis of a SiC Power Module Based on Stress Comparison to a Si Device," *IEEE Trans. Device Mater. Reliab.*, vol. 17, no. 4, pp. 727–737, Dec. 2017, doi: 10.1109/TDMR.2017.2766692.

[170] L. E. Bechtold, D. Redman, and B. Tawfellos, "Semiconductor reliability using random and

wearout failure models," *Proc. - Annu. Reliab. Maintainab. Symp.*, pp. 0–5, 2014, doi: 10.1109/RAMS.2014.6798499.

[171] Z. Qiu, J. Zhang, P. Ning, and X. Wen, "Reliability modeling and analysis of SiC MOSFET power modules," in *IECON 2017 - 43rd Annual Conference of the IEEE Industrial Electronics Society*, Oct. 2017, vol. 2017-Janua, pp. 1459–1463. doi: 10.1109/IECON.2017.8216248.

[172] V. Madonna, P. Giangrande, and M. Galea, "Introducing Physics of Failure Considerations in the Electrical Machines Design," in *2019 IEEE International Electric Machines & Drives Conference (IEMDC)*, May 2019, pp. 2233–2238. doi: 10.1109/IEMDC.2019.8785304.

[173] D. Azizi, A. Gholami, and A. Vahedi, "Analysis of the deterioration effects of stator insulation on the its electro-thermal property," *Int. J. Electr. Power Electron. Eng.*, vol. 3, no. 1, pp. 697–701, 2009.

[174] M. V. Fosnot, "NASA University Led Initiative : Electric Propulsion : Challenges and Opportunities," 2017.

[175] T. A. Lipo, *Introduction To AC Machine Design*, 3rd ed. Wisconsin Power Electronics Research Center, University of Wisconsin, 2016.

[176] T. Murata and H. Ishibuchi, "MOGA: Multi-objective genetic algorithms," in *Proc. of 1995 IEEE International Conference on Evolutionary Computation*, 1995, no. November, pp. 289–294.

[177] A. M. El-refaie, T. M. Jahns, and D. Howe, "Winding Inductances of Fractional Slot Surface- Mounted Permanent Magnet Brushless Machines," pp. 1–8, 2008.

[178] C. Carstensen, "Eddy Currents in Windings of Switched Reluctance Machines," RWTH Aachen, 2007.

[179] D. Bauer, P. Mamuschkin, H.-C. Reuss, and E. Nolle, "Influence of parallel wire placement on the AC copper losses in electrical machines," in *2015 IEEE International Electric Machines & Drives Conference (IEMDC)*, May 2015, pp. 1247–1253. doi: 10.1109/IEMDC.2015.7409221.

[180] J. Swanke, H. Zeng, D. Bobba, T. M. Jahns, and B. Sarlioglu, "Design and Testing of a Modular High-Speed Permanent-Magnet Machine for Aerospace Propulsion," in *2021 IEEE International Electric Machines & Drives Conference (IEMDC)*, May 2021, pp. 1–8. doi: 10.1109/IEMDC47953.2021.9449536.

[181] Y. Cong *et al.*, "Submodule Design of a 2 kV 1 MW Integrated Modular Motor Drive for Aviation Applications," in *2021 IEEE 8th Workshop on Wide Bandgap Power Devices and Applications (WiPDA)*, Nov. 2021, pp. 345–350. doi: 10.1109/WiPDA49284.2021.9645119.

[182] Z. Yao, R. K. Mandel, and F. P. McCluskey, "In-slot Cooling for High Power Density Electric Motor with Encapsulation Channels," in *2022 21st IEEE Intersociety Conference on Thermal and Thermomechanical Phenomena in Electronic Systems (iTherm)*, May 2022, pp. 1–6. doi: 10.1109/iTherm54085.2022.9899559.

[183] Z. Yao, R. K. Mandel, and F. P. McCluskey, “Cooling Jacket for High Power Density Segmented Electric Motor,” in *2022 IEEE Transportation Electrification Conference & Expo (ITEC)*, Jun. 2022, pp. 1082–1086. doi: 10.1109/ITEC53557.2022.9814076.

[184] D. Bobba *et al.*, “Multi-Physics Based Analysis and Design of Stator Coil in High Power Density PMSM for Aircraft Propulsion Applications,” in *AIAA Propulsion and Energy 2021 Forum*, Aug. 2021, pp. 1–9. doi: 10.2514/6.2021-3306.

[185] SKF, “Bearing rating life.” https://www.skf.com/us/products/rolling-bearings/principles-of-rolling-bearing-selection/bearing-selection-process/bearing-size/size-selection-based-on-rating-life/bearing-rating-life (accessed Feb. 10, 2022).

[186] N. Simpson, R. Wrobel, and P. H. Mellor, “Estimation of Equivalent Thermal Parameters of Impregnated Electrical Windings,” *IEEE Trans. Ind. Appl.*, vol. 49, no. 6, pp. 2505–2515, Nov. 2013, doi: 10.1109/TIA.2013.2263271.

[187] W. Zhao, L. Xu, and G. Liu, “Overview of Permanent-Magnet Fault-Tolerant Machines: Topology and Design,” *CES Trans. Electr. Mach. Syst.*, vol. 2, no. 1, 2018, [Online]. Available: http://www.cestems.org/uploads/20180322/15216967147738.pdf

[188] M. R. Shah and A. M. EL-Refaie, “Eddy-Current Loss Minimization in Conducting Sleeves of Surface PM Machine Rotors With Fractional-Slot Concentrated Armature Windings by Optimal Axial Segmentation and Copper Cladding,” *IEEE Trans. Ind. Appl.*, vol. 45, no. 2, pp. 720–728, 2009, doi: 10.1109/TIA.2009.2013599.

[189] A. M. El-Refaie, M. R. Shah, Ronghai Qu, and J. M. Kern, “Effect of Number of Phases on Losses in Conducting Sleeves of Surface PM Machine Rotors Equipped With Fractional-Slot Concentrated Windings,” *IEEE Trans. Ind. Appl.*, vol. 44, no. 5, pp. 1522–1532, Sep. 2008, doi: 10.1109/TIA.2008.2002207.

[190] J. J. Wolmarans, M. Van Der Geest, H. Polinder, J. A. Ferreira, and D. Zeilstra, “Composite materials for low loss rotor construction,” *2011 IEEE Int. Electr. Mach. Drives Conf. IEMDC 2011*, pp. 295–299, 2011, doi: 10.1109/IEMDC.2011.5994862.

[191] B. Pratap and W. F. Weldon, “Eddy currents in anisotropic composites applied to pulsed machinery,” *IEEE Trans. Magn.*, vol. 32, no. 2, pp. 437–444, Mar. 1996, doi: 10.1109/20.486530.

[192] X. Tang and C. R. Sullivan, “Optimization of stranded-wire windings and comparison with litz wire on the basis of cost and loss,” *2004 IEEE 35th Annu. Power Electron. Spec. Conf.*, no. June, pp. 854–860, 2004, doi: 10.1109/PESC.2004.1355530.

[193] J. Martin, A. Yoon, A. Jin, and K. S. Haran, “High-Frequency Litz ‘Air-Gap’ Windings for High-Power Density Electrical Machines,” *Electr. Power Components Syst.*, vol. 45, no. 7, pp. 798–805, Apr. 2017, doi: 10.1080/15325008.2017.1310951.

[194] J. E. Vrancik, “Prediction of Windage Power Loss in Alternators,” no. NASA Technical Note D-4849. 1968.

[195] M. Popescu, D. Staton, A. Boglietti, A. Cavagnino, D. Hawkins, and J. Goss, “Modern heat extraction systems for electrical machines - A review,” in *2015 IEEE Workshop on Electrical Machines Design, Control and Diagnosis (WEMDCD)*, Mar. 2015, pp. 289–296.

doi: 10.1109/WEMDCD.2015.7194542.

[196] G. Nellis and S. Klein, *Heat Transfer*. Cambridge University Press, 2012.

[197] W. Rohsenow, J. Hartnett, and Y. Cho, *Handbook of Heat Transfer*, 3rd ed. McGraw-Hill, 1998.

[198] A. Carriero, M. Locatelli, K. Ramakrishnan, G. Mastinu, and M. Gobbi, "A Review of the State of the Art of Electric Traction Motors Cooling Techniques," *SAE Tech. Pap.*, pp. 1–13, Apr. 2018, doi: 10.4271/2018-01-0057.

[199] M. Michon, K. Atallah, and G. Johnstone, "Effects of unbalanced magnetic pull in large permanent magnet machines," in *2014 IEEE Energy Conversion Congress and Exposition (ECCE)*, Sep. 2014, pp. 4815–4820. doi: 10.1109/ECCE.2014.6954061.

[200] C. Lai, B. Aiswarya, B. Vicki, K. Lakshmi Varaha Iyer, and N. C. Kar, "Analysis of stator winding inter-turn short-circuit fault in interior and surface mounted permanent magnet traction machines," *2014 IEEE Transp. Electrif. Conf. Expo Components, Syst. Power Electron. - From Technol. to Bus. Public Policy, ITEC 2014*, pp. 1–6, 2014, doi: 10.1109/itec.2014.6861775.

[201] J. G. Cintron-Rivera, S. N. Foste, and E. G. Strangas, "Mitigation of turn-to-turn faults in fault tolerant permanent magnet synchronous motors," *IEEE Trans. Energy Convers.*, vol. 30, no. 2, pp. 465–475, 2015, doi: 10.1109/TEC.2014.2360813.

[202] C. Gerada, K. Bradley, and M. Sumner, "Winding turn-to-turn faults in permanent magnet synchronous machine drives," *Conf. Rec. - IAS Annu. Meet. (IEEE Ind. Appl. Soc.*, vol. 2, pp. 1029–1036, 2005, doi: 10.1109/IAS.2005.1518481.

[203] S. Foitzik and M. Doppelbauer, "Analytical model of a six-phase PMSM for the simulation of stator winding faults on turn level," *2019 IEEE Int. Electr. Mach. Drives Conf. IEMDC 2019*, pp. 185–191, 2019, doi: 10.1109/IEMDC.2019.8785351.

[204] Z. Q. Zhu and Y. X. Li, "Modularity Techniques in High Performance Permanent Magnet Machines and Applications," *CES Trans. Electr. Mach. Syst.*, vol. 2, no. 1, pp. 93–103, 2018, doi: 10.23919.

[205] E. Levi, "Multiphase Electric Machines for Variable-Speed Applications," *IEEE Trans. Ind. Electron.*, vol. 55, no. 5, pp. 1893–1909, May 2008, doi: 10.1109/TIE.2008.918488.

[206] J. Swanke, H. Zeng, and T. M. Jahns, "Modular Fault-Tolerant Machine Design with Improved Electromagnetic Isolation for Urban Air Mobility (UAM) Aircraft," in *2021 IEEE Energy Conversion Congress and Exposition (ECCE)*, Oct. 2021, no. 2, pp. 4570–4577. doi: 10.1109/ECCE47101.2021.9595489.

[207] J. Kammermann, I. Bolvashenkov, and H.-G. Herzog, "Approach for comparative analysis of electric traction machines," in *2015 International Conference on Electrical Systems for Aircraft, Railway, Ship Propulsion and Road Vehicles (ESARS)*, Mar. 2015, vol. 2015-May, pp. 1–5. doi: 10.1109/ESARS.2015.7101459.

[208] C. Justin *et al.*, "Reliability and Safety Assessment of Urban Air Mobility Concept Vehicles (NASA/CR-20210017185)," 2021. [Online]. Available:

https://ntrs.nasa.gov/citations/20210017185

[209] S. O'Donnell, J.-L. Debauche, P. Wheeler, and A. Castellazzi, "Silicon carbide MOSFETs in more electric aircraft power converters: The performance and reliability benefits over silicon IGBTs for a specified flight mission profile," in *2016 18th European Conference on Power Electronics and Applications (EPE'16 ECCE Europe)*, Sep. 2016, pp. 1–10. doi: 10.1109/EPE.2016.7695504.

[210] TDK, "Film Capacitors Series B32774...B32778 Datasheet," 2018. https://www.tdk-electronics.tdk.com/inf/20/20/db/fc_2009/MKP_B32774_778.pdf

[211] H. Wang and F. Blaabjerg, "Reliability of Capacitors for DC-Link Applications in Power Electronic Converters—An Overview," *IEEE Trans. Ind. Appl.*, vol. 50, no. 5, pp. 3569–3578, Sep. 2014, doi: 10.1109/TIA.2014.2308357.

[212] G. Moxey, "A Designers Guide to Silicon Carbide Power,", presented November 2020.

[213] D. A. Gajewski *et al.*, "SiC power device reliability," in *2016 IEEE International Integrated Reliability Workshop (IIRW)*, 2016, pp. 29–34. doi: 10.1109/IIRW.2016.7904895.

[214] MOOG Component Group, "Synchro and Resolver Engineering Handbook," 2004.

[215] D. Strömbergsson, "Improving detection and diagnosis of bearing failures in wind turbine drivetrains," Luleå University of Technology, 2020.

[216] C. Carlson, *Effective FMEAs: Achieving Safe, Reliable, and Economical Products and Processes Using Failure Mode and Effects Analysis*. Hoboken, New Jersey: John Wiley & Sons, Inc., 2012.

[217] B. J. Baliga, "Power semiconductor device figure of merit for high-frequency applications," *IEEE Electron Device Lett.*, vol. 10, no. 10, pp. 455–457, Oct. 1989, doi: 10.1109/55.43098.

[218] W. Sung, K. Han, and B. J. Baliga, "Optimization of the JFET region of 1.2kV SiC MOSFETs for improved high frequency figure of merit (HF-FOM)," in *2017 IEEE 5th Workshop on Wide Bandgap Power Devices and Applications (WiPDA)*, Oct. 2017, vol. 31, no. 7, pp. 238–241. doi: 10.1109/WiPDA.2017.8170553.

[219] J. Borcsok, E. Ugljesa, and D. Machmur, "Calculation of MTTF values with Markov Models for Safety Instrumented Systems," in *7th WSEAS International Conference on APPLIED COMPUTER SCIENCE*, 2007, pp. 30–35.

[220] J. E. Cousineau *et al.*, "Characterization of Contact and Bulk Thermal Resistance of Laminations for Electric Machines Characterization of Contact and Bulk Thermal Resistance of Laminations for Electric Machines," no. June, 2015.

[221] T. Mulholland, R. Felber, and N. Rudolph, "Design and additive manufacturing of a composite crossflow heat exchanger," in *Solid Freeform Fabrication 2017: Proceedings of the 28th Annual International Solid Freeform Fabrication Symposium - An Additive Manufacturing Conference, SFF 2017*, 2020, pp. 2641–2649.